Engineering Research: Perspectives on Recent Advances

Vol. 5

Edited by Prof. Hasan Köten

BP International

Engineering Research: Perspectives on Recent Advances

Vol. 5

Engineering Research: Perspectives on Recent Advances

Vol. 5

India ▪ United Kingdom

Editor(s)

Prof. Hasan Köten
Istanbul Medeniyet University, Türkiye.

FIRST EDITION 2025

ISBN 978-93-49473-44-7 (Print)
ISBN 978-93-49473-43-0 (eBook)
DOI: https://doi.org/10.9734/bpi/erpra/v5

© Copyright (2025): Author(s). The licensee is the publisher (BP International).

Peer-Review Policy: Advanced Open Peer Review policy has been followed for review. All manuscripts are thoroughly checked to prevent plagiarism. As per editorial policy, a minimum two peer-reviewers reviewed each manuscript. After review and revision of the manuscript, the Book Editor approved the manuscript for final publication.

Book Editor(s)
Prof. Hasan Köten
Istanbul Medeniyet University, Türkiye.

Chapter 1
Approved by
(1) Prof. Rajendra Prasad Devathoti, St. Ann's College of Engineering and Technology, India.
Reviewers
(1) Gizachew Diga Milki, Jimma University, Ethiopia.
(2) Arathi.P.B, Ballari Institute of Technology and Management, India.

Chapter 2
Approved by
(1) Prof. Aleksandr Nikolaevich Sekisov, Kuban State Agrarian University, Kuban State Technological University, Russia.
Reviewers
(1) R. Siti Rukayah, M.T., Universitas Diponegoro, Indonesia.
(2) Rasana Shrestha, Nepal.
(3) Philipe Queiroz Rodrigues, Universidade de Campinas – UNICAMP, Brazil.

Chapter 3
Approved by
(1) Dr. Choon Wah Yuen, University of Malaya, Malaysia.
(2) Prof. Aleksandr Nikolaevich Sekisov, Kuban State Agrarian University, Kuban State Technological University, Russia.
(3) Prof. Hasan Koten, Istanbul Medeniyet University, Turkiye.
Reviewers
(1) Kamyab Habibi, Behbahan Khatam Alanbia University of Technology, Iran.
(2) P. Laxmi Narayana, Aditya University, India.
(3) Habibeh Ghodsi, Kermanshah University of Technology, Iran.

Chapter 4
Approved by
(1) Dr. Bharatish A, RV College of Engineering, India.
Reviewers
(1) Jiajun Xu, Universiti Malaya, Malaysia.
(2) Elshan Orujov, Western Caspian University, Azerbaijan University, Azerbaijan.

Chapter 5
Approved by
(1) Prof. Aleksandr Nikolaevich Sekisov, Kuban State Agrarian University, Kuban State Technological University,Russia.
Reviewers
(1) M. Rajasekar, SIMATS University, India.
(2) Lalit Kumar, Maharishi Markandeshwar Deemed to be University, India.

Chapter 6
Approved by
(1) Dr. D.B. Jani, Gujarat Technological University, India.
Reviewers
(1) Mahendra Kumar Jangid, SLIET Longowal, India.
(2) Priyanka Das, USA.
(3) Krishnavamshi Ganduri, Woxsen University, India.
(4) Ranjit Barua, OmDayal Group of Institutions, India.

Chapter 7

Approved by

(1) Dr. Chien-Jen Wang, National University of Tainan, Taiwan.
(2) Prof. Hasan Koten, Istanbul Medeniyet University, Turkiye.
(3) Dr. D.B. Jani, Gujarat Technological University, India.

Reviewers

(1) Mehmet Alper Sofuoglu, Eskisehir Osmangazi University, Turkey.
(2) Muhammad Hanif, Shenzhen University, Pakistan.

Chapter 8

Approved by

(1) Prof. Huan-Liang Tsai, Da-Yeh University, Taiwan.

Reviewers

(1) Sanjay Dhanka, SLIET Longowal, India.
(2) J. Srinivas Rao, Anurag Engineering College, India.
(3) Vilas S. Bugade, SPPU, India.

Contents

ABOUT THE EDITOR

Prof. Hasan Köten
Istanbul Medeniyet University, Türkiye.

He was graduated from Mechanical Engineering Department with honor of degree in 2007. At the same time, he received a BSc degree in Electrical and Electronics Engineering Department as a double major. Hasan KOTEN worked in the first full geometry engine design project for The Scientific and Technological Research Council of Turkey (TUBITAK). During his Ph.D., he worked as a visiting scholar at the Ohio State University Center for Automotive Research (CAR). Hasan KÖTEN also worked as a consultant for TUBITAK Domestic Electric Vehicle Design project in 2017. He attended to CEDP group at Brunel University as a post-doctorate researcher in 2018. He leaded number of projects, MSc and PhD thesis in this combustion field. He attended and presented more than 150 conference proceedings and published about 100 articles indexed in SCI and SCI-e. He is awarded by TUBITAK 2238 programme with first degree over all national PhD thesis applications. Also, he worked in CCRC, KAUST, Saudi Arabia and in University Applied Science in Germany as visiting professor. He has many patents in the field of energy systems. Dr. Hasan KÖTEN is still working at the mechanical engineering department of Istanbul Medeniyet University. Currently, He is working at Turkey's largest TÜBİTAK budgeted 2400HP 16 and 8-cylinder engine production project.
ORCID: 0000-0002-1907-9420

PREFACE

This book covers key areas of engineering research. The contributions by the authors include scour protection, downstream stilling basins, hydraulic jump, pre-engineered buildings, dynamic loading, euro code model, seismic load, design principles, floor plan, world cultural heritage, medium-voltage testbed, electrical grid events, smart grid, total harmonic distortion, novel robotic fish, PVC gel actuators, swimming mechanisms, robotic fish propulsion, pillar stability assessment, rheological behaviour, interaction principle, dry turning, EN19 steel material, sustainable manufacturing, energy efficiency, machining strategy, multilevel inverter, E-T type inverter circuit, neutral point clamped, total harmonic distortion. This book contains various materials suitable for students, researchers, and academicians in the fields of engineering research.

Chapter 1
Print ISBN: 978-93-49473-44-7, eBook ISBN: 978-93-49473-43-0

Medium-Voltage Testbed for Comparing Advanced Power Line Sensors vs. Measurement Transformers with Electrical Grid Events

Emilio C. Piesciorovsky [a*], R. J. BruceWarmack [a] and Yarom Polsky [b]

DOI: https://doi.org/10.9734/bpi/erpra/v5/4054

Peer-Review History:
This chapter was reviewed by following the Advanced Open Peer Review policy. This chapter was thoroughly checked to prevent plagiarism. As per editorial policy, a minimum of two peer-reviewers reviewed the manuscript. After review and revision of the manuscript, the Book Editor approved the manuscript for final publication. Peer review comments, comments of the editor(s), etc. are available here: https://peerreviewarchive.com/review-history/4054

ABSTRACT

Electrical utilities have relied upon potential transformers (PTs) and current transformers (CTs) for very accurate metering and to provide reliable signals for protective relays. These devices measure phase voltages and currents and are commissioned by electrical engineers. PTs/CTs can detect and react to various electrical anomalies that could adversely affect electrical grid operations. Less expensive alternative sensing technologies offer the possibility of wider deployment, particularly in grids that employ distributed energy resources. In this work, the performance of an advanced medium-voltage sensor is compared with that of a reference PT and a CT and experimentally evaluated for different power grid scenarios on an advanced outdoor power line sensor testbed at the U.S. Department of Energy's Oak Ridge National Laboratory. The sensor is based on a capacitive divider for voltage monitoring and a Rogowski coil with an integrator for current monitoring. This study simulated a power grid model based on a utility circuit at the Riverside EPB of Chattanooga. The simulation circuit was created with MATLAB/Simulink software and was integrated into an RT-LAB project to run with the OP4510 real-time simulator at the OPLST. During the tests, the real-time simulations were run for 40 s, and the signal to record the test event with the power meter was set at 30 s for the event-trigger circuit. The advanced outdoor power line sensor testbed has a real-time simulator that is used to generate transient scenarios (e.g., electrical faults, capacitor bank operation, and service

[a] *Oak Ridge National Laboratory, Electrification and Energy Infrastructures Division, One Bethel Valley Road, Oak Ridge, TN 37831, USA.*
[b] *Oak Ridge National Laboratory, Manufacturing Science Division, One Bethel Valley Road, Oak Ridge, TN 37831, USA.*
**Corresponding author: E-mail: piesciorovec@ornl.gov;*

restoration), while the analog signals are recorded by the same high-resolution power meter. The behaviors of analog signals, harmonic components, total harmonic distortion, and crest factors are assessed for this power line sensor and compared with those of the reference PT/CT because of the absence of testing standards for advanced outdoor power line sensors. The results showed that this OPLS technology responded identically to the PT and CT under all conditions.

Keywords: Sensors; monitoring and instrumentation; smart grid; simulation; testbeds.

NOMENCLATURES

Abbreviations:

CTR : Current Transformer Ratio
CT/s : Current Transformer(s)
DECC : Distributed Energy Communications and controls
EPB : Electric Power Board
LL : Line to Line
LLG : Line to Line Ground
OPLS : Outdoor Power Line Sensor
ORNL : Oak Ridge National Laboratory
PT/s : Potential Transformer/s
RMS : Root Mean Square
SEL : Schweitzer Engineering Laboratories
SLG : Single Line to Ground
3LG : Three Lines to Ground

Symbols:

CFI : Crest Factor of the Current Signal (A/A)
CFICT : Line Current Crest Factor of the CT (A/A)
CFIOPLS : Line Current Crest Factor of the OPLS (A/A)
CFVPT : Phase Voltage Crest Factor of the PT (V/V)
CFVOPLS : Phase Voltage Crest Factor of the OPLS (V/V)
CFV : Crest Factor of the Voltage Signal (V/V)
CGCA : Current Gain of the Current Amplifier for the OP4510 Real-time Simulator (V/A)
CGCT : Current Gain of the CT for the OP4510 Real-time Simulator (Unitless)
CGG : Current Gain of the Simulated Medium-voltage Loop Circuit or Power Grid for the OP4510 Real-time Simulator (V/A)
CGS : Current Gain of the OPLS for the OP4510 Real-time Simulator (Unitless)
CSFS : Current Scaling Factor of the OPLS (A/V)
CSFM : Current Scaling Factor of the SEL-735 Power Meter (A/V)

CSFU866 : Current Scaling Factor of the Ultrastab 866 Precision Current Transducer (A/V)
CTR : Current Transformer Ratio for the Simulated inverse time Overcurrent Relay (unitless)
CTratio : Current Transfer Ratio of the Ultrastab 866 Precision Current Transducer (unitless)
CTRL : Ratio of CT Connected between the Current Amplifier and Medium-Voltage Aerial Cable Loop (unitless)
CTRM : CT Ratio Set in the SEL-735 Power Meter (unitless)
E%CFI : Percentage Error of the Line Current Crest Factor (%)
E%CFV : Percentage Error of the Phase Voltage Crest Factor (%)
E%THDI : Percent Error of the Line Current Total Harmonic Distortion (%)
E%THDV : Percentage Error of the Phase Voltage Total Harmonic Distortion (%)
*GADJ : Adjusted Voltage or Current Gains of the Simulated Grid and PT/CT for the OP4510 Real-time Simulator (V/V or V/A or Unitless *) *for the PT/CT, Using Equations (15) and (18)*
G0ADJ : Adjusted Voltage or Current Gains of Amplifiers for the OP4510 Real-time Simulator (V/V or V/A)
GCA : Selected Gain of the Current Amplifier (A/V)
GCALC : Calculated Voltage or Current Gains (V/V or V/A or unitless) *for PT/CT, Using Equations (15) and (18)*
G0CALC : Calculated Voltage or Current Gains of Amplifiers (V/V or V/A)
GVA : Selected gain of the Voltage Amplifier (V/V)
I1 : Line Current Magnitude of the Fundamental Signal (A)
Iinput : Input Current (A)
In : Line Current Magnitude of the nth Generic Harmonic Component Signal (A)
In% : Individual Harmonic Component of the nth Generic Harmonic for the Line Current Signal (%)
Ip : Relay Current Pickup (A)
Ipeak : Peak Value of the Current (A)
Iprimary : Primary Current (A)
Irms : RMS Value of the Current (A)
MH : Measured Phase B Voltage or Current Values that Were Collected by Using the High-voltage/current Interfaces (V or A)
ML : Measured Phase A/B Voltage or Current that were Collected by Using the Low-voltage Interface (V or A)
Nturns : Number of Turns of Primary Cable (Turns)
PTRL : Ratio of PT Connected between the Voltage Amplifier and Medium-Voltage Aerial Cable Loop (unitless)
PTRM : PT Ratio set in the SEL-735 Power Meter (unitless)
SGRID : Simulated Phase Voltage or Current Values that were Measured from the Voltage and Current Displays of the 20/34.5 kV Loop Circuit (V or A)
TDS : Time Dial Setting (s)
THDI : Total Harmonic Distortion of the Line Current Signal (%)
THDICT : Line Current Total Harmonic Distortion of the CT (%)

THDIOPLS : Line Current Total Harmonic Distortion of the OPLS (%)
THDVOPLS : Phase Voltage total Harmonic Distortion of the OPLS (%)
THDV : Total Harmonic Distortion of the Phase Voltage Signal (%)
THDVPT : Phase Voltage total Harmonic Distortion of the PT (%)
TR : Relay Time (cycles)
V1 : Phase Voltage Magnitude of the Fundamental Signal (V)
VGG : Voltage Gain of the Simulated Medium-voltage Loop Circuit or Power Grid for the OP4510 Real-time Simulator (V/V)
VGVA : Voltage Gain of the Voltage Amplifier for the OP4510 Real-time Simulator (V/V)
VGPT : Voltage Gain of the PT for the OP4510 Real-time Simulator (Unitless)
VGS : Voltage Gain of the OPLS for the OP4510 Real-time Simulator (unitless)
Vn : Phase Voltage Magnitude of the nth Generic Harmonic Component signal (V)
Vn% : Individual Harmonic Component of the nth Generic Harmonic for the Phase Voltage Signal (%)
Voutput : Output Voltage (V)
Vpeak : Peak Value of the Voltage Signal (V)
Vrms : RMS Value of the Voltage Signal (V)
VSFDP : Voltage Scaling Factor of the Model 4232 Voltage Differential Probe (V/V)
VSFM : Voltage Scaling Factor of the SEL-735 Power Meter (V/V)
VSFS : Voltage Scaling Factor of the OPLS (V/V)
Zburden : Burden External Resistor Impedance (W)

1. INTRODUCTION

In electrical engineering, the protective relay is a relay device designed to trip a circuit breaker when a fault is detected, and has the ability to measure the power system quantities through the internal logic of a microprocessor (Sheryar et al., 2022; Shadfar et al., 2021). In electrical substations, protective relays (or power meters) are metered via potential transformers (PTs) and current transformers (CTs). These devices measure phase voltages and currents and are commissioned by electrical engineers (Atwa, 2019). PTs/CTs can detect and react to various electrical anomalies that could adversely affect electrical grid operations. However, most protective relays have low sampling frequencies and cannot detect high harmonic events, which may be related to incipient power outages (Piesciorovsky & Karnowski, 2021). For protective relays and power meters, the computational process that measures transient events with high-frequency components at electrical faults must process the phase voltage and current signals using small time steps (Piesciorovsky et al., 2023). The Nyquist sampling theorem (Das, 2016) indicates that the sampling frequency of a signal should be at least twice the highest frequency of the signal to avoid aliasing (Das, 2016). Another aspect of measuring transformers built using magnetic iron cores is that the performance of CTs can be affected by the magnetic saturation errors caused by high current faults in the power grid (Hargrave et al., 2018;

Altuve et al., 2013) yielding ratio, and phase-angle errors (IEEE, 2016), especially during transient power grid events.

Moving towards a sustainable society implies constant improvement in the way energy is supplied and consumed, with wider implementation of solar and wind energy facilities in stand-alone or hybrid configurations (Torres & Petrakopoulou, 2022). The global use of solar and wind power has rapidly grown, accelerating in recent years (Timmons et al., 2014). With the growth of solar and wind power generation, the penetration of inverter-based distributed energy resources and electronic solid-state switches to control microgrid systems has also increased (Piesciorovsky et al., 2020). These devices could introduce high harmonic components into microgrids, which can affect the power quality and grid reliability (Hong & Zuercher-Martinson, n.d.). Consequently, using more accurate high-speed sensors to measure and control the electrical power grids is crucial for detecting these events (Piesciorovsky et al., 2023).

In electrical utility substations and laboratories, PT and CT test equipment has been used by electrical engineers to assess traditional measurement transformers for several decades (Sze, 1965; Souders, 1971). Today, PT and CT test equipment involves microprocessor-based single-phase or three-phase turn ratio testers that allow for assessing PTs/CTs (Vanguard Instruments, 2018; OMICRON, n.d.). PT and CT test equipment analyzes the PT/CT by injecting analog signals into the PT/CT and determining their equivalent circuit parameters and performance. CT test equipment can determine different parameters such as voltage excitation, ratio, polarity, phase angle, and winding resistance, and perform insulation measurement (Vanguard Instruments Company Inc., 2020). PT test equipment can determine several parameters such as current excitation, ratio, polarity, power factor, and winding resistance, and perform insulation measurements (Heuston, 2007). Generally, the research testbeds used for power line sensors are set on indoor sites instead of outdoor sites. In such cases, sensors are only tested in a room environment instead of under real-weather conditions and gauge the magnitude and phase of voltage/current signals under limited conditions (Parker & McCollough, 2011). Furthermore, these research testbeds do not compare outdoor power line sensors (OPLSs) in real outdoor environments at seasonal temperatures and solar radiation conditions (Piesciorovsky et al., 2023). In addition, the absence of testing standards for the advanced OPLSs in the market could be replaced by comparing their voltage and current measurements from CTs/PTs in a testbed at the same time for different electrical events.

Today's voltage and current sensing solutions include optical sensors, air-core coil-based sensors, resistive and capacitive dividers, and hybrid solutions that have received interest for use in the digital electrical power grid (Rahmatian, 2011). Some electrical utilities have increasingly started to install these new sensor technologies for experimental monitoring; the Electrical Power Board (EPB) of Chattanooga installed optical power line sensors (26.6 kV phase-to-neutral voltage) to measure the line currents and voltages at the 46 kV EPB Chattanooga electrical substation (Piesciorovsky & Morales Rodriguez, 2022).

Advanced sensor technologies have focused on simplifying the installation of the sensors, improving the reliability of power delivery, enhancing the detection of electrical faults, and observing transient events (Piesciorovsky et al., 2023). However, it has yet to be determined whether these advanced power line sensors can replace or supplement traditional PTs/CTs in electric distribution systems for anomaly detection and/or transient events with high-frequency components. Therefore, traditional PTs/CTs must be compared with advanced voltage/current sensors to assess the ability of these new technologies to respond to steady-state operation and transient events. Using the novel OPLS testbed (OPLST) over a full range of operating conditions, this study compared new power line sensors with iron-core PTs/CTs up to 20 kV line-to-ground or 34.5 kV line-to-line.

In this study, an OPLST with an Opal-RT OP4510 real-time simulator and Schweitzer SEL-735 power meter was constructed at the Distributed Energy Communications and Controls (DECC) laboratory, located at the main campus of Oak Ridge National Laboratory (ORNL). This medium-voltage OPLST consisted of an aluminum aerial cable that passed current through the equipment under test while being floated to medium-voltage (Piesciorovsky et al., 2023). The current and voltage were both driven by amplifiers that were driven by signals from the simulator. The outdoor PTs/CTs together with advanced power line sensors were connected along this aerial cable loop. The OPLST with a real-time simulator and power meter allowed for testing conventional PT/CT and advanced power line sensors under different electrical grid operation conditions such as electrical faults, capacitor banks connection, and energy restoring services.

The main novelty of this testbed is based on assessing the current and voltage measurement behavior of a new commercial power line sensor that did not have testing procedures or standards; therefore, advanced power line sensors were compared with the PT/CT measurement transformers that were commonly used by electrical utilities and tested based on testing standards (Piesciorovsky et al., 2023). Another important aspect is the possibility of comparing advanced OPLS versus the PT/CT for different electrical grid events by observing their behavior with a high-resolution power meter. Table 1 shows the novelties of the OPLST, indicating types of tests and metering.

In the medium-voltage OPLST, the analog signals from the outdoor 20/34.5 kV PT (ratio = 175V:1V, accuracy = 0.15Y) and CT (ratio = 400A/5A, accuracy = 0.15SB − 1.8) were measured and compared with those of the OPLS. The OPLST with a real-time simulator and a high sampling frequency power meter has the advantage that electrical grid transient event tests can be simulated and performed as often as desired, instead of at an electrical substation site where events only rarely occur (Piesciorovsky et al., 2023). Because the OPLST is single-phase, the sequential playback of events is performed for each of the phases (A, B, or C). In this OPLST, the analog signals from the real-time simulator were amplified in two steps: first by the voltage/current amplifiers and then by a PT/CT that injected the voltage and current signals to the aerial cable loop.

Table 1. Novelties of the advanced medium-voltage outdoor power line sensor testbed

Methods	Types	Advanced Medium-Voltage Outdoor Power Line Sensor Testbed
20/34.5 kV OPLST with real-time simulator and power meter	Tests	• Comparison of OPLS vs. CT/PT • Outdoor testing in real weather conditions
	Metering	• Measurement of power grid test scenarios such as electrical faults (SLG, LLG, LL, 3LG), load feeder, and capacitor bank breaker operations. • Measurement of voltage and current signals with up to 512 samples/cycle. • Measurement of total harmonic distortion for voltage and current signals. • Measurement of crest factor for voltage and current signals.

OPLS: outdoor power line sensor, OPLST: outdoor power line sensor testbed, CT: current transformer, PT: potential transformer, NA: not available, SLG: single line to ground, LLG: line to line ground, LL: line to line, 3LG: three lines to ground.

2. METHODOLOGY

2.1 Individual Harmonic Component

The individual harmonic components for voltage and current signals are usually plotted in frequency plots for harmonic analysis (Piesciorovsky et al., 2023). The individual harmonic components for the voltage and current signals are defined as the percentage at the nth generic harmonic component with respect to the fundamental signal of 60 Hz. The individual harmonic components of the voltage and current signals are calculated via Equations (1) and (2), respectively.

$$V_{n\%} = \left(\frac{V_n}{V_1}\right) 100\ \% \tag{1}$$

where $V_{n\%}$ is the individual harmonic component of the nth generic harmonic for the phase voltage signal in percent, V_n is the phase voltage magnitude of the nth generic harmonic component signal in volts, and V_1 is the phase voltage magnitude of the fundamental signal in volts.

$$I_{n\%} = \left(\frac{I_n}{I_1}\right) 100\ \% \tag{2}$$

where $I_{n\%}$ is the individual harmonic component of the nth generic harmonic for the line current signal in percent, I_n is the line current magnitude of the nth generic harmonic component signal in amps, and I_1 is the line current magnitude of the fundamental signal in amps.

2.2 Total Harmonic Distortion Factor

In this study, the total harmonic distortion for phase voltage and current signals for different power grid scenarios were compared between the PT/CT and OPLS.

In power grid systems, voltages and currents have harmonics with frequencies that are integer multiples of the waveform's fundamental frequency (Piesciorovsky et al., 2023). For example, given a 60 Hz fundamental waveform, the second, third, fourth, and fifth harmonic components occur at 120, 180, 240, and 300 Hz, respectively. The total harmonic distortion is the degree to which a waveform deviates from a pure sinusoid at its fundamental frequency (e.g., 60 Hz) and is calculated from the sum of all harmonic components of the voltage or current waveform divided by the corresponding fundamental component. The total harmonic distortion for the phase voltage and current signals can be estimated using Equations (3) and (4), respectively.

$$THD_V = \left(\frac{\sqrt{\sum_{n=2}^{m} V_n^2}}{V_1} \right) 100\ \% \tag{3}$$

where THD_V is total harmonic distortion of the phase voltage signal in percent, V_n is the phase voltage magnitude of the nth generic harmonic component signal in volts, V_1 is the phase voltage magnitude of the fundamental signal in volts, and m is the harmonic limit to perform the summation in the numerator.

$$THD_I = \left(\frac{\sqrt{\sum_{n=2}^{m} I_n^2}}{I_1} \right) 100\ \% \tag{4}$$

where THD_I is total harmonic distortion of the line current signal in percent, I_n is the line current magnitude of the nth generic harmonic component signal in amps, I_1 is the line current magnitude of the fundamental signal in amps, and m is the harmonic limit to perform the summation in the numerator.

2.3 Total Harmonic Distortion Factor

In this study, the crest factor for the voltage and current signals for different power grid scenarios was compared for the PT/CT vs. the OPLS. The crest factor is defined as the ratio between the peak amplitude value and its root mean square (RMS) value (Piesciorovsky et al., 2023). The crest factor of a perfect sinusoid is 1.414. The crest factor for the voltage and current signals can be estimated using Equations (5) and (6), respectively.

$$CF_V = \frac{V_{peak}}{V_{rms}} \tag{5}$$

where CF_V is the crest factor of the voltage signal in volts/volt, V_{peak} is the peak value of the voltage signal in volts, and V_{rms} is the RMS value of the voltage signal in volts.

$$CF_I = \frac{I_{peak}}{I_{rms}} \tag{6}$$

where CF_I is the crest factor of the current signal in amps/amps, I_{peak} is the peak value of the current in amps, and I_{rms} is the RMS value of the current in amps.

2.4 Percentage Errors of Total Harmonic Distortion and Crest Factor

In this study, the percentage errors for the total harmonic distortion and crest factor of the measured phase voltage/current signals between the PT/CT and the OPLS were calculated (Piesciorovsky et al., 2023). The percentage error for the total harmonic distortion of the measured phase voltage/current can be estimated by Equations (7) and (8), respectively.

$$E_{\%THDV} = \frac{THD_{VOPLS} - THD_{VPT}}{THD_{VPT}} \% \quad (7)$$

where $E_{\%THDV}$ is the percentage error of the phase voltage total harmonic distortion in percent, THD_{VOPLS} is the phase voltage total harmonic distortion of the OPLS in percent, and THD_{VPT} is the phase voltage total harmonic distortion of the PT in percent.

$$E_{\%THDI} = \frac{THD_{IOPLS} - THD_{ICT}}{THD_{ICT}} \% \quad (8)$$

where $E_{\%THDI}$ is the percentage error of the line current total harmonic distortion in percent, THD_{IOPLS} is the line current total harmonic distortion of the OPLS in percent, and THD_{ICT} is the line current total harmonic distortion of the CT in percent.

Consequently, the percentage error for the crest factor of the measured phase voltage and current signals can be estimated by Equations (9) and (10), respectively.

$$E_{\%CFV} = \left(\frac{CF_{VOPLS} - CF_{VPT}}{CF_{VPT}}\right) 100 \% \quad (9)$$

where $E_{\%CFV}$ is the percentage error of the phase voltage crest factor in percent, CF_{VOPLS} is the phase voltage crest factor of the OPLS in volts/volt, and CF_{VPT} is the phase voltage crest factor of the PT in volts/volt.

$$E_{\%CFI} = \left(\frac{CF_{IOPLS} - CF_{ICT}}{CF_{ICT}}\right) 100 \% \quad (10)$$

where $E_{\%CFI}$ is the percentage error of the line current crest factor in percent, CF_{IOPLS} is the line current crest factor of the OPLS in amps/amps, and CF_{ICT} is the line current crest factor of the CT in amps/amps.

3. MATERIALS

3.1 Diagram of Medium-Voltage Outdoor Power Line Sensor Testbed

Fig. 1 shows a diagram of the medium-voltage OPLST. The area outside the dashed line (Fig. 1a) shows the 20/34.5 kV aerial cable loop with the PTs/CTs

and the OPLS. The area inside the dashed line (Fig. 1b) shows the equipment installed in the rack unit (indoor), including an OP4510 real-time simulator, an SEL-735 power meter, and current/voltage amplifiers (Piesciorovsky et al., 2023). The OP4510 real-time simulator was connected to a host computer to run the tests, and the SEL-735 power meter was connected to another computer to collect the events after running the tests. The analog inputs of the OP4510 real-time simulator were connected to the PT/CT and to the OPLS, and the analog outputs were connected to the power meter and voltage/current amplifiers (Fig. 1b). The SEL-735 power meter was connected to the high-voltage/current interface and to the low-voltage interface. Fig. 1b shows that by opening the switch of the low-voltage interface, the high-current/voltage interface was enabled, and it was used to adjust the gains of the amplifiers (CG_{CA} and VG_{VA}) for the real-time simulator (Piesciorovsky et al., 2023). However, by closing the switch of the low-voltage interface, the high-current/voltage interface was disabled, and the low-voltage interface was used to adjust the gains of the simulated medium-voltage loop circuit or power grid (CG_G, VG_G) and PT/CT (VG_{PT}, CG_{CT}) for the real-time simulator. As shown in Fig. 1b, the voltage (VG_{VA}, VG_G, VG_{PT}, VG_S) and current (CG_{CA}, CG_G, CG_{CT}, CG_S) gains for analog outputs were calculated to set the RT-LAB project in the OP4510 real-time simulator. The gains to connect the SEL-735 power meter were calculated using the voltage (750 *V*/*V*) and current (16.53 *A*/*V*) scaling factors of the low-voltage interface. The gains to connect the voltage/current amplifiers were calculated using the amplifier gains and PT/CT ratios that were wired between the amplifiers and the medium-voltage aerial cable loop. From the low-voltage interface of the power meter (Fig. 1b), phase A measured the voltage/current of the simulated medium-voltage loop circuit or power grid, phase B measured the voltage/current of the PT/CT, and phase C measured the voltage/current of the OPLS (Piesciorovsky et al., 2023). To record the phase A, B, and C voltage/current signals during the tests, the OP4510 real-time simulator generated a 16 VDC signal (Fig. 1b) that allowed the recording of the test events inside the SEL-735 power meter.

3.2 Voltage and Current Gains for the Real-Time Simulator

In the medium-voltage OPLST, the OP4510 real-time simulator (Fig. 1b) was the main interconnection used to adapt the voltage and current signals from all devices. The voltage and current gains were calculated for the low-voltage interface of the SEL-735 power meter and the voltage/current amplifiers. The gains of the amplifiers, power grid, and PT/CT for the OP4510 real-time simulator were calculated (Piesciorovsky et al., 2023). The voltage and current gains were calculated and then adjusted using the OP4510 real-time simulator and SEL-735 power meter. Table 2 shows the voltage and current gains of the OP4510 real-time simulator.

3.3 Calculation of Voltage and Current Gains for Amplifiers at the Real-Time Simulator

The voltage and current amplifiers used in OPLST are the AE TECHRON Model 7228 (AE Techron, 2020). These linear amplifiers can be used as single units or

connected in series or parallel to increase the voltage and current outputs, respectively. Here, these amplifiers were used as single units by connecting one as a voltage-to-current amplifier and another as a voltage amplifier (Piesciorovsky et al., 2023). The manufacturer default voltage and current gains of these amplifiers are 20 *v/v* and 5 A/V, respectively (AE Techron, 2020). However, these gains were set by the gain control knob that can change the gain from 0% to 100% (AE Techron, 2020). The voltage and current gains were set at approximately 20 *v/v* and 0.11 *A/V*, respectively. The voltage (VG_{VA}) and current (CG_{CA}) gains of the amplifiers for the OP4510 real-time simulator were calculated by using Equations (11) and (12), respectively.

$$VG_{VA} = \frac{1}{G_{VA}\,(PTR_L)} = \frac{1}{20\,\frac{V}{V}\;(175)} = 0.00028571\,\frac{V}{V} \tag{11}$$

where the VG_{VA} is the voltage gain of the voltage amplifier for the OP4510 real-time simulator in volts/volt, G_{VA} is the selected gain of the voltage amplifier in volts/volt, and PTR_L is the ratio of PT connected between the voltage amplifier and medium-voltage aerial cable loop.

$$CG_{CA} = \frac{1}{G_{CA}\,(CTR_L)} = \frac{1}{0.11\,\frac{A}{V}\;(80)} = 0.11363636\,\frac{V}{A} \tag{12}$$

where the CG_{CA} is the current gain of the current amplifier for the OP4510 real-time simulator in volts/amp, G_{CA} is the selected gain of the current amplifier in amps/volt, and CTR_L is the ratio of CT connected between the current amplifier and medium-voltage aerial cable loop.

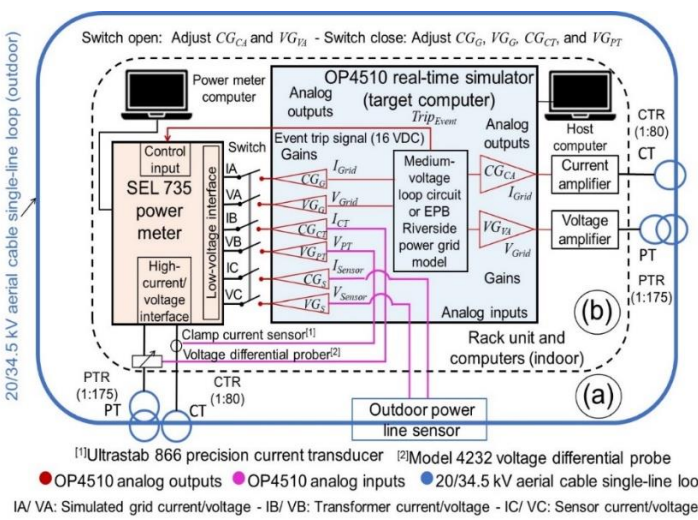

Fig. 1. Diagram of testbed with 20/34.5 kV aerial cable loop (a) and rack unit (b)

Table 2. Voltage and current gains for the OP4510 real-time simulator

Gains (ID)	Gain Interface	Gain Area	Gain Function	Calculated Gains	Equation
Voltage gain of voltage amplifier (VG_{VA})	20/34.5 kV aerial cable loop	Grid simulation	To scale voltage signal from simulated power grid to voltage amplifier and PT	0.00028571 0.00028492 *	(11)
Current gain of current amplifier (CG_{CA})			To scale current signal from simulated power grid to current amplifier and CT	0.11363636 0.11172054 *	(12)
Voltage gain of the simulated grid (VG_G)	Low-voltage interface of SEL-735 power meter	Grid simulation	To scale voltage signal from the simulated power grid to SEL-735 power meter ▲	1/131250 1/130903 *	(13)
Current gain of the simulated grid (CG_G)			To scale current signal from the simulated power grid to SEL-735 power meter ▲	1/1322.4 1/1315.5 *	(14)
Voltage gain of the PT (VG_{PT})		PT/CT	To scale voltage signal from the PT to SEL-735 power meter ▲	0.13333333 0.13383402 *	(15)
Current gain of the CT (CG_{CT})			To scale current signal from the CT to SEL-735 power meter ▲	0.30248033 0.30130787 *	(18)
Voltage gain of the OPLS (VG_S)		Outdoor power line sensor (OPLS)	To scale voltage signal from the OPLS to SEL-735 power meter ▲	0.038095	(19)
Current gain of the OPLS (CG_S)			To scale current signal from the OPLS to SEL-735 power meter ▲	2.520	(20)

** Adjusted gains, ▲ Connected to the low-voltage interface of the SEL-735 power meter.*

3.4 Calculation of Voltage and Current Gains for Power Meter at the Real Time Simulator

In the OPLST (Fig. 1), the SEL-735 power meter measured the voltage and current signals, and the OP4510 real-time simulator was the main interface between the SEL-735 power meter and the testbed devices. Therefore, the voltage/current gains for the OP4510 real-time simulator were calculated based on Table 2 (Piesciorovsky et al., 2023). The voltage and current gains of the simulated medium-voltage loop circuit or power grid for the OP4510 real-time simulator were calculated by Equations (13) and (14), respectively.

$$VG_G = \frac{1}{VSF_M\ (PTR_M)} = \frac{1}{750\frac{V}{V}\ (175)} = \frac{1}{131250} = 7.619\ \times 10^{-6}\frac{V}{V} \tag{13}$$

where the VG_G is the voltage gain of the simulated medium-voltage loop circuit or power grid for the OP4510 real-time simulator in volts/volt, VSF_M is the voltage scaling factor of the SEL-735 power meter in volts/volt, and PTR_M is the PT ratio set in the SEL-735 power meter.

$$CG_G = \frac{1}{CSF_M\ (CTR_M)} = \frac{1}{16.53\frac{A}{V}\ (80)} = \frac{1}{1322.4} = 7.562 \times 10^{-4}\frac{V}{A} \tag{14}$$

where the CG_G is the current gain of the simulated medium-voltage loop circuit or power grid for the OP4510 real-time simulator in volts/amp, CSF_M is the current scaling factor of the SEL-735 power meter in amps/volt, and CTR_M is the CT ratio set in the SEL-735 power meter.

The voltage and current gains of the PT/CT for the OP4510 real-time simulator were calculated to connect the PT/CT signals at the low-voltage interface of the SEL-735 power meter. Therefore, a differential voltage probe and clamp current sensor were used to collect the PT/CT signals with the OP4510 real-time simulator (Fig. 1b) (Piesciorovsky et al., 2023). For the PT connected to the SEL-735 power meter (Fig. 1b), the voltage signal was collected using a Model 4232 differential voltage probe (Probe Master, n.d.) that had a voltage scaling factor of 100 V/V. The voltage gain of the PT for the OP4510 real-time simulator is given by Equation (15).

$$VG_{PT} = \frac{VSF_{DP}}{VSF_M} = \frac{100\frac{V}{V}}{750\frac{V}{V}} = 0.13333333 \tag{15}$$

where the VG_{PT} is the voltage gain of the PT for the OP4510 real-time simulator, VSF_{DP} is the voltage scaling factor of the Model 4232 voltage differential probe in volts/volt, and VSF_M is the voltage scaling factor of the SEL-735 power meter in volts/volt.

For the CT connected to the SEL-735 power meter (Fig. 1b), the current signal was collected with an Ultrastab 866 precision current transducer (Ultrastab, n.d.) with a current transfer ratio of 1500:1, three turns of primary cable, and a burden external resistor impedance of 100 Ω. Fig. 2 shows the circuit of the Ultrastab 866 precision current transducer (Piesciorovsky et al., 2023).

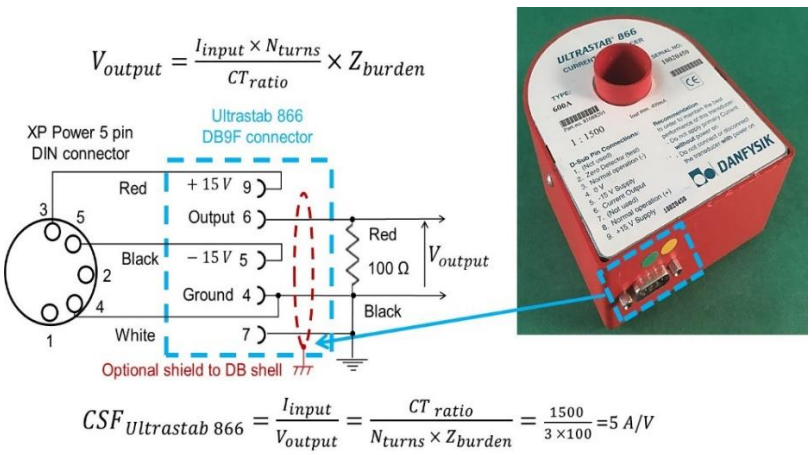

Fig. 2. Circuit of the Ultrastab 866 precision current transducer

From Fig. 2 and Equations (16) and (17), the current scaling factor of the Ultrastab 866 precision current transducer (CSF_{U866}) was determined to be 5 *A*/*V*.

$$V_{output} = \left(\frac{I_{input}\,(N_{turns})}{CT_{ratio}}\right) Z_{burden} \tag{16}$$

$$CSF_{U866} = \frac{I_{input}}{V_{output}} = \frac{CT_{ratio}}{N_{turns}\,(Z_{burden})} = \frac{1500}{3\,(100)} = 5\frac{A}{V} \tag{17}$$

where V_{output} is the output voltage in volts, I_{input} is the input current in amps, N_{turns} is the number of turns of primary cable, CT_{ratio} is the current transfer ratio of the Ultrastab 866 precision current transducer (1500:1), CSF_{U866} is the current scaling factor of the Ultrastab 866 precision current transducer in amps/volt, and Z_{burden} is the burden external resistor impedance in ohms.

Because the CT was connected to the Ultrastab 866 precision current transducer, the current gain of the CT for the OP4510 real-time simulator was calculated using Equation (18).

$$CG_{CT} = \frac{CSF_{U866}}{CSF_M} = \frac{5\frac{A}{V}}{16.53\frac{A}{V}} = 0.30248033 \tag{18}$$

where the CG_{CT} is the current gain of the CT for the OP4510 real-time simulator, CSF_{U866} is the current scaling factor of the Ultrastab 866 precision current transducer in amps/volt, and CSF_M is the current scaling factor of the SEL-735 power meter in amps/volt.

The voltage and current gains of the OPLS for the OP4510 real-time simulator were calculated using Equations (19) and (20), respectively (Piesciorovsky et al., 2023). This calculation process required the voltage (5000 *V*/*V*) and current (3333.3 *A*/*V*) scaling factors of the OPLS, voltage (750 *V*/*V*) and current (16.53 *A*/*V*) scaling factors of the SEL-735 power meter, and the PT (175:1) and CT (80:1) ratios set in the SEL-735 power meter.

$$VG_S = \frac{VSF_S}{VSF_M\ (PTR_M)} = \frac{5000\frac{V}{V}}{750\frac{V}{V}\ (175)} = 0.038095 \tag{19}$$

where the VG_S is the voltage gain of the OPLS for the OP4510 real-time simulator, VSF_S is the voltage scaling factor of the OPLS in volts/volt, VSF_M is the voltage scaling factor of the SEL-735 power meter in volts/volt, and PTR_M is the PT ratio set in the SEL-735 power meter.

$$CG_S = \frac{CSF_{G\&W}}{CSF_M\ (CTR_M)} = \frac{3333.3\frac{A}{V}}{16.53\frac{A}{V}\ (80)} = 2.520 \tag{20}$$

where the CG_S is the current gain of the OPLS for the OP4510 real-time simulator, CSF_S is the current scaling factor of the OPLS in amps/volt, CSF_M is the current scaling factor of the SEL-735 power meter in amps/volt, and CTR_M is the CT ratio set in the SEL-735 power meter.

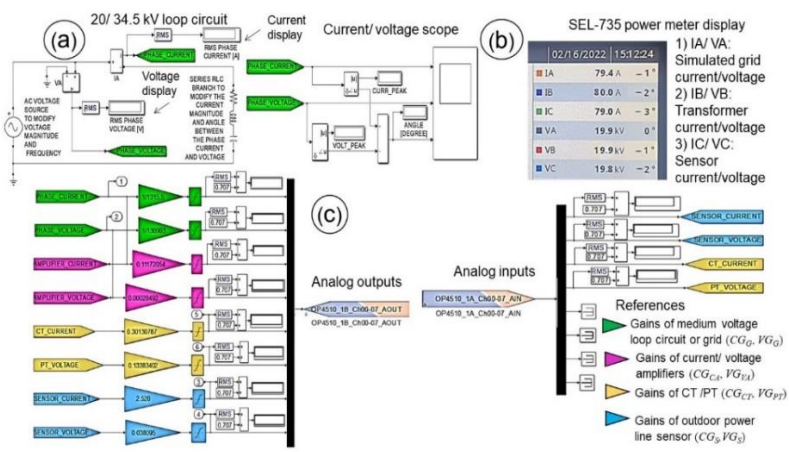

Fig. 3. Medium-voltage loop circuit (a), SEL-735 power meter display (b), and gains (c)

Table 3. Adjustment of voltage and current gains for the OP4510 real-time simulator

Gains (ID)	SEL-735 Power Meter		Conditions
	Connect Interface	Measure Phase (Device)	
Voltage gain of voltage amplifier (VG_{VA})	H	VB * (PT) *V simulated*	Up to match the PT/CT measurements (phase B voltage/current from the SEL-735 power meter with the high-voltage/current interface) vs. the voltage/current simulated at the medium-voltage loop circuit (Fig. 3a).
Current gain of current amplifier (CG_{CA})	H	IB * (CT) *I simulated*	
Voltage gain of simulated grid (VG_G)	H L	VB * (PT) VA (Grid)	Up to match the PT/CT measurements (phase B voltage/current from the SEL-735 power meter with the high-voltage/current interface) vs. the simulated medium-voltage loop circuit measurements (phase A voltage/current from the SEL-735 power meter with the low-voltage interface).
Current gain of simulated grid (CG_G)	H L	IB * (CT) IA (Grid)	
Voltage gain of PT (VG_{PT})	H L	VB * (PT) VB (PT)	Up to match the PT/CT signal (phase B voltage/current from the SEL-735 power meter with the low-voltage interface) vs. the PT/CT signal (phase B voltage/current from the SEL-735 power meter with the high-voltage/current interface).
Current gain of CT (CG_{CT})	H L	IB * (CT) IB (CT)	

*H: high-current/voltage interface, L: low-voltage interface, PT: potential transformer, CT: current transformer, and * measurement used as main reference in the adjustment of voltage/current gains*

3.5 Adjustment of Voltage and Current Gains

The calculated voltage and current gains for the OP4510 real-time simulator were adjusted by creating an RT-LAB project that simulated a medium-voltage loop circuit, as shown in Fig. 3.

This circuit was formed by a sinusoidal source and an impedance in series (Fig. 3a) that simulated the line-to-ground voltage of 19.9 kV and line current of 80 A. The adjusting process of the gains for the OP4510 real-time simulator was based on running a simulation test of the medium-voltage loop circuit and comparing the measurements with those on the display of the SEL-735 power meter (Fig. 3b) (Piesciorovsky et al., 2023). The gains calculated using Equations (11)–(15) and (18) were initially set in the model (Fig. 3c). Then, these values were adjusted to match the conditions shown in Table 3.

The amplifier gains (VG_{VA} and CG_{CA}) for the OP4510 real-time simulator were adjusted by using the measured the voltage/current from the PT/CT of phase B at the high-voltage/current interface in the SEL-735 power meter as a reference that represented the real voltage/current from the outdoor medium-voltage aerial cable loop in the OPLST. These gains were adjusted using Equation (21).

$$G'_{ADJ} = G'_{CALC} \left(\frac{M_H}{S_{GRID}}\right) \tag{21}$$

where G'_{ADJ} are the adjusted voltage and current gains of the amplifiers for the OP4510 real-time simulator in volts/volt and volts/amp, respectively; G'_{CALC} are the calculated voltage/current gains of the amplifiers from Equations (11) and (12), respectively; M_H are the measured phase-B voltage and current values that were collected by using the high-voltage/current interface in volts and amps; and S_{GRID} are the simulated phase voltage/current values that were measured from the voltage and current displays of the 20/34.5 kV loop circuit in volts and amps, respectively (Fig. 3a) (Piesciorovsky et al., 2023).

Additionally, the gains of the simulated grid (VG_G and CG_G) and PT/CT (VG_{PT} and CG_{CT}) for the OP4510 real-time simulator were adjusted by using the measured voltage/current from the phase-B PT/CT at the high-voltage/current interface in the SEL-735 power meter as a reference. These gains were adjusted using Equation (22).

$$G_{ADJ} = G_{CALC} \left(\frac{M_H}{M_L}\right) \tag{22}$$

where G_{ADJ} are the adjusted voltage/current gains of the simulated grid (in volts/volt and volts/amp, respectively) and PT/CT (unitless) for the OP4510 real-time simulator; G_{CALC} are the calculated voltage/current gains from Equations (13)–(15); and (18); M_H are the measured phase B voltage/current that were collected using the high-voltage/current interface in volts and amps, respectively; and M_L are the measured phase A or B voltage/current that were collected by using the low-voltage interface in volts and amps, respectively, based on the conditions in Table 3 (Piesciorovsky et al., 2023).

In this gain adjustment process for the OP4510 real-time simulator, when the low-voltage interface was connected at the SEL-735 power meter, the measurements from the high-voltage/current interface were not available from the SEL-735 power meter's display (Piesciorovsky et al., 2023). Then, during the simulation of the 20/34.5 kV loop circuit tests (Fig. 3a), the low-voltage interface of the SEL-735 power meter was connected and disconnected to adjust the voltage/current gains with Equations (21) and (22), based on the conditions shown in Table 3.

3.6 Medium-Voltage Outdoor Power Line Sensor Testbed

The 20/34.5 kV OPLST (Figs. 4a,b) was located at the DECC laboratory at ORNL. Fig. 4 shows the medium-voltage aerial cable loop, power line poles, sensors (including others not mentioned in this report), control rack unit, and computers. The PTs were ABB VOG-20B voltage transformers, with a ratio of 20,125 V/115 V, or a potential transformer ratio (PTR) of 175, and the CTs were ABB KOR-20ER current transformers with a ratio of 400A:5A or with a current transformer ratio (CTR) of 80. A mounting bracket (Fig. 4b) allowed for mounting the OPLS and PTs/CTs. Inside the DECC lab, the rack unit (Fig. 4c) housed the power meter, simulator, and amplifiers (Techron Model 7228). The OPLST accurately reproduced the current and voltage waveforms under most conditions but within limits because of the nature of the transformers operated under reverse conditions. The current amplifier that fed the CT in the OPLST (Fig. 1) could not generate currents greater than 80 A in the aerial cable single loop circuit without introducing distortions caused by core nonlinearities. Thus, high current faults could not be directly generated by the OPLST. Additionally, the PT used to increase the voltage had an intrinsic resonance at roughly 1500 Hz, which became evident during events with abrupt voltage changes by a ringing of the applied voltage. The CT and PT used as reference sensors were extensively tested during the commissioning of the OPLST and found to be very accurate to beyond the 100th harmonic (Piesciorovsky et al., 2023).

In the rack unit, an advanced meter computer (Fig. 4d) was used to set the power meter and to collect the transient events as COMTRADE files after running the tests. In the power meter, phase A was configured to measure the voltage/current of the simulated circuit or power grid, phase B measured the voltage/current signals of the PT/CT, and phase C measured the voltage/current signals of the OPLS (Piesciorovsky et al., 2023). Fig. 5a shows the rear side of the power meter on the rack unit. In the power meter, the low-voltage interface measured the voltage and current signals via a DB-25 connector that had a voltage scaling factor of 750 *v/v* and a current scaling factor of 16.53 *A/V*. These voltage and current scaling factors were used to integrate the signals from the power grid simulation, PT/CT, and OPLS with the power meter through the simulator using the Equations (13)–(15) and (18)–(20). In Fig. 5b, the "Event Report Equations" setting for the power meter is shown (Piesciorovsky et al., 2023). The power meter could save the voltage/current signal events as COMTRADE files. The power meter was set using AcSELerator Quickset software (version 7.1.4.0), and the event was triggered by the control input IN401

that was controlled with a signal of 16 VDC (Pickup 15–30 VDC) that was generated by the simulator. In the power meter, the waveform capture sample rate was set to 512 samples per cycle, and the event length was set to 300 cycles to record the test events for 5 s (Piesciorovsky et al., 2023). The power meter had a color touchscreen that facilitated observation of the sinusoidal and phasor diagrams of voltage/current signals with 256 samples per cycle (Schweitzer Engineering Laboratories Inc., n.d.). During the tests, the signals could be supervised from the display of the power meter practically in real time.

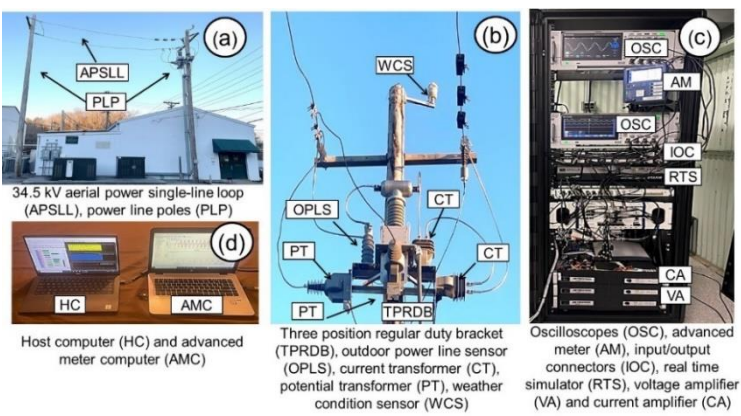

Fig. 4. Medium-voltage aerial cable loop (a), power line pole with sensors (b), rack unit (c), and computers (d)

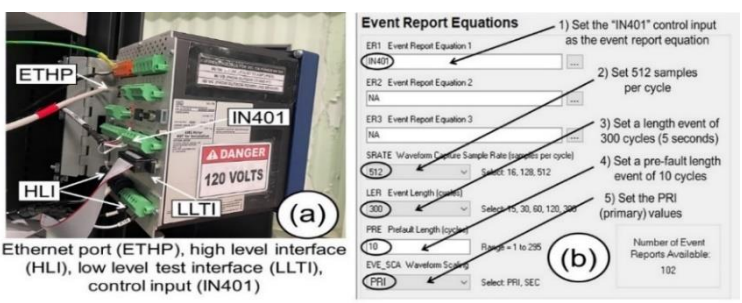

Fig. 5. Power meter rear side (a) and event report settings (b)

4. EXPERIMENTAL MODEL

4.1 Single Line Diagram

This study simulated a power grid model based on a utility circuit at the Riverside EPB of Chattanooga. The simulation circuit was created with MATLAB/Simulink

software and was integrated into an RT-LAB project to run with the OP4510 real-time simulator at the OPLST. Fig. 6 shows the single line diagram (Piesciorovsky et al., 2023).

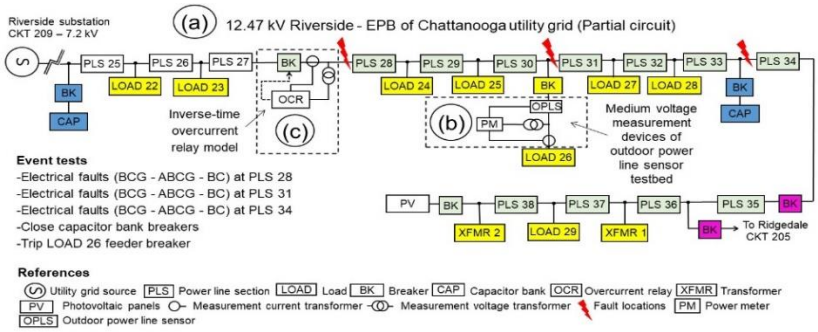

Fig. 6. Single line diagram of 12.47 kV Riverside utility grid partial circuit (a), outdoor power line sensor location (b) and inverse-time overcurrent relay site (c)

This network configuration is a radial power system (7.2 kV phase-to-ground voltage) that is fed by a three-phase source with a Wye-grounded configuration (Fig. 7a). At load 26 (Fig. 6b), the voltage and current were measured by the OPLS and PT/CT at the load feeder (Piesciorovsky et al., 2023). The overcurrent relay (Fig. 6c) was located between power line sections 27 (PLS 27) and 28 (PLS 28) to clear the electrical faults along the power lines. This experimental model performed various tests such as the line to line ground (LLG), line to line (LL), and three-line to ground (3LG) electrical faults; capacitor bank operation; and load 26 fuse switch events.

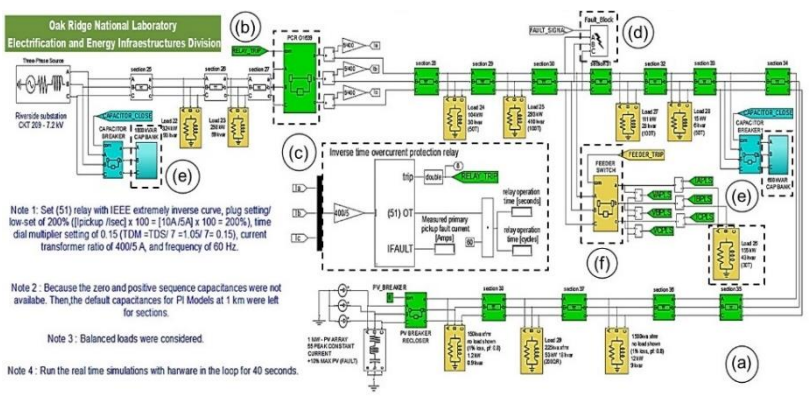

Fig. 7. Three-line diagram of power grid circuit (a), relay breaker (b), inverse-time overcurrent relay (c), fault block (d), capacitor banks (e), and feeder switch (f)

4.2 RT-LAB Project

Fig. 7 shows the three-line circuit in the RT-LAB project, including a relay breaker (Fig. 7b), an inverse-time overcurrent relay (Fig. 7c), a fault block (Fig. 7d), capacitor banks (Fig. 7e), and a feeder switch (Fig. 7f) (Piesciorovsky et al., 2023). This power grid circuit included the utility source, power line sections, feeder loads, breakers, and capacitor banks.

Power line sections were simulated with a three-phase π-section line block. IntelliRupters were used in the EPB grid (Piesciorovsky et al., 2020); however, an inverse-time overcurrent relay MATLAB/Simulink model (Tan, 2016) was used in this study (Piesciorovsky et al., 2023). The ratio of the CTs for the relay's breaker was 400A:5A = 80. The inverse-time overcurrent relay model (Fig. 7c) was set with a time dial setting of 1.05 s, current transformer ratio of 80, relay current pickup of 10 amps, and IEEE extremely inverse curve as shown in Equation (23):

$$T_R = \frac{TDS}{7}\left(0.1217 + \frac{2.82}{\left(I_{primary}/\,CTR/I_P\right)^2 - 1}\right)60 \tag{23}$$

where T_R is the relay time in cycles, *TDS* is the time dial setting in seconds, $I_{primary}$ is the primary current in amps, *CTR* is the current transformer ratio, and I_p is the relay current pickup in amps.

The inverse-time overcurrent relay allowed the opening of the breaker (Fig. 7b) at the electrical fault currents. The grid simulation events were run to observe the prefault, fault, and postfault states for each test. The simulated grid test events included the effect of the electrical fault resistance, with the fault block (Fig. 7d) set to an electrical fault resistance of 0.001 Ω. The OPLST was given by a medium-voltage aerial cable loop (Piesciorovsky et al., 2023). Therefore, before running a test for the three-line diagram (Fig. 7), the A, B, and C phases to be measured by the OPLS was selected from the phase-setting circuit (Fig. 8a) by selecting 1, 2, or 3 for measuring the A, B, or C phase, respectively.

During the tests, the real-time simulations were run for 40 s, and the signal to record the test event with the power meter was set at 30 s for the event-trigger circuit (Fig. 8b) (Piesciorovsky et al., 2023). To record the test event with the voltage/current signals before and after the transient events, the selected test scenario was tripped at 31 s, and the other test scenarios were set at 50 s. As shown in Fig. 8, the electrical fault block circuit (Fig. 8c) was set at 31 s, and the capacitor bank (Fig. 8d) and feeder switch (Fig. 8e) circuits were set at 50 s to run an electrical fault test by tripping the fault block (Fig. 7d) (Piesciorovsky et al., 2023). The OpWrite File block (Fig. 8f) allowed the collection of test results as MATLAB files. Additionally, the capacitor bank, relay breaker, and feeder switch states were collected. Fig. 9 shows the interface circuits for the analog outputs and inputs of the simulator based on Fig. 1b. The circuit for the event-trip output signal for the power meter is shown in Fig. 9a. The interface circuit for the voltage and current signals of the OPLS and PT/CT are shown in Fig. 9b. The

analog outputs of the interface circuit for the gains of the simulator at the voltage/current amplifiers, PT/CT, and OPLS are shown in Fig. 9c.

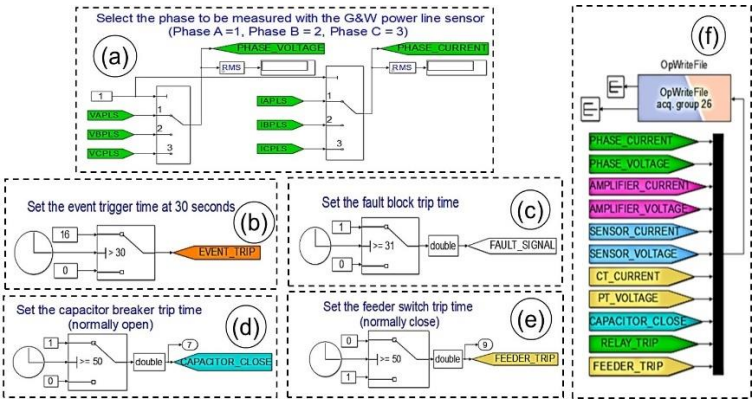

Fig. 8. Phase-setting circuit (a), event-trigger circuit (b), electrical fault circuit (c), capacitor bank circuit (d), feeder switch circuit (e), and OpWrite File block (f)

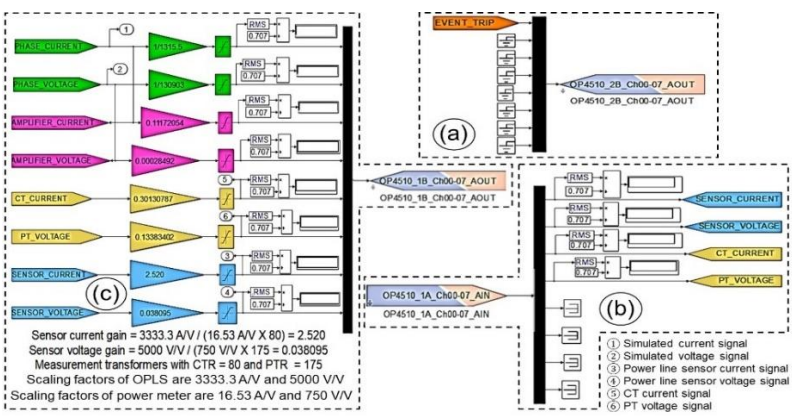

Fig. 9. Event-trip output signal (a), OPLS and PT/CT input signals (b), and amplifier/PT/CT and OPLS output signals (c)

4.3 Experimental Model Flowchart

The flowchart for the experimental model (Fig. 10a) is based on the (1) pretest setting, (2) simulation and data collection, and (3) data plot and analysis. The tests were recorded by the power meter at 30 s (Fig. 8b) and the start of the simulations, and the recorded data for all tests included 300 cycles (5 s) (Piesciorovsky et al., 2023). The data from the events were analyzed around the time when the electrical faults happened (i.e., when the breakers of feeders and

capacitor banks were operated). This process allowed the observation of the behavior of the phase voltage/current signals (Fig. 10b,c) and harmonic analysis (Fig. 10d,e) at transient events to compare the performance of the OPLS with that of the PT/CT.

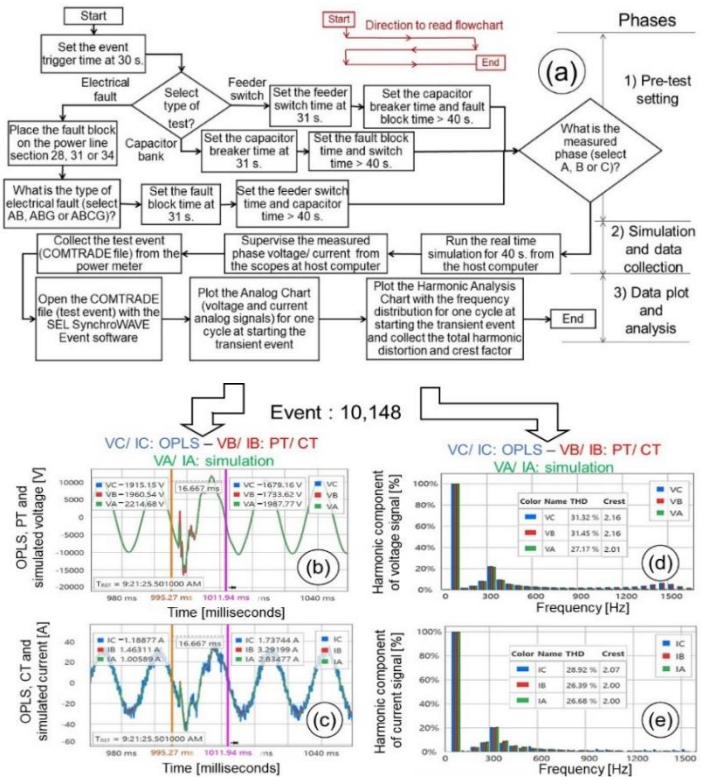

Fig. 10. Flowchart (a) to run the tests with the outdoor power line sensor versus CT/PT with the phase voltage (b) and current (c) signals, and voltage (d) and current (e) harmonic components.

In the experimental model (Fig. 10a), initially, the event trigger circuit was set to record the test events in the power meter at 30 s. Then, the type of the test event was selected (electrical faults, capacitor bank, or feeder switch). If the electrical fault tests were selected, then the fault block was placed on the power line section 28, 31, or 34 (Fig. 6), and the AB (phase A and B), ABG (phase A and B to ground), or ABCG (phases A, B, and C to ground) electrical faults were set on the fault block (Fig. 7d) (Piesciorovsky et al., 2023). The fault block time was set at 31 s (Fig. 8c) to generate the electrical fault, and the feeder switch and capacitor time blocks (Fig. 8d,e) were set at 50 s to not trip these scenarios during the simulation. If the capacitor bank test was selected, then the capacitor breaker time was set at 31 s (Fig. 8d), and the electrical fault and feeder switch

time blocks (Fig. 8c,e) were set at 50 s to not trip these scenarios at the tests. Finally, if the feeder switch test was selected, then the feeder switch breaker time was set at 31 s (Fig. 8e), and the electrical fault and capacitor bank switch time blocks (Fig. 8c,d) were set at 50 s to not trip these scenarios at the tests (Piesciorovsky et al., 2023).

As shown in Fig. 10a, once the electrical fault, capacitor bank, or feeder switch time blocks were set, the A, B, or C phase to be measured in the simulated power grid circuit (Fig. 7) was selected using the phase-setting circuit (Fig. 8a) (Piesciorovsky et al., 2023). The real-time simulation tests were then run and observed using the voltage/current scopes on the host computer; the test event data were collected by the power meter to plot signals in the time domain (Fig. 10b,c) and their harmonic components in the frequency domain (Fig. 10d,e).

5. RESULTS AND DISCUSSION

5.1 Total Harmonic Distortion and Crest Factor

The numerical results of the tests given by the total harmonic distortion and crest factor values for each voltage and current phase (A, B, and C) were collected in a published report (Piesciorovsky et al., 2022). The measured total harmonic distortion and crest factors for the voltage and current signals of the OPLS and PT/CT were collected from the frequency plots and listed in Table 4 (Piesciorovsky et al., 2022). The tests were grouped by the power grid measured phase (A, B, or C). The tests were named according to the load and type of event (electrical faults and location, capacitor bank operation, or feeder switch). The total harmonic distortion and crest factors for each event and for each voltage and current phase A, B, and C are plotted in Figs. 11 and 12 (Piesciorovsky et al., 2023).

These figures indicate reasonable agreement between the simulated signals, PT and CT signals, and OPLS signals. In general, the observed THD_V of the PT and OPLS were in very good agreement, but for some events, they were substantially higher than the measured simulation signals input to the voltage amplifier. This effect is attributed to a resonance in the neighborhood of 1500 Hz for the excitation PT in especially fast transients that was followed by both the reference PT and the OPLS (Piesciorovsky et al., 2023). Such resonance was not observed in the CT; however, the relative background noise of the OPLS was substantially higher (Fig. 10c) because the OPLS had a current range that extends to >20 kA, far exceeding the excitation levels of 20–30 A of the present study. Consequently, the THD_I and CF_I of the OPLS were slightly higher than those of the simulation and CT sensor currents. In Figs. 11 and 12, the measured total harmonic distortion and crest factor values correspond to the first one-cycle (~16.6 ms) transient event of the simulated tests. The total harmonic distortion of the voltage and current signals for the OPLS varied from 11.59% to 276.51% (Fig. 11a) and from 17.56% to 254.08% (Fig. 11b), respectively (Piesciorovsky et al., 2023). The minimum and maximum total harmonic distortion corresponded to the closed capacitor bank test and the BCG electrical fault test, respectively. In

Fig. 11, total harmonic distortions (*THD$_V$* or *THD$_I$*) greater than 0% indicate that the numerator is greater than the denominator in Equations (3) and (4). Then, the contribution of the harmonic components with respect to the fundamental frequency (60 Hz) are available in the measured signals (Piesciorovsky et al., 2023). A pure signal based on the fundamental (60 Hz) with low harmonic components resulted in measured total harmonic distortions (*THD$_V$* or *THD$_I$*) near 0%.

5.2 Total Harmonic Distortion and Crest Factor Percentage Errors

The total harmonic distortion and crest factor percentage errors of the test events (electrical faults, capacitor bank operators, and load feeder switch) for the measured phase A, B, and C voltage (Fig. 13a) and current (Fig. 13b) signals in the power grid feeder were plotted, comparing the performance of the OPLS with that of the PT/CT (Piesciorovsky et al., 2023). The percentage errors for the total harmonic distortion and crest factor values correspond to the first one-cycle (~16.6 ms) transient event of the simulated tests. The total harmonic distortion and crest factor percentage errors were calculated using Equations (7)–(10).

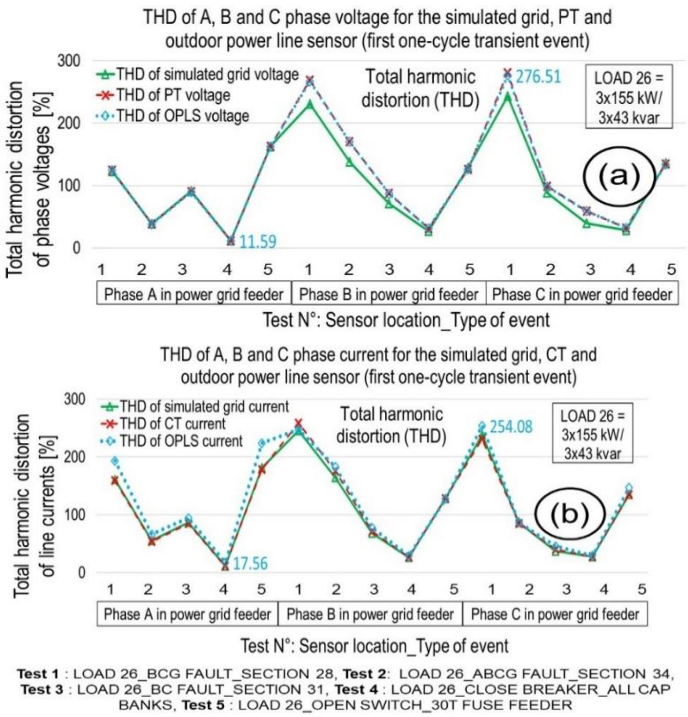

Fig. 11. Total harmonic distortion of phases A, B, and C voltage (a) and current (b) signals for the simulated grid, PT/CT, and outdoor power line sensor

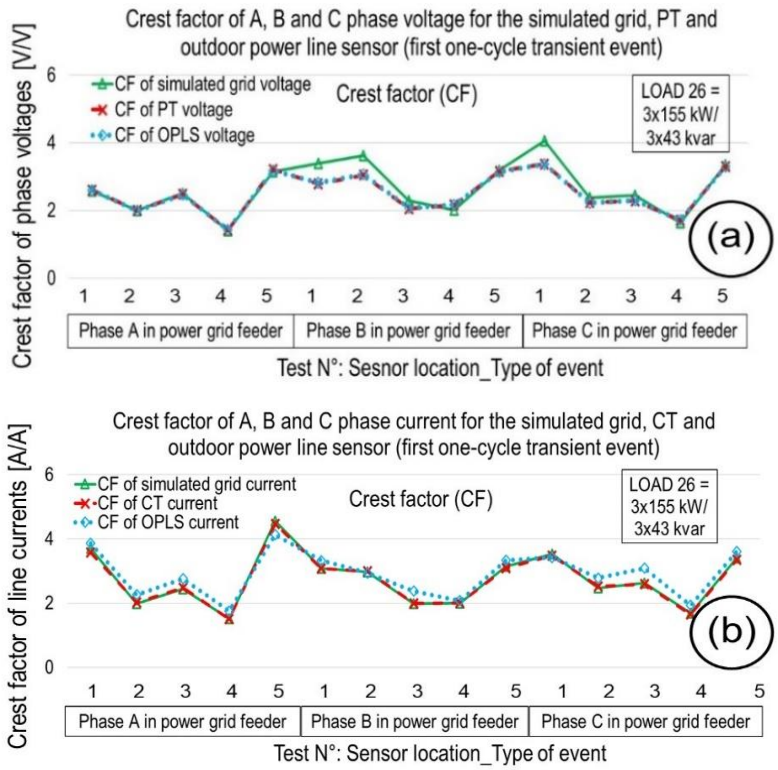

Test 1 : LOAD 26_BCG FAULT_SECTION 28, **Test 2**: LOAD 26_ABCG FAULT_SECTION 34, **Test 3** : LOAD 26_BC FAULT_SECTION 31, **Test 4** : LOAD 26_CLOSE BREAKER_ALL CAP BANKS, **Test 5** : LOAD 26_OPEN SWITCH_30T FUSE FEEDER

Fig. 12. Crest factor of phase A, B, and C voltage (a) and current (b) signals for the simulated grid, PT/CT, and outdoor power line sensor.

To calculate the percentage errors, the signals from the PT/CT and the OPLS power line sensor were considered as the expected and measured values, respectively. In Fig. 13a, the pink bars are the total harmonic distortion (0.05% to −1.49%) of the voltage signals, and the blue bars are the crest factor (1.08% to −0.93%) percentage errors of the voltage signals (Piesciorovsky et al., 2023). In Fig. 13b, the green bars are the total harmonic distortion (52.96% to −4.40%) percentage errors of the current signals, and the red bars represent the crest factor (19.31% to −7.4%) percentage errors of the current signals.

5.3 Voltage and Current Signals from Test Events

In the electrical fault events, the phase voltage and current signals were generated, and different transient events were consequently plotted. The test

events (electrical faults, capacitor bank operation, and load feeder switch) were run for phases A, B, and C. Because the test events were triggered at the same time, the measured phase A, B, and C current and voltage signals were generated at different angles based on a three-phase system definition (Vadari, 2020), which had a phase difference of 120 degrees (Piesciorovsky et al., 2023). Figs. 14 and 15 show the voltage and current of phase A (a, d), B (b, e), and C (c, f) for the outdoor power line sensor, PT/CT, and simulated power grid when the capacitor banks were closed and when an ABCG electrical fault in the main feeder was set, respectively.

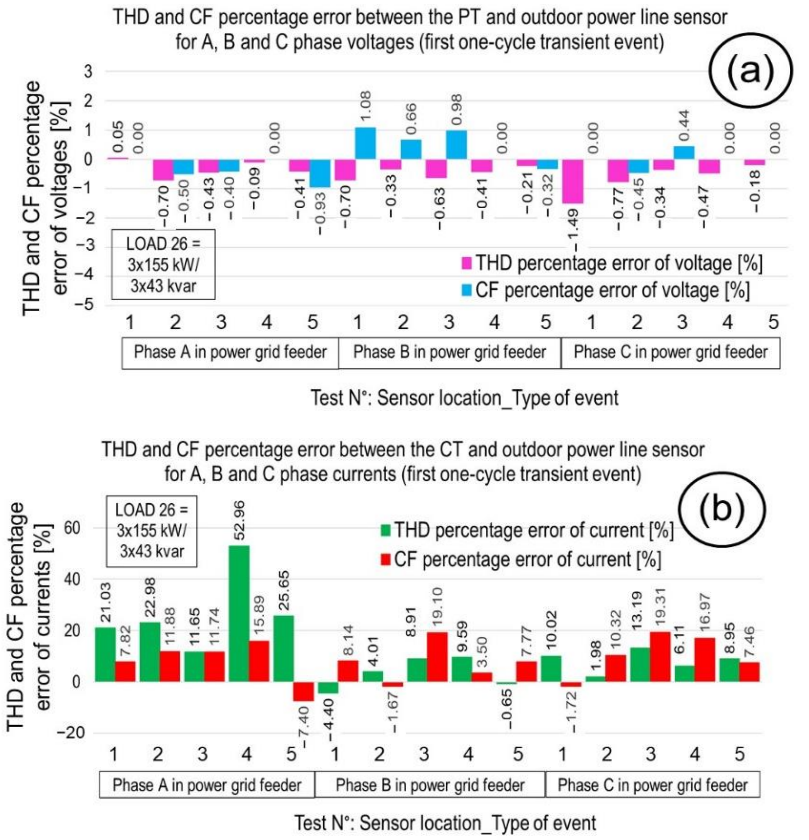

Test 1 : LOAD 26_BCG FAULT_SECTION 28, **Test 2**: LOAD 26_ABCG FAULT_SECTION 34, **Test 3** : LOAD 26_BC FAULT_SECTION 31, **Test 4** : LOAD 26_CLOSE BREAKER_ALL CAP BANKS, **Test 5** : LOAD 26_OPEN SWITCH_30T FUSE FEEDER

Fig. 13. Total harmonic distortion and crest factor percentage error of phase A, B, and C for the voltage (a) and current (b) signals between the OPLS and the PT/CT

Table 4. Total harmonic distortion and crest factor of phases A, B, and C for the OPLS vs. the PT/CT

Phase [a]	Test (Event)	Test Name [b,c]	THD Factor of Voltage (THD Factor of Current)			Crest Factor of Voltage (Crest Factor of Current)		
			OPLS	PT/CT	Grid	OPLS	PT/CT	Grid
A	1 (10,139)	LOAD 26_BCG FAULT_SECTION 28	124.46 (193.13)	124.40 (159.57)	122.91 (160.93)	2.60 (3.86)	2.60 (3.58)	2.57 (3.70)
	2 (10,140)	LOAD 26_ABCG FAULT_SECTION 34	38.10 (66.14)	38.37) (53.78)	38.82 (55.71)	1.99 (2.26)	2.00) (2.02)	2.00 (1.98)
	3 (10,141)	LOAD 26_BC FAULT_SECTION 31	89.50 (94.57)	89.89 (84.70)	91.32 (86.28)	2.47 (2.76)	2.48 (2.47)	2.51 (2.44)
	4 (10,142)	LOAD 26_CLOSE BREAKER_ALL CAP BANKS	11.59 (17.56)	11.60 (11.48)	11.35 (11.50)	1.42 (1.75)	1.42 (1.51)	1.40 (1.51)
	5 (10,143)	LOAD 26_OPEN SWITCH_30T FUSE FEEDER	161.95 (223.69)	162.61 (178.03)	162.43 (181.15)	3.18 (4.13)	3.21 (4.46)	3.14 (4.56)
B	1 (10,145)	LOAD 26_BCG FAULT_SECTION 28	266.90 (247.35)	268.77 (258.73)	230.88 (245.45)	2.81 (3.32)	2.78 (3.07)	3.39 (3.08)
	2 (10,146)	LOAD 26_ABCG FAULT_SECTION 34	169.91 (182.86)	170.47 (175.81)	138.02 (164.55)	3.06 (2.94)	3.04 (2.99)	3.62 (2.97)
	3 (10,147)	LOAD 26_BC FAULT_SECTION 31	87.07 (77.60)	87.62 (71.25)	71.08 (68.65)	2.07 (2.37)	2.05 (1.99)	2.28 (1.98)
	4 (10,148)	LOAD 26_CLOSE BREAKER_ALL CAP BANKS	31.32 (28.92)	31.45 (26.39)	27.17 (26.68)	2.16 (2.07)	2.16 (2.00)	2.01 (2.00)
	5 (10,149)	LOAD 26_OPEN SWITCH_30T FUSE FEEDER	125.89 (127.49)	126.15 (128.33)	128.78 (128.79)	3.14 (3.33)	3.15 (3.09)	3.19 (3.14)
C	1 (10,150)	LOAD 26_BCG FAULT_SECTION 28	276.51 (254.08)	280.70 (230.95)	243.53 (237.88)	3.37 (3.42)	3.37 (3.48)	4.06 (3.53)

Phase [a]	Test (Event)	Test Name [b,c]	THD Factor of Voltage (THD Factor of Current)			Crest Factor of Voltage (Crest Factor of Current)		
			OPLS	PT/CT	Grid	OPLS	PT/CT	Grid
	2 (10,151)	LOAD 26_ABCG FAULT_SECTION 34	98.14 (86.91)	98.90 (85.22)	88.44 (86.65)	2.22 (2.78)	2.23 (2.52)	2.37 (2.47)
	3 (10,152)	LOAD 26_BC FAULT_SECTION 31	58.69 (45.84)	58.89 (40.50)	39.24 (37.09)	2.29 (3.09)	2.28 (2.59)	2.45 (2.62)
	4 (10,153)	LOAD 26_CLOSE BREAKER_ALL CAP BANKS	32.03 (29.33)	32.18 (27.64)	27.95 (27.42)	1.71 (1.93)	1.71 (1.65)	1.64 (1.68)
	5 (10,154)	LOAD 26_OPEN SWITCH_30T FUSE FEEDER	133.96 (146.97)	134.20 (134.90)	136.34 (134.99)	3.30 (3.60)	3.30 (3.35)	3.34 (3.40)

[a] A, B, or C phase of power grid feeder measured during the test. [b] Test name (measured load_ type of event and location). [c] The electrical fault, capacitor bank, and feeder switch tests were based on events with a time length of 300 cycles (5 s) that were analyzed to the first one-cycle (~16.6 ms) transient event from the simulated tests, the capacitor bank breakers were closed, and the 30 T fuse feeder switch was opened. OPLS: outdoor power line sensor. PT: potential transformer. CT: current transformer.

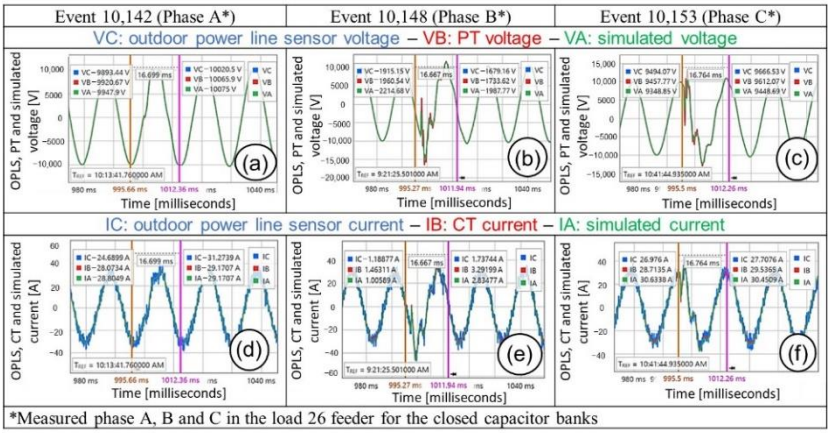

Fig. 14. Voltage and current of phases A (a,d), B (b,e), and C (c,f) for the outdoor power line sensor, PT/CT, and simulated power grid at the load 26 feeder when the capacitor banks are closed

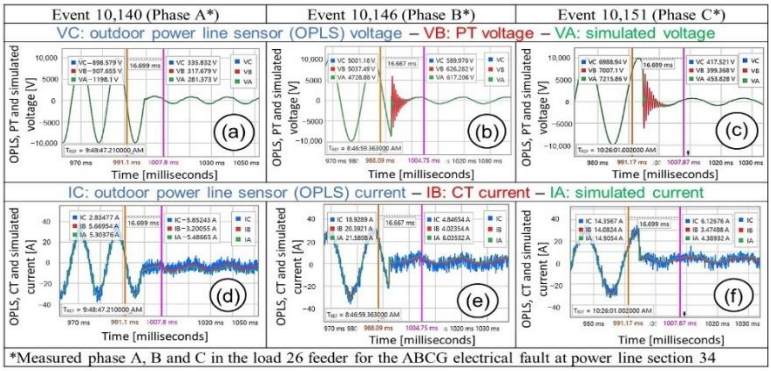

Fig. 15. Voltage and current of phase A (a,d), B (b,e), and C (c,f) for the outdoor power line sensor, PT/CT, and simulated power grid at load 26 feeder and ABCG electrical fault in power line section 34 (PLS 34)

In the capacitor bank operation tests (Events 10142, 10148, and 10153), the voltage and current signals were observed by plotting the first one-cycle (~16.6 ms) transient event at the measured phases A, B, and C (Piesciorovsky et al., 2023). These events represented the time when the capacitor banks along the power line sections were closed in the simulated power grid (Fig. 6). The voltage and current signals at the load feeder (Fig. 6b) were measured at the medium-voltage OPLST. The measured voltage (Fig. 14a–c) and current (Fig. 14d–f) signals for phases A, B, and C were compared for the OPLS vs. the PT/CT. In Fig. 14, the blue, red, and green lines are the voltage/current signals for the

OPLS, PT/CT, and simulated power grid, respectively (Piesciorovsky et al., 2023). For the first one-cycle (~16.6 ms) transient event, the behaviors of the voltage and current signals for the OPLS and PT/CT were similar for the same measured phase.

In the ABCG electrical fault event tests (Events 10140, 10146, and 10151), the voltage signals were plotted for the first one-cycle (~16.6 ms) transient event for phase A, B, and C. These events represented the time when the electrical fault happened at power line section 34 (PLS 34) in the simulated power grid (Fig. 6). Then, the voltage and current signals at the load feeder (Fig. 6b) were generated at the medium-voltage OPLST (Piesciorovsky et al., 2023). The effect of the ABCG electrical fault at the power line produced the line currents and voltages decreased on the load feeder (Fig. 15). The measured voltage (Fig. 15a–c) and current (Fig. 15d–f) signals for phase A, B, and C were compared with the OPLS vs. the PT/CT. In Fig. 15, the blue, red, and green lines are the voltage/current signals for the OPLS, PT/CT, and simulated power grid, respectively. For the first one-cycle (~16.6 ms) transient event, the behaviors of the voltage and current signals for the OPLS and PT/CT were similar for the same measured phase. In the first one-cycle (~16.6 ms) transient event, the voltage and current signals of phase A had a sinusoidal form (Fig. 15a,d), whereas the voltage signals of phases B and C had a distortion (Fig. 15b,c) that generated a ringing frequency for the OPLS and PT (Piesciorovsky et al., 2023).

The capability of measuring current and voltage harmonics with power line sensors is very important. When harmonics are presented in the main voltage or line currents for permanent states (non-transient states), the power quality of the electrical grid can decrease. Another effect of the harmonics is to increase the current in transformers and the electrical grid with consequent rise in device temperature and power losses (Piesciorovsky et al., 2023). For example, the third harmonic causes a sharp increase in the zero-sequence current and increases the current in the neutral conductors. A non-linear load connected to the electrical grid draws a current that is not necessarily sinusoidal, and therefore it generates harmonics. The voltage harmonics are mostly caused by current harmonics. However, if the source impedance of the voltage source is small, current harmonics will cause only small voltage harmonics. It is typically the case that voltage harmonics are indeed small compared to current harmonics. In the results, from Fig. 11a,b, the behavior of the total harmonic distortion for the current and voltage signals had shown a similar behavior for the same phase and event test, observing a similar conduct for the current and voltage signals (Piesciorovsky et al., 2023).

In this study, the proposed methodology was implemented in an OPLS testbed instead of a real grid. It is because electrical fault grid events are not likely to be run by an electrical utility for safety concerns and possible infrastructure damages in the electrical grid. In addition, the electrical grid events presented in the experimental model could be run at any time, however, in a real electrical grid, these events like capacitor bank operation, electrical faults and breaker operations at a specific site could happen after weeks or months (Piesciorovsky et al., 2023). The limitation of this testbed is based on the maximum current

magnitude that could be generated during the event tests that will depend on the number of current amplifiers to be connected in parallel, in most of the use case scenarios the OPLS testbed was run for current magnitudes up to 40 amps (Piesciorovsky et al., 2023).

An advantage of this methodology is that the testbed could be used for testing other similar power line sensors. In this study, the OPLS was a Rogowski coil (current sensor) and capacitive divider (voltage sensor) power line sensor that has a current and voltage scaling factor of 3333.3 *A*/*V* and voltage 5000 *V*/*V*, respectively. However, if the current and voltage scaling factors of the OPLS had different numerical values, the voltage and current gains of the OPLS for the OP4510 real-time simulator could be re-calculated by Equations (19) and (20). Therefore, this methodology can show certain flexibility for comparing other Rogowski coil/capacitive divider power line sensors with the traditional CT/PT sensors (Piesciorovsky et al., 2023).

Advanced OPLSs like the Rogowski coil should be installed in the electrical distribution grid (Why and where Rogowski coil current sensors are favorable, 2020). However, sensors' metering, protection and control applications should be studied in detail (Piesciorovsky et al., 2023). For example, based on the core saturation curves of CTs, different CT types are used for metering and protection applications (Hargrave et al., 2018; Altuve et al., 2013). In addition, while the Rogowski coil (current sensor) could be used in protection applications, the interface of analog signals must be considered to adapt the connection of protective relays or meters (Why and where Rogowski coil current sensors are favorable, 2020). While CTs require heavy gauge secondary wires for interconnection to relays and other metering and control equipment, the Rogowski coils may be connected to relays via twisted pair shielded cables with connectors (Why and where Rogowski coil current sensors are favorable, 2020). Another aspect is that some advanced sensors integrate the current (Rogowski coil) and voltage (capacitive divider) measurements in the same OPLS device, reducing the installation cost when both measurements are needed at the same site (Piesciorovsky et al., 2023). Therefore, the Rogowski coil (current sensor)/capacitive divider (voltage sensor) power line sensor can be installed for a small fraction of the cost of conventional CT and PT.

In this study, the voltage swells and sags as specific test events were not considered. However, based on the definition that voltage swells are the opposite of voltage sags (dips) and they are defined as a momentary increase in the RMS voltage of 10% or more above recommended voltage range for a period of 1/2 cycle to 1 min, according to the IEEE Std 1159-2009 (IEEE, 2019), these type of test events could be performed in a future test plan to compare the Rogowski coil (current sensor) and capacitive divider (voltage sensor) versus the CT (current sensor)/PT (voltage sensor) in the OPLS testbed. Electrical utilities have used PTs and CTs for several decades, and PTs and CTs have been tested using procedures based on the IEEE Std C57-13 2016 (IEEE, 2016). However, new OPLSs based on advanced technologies (voltage divider and Rogowski coil) do not have testing procedures based on electrical apparatuses or instrument

standards (Piesciorovsky et al., 2023). Therefore, the assessment of these advanced OPLS is crucial. In this work, the comparison test procedure for the OPLS vs. the PT/CT was an effective method to evaluate the performance of these advanced technologies vs. iron core measurement transformers.

6. CONCLUSIONS

In this study, an advanced commercial medium-voltage power line voltage and current sensor was tested alongside conventional magnetic-core PT and CT under outside conditions. The tests consisted of various simulated steady-state and transient conditions with an actual utility grid to compare the responses of the new technology with those of accepted instrument transformers (Piesciorovsky et al., 2023). A real-time simulator was used in conjunction with amplifiers and transformers to excite the aerial loop, while a conventional power meter recorded the responses of the simulation, PT and CT, and the OPLS signals. The results showed that this OPLS technology responded identically to the PT and CT under all conditions. The only difference noted is that the OPLS current noise is greater than that of the instrument CT because of its much wider range (>20 kA compared with ~1 kA for the CT).

The technology in OPLS is based on a capacitive divider for voltage monitoring and a Rogowski coil with an integrator for current sensing. The capacitive divider principle is well known for its ability to transmit higher harmonics and thus respond well to fast transients, and the present results are consistent with this principle (Piesciorovsky et al., 2023). The known issues include recalibration during temperature swings and aging, as well as some sensitivity to stray electric fields. These effects are minimized in PTs; however, PTs evince various resonance effects at higher harmonics. The air-core Rogowski-coil technology can be made linear at currents that saturate magnetic-core CTs and can have excellent responses at high harmonics. However, it must be carefully shielded to avoid stray electric-field effects. The response of this OPLS technology was compared with that of the conventional instrument transformers for the scenarios that were tested. These devices can be installed for a small fraction of the cost of that of conventional CTs and PTs and should be considered for deployment of additional sensors in distribution grids.

DISCLAIMER (ARTIFICIAL INTELLIGENCE)

Author(s) hereby declare that NO generative AI technologies such as Large Language Models (ChatGPT, COPILOT, etc.) and text-to-image generators have been used during writing or editing of this manuscript.

AUTHORS' CONTRIBUTIONS

This work was carried out in collaboration with all authors. Authors E.C.P. and R.J.B.W conceptualized the manuscript. Authors ECP and RJBW conducted a formal analysis. Authors ECP and RJBW were involved in the investigation and author ECP completed the methodology. Author YP was involved in project

administration. Author RJBW obtained the resources. Authors ECP and RJBW were involved in the supervision process. Authors ECP and RJBW visualized the manuscript. Author ECP wrote the original draft. Authors ECP, RJBW and YP were involved in the writing, reviewing and editing of the manuscript. All authors read and approved the final manuscript.

FUNDING

This research is supported by the US Department of Energy (DOE), Office of Electricity, under Contract DE-AC05-00OR22725 with UT-Battelle, LLC, for the US DOE. This manuscript has been authored by UT-Battelle, LLC, under Contract DE-AC05-00OR22725 with the US Department of Energy (DOE). The US government retains and the publisher, by accepting the article for publication, acknowledges that the US government retains a nonexclusive, paid-up, irrevocable, worldwide license to publish or reproduce the published form of this manuscript, or allow others to do so, for US government purposes. DOE will provide public access to these results of federally sponsored research in accordance with the DOE Public Access Plan (http://energy.gov/downloads/doe-publicaccess- plan (accessed on 2 May 2023)).

DATA AVAILABILITY STATEMENT

The data presented in this study are openly available in reference (Piesciorovsky et al., 2022), https://doi.org/10.2172/1899828.

SPECIAL NOTE

This manuscript was authored by UT-Battelle, LLC, under contract DE-AC05-00OR22725 with the U.S. Department of Energy (DOE). The U.S. government retains and the publisher, by accepting the article for publication, acknowledges that the U.S. government retains a nonexclusive, paid-up, irrevocable, worldwide license to publish or reproduce the published form of this manuscript or allow others to do so, for U.S. government purposes. The DOE will provide public access to these results of federally sponsored research in accordance with the DOE Public Access Plan (http://energy.gov/downloads/doe-public-access-plan) (accessed on 2 May 2023).

COMPETING INTERESTS

Authors have declared that no competing interests exist.

REFERENCES

AE TECHRON. (2020). *7228 Operator's manual, single-channel industrial amplifier for demanding, high-power systems*. Available online: https://aetechron.com/pdf/7228_OperatorManual.pdf

Altuve, H. J., Fischer, N., Benmouyal, G., & Finney, D. (2013). Sizing current transformers for line protection applications. In *Proceedings of the 66th Annual Conference for Protective Relay Engineers* (pp. 1–12). College Station, TX, USA.

Atwa, O. S. E. (2019). *Practical power system and protective relays commissioning* (1st ed.). Academic Press; Cambridge, MA, USA; Elsevier. Amsterdam, The Netherlands, 1–420.

Das, S. (2016). Sub-Nyquist rate ADC sampling in digital relays and PMUs: Advantages and challenges. In *Proceedings of the 6th IEEE International Conference on Power Systems* (pp. 1–6). New Delhi, India.

Hargrave, A., Thompson, M. J., & Heilman, B. (2018). Beyond the knee point: A practical guide to CT saturation. In *Proceedings of the 71st Annual Conference for Protective Relay Engineers* (pp. 1–12). College Station, TX, USA.

Heuston, G. (2007). Doble® testing voltage (potential) transformers and metering units. In *Proceedings of the 74th Annual International Doble Client Conference* (pp. 1–12). Boston, MA, USA.

Hong, S., & Zuercher-Martinson, M. (n.d.). Harmonics and noise in photovoltaic (PV) inverter and the mitigation strategies. *Solectria Renewables*. Available online: https://www.solectria.com/site/assets/files/1482/solectria_harmonics_noise_pv_inverters_white_paper.pdf

IEEE. (2016). *IEEE standard requirements for instrument transformers* (IEEE Std C57.13-2016). IEEE.

IEEE. (2019). *IEEE recommended practice for monitoring electric power quality* (IEEE Std 1159-2019). IEEE.

OMICRON. (n.d.). *Diagnostic testing of instrument transformers*. Available online: https://www.omicronenergy.com/en/news/details/diagnostic-measurements-on-instrument-transformers/

Parker, D. M., & McCollough, N. D. (2011). Medium-voltage sensors for the smart grid: Lessons learned. In *Proceedings of the 2011 IEEE Power and Energy Society General Meeting* (pp. 1–5). Detroit, MI, USA.

Piesciorovsky, E. C., & Karnowski, T. (2021). Variable frequency response testbed to validate protective relays up to 20 kHz. *Electrical Power and Energy Systems Research, 194*, 107071. https://doi.org/10.1016/j.epsr.2021.107071

Piesciorovsky, E. C., & Morales Rodriguez, M. E. (2022). Assessment of the phase to ground fault apparent admittance method with phase/ground boundaries to detect types of electrical faults for protective relays using signature library and simulated events. *International Transactions on Electrical Energy Systems, 32*, e1951836.

Piesciorovsky, E. C., Smith, T., & Ollis, T. B. (2020). Protection schemes used in North American microgrids. *International Transactions on Electrical Energy Systems, 30*, e12461.

Piesciorovsky, E. C., Warmack, R. J. B., & Polsky, Y. (2023). Medium-voltage testbed for comparing advanced power line sensors vs. measurement transformers with electrical grid events. *Energies, 16*, 4944.

Piesciorovsky, E. C., Warmack, R. J., & Polsky, Y. (2022). Outdoor test bed performance of a power line sensor using a real-time event simulator (ORNL/TM-2022/2751). Oak Ridge National Laboratory.

Probe Master. (n.d.). *Differential probe for power management model 4232, technical data sheet*. Available online: https://probemaster.com/4232-differential-probe-1-10-100-25-mhz-1400v/

Rahmatian, F. (2011). High-voltage current and voltage sensors for a smarter transmission grid and their use in live-line testing and calibration. In *Proceedings of the 2011 IEEE Power and Energy Society General Meeting* (pp. 1–5). Detroit, MI, USA.

Schweitzer Engineering Laboratories Inc. (n.d.). *SEL-735 power quality and revenue meter instruction manual*. Available online: https://selinc.com/products/735/docs/

Shadfar, H., Ghorbani Pashakolaei, M., & Akbari Foroud, A. (2021). Solid-state transformers: An overview of the concept, topology, and its applications in the smart grid. *International Transactions on Electrical Energy Systems, 31*(9), e12996.

Sheryar, M., Ali, M. A., Umer, F., Rashid, Z., Amjad, M., Haider, Z. M., & Khan, M. O. (2022). An approach to performing stability analysis for power transformer differential protection: A case study. *Energies, 15*(24), 9603.

Souders, T. M. (1971). A wide range current comparator system for calibrating current transformers. *IEEE Transactions on Power Apparatus and Systems, PAS-90*, 318–324. https://doi.org/10.1109/TPAS.1971.294464

Substation test equipment guidebook, Vanguard Instruments (Rev. i). (2018). Available online: https://www.vanguardinstruments.com/resources

Sze, W. C. (1965). Comparators for voltage transformer calibrations at NBS. *Journal of Research of the National Bureau of Standards-C, Engineering and Instrumentation, 69C*, 257–263. https://doi.org/10.6028/jres.069C.031

Tan, R. (2016). AC time overcurrent relay block MATLAB model (Version 1.0). Available online: https://www.mathworks.com/matlabcentral/fileexchange/57521-ac-time-overcurrent-relay-block

Timmons, D., Harris, J. M., & Roach, B. (2014). *The economics of renewable energy*. Global Development and Environment Institute, Tufts University.

Torres, J. F., & Petrakopoulou, F. (2022). A closer look at the environmental impact of solar and wind energy. *Global Challenges, 6*(8), 2200016.

Ultrastab. (n.d.). *866 precision current transducer user manual*. Available online: https://pdf4pro.com/amp/view/ultrastab-866-precision-current-transducer-user-manual-423ee8.html

Vadari, M. (2020). *Electric system operations: Evolving to the modern grid* (2nd ed.). Artech House.

Vanguard Instruments Company Inc. (2020). *EZCT-2KA current transformer test set, user manual* (Rev. 1.1). Available online: https://downloads.vanguard-instruments.com/categories/current-transformer-testers/ezct-2ka

Why and where Rogowski coil current sensors are favorable when compared to CTs, Relay Control and Protection Guides. (2020). https://electrical-engineering-portal.com/download-center/books-and-guides/relays/rogowski-coil-cts

Disclaimer/Publisher's Note: The statements, opinions and data contained in all publications are solely those of the individual author(s) and contributor(s) and not of the publisher and/or the editor(s). This publisher and/or the editor(s) disclaim responsibility for any injury to people or property resulting from any ideas, methods, instructions or products referred to in the content.

© Copyright (2025): Author(s). The licensee is the publisher (BP International).

DISCLAIMER
This chapter is an extended version of the article published by the same author(s) in the following journal.
Energies, 16: 4944, 2023. Available: https://doi.org/10.3390/en16134944, https://www.mdpi.com/1996-1073/16/13/4944

Peer-Review History:
This chapter was reviewed by following the Advanced Open Peer Review policy. This chapter was thoroughly checked to prevent plagiarism. As per editorial policy, a minimum of two peer-reviewers reviewed the manuscript. After review and revision of the manuscript, the Book Editor approved the manuscript for final publication. Peer review comments, comments of the editor(s), etc. are available here: https://peerreviewarchive.com/review-history/4054

Chapter 2
Print ISBN: 978-93-49473-44-7, eBook ISBN: 978-93-49473-43-0

Analyzing Design Principles of Floor Plan of Hue Imperial Palaces, Vietnam

An Vinh Le [a*]

DOI: https://doi.org/10.9734/bpi/erpra/v5/3713

Peer-Review History:
This chapter was reviewed by following the Advanced Open Peer Review policy. This chapter was thoroughly checked to prevent plagiarism. As per editorial policy, a minimum of two peer-reviewers reviewed the manuscript. After review and revision of the manuscript, the Book Editor approved the manuscript for final publication. Peer review comments, comments of the editor(s), etc. are available here: https://peerreviewarchive.com/review-history/3713

ABSTRACT

The Complex of Hue Monuments (abbreviated as the Monuments), the first UNESCO World Cultural Heritage site in Vietnam (UNESCO), is well-known for its wealth of scientific materials for research. This paper begins by providing a general introduction to the construction history and architectural typology of the Hue Imperial Palaces (abbreviated as the Imperial Palaces), a key component of the Monuments. These include the existing heritage buildings located within the Hue Citadel and the Emperor Mausoleums of the Nguyen dynasty (1802–1945).

Next, this paper examines the floor plan design methods of the Imperial Palaces, with particular focus on the Twin-Ridge Beam Buildings (abbreviated as Twin Buildings), which are unique in ancient Asia. The name of this building type is derived from its characteristic design, which consists of two or three buildings connected and placed on the same platform. This construction style represents the highest level of architectural achievement during the Nguyen dynasty.

Drawing mainly from historical documents of the Nguyen dynasty, surveys of remaining heritage Twin Buildings, dimensional analysis, investigations into traditional design methods, and interviews with master carpenters, the proportions of the floor plans were analyzed and the primary architectural design methods used were re-determined. Through this study, the units of measurement, parametric factors, design principles, and design processes for the floor plans of Twin Buildings have been clearly defined.

In addition, this study provides a comprehensive understanding of the principles behind the floor plan design of the Twin Buildings in Hue imperial architecture. It also offers valuable guidance for the precise restoration and reconstruction of the

---

[a] *Faculty of Civil Engineering, Industrial University of Ho Chi Minh City, 71408, Ho Chi Minh City, Vietnam.*
**Corresponding author: E-mail: levinhan@iuh.edu.vn, ankhang.vip@gmail.com;*

Monuments. Moreover, the findings published in this paper serve as a valuable reference for researchers, graduate students, and architecture students, contributing to academic education and scientific research.

Keywords: Design principle; floor plan; hue imperial palace; Nguyen dynasty; Vietnam; world cultural heritage.

1. INTRODUCTION OF THE HUE IMPERIAL PALACES

1.1 Construction History and Modification

According to historical sources from the Nguyen dynasty (Cabinet of Nguyen dynasty (1802-1945), although the construction of the Hue capital city began during the early Gia Long period (1802–1820), it was initially carried out on a small scale. This early phase mainly involved the construction of buildings for the activities of the Nguyen cabinet, accommodations for the royal family, and a portion of the imperial mausoleums located in the southwestern hilly area of the Hue capital.

In Table 1, Emperor Minh Mang is the second emperor of the Nguyen dynasty, during this period, construction activities expanded significantly. To gradually complete the capital city and redesign the Citadel (Fig. 1), the Nguyen court relocated 10 villages, dug a lake to fill the citadel walls, and diverted the flow of two natural rivers (the *Kim Long* River and the *Bach Yen* River) to establish an uninterrupted hydrological system within the Citadel (Cadiere 1924). Additionally, a series of buildings, including palaces, temples, and pavilions inside the Imperial City, as well as many other structures, were constructed.

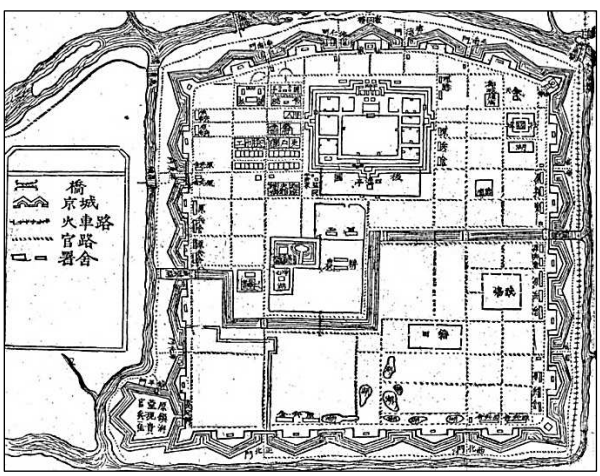

Fig. 1. Drawing of Site-plan of the Hue Citadel (Historic document of the Nguyen dynasty published under Duy Tan period, 1907-1916)

Table 1. Chronology of the Nguyen's emperors

No.	Date of succeed Emperors			Period of Throne	Born and Dead	Name of Royal Family
	English	Vietnamese	Chinese			
1	Gia Long	Gia Long	嘉隆	1802 - 1820	1762 - 1820	Nguyễn Phúc Ánh
2	Minh Mang	Minh Mạng	明命	1820 - 1840	1791 - 1840	Nguyễn Phúc Đảm
3	Thieu Tri	Thiệu Trị	紹治	1841 - 1847	1807 - 1847	Nguyễn Phúc Miên Tông
4	Tu Duc	Tự Đức	嗣德	1847 - 1883	1829 - 1883	Nguyễn Phúc Hồng Nhậm
5	Duc Duc	Dục Đức	育德	1883	1853 - 1883	Nguyễn Phúc Ưng Chân
6	Hiep Hoa	Hiệp Hòa	協和	1883	1847 - 1883	Nguyễn Phúc Hường Dật
7	Kien Phuc	Kiến Phúc	建福	1884	1869 - 1884	Nguyễn Phúc Ưng Đăng
8	Ham Nghi	Hàm Nghi	咸宜	1884 - 1885	1871 - 1943	Nguyễn Phúc Ưng Lịch
9	Dong Khanh	Đồng Khánh	同慶	1885 - 1889	1864 - 1889	Nguyễn Phúc Chánh Mông
10	Thanh Thai	Thành Thái	成泰	1889 - 1907	1879 - 1954	Nguyễn Phúc Bửu Lân
11	Duy Tan	Duy Tân	維新	1907 - 1916	1900 - 1945	Nguyễn Phúc Vĩnh San
12	Khai Dinh	Khải Định	啓定	1916 - 1925	1885 - 1925	Nguyễn Phúc Bửu Đảo
13	Bao Dai	Bảo Đại	保大	1925 - 1945	1913 - 1997	Nguyễn Phúc Vĩnh Thụy

During the Thieu Tri period (1841–1847), the capital's institutions and architecture within the Citadel were largely completed. The main construction activities at this time involved building additional necessary structures and improving some residences inside the Imperial City.

From the Tu Duc period (1847–1883) to the Thanh Thai period (1889–1907), the focus shifted to renovation, repairs, and maintenance of buildings and structures that had been built earlier within the Citadel. Renovation and repair activities were especially intensive during the Tu Duc period inside the Imperial City and Forbidden City (square-enclosed walls inside the Imperial City). Beginning in the Thanh Thai period, new construction materials from Europe—such as cement, decorative printing bricks, and mirror glass—began to be imported into Vietnam. These materials had a significant impact on architecture in the Hue capital. Traditional mortar was gradually replaced by cement or used in combination with it. Due to the introduction of these materials, construction techniques also evolved, laying the foundation for changes in architectural styles and construction practices in the later years of the Nguyen dynasty.

From the Thanh Thai period to the Dong Khanh period (1885–1889), due to changing political and economic circumstances, there were few new construction projects. On the contrary, many buildings were either destroyed or repurposed for other uses, while the remainder saw only minor repairs and improvements.

From the Khai Dinh period (1916–1925) onward, the architecture of the Nguyen dynasty underwent a significant transformation. Reinforced concrete gradually replaced traditional wood as the primary building material, allowing for the construction of taller and more magnificent structures. Additionally, the Western garden style began to appear within the Forbidden City. The architectural decoration of this period combined both Eastern and Western motifs, a characteristic feature of the architectural style developed during the Khai Dinh period.

The construction history of the Complex of Hue Monuments can be divided into four stages as follows:

- **First stage:** From the Gia Long period to the Minh Mang period (1802–1841), a period of planning and initial construction.
- **Second stage:** From the Thieu Tri period to the early part of the Tu Duc period (1841–1865), a period of repair and renovation of earlier constructions.
- **Third stage:** From the later part of the Tu Duc period to the Thanh Thai period (1865–1907), a period of maintenance and reduction in scale.
- **Fourth stage:** From the Khai Dinh period to the end of the Bao Dai period (1916–1945), a period of transformation in architectural style and changes in construction techniques.

From the late 18th century to the early 19th century, most Southeast Asian countries were colonized by European powers, but Vietnam remained an independent nation, maintaining a centralized, autocratic monarchical political system, with the emperor at the center of this structure. Although there was some influence from Western construction techniques in the design and construction of military defensive fortifications (such as the Vauban-style fortresses), and some Western materials were imported in the late 19th century, the architectural form and construction techniques of the Nguyen dynasty's palaces in Hue largely preserved indigenous Vietnamese elements. These elements have created a unique and distinctive identity for Vietnamese traditional architecture, which has been preserved to this day.

In this study, the author aims to clarify the indigenous Vietnamese elements through an analysis of the design methods of the floor plans of the Hue imperial palaces. The emergence of Nguyen's imperial palaces in this historical context is clear evidence of the fusion between traditional local conservatism and the global trend of Westernization brought about by the colonial expansion of European powers during the 18th and 19th centuries.

1.2 Types of the Imperial Palaces

1.2.1 Classification according to the categories recorded in historical documents

According to the descriptions from the "Cong Bo" Ministry of Construction of the Nguyen Dynasty Cabinet of Nguyen dynasty (1802-1945), the building categories listed under each functional group include:

- *"Cung Dien"* imperial palace (宮殿), which refers to civil architecture inside the Imperial City and the Citadel;
- *"Dan Mieu"* altar and shrine (壇廟), which refers to architecture used for religious and spiritual purposes;
- *"Hanh Cung"* residence for travel inspection (行宮), which refers to architecture in the Citadel or the provinces used for the Emperor's travel inspections;

- "Thanh Dai" military port (城臺);
- "Dinh Thu" edifice (營署), which refers to architecture in the Citadel or the provinces used for government offices;
- "Lang Tam" imperial mausoleum (陵寢), which refers to the mausoleums of the Nguyen imperial family.

The architectural hierarchy for each type of building includes:

- *"Dien"* palace/temple (殿),
- *"Mieu"* shrine (廟),
- *"Duong"* hall (堂),
- *"Vu"* eave (廡),
- *"Lau"* pavilion (樓),
- *"Cac"* pavilion tower (閣),
- *"Vien"* institute (院),
- *"Phong"* chamber (房),
- *"Mon"* gate (門),
- *"Dinh"* public hall (亭),
- *"Ta"* floating pavilion (榭),
- *"Phu"* residence (府),
- *"Sanh"* office *building (廳), depending on their function and/or their symbolic importance.*

Among these, the "Dien" palace/temple (殿) and *"Mieu"* shrine (廟) categories are always the largest and highest in class, serving as the main architectural structures of each imperial residence (Figs. 2–3).

Additionally, the *"Dien"* category (殿) is divided into two different functional types:

- *"Chinh Dien"* main imperial palace (正殿), located inside the Hue Imperial City or the Citadel;
- *"Tam Dien"* mausoleum temple (寢殿), located at the Imperial Mausoleums, used for the worship of the emperors.

Furthermore, the *"Mieu"* category (廟) refers to the imperial shrines used for the worship of the ancestors of the Nguyen royal family. These shrines are found in sacred areas of the Imperial City and serve religious purposes over the Hue ancient capital city.

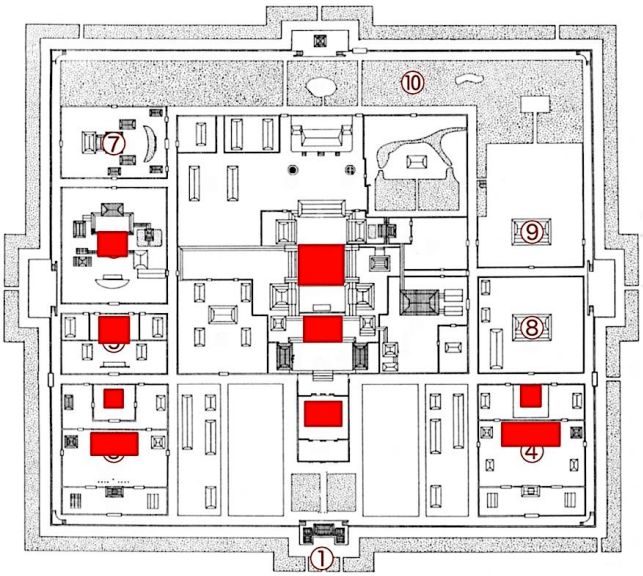

Fig. 2. Location of the targeted twin buildings in the Hue Imperial City

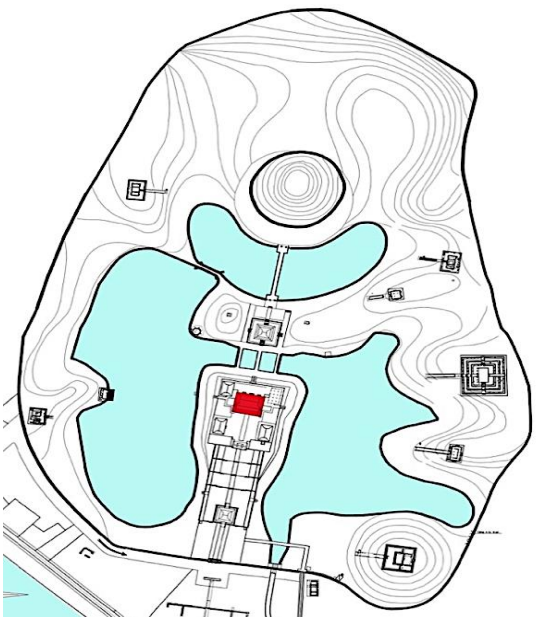

Fig. 3. Location of the twin buildings in Emperor Minh Mang's mausoleum

1.2.2 Classification according to the geometric layout and the architectural typology

If classified based on geometric layout, the architecture of the Hue imperial palaces was developed from three basic types: Type A (rectangular layout), Type B (square layout), and Type C (octagonal layout). Among these, Type A is the most common and can be applied to all categories (Fig. 4).

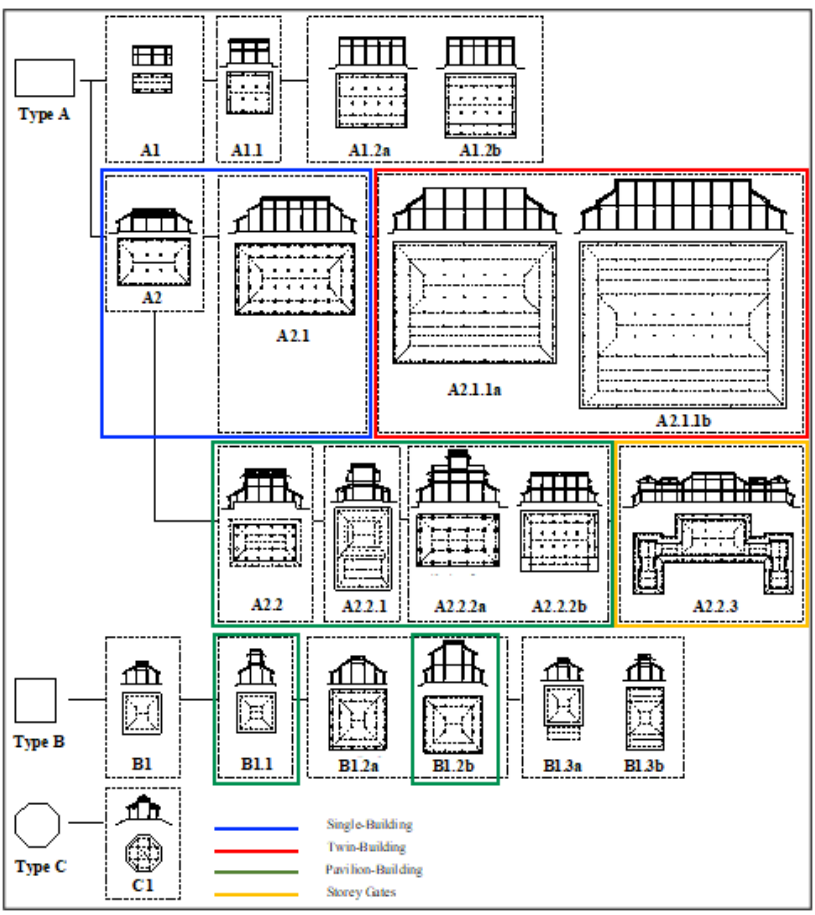

Fig. 4. Typological diagram of the Hue imperial architecture (developed from Fig. 24, p. 546, "An Architectural Study on Hue Imperial City (1802-1883) of the Nguyen Dynasty and Its Original Characteristics, Vietnam", Civil Engineering and Architecture 12(1): 520-547, 2024, DOI: 10.13189/cea.2024.120138)

When classifying the Imperial Palaces based on their appearance, the following typical typologies can be identified: Single-ridge beam buildings (abbreviated as Single Buildings), Twin-ridge beam buildings (abbreviated as Twin Buildings), Pavilion tower buildings (abbreviated as Pavilion-Buildings), Storey main gates (abbreviated as Storey Gates), and others. The remaining structures within the Monuments fall into these main typologies, with the corresponding proportions being 52%, 26%, 11%, and 11%, based on the total number of buildings surveyed.

a) **Single Buildings (Fig. 5):** These are independent structures that either complement the function of a main building or serve distinct purposes. Each Single-Building typically comprises a wooden frame placed on a square or rectangular elevated platform, covered by one or two layers of roofing. The roofs are classified into two types: single-layered and double-layered. Double-layered roofs signify higher importance and are often found in significant areas or fulfilling special roles, whereas single-layered roofs indicate a lower classification within the Imperial Palaces.
b) **Twin Buildings (Fig. 6):** These serve as the primary architectural structures within each imperial residence. They are generally the largest and belong to the highest classification. Twin Buildings consist of two or three interconnected structures, often referred to as *"Trung Thiem Diep Oc"*, meaning two or three buildings connected on the same platform. The front building is called *"Tien Doanh"* (前楹), while the back building is called *"Chinh Doanh"* (正楹). In cases with three interconnected buildings, the front structure is *"Tien Doanh"*, the middle one is *"Chinh Doanh"*, and the rear building is *"Hau Doanh"* (後楹). These buildings are linked by a structure called *"Thua Luu"* (承霤), which features a drainage system to channel rainwater to the sides.
c) **Pavilion-Buildings (Fig. 7):** These buildings generally feature two or three floors and are situated in prominent areas of the residences. They serve special functions, such as acting as symbols, monuments of victory, or spiritual towers. The platforms are typically square or rectangular, with the floors separated by wooden structures dividing the roof into upper, middle, and lower sections. This unique architectural style plays a significant role in defining the height and prominence of the residences.
d) **Storey Gates (Fig. 8):** These gates, often rectangular in platform, usually have two or three floors and serve as the main entrances to the residences. They typically feature three central pathways, also known as *"Tam Quan"*. This type of gate is a characteristic feature found in almost all residences within the Monuments.
e) **Other Structures:** These include various types of buildings derived from the four primary architectural styles mentioned above.

Among the above-mentioned categories, the Twin Buildings category stands out as the largest in scale and represents the highest level of importance. These structures are often used for Palaces, Temples, and Shrines and are typically located on the central symmetrical axis of each significant residence within the

Monuments. Consequently, this category has been chosen as the primary subject of our study (Table 2).

Within the scope of this research, our focus is primarily on the floor plan, its components, and functional uses, to unravel the spatial conception of the architecture concerning its wooden framework. From the perspective of architectural design methodology, we will conduct a series of dimensional analyses to re-determine the original design methods employed.

Fig. 5. Ta Vu eave (Single-Building)

Fig. 6. Thai Hoa Dien palace (Twin-Building)

Fig. 7. Hien Lam Cac pavilion (Pavilion-Building)

Fig. 8. Ngo Mon main gate (Storey Gate)

Table 2. List of the remaining twin-buildings of the monuments

No	Name of buildings		Types	Location	Used-function	Year of Const.	Sources (Historic documents)
	English	Chinese					
1	Thai Hoa Dien	太和殿	Palace	Imperial Court	Imperial conferent hall	1805	事例205-18, 統志1-5
2	Can Chanh Dien	勤政殿	Palace	Forbiddent City	Cabinet working hall	1811	事例205-10, 統志1-06
3	Can Thanh Dien	乾成殿	Palace	Forbiddent City	Living of Emperor	1811	事例205-11, 統志1-06
4	Dien Tho Chinh Dien	延壽正殿	Palace	Dien Tho Residence	Living of Queen mother	1849	事例205-21
5	Long An Dien	隆安殿	Palace	Citadel	Restting of Emperor	1845	事例208-23
6	Trieu To Mieu	肇祖廟	Shrine	Thai Mieu Residence	Worshipping of the Founder	1814	事例207-03, 事例208-06, 統志1-10
7	Thai To Mieu	太祖廟	Shrine	Thai Mieu Residence	Worshipping of the Lords	1803	事例207-04, 事例208-06, 統志1-08
8	The To Mieu	世祖廟	Shrine	The Mieu Residence	Worshipping of the Emperors (available for male)	1821	事例207-06, 事例208-11, 統志1-09
9	Phung Tien Mieu	奉先廟	Shrine	Phung Tien Residence	Worshipping of the Emperors (available for female)	1814	事例207-08, 事例208-14, 統志1-11
10	Minh Thanh Dien	明成殿	Temple	Thien Tho Mausoleum	Worshipping of Emperor Gia Long	1814	事例216-07, 20
11	Sung An Dien	崇恩殿	Temple	Hieu Mausoleum	Worshipping of Emperor Minh Mang	1841	事例216-10, 21
12	Bieu Duc Dien	表德殿	Temple	Xuong Mausoleum	Worshipping of Emperor Thieu Tri	1847	事例216-13, 30
13	Hoa Khiem Dien	和謙殿	Temple	Khiem Mausoleum	Worshipping of Emperor Tu Duc	1864	扁額
14	Luong Khiem Dien	良謙殿	Temple	Khiem Mausoleum	Worshipping of the Queen mother	1864	扁額

2. MATERIALS AND METHODS

2.1 Survey Targeted Twin Buildings

Table 2 provides a list of Twin Buildings that were included in the measuring survey. These consist of five main imperial palaces (abbreviated as the Palaces), four imperial shrines (abbreviated as the Shrines) located within the Imperial City and inside the Citadel, and five mausoleum temples (abbreviated as the Temples) located at the Imperial Mausoleums.

Among the Palaces, Shrines, and Temples, the *Can Thanh Dien* Palace, *Can Chanh Dien* Palace, *Thai To Mieu* Shrine, and *Phung Tien Mieu* Shrine have lost their wooden structures and roofs, with only the ruins of their platforms remaining. In contrast, the wooden structures and roofs of the other buildings are still intact. This study collectively refers to these three categories—Palaces, Shrines, and Temples—as the Twin Buildings and analyzes a total of 14 structures based on the results of the measuring surveys.

2.2 Measuring Methods

We conducted both longitudinal and latitudinal transverse wooden-structure measuring surveys on 10 buildings whose wooden structures still exist. For the four buildings where only the platform remains, center-to-center measurements of the remaining basement stones were analyzed.

Before reconstructing the original design procedure and method of floor plans based on the actual measurements, it is essential to replicate the lines that serve as design reference lines and/or the center lines of column rows, corresponding to the central symmetric axes that are no longer visible on-site.

No significant traces of the cross ink-lines marking column rows have been found on the existing ruin-platforms. However, by examining the column diameters traced on the upper surfaces of the basement stones of these ruin-platforms and drawing on experience—particularly from a case study of the ruin-platform of Can Chanh Dien Palace (An et al., 2008) (Figs. 9–11)—it is possible to reconstruct the design reference line system on the floor plan, known as "Luoi Cot" (grid of column rows). This system has been confirmed and is referred to as appropriate in the analysis presented in this study.

2.3 Units for Analyzing

Identifying the specific unit of measurement used in the construction of a building is a crucial concern in restoration design. It was not uncommon for different buildings to be constructed using different units of measurement, so determining a "building-specific measure" for each structure is essential. In this study, we aim to estimate platform-specific measurements primarily through an analysis of the floor plans of buildings. Before proceeding, it is necessary to examine the specific units of measurement used during the Nguyen dynasty.

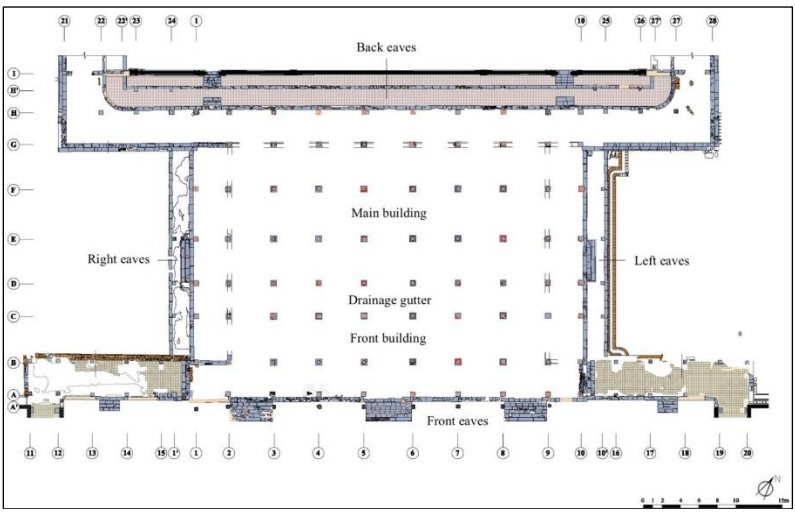

Fig. 9. Present status drawing of the ruin-platform of Dien Can Chanh palace

Fig. 10. Ruin-platform of Can Chanh Dien palace

Fig. 11. Diameter traced on the basement stone (D3)

Several artifacts providing references to the official measurement units used in the Nguyen dynasty are preserved in museums in Vietnam (Table 3, Fig. 12). These references indicate that the official measurement units of the Nguyen dynasty included various types designed for different applications. Among these, the "Quan Moc Xich" ruler (官木尺) and the "Lu Ban Xich" ruler (魯班尺) were specifically used for building construction. These measurement systems were based on either a decimal or an octal number system, though it seems unlikely that the two systems were used separately for different aspects of building design.

In addition, the historical documents have recorded that “勤政殿基高二尺三寸” Cabinet of Nguyen dynasty (1802-1945), (means the height of platform equal 2.3

units), the actual height of its platform is 985mm ÷ 2.3 units = 428mm/unit (case of *Can Chanh Dien* Palace); "肇祖廟基高二尺" (means height of platform equal 2.0 units) (Cabinet of Nguyen dynasty (1802-1945), the actual height of its platform is 765mm ÷ 2.0 units = 382mm/unit (case of *Trieu To Mieu* Shrine).

Based on this information, we assume that during the early periods of the Nguyen dynasty, a "Quan Moc Xich" ruler (abbreviated as the Large Ruler) measured 424–428 mm per unit, and a "Lu Ban Xich" ruler (abbreviated as the Small Ruler) measured 382–384 mm per unit (Shin-Ichiro 1996).

Table 3. List and feature of the investigated Rulers

No	Name of Rulers			mm /Unit	Inchs	mm /Inch	Displaying
	English	Vienamese	Chinese				
1	Chu Nguyen ruler	Chu Nguyên Xích	周元尺	559	8	70	Hue Museum of Imperial Fine Art
2	Chu Nguyen ruler	Chu Nguyên Xích	周元尺	286	10	28.6	Ha Noi Historic Museum
3	Kinh Xich ruler	Kinh Xích	経尺	402	10	40.2	Hue Museum of Imperial Fine Art
4	Phung Xich ruler	Phùng Xích	縫尺	596	10	59.6	Hue Museum of Imperial Fine Art
5	Lo Ban Xich ruler	Lỗ Ban Xích	魯班尺	382	10	38.2	Ha Noi Historic Museum
6	Lo Ban Xich ruler	Lỗ Ban Xích	魯班尺	298	8	37	Ha Noi Historic Museum
7	Bac Tuc Phung Xich ruler	Bắc Tục Phùng Xích	北俗縫尺	400	10	40	Ha Noi Historic Museum
8	Do Dien Xich ruler	Độ Điền Xích	度田尺	402	10	40.2	Ha Noi Historic Museum
9	Quan Dien Xich ruler	Quan Điền Xích	官田尺	320	8	40	Ha Noi Historic Museum
10	Quan Phung Xich ruler	Quan Phùng Xích	官縫尺	636	10	63.6	Ha Noi Historic Museum
11	Quan Phung Xich ruler	Quan Phùng Xích	官縫尺	642	10	64.2	Ha Noi Historic Museum
12	Quan Moc Xich ruler	Quan Mộc Xích	官木尺	426	10	42.6	Ha Noi Historic Museum
13	Quan Moc Xich ruler	Quan Mộc Xích	官木尺	422	10	42.2	Ha Noi Historic Museum
14	Quan Moc Xich ruler	Quan Mộc Xích	官木尺	421	10	42.1	Ha Noi Historic Museum
15	Quan Moc Xich ruler	Quan Mộc Xích	官木尺	419	10	41.9	Ha Noi Historic Museum
16	Tay Xich ruler	Tây Xích	西尺	1000	10	100	Ha Noi Historic Museum
17	Nam xich ruler	Nam Xích	南尺	1000	25	40	Ha Noi Historic Museum

Fig. 12. List and feature of the investigated rulers

3. STUDY RESULTS

3.1 The Twin Buildings Seen from Historical Documents

3.1.1 Description in the investigated historic documents

The historical documents of the Nguyen dynasty primarily focus on special or important buildings, while others are only mentioned briefly. As the aforementioned Twin Buildings represent paramount architectural structures serving three key functions—the Palace, Shrine, and Temple—they are more carefully described in historical records. However, these descriptions often lack

sufficient detail for the analysis conducted in this study. Nevertheless, we must rely on the historical information regarding the scale of the architecture to verify and supplement the findings from our actual surveys.

Typically, historical records provide only basic details, such as the location of the buildings, the year of construction and repairs, the height of the foundation, the number of compartments and wings, and a brief mention of the type of wooden frame and roof. Detailed information about the interior and architectural structure of the Twin Buildings is absent, particularly concrete dimensions of compartments, wings, and building heights.

It is possible that documenting interior details was considered taboo during the Nguyen dynasty (Association of History of Nguyen dynasty (1802-1945), leading historians to describe the buildings primarily from an external perspective. Alternatively, technical documents detailing the architectural construction techniques of the Nguyen dynasty may have existed but were lost or destroyed during wars, natural disasters, or fires.

For example, the Tang Thu Lau Pavilion, located at the center of Ho Hoc Hai Lake inside the Citadel, was designed to store books and administrative documents of the Nguyen dynasty. However, this building was burned during the Vietnam-France war (Chi, 1948) making it likely that many important records were lost in the process.

3.1.2 Regarding twin-building architectural features and scale

In Table 4, we statistically filter information related to the building scale to analyze the relationship between architectural features and the scale of the Twin Buildings. This includes details about the number of compartments, wings, and platform heights. Additionally, we conduct a comparative study of the information recorded in historical documents against the actual measurement results of the existing buildings (Fig. 13). This is done to verify the database and explore the relationship between the type of Twin Buildings and their scale. The analytical results allow us to make the following observations:

- Lack of proportional relationship: There appears to be no proportional relationship between the building scale and the platform height. In some cases, the platform height information is omitted altogether. For example, the platform of the *Can Thanh Dien* Palace has the largest ground area, but its platform height is only equal to that of the *Can Chanh Dien* Palace, even though the ground area of the latter is only approximately half that of the former. Similarly, the *Thai To Mieu* Shrine has the largest number of compartments (in the ridge direction), yet its platform height is among the lowest compared to the other buildings.
- Ground area vs. number of compartments and wings: The *Thai To Mieu* Shrine has the largest total number of compartments and wings (in the ridge direction), but its ground area is much smaller than that of the *Can Thanh Dien* Palace. This discrepancy can be explained by the fact that the *Can Thanh Dien* Palace has three ridge beams, whereas the *Thai*

To Mieu Shrine has only twin ridge beams. Another observation is that when the number of compartments and wings is the same, the ground area can still differ, as seen in the cases of *Minh Thanh Dien* Temple and *Sung An Dien* Temple. Conversely, the ground area is the same when the number of compartments and wings is identical, such as in the cases of *The To Mieu* Shrine and *Phung Tien Mieu* Shrine or *Thai Hoa Dien* Palace and *Can Chanh Dien* Palace. These three scenarios occur regardless of whether the buildings belong to the same or different categories.

- Comparison between Palaces and Temples: The *Can Thanh Dien* Palace, built during the Gia Long period (1811) as the residence of Emperor Gia Long (and later used by succeeding emperors), has the largest platform ground area, approximately 2,257m². In contrast, the *Minh Thanh Dien* Temple, constructed in 1814 during the same period as a temple to worship Emperor Gia Long's soul, has the smallest platform ground area, approximately 347m²—only about 1/6 of the *Can Thanh Dien* Palace. Moreover, while historical documents indicate the same number of compartments and wings for certain Palaces (e.g., *Thai Hoa Dien* Palace and *Can Chanh Dien* Palace) and Temples (e.g., *Minh Thanh Dien* Temple, *Sung An Dien* Temple, and *Bieu Duc Dien* Temple), the dimensional scale of the Palace category is almost three times larger than that of the Temple category (Table 4).
- Inaccuracy of historical descriptions: The architectural scales described in historical documents do not accurately reflect the actual dimensions of the buildings. These descriptions seem to provide only qualitative distinctions between buildings, omitting quantitative architectural dimensions. Why is there such a significant difference between the actual dimensional scales of the Palace and Temple categories when their scales are described similarly in historical records?

Based on the analysis presented below in Tables 5, 6, and 7, as well as the use of the two types of rulers mentioned earlier, we propose that the first quantitative factor influencing architectural scale during the Nguyen dynasty was parameterized by the lengths of the Large Ruler and Small Ruler (referred to as the 1st level of parametric, abbreviated as *Parametric 1*). It is plausible that the Large Ruler was applied in the construction of Palaces and Shrines (in the Imperial City), while the Small Ruler was used for Temples (in the Imperial Mausoleums). Consequently, by simply adjusting the length of the ruler, the entire dimensional scale (quantitative factors) of a building could be altered.

3.2 Characteristics of the Twin-Building Floor Plans

3.2.1 Components of the interior spatial

Based on literary references (An1802-1945), the parts of the floor plan will be referred to as follows:

- "Chinh Trung Gian" (central compartment, 正中間, hereafter A).
- "Thu Gian" (left/right compartment, 左/右次間, hereafter B).

- "Noi Suong" (inter-wing, 內廂, hereafter C).
- "Ngoai Suong" (outer wing, 外廂, hereafter D) in the ridge direction (latitude).
- "Chinh Doanh Luong Tam" (big beam span of the main building, 正楹梁心, hereafter E).
- "Tien Doanh Luong Tam" (big beam span of the front building, 前楹梁心, hereafter F).
- "Thua Luu" (drainage gutter span, 承霤, hereafter G).
- "Tien Khuynh" (front diagonal beam span, 前傾, hereafter H).
- "Hau Khuynh" (back diagonal beam span, 後傾, hereafter H).
- "Tien Suong" (front wing span, 前廂, hereafter I).
- "Hau Suong" (back wing span, 後廂, hereafter I) in the beam direction (longitude).
- "Tien/Hau Quyet" (front/back corners, 前後決, hereafter K).
- "Ta/Huu Quyet" (left/right corners, 左右決, hereafter K) at the four outermost corners.

Additionally, according to the ridge direction, the interior space from the drainage gutter span to the front side of the building is defined as the "Tien Doanh" (front building, 前楹, hereafter the Front Building). The space from the drainage gutter span to the back side of the building is defined as the "Chinh Doanh" (main building, 正楹, hereafter the Main Building).

Furthermore, the stairs made of natural stone, symmetrically attached at the center and both the front-left and back-right sides of the floor plan, are shown in Fig. 14.

Table 4. Relationship between the types and scale of the twin buildings

No.	Name of buildings	Types	Scale of Building (Historic documents)			Scale of Building (Site observation)					Sources (Historic documents)
			Compartments	Wings	Height of Platform (Unit)	Number of Spans	Lenght of Spans (Unit)		Length of Platform (mm)		Area of Platform (mm2)	
							Ridge	Beam	Ridge	Beam		
1	Thai Hoa Dien	Palace	Front building 7 Main building 5	2	5.8	Ridge 9 Beam 7	97.4	68.6	43,298	30,829	1,334,834,042	事例205-18, 統志1-5
2	Can Chanh Dien	Palace	Front building 7 Main building 5	2	3.2	Ridge 9 Beam 7	97.1	72.0	43,014	32,400	1,393,653,600	事例205-10, 統志1-06
3	Can Thanh Dien	Palace	Front building 9 Main building 7 Back building 9	2	3.2	Ridge 11 Beam 9	122.9	94.7	53,889	41,876	2,256,655,764	事例205-11, 統志1-06
4	Dien Tho Chinh Dien	Palace	Front building 5 Main building 3	2	1.4	Ridge 9 Beam 7	79.2	45.5	34,932	24,325	849,720,900	事例205-21
5	Long An Dien	Palace	Front building 7 Main building 5	X	3.2	Ridge 9 Beam 7	81.4	58.4	35,616	28,026	998,174,016	事例208-23
6	Trieu To Mieu s	Shrine	Front building 5 Main building 3	2	2.0	Ridge Beam 7	57.8	55.8	23,073	22,576	520,896,048	事例207-03, 事例208-06, 統志1-10
7	Thai To Mieu	Shrine	Front building 15 Main building 13	2	1.5	Ridge 17 Beam 7	163.9	60.9	71,062	27,390	1,946,388,180	事例207-04, 事例208-06, 統志1-08
8	The To Mieu	Shrine	Front building 11 Main building 9	2	3.6	Ridge 13 Beam 7	123.9	61.0	54,613	27,692	1,512,343,196	事例207-06, 事例208-11, 統志1-09
9	Phung Tien Mieu	Shrine	Front building 11 Main building 9	X	X	Ridge 13 Beam 7	121.8	60.5	53,080	29,053	1,542,133,240	事例207-08, 事例208-14, 統志1-11
10	Minh Thanh Dien	Temple	Front building 7 Main building 5	X	X	Ridge 7 Beam 7	47.4	42.3	19,661	17,626	346,544,786	事例216-07, 20
11	Sung An Dien	Temple	Front building 7 Main building 5	X	X	Ridge 7 Beam 7	57.9	54.5	23,485	22,099	518,995,015	事例216-10, 21
12	Bieu Duc Dien	Temple	Front building 7 Main building 5	X	X	Ridge 7 Beam 7	58.0	54.0	23,516	21,831	513,377,796	事例216-13, 30
13	Hoa Khiem Dien	Temple	X	X	X	Ridge 9 Beam 7	75.6	53.6	30,182	21,734	655,975,588	統編
14	Luong Khiem Dien	Temple	X	X	X	Ridge 7 Beam 7	55.8	49.2	22,656	20,045	454,139,520	統編

Note: Miss information in historical documents (X)

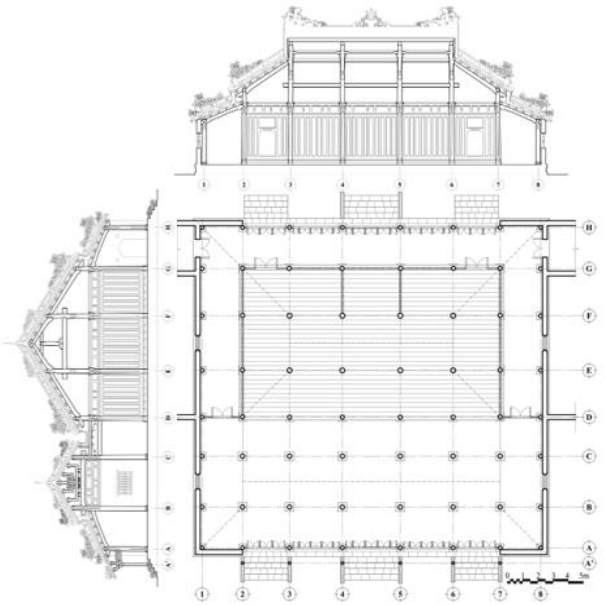

Fig. 13. Architectural drawings of the typical twin-building (case of the Sung An Dien temple)

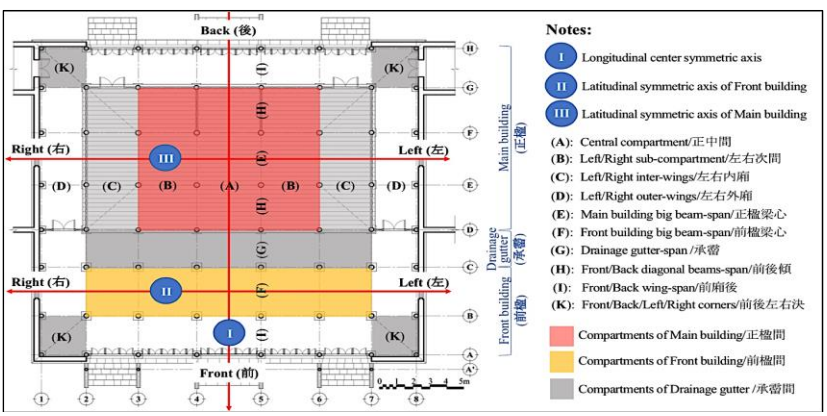

Fig. 14. Spatial arrangement on the floor-plan of the twin buildings

3.3 Symmetrical Axes and Column Rows

Accordingly, the concepts of central, left and right, front and back, as expressed on the floor plan, determine the spatial components of the floor plan arranged

according to the symmetrical axes designed in both the latitudinal and longitudinal directions. The above-displayed Fig. 14 shows the features and location of the longitudinal center symmetrical axis (I), which plays an important role not only in constructional techniques but also in spiritual symbolism. Thus, the central compartment, which contains the longitudinal center symmetrical axis, is usually designed as the largest span (as discussed below). The most treasured items of the dynasty, such as the throne and the emperor's altar, must be placed in this central compartment.

Additionally, the latitudinal symmetrical axes of the Front Building (II) and the Main Building (III) are essential for the arrangement of latitudinal column rows, as well as for the assembly of the other component timbers. The column rows are drawn parallel, following the symmetrical axes, and are set symmetrically according to them.

Specifically, in Fig. 15, line 5 represents the first left longitudinal column row, while line 4 represents the first right longitudinal column row, and so on. Additionally, lines B and line C represent the first front and first back latitudinal column rows of the Front Building, while lines E and F represent the first front and first back latitudinal column rows of the Main Building. Lines D and G represent the second front and second back latitudinal column rows of the Main Building.

Continuing, the positions E5 and E4 will be the front first-left and front first-right big columns, while F5 and F4 will be the back first-left and back first-right big columns of the Main Building. Similarly, B5 and B4 will be the front first-left and front first-right big columns, and C5 and C4 will be the back first-left and back first-right big columns of the Front Building, and so on.

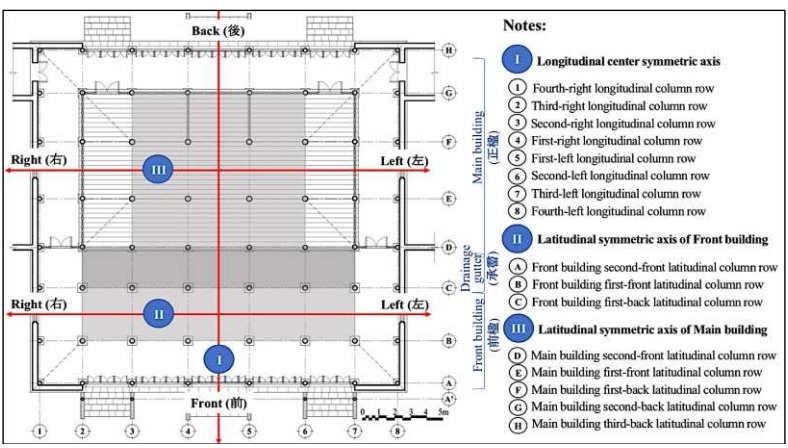

Fig. 15. Axes and column rows of the twin buildings shown on the floor-plan

3.4 Analyzing the Twin Building Floor Plans Design Methods

3.4.1 Dimensional analysis

We first analyzed the estimated construction measurements of each Twin Building for reference. Actual measurements were converted to units according to the existing measurement units of the Nguyen dynasty, as mentioned above. These were also calculated based on measurement values described in literary sources. To assess the validity of the estimated construction measures, we compared the actual measurements of all column spans and platform lengths with restoration values derived from the estimated construction measures. The maximum margin of error was 88 mm, the minimum margin of error was 0 mm, and the average difference was approximately 25 mm (Table 5). Therefore, the estimated construction measures were generally proven to be highly valid.

The aforementioned literary references of the Nguyen dynasty do not contain information on the unit measurements of the platforms of the architecture nor the unit measurements of the height of the large columns in some of the Twin Buildings. However, based on these sources, the central compartment in the ridge direction (referred to as A) is officially called *"Chan Tam"* (振心), and the main span of the main building in the beam direction (referred to as E) is called *"Luong Tam"* (梁心). It can be reasonably concluded that A and/or E serve as dimensional origins of the architecture. Therefore, they have official names that express special concepts, as recorded in the historical documents of the Nguyen dynasty (An et al. 2009). The major findings of our analysis are presented below.

a) Column span is largest in the Central compartment
In both the ridge direction and beam direction, the column span is largest in the central span (span 4-5, mentioned as A) and the main span (span E-F, mentioned as E). The span becomes smaller toward the outer sides. In the Palaces and Shrines, the largest column span is around 12 to 13 units (using the Large Ruler), while in the Temples, it is around 10 units (using the Small Ruler). Other column spans were likely designed based on this standard, with each span being established to a tenth of a unit based on the decimal number system. For example, adjacent compartments have spans of ±1 units, ±0.9 units, ±0.1 units, and so on (Table 6). This system, which is based on addition and/or subtraction rather than proportion, is called the "Gia-Giam" method in the traditional technique of Hue, and there are skilled master carpenters who possess this traditional method.

b) Three types of mutual relationships among Column spans
According to the master carpenters who possess the aforementioned traditional skills, the mutual relationship between columns is based on three default principles (Fig. 16):

- First principle: *"Khep Chuong"* — This means the spans between all large columns are the same. This can be observed in the dimensional relationships: span 4-5 = span E-F, and span 5-6 = span B-C.
- Second principle: *"Con Lon Me"* — This means the spans between subsequent pairs of columns decrease relative to the initially

established spans. This can be observed in the dimensional relationships: span 4-5 > span 5-6 > span 6-7 > span 7-8; span E-F > span B-C; span D-E > span C-D.

- Third principle: *"Bat Van"* — This means the spans between corner columns are the same. This can be observed in the dimensional relationships: span D-E = span 6-7; span A-B = span 7-8.

c) Central span (A) in the ridge direction is established first

In general, for Twin Buildings, the central span in the ridge direction (span 4-5) was likely established first, using either the Large Ruler or the Small Ruler. The actual measurement of this span ranged from 9 units to 13 units. Each Twin-Building has a different span, possibly because a specific measurement value that holds particular significance to the size, function, and position of the building was established first. Deciding on the span of columns in the ridge direction is crucial to the building's elevation structure. Since there is normally no column inclination, the length of the horizontal ridge-direction element becomes the span in the beam direction, with adjustments and changes made accordingly. On the other hand, establishing the span in the ridge direction first is likely easier to do arbitrarily, particularly because the central span (A) is often the first to be set, aided by its repetitiveness. The spans in the ridge direction help set the scale and expression of the entire architecture, while the spans in the beam direction are more closely related to technical factors (Table 6).

d) The Next spans (B) in the ridge direction are smaller than the Central span (A)

The next spans (referred to as B), or those on the outer sides of A, are clearly designed to be smaller than A, as shown in the second principle. In each case, B is smaller than A by a range of 0.4 units to 1 unit. Interestingly, in terms of actual values, the measurement of B is a fraction of A in the Can Thanh Dien Palace, Can Chanh Dien Palace, and Thai Hoa Dien Palace, all of which are located along the center symmetric axis of the Imperial City. In contrast, B is a whole number of 10 units in the Thai To Mieu Shrine, The To Mieu Shrine, Phung Tien Mieu Shrine, and Dien Tho Chinh Dien Palace, which are located along other sub-parallel axes. Additionally, it is also a whole number in all the buildings within the Imperial Mausoleums complex: B = 8 units in the Minh Thanh Dien Temple and B = 9 units in the other four temples. It seems that the column span was consciously determined based on the location and function of the buildings.

e) Main spans in the beam direction (E, F) and Inward column inclinations

The relationship between A and E is interrelated in one of three ways:
(i) E = A (center-to-center measurement between column bases);
(ii) A = E + 2e + 2f (both inward inclinations of columns in span E and span F, or span B-C);
(iii) E = A ± 0.1 unit.

The relationship between E and B is such that the span E (center-to-center measurement between column bases, or center-to-center

measurement of the beams) is equal to either E = B, E = B - 1 unit, or E = B ± 0.1 unit. The span F is equal to either F = B or within the range of F = E - 0.4 units to 1 unit. Only in the case of the Dien Tho Chinh Dien Palace is F = E - 1.7 units (Tables 6-8).

Table 5. Dimensional analysis of the total spans of the Twin Buildings

No.	Name of buildings	mm/Unit	Ridge direction/Latitude (mm)						Beam direction/Longitude (mm)					
			Length of total Spans			Length of Platform			Length of total Spans			Length of Platform		
			Measure	Restored	Error	Measure	Restored	Error	Measure	Restored	Error	Measure	Restored	Error
1	Thai Hoa Dien palace	427	41635	41590	*45*	43285	43298	*13*	29249	29292	*43*	30832	30829	*3*
2	Can Chanh Dien palace	428	41585	41559	*26*	42988	43014	*26*	30823	30816	*7*	32396	32400	*4*
3	Can Thanh Dien palace	426	52408	52355	*53*	53944	53889	*55*	40370	40342	*28*	41904	41876	*28*
4	Dien Tho Chinh Dien palace	426	33707	33739	*32*	34894	34932	*38*	23188	23217	*29*	24360	24325	*35*
5	Long An Dien palace	424	34568	34514	*54*	35663	35616	*47*	24778	24762	*16*	28024	28026	*2*
6	Phung Tien Mieu shrine	426	51880	51887	*7*	53069	53080	*11*	25761	25773	*12*	29063	29053	*10*
7	Thai To Mieu shrine	424	69473	69494	*21*	71039	71062	*23*	25734	25822	*88*	27317	27390	*73*
8	The To Mieu shrine	428	52990	53029	*39*	54596	54613	*17*	26104	26108	*4*	27680	27692	*12*
9	Trieu Tor Mieu shrine	382	22113	22080	*33*	23085	23073	*12*	21257	21316	*59*	22570	22576	*6*
10	Minh Thanh Dien temple	384	18259	18202	*57*	19721	19661	*60*	16214	16243	*29*	17626	17626	*0*
11	Sung An Dien temple	384	22301	22292	*9*	23489	23485	*4*	20938	20983	*45*	22065	22099	*34*
12	Bieu Duc Dien temple	383	22217	22214	*3*	23541	23516	*25*	20683	20682	*1*	21820	21831	*11*
13	Hoa Khiem Dien temple	384	29025	29030	*5*	30183	30182	*1*	20579	20582	*3*	21737	21734	*3*
14	Luong Khiem Dien temple	384	21451	21427	*24*	22654	22656	*2*	18822	18893	*71*	20019	20045	*26*

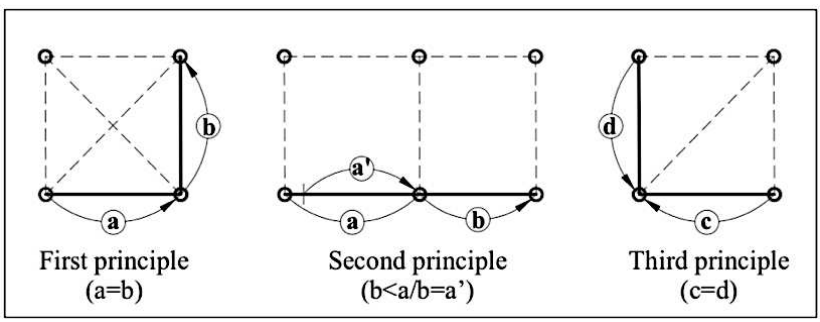

Fig. 16. Three basic principles applied for the Platform

Table 6. Dimensional analysis of column spans on the ridge direction (latitude) of the Twin Buildings

No.	Name of buildings	Right (D)	Right (C)	Right (B)	Right (B)	Right (B)	Right (B)	Right (B)	Right (B)	Central (A)	Left (B)	Left (B)	Left (B)	Left (B)	Left (B)	Left (B)	Left (C)	Left (D)	Total (Unit)
1	Thai To Mieu shrine	8.30	8.30	10.00	10.00	10.00	10.00	10.00	10.00	**10.70**	10.00	10.00	10.00	10.00	10.00	10.00	8.30	8.30	**163.90**
2	The To Mieu shrine	8.30	8.30			10.00	10.00	10.00	10.00	**10.70**	10.00	10.00	10.00	10.00			8.30	8.30	**123.90**
3	Phung Tien Mieu shrine	7.70	8.00			10.00	10.00	10.00	10.00	**10.40**	10.00	10.00	10.00	10.00			8.00	7.70	**121.80**
4	Dien Tho Chinh Dien palace	6.40	8.20					10.00	10.00	**10.00**	10.00	10.00					8.20	6.40	**79.20**
5	Long An Dien palace	7.30	9.00					9.50	9.50	**10.80**	9.50	9.50					9.00	7.30	**81.40**
6	Trieu To Mieu shrine	6.90	7.70						9.30	**10.00**	9.30						7.70	6.90	**57.80**
7	Can Thanh Dien palace	8.80	11.60				11.60	11.60	11.60	**12.50**	11.60	11.60	11.60				11.60	8.80	**122.90**
8	Thai Hoa Dien palace	8.50	9.10					12.30	12.30	**13.00**	12.30	12.30					9.10	8.50	**97.40**
9	Can Chanh Dien palace	8.30	11.30					11.40	11.40	**12.30**	11.40	11.40					11.30	8.30	**97.10**
10	Minh Thanh Dien temple	5.10	6.10						8.00	**9.00**	8.00						6.10	5.10	**47.40**
11	Sung An Dien temple	7.00	8.00						9.00	**9.90**	9.00						8.00	7.00	**57.90**
12	Bieu Duc Dien temple	7.00	8.00						9.00	**10.00**	9.00						8.00	7.00	**58.00**
13	Hoa Khiem Dien temple	7.00	7.80					9.00	9.00	**10.00**	9.00	9.00					7.80	7.00	**75.60**
14	Luong Khiem Dien temple	6.40	7.50						9.00	**10.00**	9.00						7.50	6.40	**55.80**

Table 7. Dimensional analysis on the beam direction (longitude) of the twin buildings

No.	Name of buildings	Front (I)	Front (F)	Front (G)	Front (H)	Main (E)	Back (H)	Back (G)	Back (F)	Back (I)	Total (Unit)
1	Thai To Mieu shrine	8.20	**10.40**	7.10	8.30	**10.40**	8.30			8.20	**60.90**
2	The To Mieu shrine	8.30	**10.30**	7.10	8.30	**10.40**	8.30			8.30	**61.00**
3	Phung Tien Mieu shrine	7.60	**11.70**	7.00	8.10	**10.40**	8.10			7.60	**60.50**
4	Dien Tho Chinh Dien palace	6.40	**8.60**	6.20	8.20	**10.50**	8.20			6.40	**54.50**
5	Long An Dien palace	7.30	**9.30**	6.20	9.00	**10.30**	9.00			7.30	**58.40**
6	Trieu To Mieu shrine	6.80	**9.60**	6.80	7.80	**10.20**	7.80			6.80	**55.80**
7	Can Thanh Dien palace (*)	8.80	**11.90**	8.60	11.60	**12.90**	11.60	8.60	**11.90**	8.80	**94.70**
8	Thai Hoa Dien palace	8.60	**11.80**	8.20	9.10	**13.00**	9.30			8.60	**68.60**
9	Can Chanh Dien palace	8.30	**11.70**	8.40	11.30	**12.70**	11.30			8.30	**72.00**
10	Minh Thanh Dien temple	5.00	**7.10**	4.80	6.10	**8.20**	6.10			5.00	**42.30**
11	Sung An Dien temple	7.00	**8.70**	6.50	8.00	**9.30**	8.00			7.00	**54.50**
12	Bieu Duc Dien temple	7.00	**8.40**	6.60	8.00	**9.00**	8.00			7.00	**54.00**
13	Hoa Khiem Dien temple	6.90	**8.50**	6.60	7.90	**8.90**	7.90			6.90	**53.60**
14	Luong Khiem Dien temple	6.40	**7.60**	5.60	7.60	**8.00**	7.60			6.40	**49.20**

f) Span of Wings (C, D, and H)

Span C (span 6-7) can be discussed about A or B. If considered about A, it falls within the range of C = A - 0.9 units to A - 2.4 units. In the case of the Thai Hoa Dien Palace, the span reduction is significantly larger: it is 3.9 units shorter in the ridge direction (C = A - 3.9 units) and 3.7 units shorter in the beam direction (G = A - 3.7 units). If considered B, the span of C ranges from C = B - 1 unit to B - 1.9 units.

Span H (span D-E) should theoretically be similar to C (span 6-7), as per the above-mentioned third principle (location corresponding to the corner of the hip-and-gable roof). However, in reality, H is 0.1 unit longer than C. This adjustment was likely made to account for the inclination of the columns in the beam direction. Therefore, span H was probably determined by considering column inclination, using span C in the ridge direction as a reference.

Span D (span 7-8) in the ridge direction is based on span C and is equal to span I. In some cases, D equals C or is slightly shorter. Depending on the type of Twin-Building, span D tends to be:

(i) 0.3 to 0.8 units shorter (in Shrines);
(ii) 0.6 to 3 units shorter (in Palaces), or
(iii) 0.8 to 1.1 units shorter (in Temples).

The span of I in the beam direction is approximately 0.1 unit shorter or longer than span D and was likely established similarly to the relationship between C and H (Tables 6-8).

g) Span of the Drainage gutter (G)

A relationship exists between span G and span H when analyzing the distance between the top of the columns in the drainage gutter (span C-D), the centers of medium columns in the main building, and the intersection point where the center of the large columns in the front building meets the centerline of the beams. This distance equals span H minus a certain unit or fraction of a unit. It appears that the span of G was arbitrarily determined on the condition that it be smaller than span H. Adjustments were likely made to ensure that the buildings corresponded to the overall layout plan of their respective structures (Tables 8, 9).

Table 8. Analyzing the interrelation between column spans in the ridge direction and the beam direction (1)

No.	Name of buildings	Column streets	mm/Unit	Span of columns	Ridge direction			Beam direction		Different in length						
					(A)	(B)	(C)	(E)	(F)	(A-E)	(A-B)	(B-C)	(B-E)	(B-F)	(E-F) Top	(E-F) Bottom
1	Thai To Mieu shrine	14 str.	424	Top	10.70	10.00	8.30	※	※	※	0.70	1.70	※	※	※	※
		C str.		Bottom				10.40	10.40	0.30			(0.40)	(0.40)	※	0.00
2	The To Mieu shrine	8 str.	428	Top	10.70	10.00	8.30	10.00	10.00	0.70	0.70	1.70	0.00	0.00	0.00	0.40
		C str.		Bottom				10.40	10.30	0.30			(0.40)	(0.30)	(0.30)	0.10
3	Phung Tien Mieu shrine	14 str.	426	Top	10.40	10.00	8.00	※	※	※	0.40	2.00	※	※	※	※
		C str.		Bottom				10.40	11.70	0.00			(0.40)	(1.70)	※	(1.30)
4	Dien Tho Chinh Dien palace	6 str.	426	Top	10.00	10.00	8.20	10.10	8.40	(0.10)	0.00	1.80	(0.10)	1.60	1.70	2.10
		B str.		Bottom				10.50	8.60	(0.50)			(0.50)	1.40	1.50	1.90
5	Long An Dien palace	7 str.	424	Top	10.80	9.50	9.00	10.00	9.00	0.80	1.30	0.50	(0.50)	0.50	1.00	1.30
		B str.		Bottom				10.30	9.30	0.50			(0.80)	0.20	0.70	1.00
6	Trieu To Mieu shrine	7 str.	382	Top	10.00	9.30	7.70	9.90	9.30	0.10	0.70	1.60	(0.60)	0.00	0.60	0.90
		B str.		Bottom				10.20	9.60	(0.20)			(0.90)	(0.30)	0.30	0.60
7	Can Thanh Dien palace	10 str.	426	Top	12.50	11.60	11.60	※	※	※	0.90	0.00	※	※	※	※
		A str.		Bottom				12.90	11.90	(0.40)			(1.30)	(0.30)	※	1.00
8	Thai Hoa Dien palace	4 str.	427	Top	13.00	12.30	9.10	12.50	11.50	0.50	0.70	3.20	(0.20)	0.80	1.00	1.50
		B str.		Bottom				13.00	11.70	0.00			(0.70)	0.60	0.80	1.30
9	Can Chanh Dien palace	平均値	428	Top	12.30	11.40	11.30	※	※	※	0.90	0.10	※	※	※	※
				Bottom				12.70	11.70	(0.40)			(1.30)	(0.30)	※	1.00
10	Minh Thanh Dien temple	4 str.	384	Top	9.00	8.00	6.10	8.10	7.00	0.90	1.00	1.90	(0.10)	1.00	1.10	1.20
		C str.		Bottom				8.20	7.10	0.80			(0.20)	0.90	1.00	1.10
11	Sung An Dien temple	4 str.	384	Top	9.90	9.00	8.00	9.00	8.50	0.90	0.90	1.00	0.00	0.50	0.50	0.80
		C str.		Bottom				9.30	8.70	0.60			(0.30)	0.30	0.30	0.60
12	Bieu Duc Dien temple	5 str.	383	Top	10.00	9.00	8.00	8.70	8.10	1.30	1.00	1.00	0.30	0.90	0.60	0.90
		B str.		Bottom				9.00	8.40	1.00			0.00	0.60	0.30	0.60
13	Hoa Khiem Dien temple	5 str.	384	Top	10.00	9.00	7.80	8.60	8.10	1.40	1.00	1.20	0.40	0.90	0.50	0.80
		B str.		Bottom				8.90	8.50	1.10			0.10	0.50	0.10	0.40
14	Luong Khien Dien temple	4 str.	384	Top	10.00	9.00	7.50	7.60	7.20	2.40	1.00	1.50	1.40	1.80	0.40	0.80
		C str.		Bottom				8.00	7.60	2.00			1.00	1.40	0.00	0.40

Table 9. Analyzing the interrelation between column spans in the ridge direction and the beam direction (2)

No.	Name of buildings	Column streets	mm/Unit	Span of columns	Ridge direction				Beam direction			Different in length					
					(A)	(B)	(C)	(D)	(I)	(G)	(H)	(A-C)	(B-C)	(C-D)	(G-I)	(C-G)	(D-H)
1	Thai To Mieu shrine	14 str.	424	Top	10.70	10.00	8.30	8.30	※	※	※	2.40	1.70	0.00	※	※	※
		C str.		Bottom						8.30	8.20				※	0.00	0.10
2	The To Mieu shrine	8 str.	428	Top	10.70	10.00	8.30	8.30	7.50	8.30	8.30	2.40	1.70	0.00	0.80	0.00	0.00
		C str.		Bottom						8.30	8.30				0.80	0.00	0.00
3	Phung Tien Mieu shrine	14 str.	426	Top	10.40	10.00	8.00	7.70	※	※	※	2.40	2.00	0.30	※	※	※
		C str.		Bottom						8.10	7.60				※	(0.10)	0.10
4	Dien Tho Chinh Dien palace	6 str.	426	Top	10.00	10.00	8.20	6.40	6.60	8.10	6.50	1.80	1.80	1.80	1.50	0.10	(0.10)
		B str.		Bottom						8.20	6.40				1.60	0.00	0.00
5	Long An Dien palace	7 str.	424	Top	10.80	9.50	9.00	7.30	6.40	9.10	7.30	1.80	0.50	1.70	2.70	(0.10)	0.00
		B str.		Bottom						9.00	7.30				2.60	0.00	0.00
6	Trieu To Mieu shrine	7 str.	382	Top	10.00	9.30	7.70	6.90	7.10	7.70	6.90	2.30	1.60	0.80	0.60	0.00	0.00
		B str.		Bottom						7.80	6.80				0.70	(0.10)	0.10
7	Can Thanh Dien palace	10 str.	426	Top	12.50	11.60	11.60	8.80	※	※	※	0.90	0.00	2.80	※	※	※
		A str.		Bottom						11.60	8.80				※	0.00	0.00
8	Thai Hoa Dien palace	4 str.	427	Top	13.00	12.30	9.10	8.50	8.40	9.30	8.60	3.90	3.20	0.60	0.90	(0.20)	(0.10)
		B str.		Bottom						9.10	8.60				0.70	0.00	(0.10)
9	Can Chanh Dien palace	平均値	428	Top	12.30	11.40	11.30	8.30	※	※	※	1.00	0.10	3.00	※	※	※
				Bottom						11.30	8.30				※	0.00	0.00
10	Minh Thanh Dien temple	4 str.	384	Top	9.00	8.00	6.10	5.10	5.30	6.00	5.00	2.90	1.90	1.00	0.70	0.10	0.10
		C str.		Bottom						6.10	5.00				0.80	0.00	0.10
11	Sung An Dien temple	4 str.	384	Top	9.90	9.00	8.00	7.00	6.90	8.00	6.90	1.90	1.00	1.00	1.10	0.00	0.10
		C str.		Bottom						8.00	7.00				1.10	0.00	0.00
12	Bieu Duc Dien temple	5 str.	383	Top	10.00	9.00	8.00	7.00	7.00	8.10	7.00	2.00	1.00	1.00	1.10	(0.10)	0.00
		B str.		Bottom						8.00	7.00				1.00	0.00	0.00
13	Hoa Khiem Dien temple	5 str.	384	Top	10.00	9.00	7.80	7.00	6.90	8.00	7.00	2.20	1.20	0.80	1.10	(0.20)	0.00
		B str.		Bottom						7.90	6.90				1.00	(0.10)	0.10
14	Luong Khien Dien temple	4 str.	384	Top	10.00	9.00	7.50	6.40	5.80	7.70	6.40	2.50	1.50	1.10	1.90	(0.20)	0.00
		C str.		Bottom						7.60	6.40				1.80	(0.10)	0.00

3.4.2 Categories of the twin-building floor plans

The above analysis results can be categorized into the following three types of Twin Buildings (Fig. 17):

(1) Type A "10-Unit Twin Building": These Twin Buildings have spans of E = B = 10 units (as measured with the Large Ruler). They include:

- Thai To Mieu Shrine
- The To Mieu Shrine
- Phung Tien Mieu Shrine
- Dien Tho Chinh Dien Palace

(2) Type B "12-Unit Twin Building": These Twin Buildings have spans of E = A = 12 to 13 units (as measured with the Large Ruler). They include:
- Thai Hoa Dien Palace
- Can Chanh Dien Palace
- Can Thanh Dien Palace

These buildings can be further classified as "Big Palaces." Positioned along the principal symmetric axis of the Imperial City, these Twin Buildings hold primary importance and were likely designed on a larger scale to reflect their significance.

(3) Type C "Mausoleum Twin Building": These Twin Buildings are temples located within the complexes of Imperial Mausoleums. The spans in the ridge direction have actual measurements of A = 10 units (as measured with the Small Ruler), and span B is always a subtraction of span A.

(4) "Relocated Twin Buildings": This category is not based on design methods but rather on the circumstances of relocation or reconstruction. The spans in both the ridge and beam directions, as well as other measurements, may have been altered during this process. For example:
- Long An Dien Palace
- Thai Hoa Dien Palace

Both are relocated palaces, and some of their dimensions appear inconsistent with others of their type (Tables 6-7, Fig. 17).

3.5 Assuming the Design Methods of the Twin Building Floor Plans Based on Analyzing Results

As mentioned above, the categories of Twin Buildings—comprising Palaces, Shrines, and Temples—are defined based on the historical hierarchy of buildings. This classification suggests a meaningful framework for analyzing and re-determining the design principles applied to the floor plans of the targeted Twin Buildings in this study.

Logically, span A is considered the primary dimensional origin from which other dimensions are derived. In combination with the findings outlined in section 3.3, it can be assumed that A represents the second quantitative factor that was parameterized (referred to as *Parametric 2*) in the architectural design principles of the Nguyen dynasty. By altering the dimension of A, the entire column grid of the building changes simultaneously. The qualitative factors of the buildings, therefore, dictate the unit size and dimension of A, along with its relationships with other spans.

The results of the dimensional analysis reveal that spans in the ridge direction (latitude) are often expressed using specific proportions or "magical numbers," which establish the aesthetic scale of the architecture. In contrast, spans in the

beam direction (longitude) vary and appear to be more closely related to technical considerations, such as column inclinations to reduce load pressure and enhance aesthetic harmony.

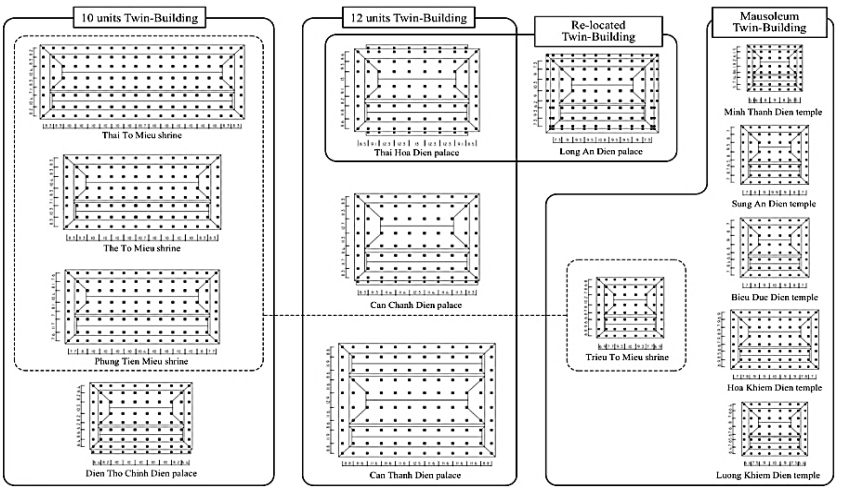

Fig. 17. Categorization of the targeted twin-building floor plan

Additionally, the spans of sub-compartments (B) appear to follow consistent rules. In Shrines and Temples, B often adheres to a whole number unit, and the floor plan design reflects the functional importance of sanctuaries. This distinction is evident in the Twin Buildings of the Imperial City, where the Large Ruler was used, symbolizing the "Yang" (life). In contrast, the Twin Buildings within the Imperial Mausoleums employed a Small Ruler, representing the "Yin" (afterlife). An exception is the *Trieu To Mieu* shrine, which, although a Shrine, was uniquely constructed like a Temple using the Small Ruler for "Yin."

In the Twin Buildings located on the center-symmetric axis of the Imperial City, the measurement of span B is typically a fraction of A. In contrast, for Twin Buildings situated on the left/right parallel symmetric axes, B is often a whole number, such as 10 units. Similarly, within the Imperial Mausoleums, B is derived by subtracting from A (ranging from 0.9 to 1 unit). These patterns suggest that column spans were consciously designed based on the location and function of the Twin Buildings (Table 6).

Fig. 17 summarizes the typological categorization of Twin Building Floor Plans based on these analyses. The ground area does not necessarily correlate with the importance of the building but rather depends on its function and location. The blend of similarities and differences in design principles reflects either the evolution of construction techniques over time or the movement and reconstruction of certain buildings.

The emergence of parametric factors in architectural design principles indicates a high degree of modularization and formalization, demonstrating the advanced mathematical and logical approach to construction during the Nguyen dynasty. Parametric adjustments in architectural dimensions ensured stylistic consistency, simplified the design process, and minimized construction time and costs. To explore this further, we hypothesize below about the design methods for Twin-Building floor plans, focusing on their significance within the Imperial Palaces.

4. DISCUSSION

4.1 Re-determined Design Methods of the Twin-Building Floor Plans

Accordingly, column spans that are central to the floor plan design (Fig. 18) include: A (span 4-5), B (span 5-6), E (span E-F), and F (span B-C). In terms of mutual relationships, the general trend reveals the following:

A = E > B ≥ F in the Palaces (square-shaped central spans).
A > E = B ≥ F in the Shrines and Temples (rectangular-shaped central spans).

Based on this trend, it appears that two primary methods of floor plan design can be identified and re-evaluated as follows.

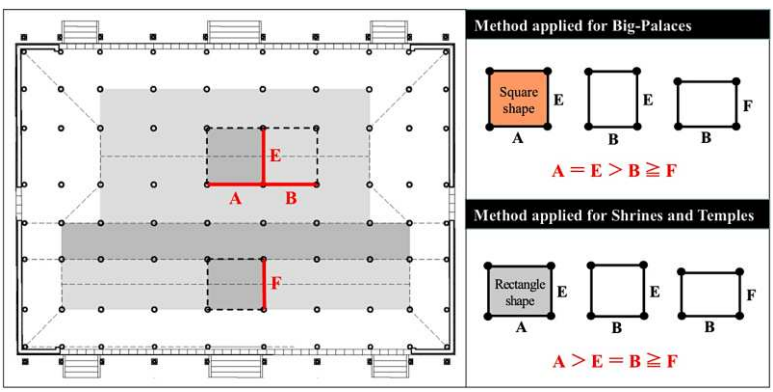

Fig. 18. Explained drawing on the relationship among the spans

4.2 The Proposed Design Method applied for the Big Palaces Floor Plan

In this method, either span A or span E is established first. In principle, they are identical in dimension. The established span represents the measurement between the tops of the columns or the intersection points of the big column centerlines and the big beam centerline of the main building. At the column bases, the width of the column inclinations is taken into account.

Next, span B is determined by subtracting a specific unit or fraction of a unit from A, and span F is set to be approximately equal to B. Span C is derived from B, and D is derived from C. Lastly, span G (drainage gutter) and span I are sequentially set to match D according to the third principle (Figs. 19a, 19b, 19c, 19d).

This design method is specifically applied to the Big Palaces located on the central symmetrical axis of the Imperial City, including the Thai Hoa Dien Palace, Can Chanh Dien Palace, and Can Thanh Dien Palace, which were among the earliest buildings constructed during the Gia Long period. These palaces served as working and living quarters for successive Emperors. Consequently, the ideal design method for these structures is more highly parameterized, and constructional regulations are more rigorous and strictly enforced compared to others.

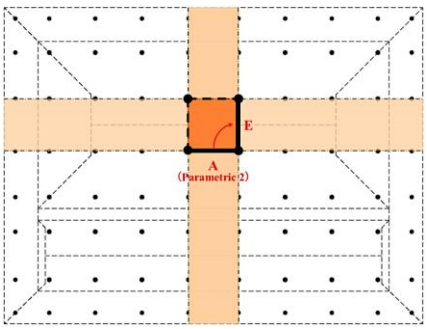

Fig. 19a. Relationship between A and E (dimetional origin)

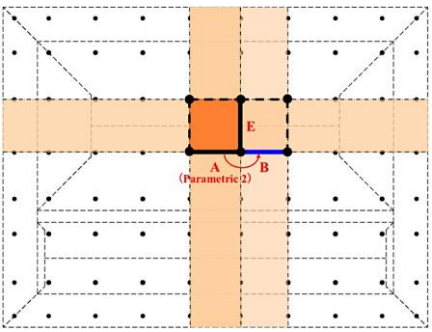

Fig. 19b. Relationship between A or E and B

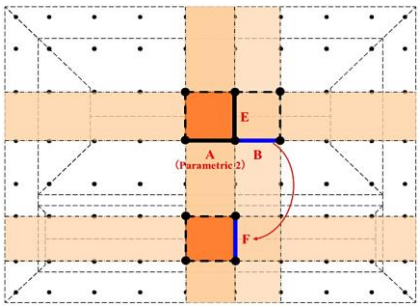

Fig. 19c. Relationship between B and F

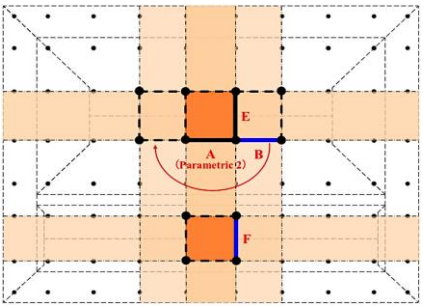

Fig. 19d. Relationship between B and the others

4.3 The proposed Design Method applied for the Shrines Floor Plan and the Temples Floor Plan

In this method, span A is established first, followed by span B, which is set to be smaller than A. Next, span E (measured at the top of the column) is set to be approximately equal to B. From this point, the method diverges from that of the Big Palaces. Span F is established based on E; span C is determined based on B, and span D is derived from C. Finally, spans G and I are assigned the same measurement based on D, following the third principle (Figs. 20a, 20b, 20c, 20d).

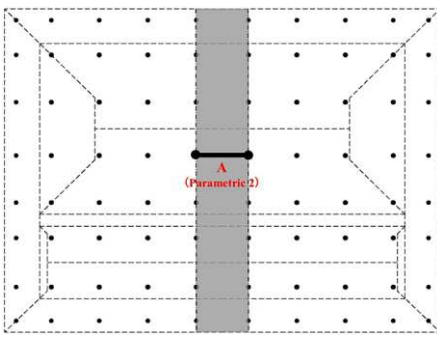

Fig. 20a. A is the dimensional origin plays as a 2nd level of parametric

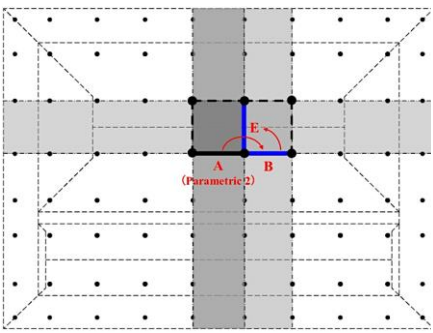

Fig. 20b. Relationship between A and B, B and E

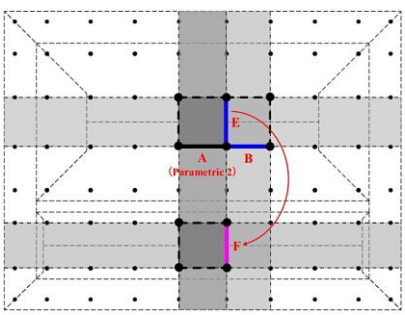

Fig. 20c. Relationship between E and F

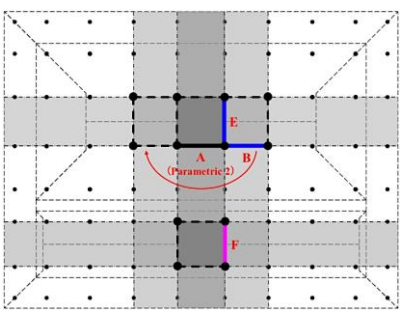

Fig. 20d. Relationship between B and the others

This designing method is primarily applied to the Twin Buildings located on the left/right parallel axes of the Imperial City, which belong to the category of “10 Units Twin Buildings.” These include the *Thai To Mieu* Shrine, *The To Mieu* Shrine, *Phung Tien Mieu* Shrine, and *Dien Tho Chinh Dien* Palace. Additionally, this method is also applied to the Twin Buildings situated along the main central axis of the Imperial Mausoleum complex, which belongs to the category of “Mausoleum Twin Buildings.” These include *Minh Thanh Dien* Temple, *Sung An*

Dien Temple, Bieu Duc Dien Temple, Hoa Khiem Dien Temple, and Luong Khiem Dien Temple.

In the case of *Dien Tho Chinh Dien* Palace, although it was built as the Queen Mother's palace, it is located on the right-side parallel axis. Therefore, it may have been influenced by the regulations applied to buildings on the parallel axes, categorizing it as one of the “10 Units Twin Buildings.”

In the case of Long An Dien Palace, which was originally a resting palace for Emperor Thieu Tri, but it was relocated and rebuilt at its current location (outside the Imperial City) during the Khai Dinh period (Cadiere, 1933). As a result, some changes may have been made during its reconstruction.

For Trieu To Mieu Shrine, although it was constructed as a shrine on the left-side parallel axis of the Imperial City, it may have been regarded as a temple and influenced by the regulations for the category of “Mausoleum Twin Buildings.” Consequently, the Small Ruler was likely applied in its design, aligning its dimensional scale with that of the Temples.

4.4 Characteristics and Practicality of the Design Methods

Based on the analysis presented above, the floor plan design methods of Twin Buildings under the Nguyen dynasty can be hypothesized as follows:

(1) Establishment of dimensional origins
The design process likely began with the determination of the primary dimensional origins, particularly span A, which served as the foundational parameter (Parametric 2). This span set the structural grid for the entire building and influenced the dimensions of other spans. By selecting a specific dimension for A, the overall proportions and spatial organization of the floor plan were established.

(2) Parametric design principles
The parametric approach enabled the adaptation of spans and grid patterns to suit the building's function and location. Spans in the ridge direction were adjusted according to "magical numbers," emphasizing aesthetic harmony, while spans in the beam direction were tailored to accommodate structural and technical requirements, such as reducing column inclination and balancing load distribution.

(3) Hierarchical design based on function and symbolism
The dimensions of A and related spans were determined by the building's symbolic and functional significance. For example, Yang-oriented structures (e.g., Palaces in the Imperial City) were designed using the Large Ruler, emphasizing life and grandeur, and Yin-oriented structures (e.g., Temples in the Mausoleums) employed the Small Ruler, signifying the afterlife and solemnity.

(4) Sub-compartment adjustments
Spans B and others were adjusted relative to A to achieve harmonious proportions. For the Twin Buildings located on the center-symmetric axis,

B was a fraction of A, while in other buildings, B followed whole-unit measurements based on the function and position of the structure.

(5) Modularization and Formalization
The modularity of these designs allowed for consistent architectural styles across different periods. By using formulaic relationships and parametric adjustments, the Nguyen dynasty achieved a balance between uniformity and flexibility. This approach minimized construction time and costs while maintaining the distinctiveness of each building type.

(6) Adaptability to rebuilding and relocation
The design method also accounted for circumstances such as relocation or reconstruction. Adjustments to spans and other dimensions were made to accommodate new contexts while retaining the original design principles.

In summary, the design methods of Twin Building Floor Plans were grounded in a sophisticated interplay of parametric logic, aesthetic principles, and symbolic considerations. These methods not only reflect the advanced architectural techniques of the Nguyen dynasty but also illustrate their emphasis on balancing functionality, symbolism, and construction efficiency.

5. CONCLUSION

As a result of conducting a comparative analysis of the relevant Twin Buildings and a chronological observation, it was found that the Twin Buildings in architecture can be categorized into three types based on their floor-plan regulation: “10-unit Twin Buildings,” “12-unit Twin Buildings,” and “Mausoleum Twin Buildings.” Each type corresponds to a specific function and the axis on which they are located. Two design methods for the floor plan have been confirmed: one applied to the big palaces used for the work and residence of the succeeding emperors, which were situated along the central symmetric axis of the Imperial City, and another applied to shrines and temples used for worship, which were located along the left/right parallel axes of the Imperial City or the central axis of the Imperial Mausoleum complex.

While the Twin Buildings in the Imperial City were designed according to the Large Ruler, associated with the “Yang,” the Twin Buildings in the Imperial Mausoleums were designed according to the Small Ruler, associated with the “Yin.” As a result, they vary in size, but both embody the philosophy that *"life and the afterlife run in the same way,"* a common belief in traditional Vietnamese society.

The principle of spatial symmetry, applied along both the latitudinal and longitudinal axes in the floor plans of the Twin Buildings, is a key characteristic of the site planning principles of the Hue Imperial City and Hue Citadel. This highlights the consistency in architectural thinking and the governing principles of the Nguyen dynasty from the early 19th century to the mid-20th century in Vietnam.

The concept of parametrization has been skillfully incorporated into architectural design methodology since the early Nguyen dynasty, contributing to the uniqueness of the entire complex of monuments. The first quantitative factor in architectural design was parameterized as the length of the rulers (Parametric 1). The second was applied to the actual dimensions of the central-origin spans (Parametric 2). Any change in either or both of these parameters would result in corresponding changes in the two-dimensional scale (2D) of the floor plan. This demonstrates an impressive mathematical approach created during the early period of the Nguyen dynasty. These considerations contribute to an understanding of how the balance between qualitative and quantitative consciousness in architectural design played a role in creating a new methodology, one that influenced social modernization and industrialization.

DISCLAIMER (ARTIFICIAL INTELLIGENCE)

Author(s) hereby declare that NO generative AI technologies such as Large Language Models (ChatGPT, COPILOT, etc.) and text-to-image generators have been used during writing or editing of this manuscript.

COMPETING INTERESTS

Author has declared that no competing interests exist.

REFERENCES

An, V. L. (2009). *Reconstruction study on the Plan and Section of the 'Can Chanh Dien' main palace of the Nguyen dynasty* (Doctoral thesis), Waseda University.
Retrieved from: https://ndlsearch.ndl.go.jp/books/R100000002-I000010368575

An, V. L., Takeshi, N., Shin Ichiro, N., & Hideaki, H. (2008). Study on the foundation of the Can Chanh Dien main palace of the Nguyen dynasty. *Journal of Architecture and Planning (Transactions of AIJ)*, 73(632), 2241–2248. https://doi.org/10.3130/aija.73.2241

Association of History of Nguyen dynasty (1802-1945). (2006). *Dai Nam Nhat Thong Chi*, volume of 京師 ("Kinh Su Capital City"), Tu Cam Thanh (Forbidden City). Thuan Hoa Publisher.

Cabinet of Nguyen dynasty (1802-1945). *Kham Dinh Dai Nam Hoi Dien Su Le Chinh Bien* & *Kham Dinh Dai Nam Hoi Dien Su Le Tuc Bien* & *Dai Nam Thuc Luc* & *Dai Nam Nhat Thong Chi*.

Cabinet of Nguyen dynasty (1802-1945). *Kham Dinh Dai Nam Hoi Dien Su Le Chinh Bien*, volume of 工部 ("Cong Bo" Ministry of Construction).

Cabinet of Nguyen dynasty (1802-1945). *Kham Dinh Dai Nam Hoi Dien Su Le Tuc Bien*, volume of 工部 ("Cong Bo" Ministry of Construction), 205–210.

Cabinet of Nguyen dynasty (1802-1945). *Kham Dinh Dai Nam Hoi Dien Su Le Tuc Bien*, volume of 工部 ("Cong Bo" Ministry of Construction), 207–208; *Dai Nam Nhat Thong Chi*, volume of 京師 ("Kinh Su Capital City"), 1–6.

Cadiere, L. P. (1933). Les quartiers de la Citadelle de Huế: Onomastique, des Missions Etrangères de Paris. *Bulletin des Amis du Vieux Huế*, 20(12), 75. Planche XXXII (Dessiné par M. Nguyễn Thứ). Ardant, L. C. (1924). Les Fortifications de la Citadelle de Hue. *Bulletin des Amis du Vieux Huế*, 11(3), 222–227. Planche LXXXIV.

Cadiere, L. P. (1933). Les quartiers de la Citadelle de Huế: Onomastique, des Missions Etrangères de Paris. *Bulletin des Amis du Vieux Huế*, 20(12), 91.

Cadiere, L. P. (1933). Les quartiers de la Citadelle de Huế: Onomastique, des Missions Etrangères de Paris. Bulletin des Amis du Vieux Huế, 20(12), 91.

Chi, B. N. (1948). Compte-rendu d'une mission a Hué. *DÂN VIỆT NAM*, 1, 81–85.

Shin-Ichiro, N. (1996). ものさしの用い方と単位長さについて (Regarding the traditional rule and unit for measurement). *ヴィエトナム・フエ・阮朝王宮の復原的研究 (Vietnam, Hue, Nguyen Dynasty Palace Restoration Studies)*, 日本建築学会大会学術講演梗概集 F-2, 491–492. Hai, T. P. (2003). Hệ thống thước đo thời Nguyễn (Measurement units of the Nguyen dynasty). *Magazine of Hue Study*, 5, 319–327. Dau, D. N. (1997). *Nghiên cứu Địa bạ triều Nguyễn* (Study on the Land Register of the Nguyen dynasty), Thua Thien Phu, 42–43.

UNESCO World Heritage List. (n.d.). *Description is available under license CC-BY-SA IGO 3.0*. Retrieved from https://whc.unesco.org/en/list/678

Disclaimer/Publisher's Note: The statements, opinions and data contained in all publications are solely those of the individual author(s) and contributor(s) and not of the publisher and/or the editor(s). This publisher and/or the editor(s) disclaim responsibility for any injury to people or property resulting from any ideas, methods, instructions or products referred to in the content.

© Copyright (2025): Author(s). The licensee is the publisher (BP International).

Peer-Review History:
This chapter was reviewed by following the Advanced Open Peer Review policy. This chapter was thoroughly checked to prevent plagiarism. As per editorial policy, a minimum of two peer-reviewers reviewed the manuscript. After review and revision of the manuscript, the Book Editor approved the manuscript for final publication. Peer review comments, comments of the editor(s), etc. are available here: https://peerreviewarchive.com/review-history/3713

Chapter 3
Print ISBN: 978-93-49473-44-7, eBook ISBN: 978-93-49473-43-0

Optimizing Scour Protection in Downstream Stilling Basins: Insights from USBR-Type Weirs

Jaji Abdurrosyid [a*] and Gurawan Jati Wibowo [a]

DOI: https://doi.org/10.9734/bpi/erpra/v5/4261

Peer-Review History:
This chapter was reviewed by following the Advanced Open Peer Review policy. This chapter was thoroughly checked to prevent plagiarism. As per editorial policy, a minimum of two peer-reviewers reviewed the manuscript. After review and revision of the manuscript, the Book Editor approved the manuscript for final publication. Peer review comments, comments of the editor(s), etc. are available here: https://peerreviewarchive.com/review-history/4261

ABSTRACT

In the downstream part of the weir, especially in the stilling basin, there is a hydraulic jump phenomenon caused by the change in flow from supercritical flow to subcritical flow. The hydraulic jump in the stilling basin of the weir causes bottom scouring, especially in the unprotected downstream part of the weir. This can result in significant damage to the overall structure of the weir. So that this downstream part requires protection to overcome scouring. Therefore, to overcome this problem, a laboratory study is needed on scouring and its mitigation in the downstream part of the weir.

This research was conducted at the Hydraulics Laboratory of the Surakarta River Research Center using a recirculation channel. The dimensions of the recirculation channel are: length = 24 m; width = 0.49 m; and height = 0.60 m. The basic material of the recirculation channel is fine sand (sieve diameter = 2 mm) with a thickness of 0.20 m layered along the channel. The channel slope is 0.004, and it is assumed that there is no sediment load in the upstream part of the weir. This study uses a USBR (United States Bureau of Reclamation) type weir model consisting of USBR-I, USBR-II, USBR-III, and USBR-IV types. The model is placed approximately ± 9.0 m from the upstream with the aim of not being affected by wave ripples from the Inlet. The experiment was conducted using 4 variations of running discharge and 3 variations of running protection.

The results showed that the maximum scour depends on the flow velocity, shear velocity, and flow height downstream of the stilling basin. In addition, the maximum scour is also affected by the Reynolds number and gravity (as the Froude number). These parameters are significantly interdependent. Furthermore, there is a significant reduction in scour downstream of the stilling

[a] *Department of Civil Engineering, Faculty of Engineering, Universitas Muhammadiyah Surakarta, Indonesia.*
**Corresponding author: E-mail: jajiabdurrosyid@gmail.com, ja199@ums.ac.id;*

basin protected by Rip-rap (RR) ¼ Lmax, RR ½ Lmax, and RR Lmax. In addition, protection using rip-rap length Lmax or loose gravel can protect scour with the smallest scour depth. However, scour still occurs downstream of the stilling basin even though there is protection along Lmax.
Scouring depth reduction (Ym Reduction) on Rip-rap installation = Lmax RR with the largest reduction is USBR-IV type 92.94%, and the smallest is USBR-II type 81.21%. While the largest reduction in Scouring Length (Lm Reduction) is USBR-IV type 75.55%, and the smallest is USBR-I type 47.32%. So overall, the maximum Scouring Depth reduction (Ym Reduction) occurs in USBR-IV type, and the smallest in USBR-II type. While the maximum Scouring Length reduction (Lm Reduction) occurs in USBR-IV type, and the smallest in USBR-I type.

Keywords: Hydraulic jump; scour depth; scour protection; rip-rap; loose gravel.

1. INTRODUCTION

The increase in water level due to the dam causes a difference in energy height (head) between the upstream and downstream parts of the dam, therefore the flow flowing on the sloping dam surface is in a supercritical state while the flow conditions in the downstream part are in a subcritical state. The change in flow from supercritical to subcritical causes a hydraulic jump (Raju, 1986). The result of the hydraulic jump often causes waves or eddies that can cause erosion of the channel bed, especially the unprotected downstream part (Kironoto, 2020). The occurrence of a water jump in the downstream part of the dam can reduce the flow energy. Therefore, a retention pond is needed that can protect the river bed. Several stilling basin models have been introduced by the United States Bureau of Reclamation (USBR) which have been tested for construction to facilitate research. This USBR type consists of USBR-I type with Froude number <2.5, USBR-II with Froude number >3, USBR-III with Froude number >4.5, and USBR-IV with Froude number between 2.5-4.5 (Mays, 1999; Djunur, 2022). Although using USBR type retention ponds that can absorb energy, in reality erosion still occurs at the bottom of the channel downstream of the retention pond (Abdurrosyid, 2005), this can cause damage to the structure. Therefore, laboratory research is needed on erosion and its control/protection downstream of the stilling basin.

This study will examine the scour downstream of the USBR type dam stilling basin and its mitigation by using stone mattresses/gabions (riprap) tied with wire mesh. The use of gabions is the cheapest and most practical when applied in the field, so it is used as a protection model in this study. In detail, the specific objectives of this study are to determine the optimal length of the protection structure installed downstream of the stilling basin, to determine the scour pattern that occurs downstream of the stilling basin without protection and with protection, and to determine the function of variables that affect local scour downstream of the USBR type stilling basin.

There are several similar studies that have been conducted on the phenomenon of scour in the downstream part of the dam's stilling basin, but until now studies on scour protection in the downstream part of the dam's stilling basin have not been widely studied. As with several scientists who have studied the scour process in the downstream part of the dam mentioned in (Breusers & Raudkivi, 1991), including: Schoklitsch (1932), Eggenberger (1944), Muller (1944), Ghetti and Zanovello (1954), Li (1955), Hartung (1957), Shalash (1982), Breusers (1966), Raudkivi (1967), Kotoulas (1967), Dietz (1969), Catakli et al (1973). Meanwhile, in Hoffmans and Verhejj (2021), it is mentioned among others: Mosonyi and Schoppmann (1968), Van der Meulen and Vinje (1977), Popova (1999), Buchko (1986), Blazejemski (1991). All of these studies have not examined scour protection downstream of the stilling basin. These studies are limited to observing the scour depth downstream of the weir, the geometric shape of the scour hole, the effect of the stilling basin on scour reduction. USBR (1955), (Chow, 1995) studied the effect of the stilling basin on energy damping that can reduce scour, Novak (1955, in (Breusers & Raudkivi, 1991)) reported the results of his observations on the use of a stilling basin that is long enough for a hydraulic jump can reduce scour by 45% to 65% when compared to not using a stilling basin. Kumar et al (1982) studied scour downstream of the weir (Kumar et al., 1982). Farhoudi and Smith (1985) studied the local scour profile downstream of the hydraulic jump (Farhoudi & Smith, 1985). Mohammed and McCorquodale (1992) studied scour downstream of the apron of the sluice gate (Mohamed & McCorquodale, 1992). Hoffmans and Pilarczyk (1995) studied local scour downstream of hydraulic structures that were given an apron or protective layer in the hydraulic jump area (Hoffmans & Pilarczyk, 1995). Peterka (1964, in Mays 1999, in Van Rijn, 1984) studied the size of rocks in coarse artificial riprap in the form of warts. Mista Castelino, et.al (2021) conducted a study on scour protection in the downstream of the spillway stilling basin of the Dam using Antifer block protection. Various protection strategies were tested to assess the effects of different placement methods and packing densities on the stability of the Antifer block protection layer. The experimental findings revealed that regular placement is more stable than irregular placement with the same packing density (Castelino et al., 2021). Abdurrosyid (2005) studied scour downstream of the USBR-III type stilling basin without studying its scour protection (Abdurrosyid, 2005). Monica Moroni, et.al.,2022, examined and analyzed the results of physical and numerical models, it is clear that the stilling basin is too small and therefore insufficient to manage the energy content of the fluid output to the river, with a significant impact on the downstream riverbed which is easily eroded in terms of scour depth (Moroni et al., 2022). Djunur (2022) conducted a study on scour in the downstream of the USBR III type Stilling Basin using 3 different dimensional baffle block models providing three different discharge variations in four flow simulations. Based on the results of the analysis and planning of the baffle block, the effectiveness in protecting the spillway scour downstream was obtained, namely the baffle block dimensions of 1: 1, 1: 3 and 1: 5. The three baffle block models were used to determine changes in channel cross-section, scour patterns, scour volume and flow parameters that occurred downstream of the spillway. The results of the study showed that the reduction in scouring depth without baffle block was 32.80%, baffle block 1:1 was 43.24%, baffle block 1:3

was 10.01% and baffle block 1:5 was 47.77% (Djunur, 2022). Cahya, E.N., et.al, 2024, conducted a study on the dam spillway, this study aims to determine the hydraulic flow in the side spillway system and downstream scour due to flood discharge using a physics model test in the laboratory with a scale of 1:60. The model is used to measure hydraulic parameters in the form of speed, depth, and pressure, at discharges Q100, Q1000, and QPMF. The results of the analysis show the behavior of hydraulic flow, especially in the phenomenon of water flow energy damping in the calming pool (energy damper) and scour at the bottom of the downstream river (Cahya et al., 2024).

This study is a study of scour protection downstream of the USBR type weir stilling basin, including: USBR-I, SBR-II, USBR-III, USBR-IV, namely by installing riprap or a woven wire stone gabion mattress in the downstream part of the stilling basin.

2. RESEARCH METHOD

The research was conducted at the Hydraulics Laboratory of the River Center (PUSLITBANG) Surakarta Water Resources, using a sediment-recirculating flume measuring 0.48 m wide and 20 m long, with the position of The USBR weir model is placed at a distance of ± 9 m from the upstream (tank) so that it is not disturbed by the flow waves as seen in Fig. 1.

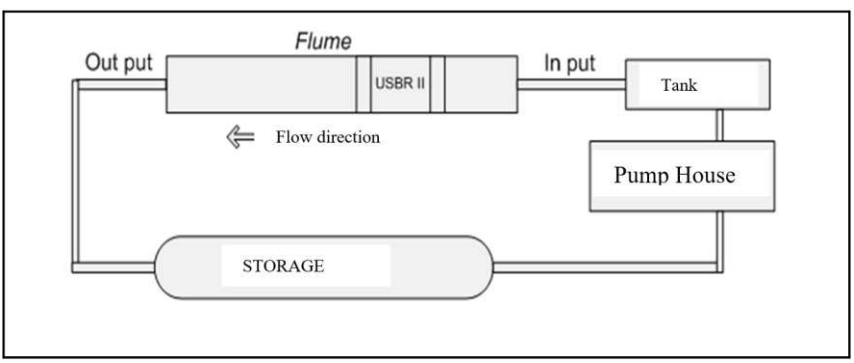

Fig. 1. Recirculating flume

Weir models with round type fountains and USBR type stilling basin/ponds include USBR-I, USBR-II, USBR-III, USBR-IV with dimensions according to Figs. 2, 3, 4 and 5. Meanwhile, the protection model is in the form of rip-rap with woven wire, as in Fig. 6.

USBR-I Model: L_j = 71,52 cm; P = 20,0 cm; X_m = 27,65 cm; B = 48,0 cm

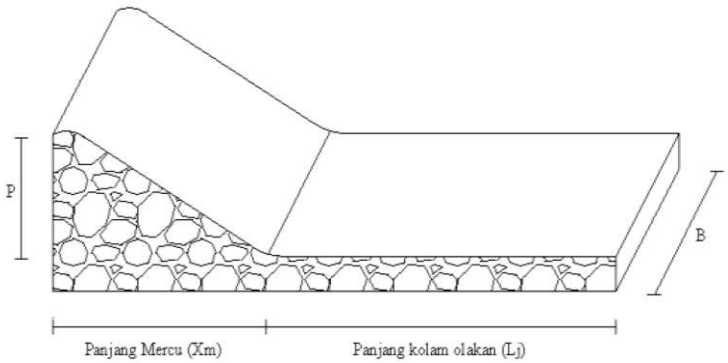

Fig. 2. USBR-I type weir and stilling basin

USBR-II Model: L_j = 57,10 cm; P = 20,0 cm; X_m = 27,65 cm; B = 48,0 cm

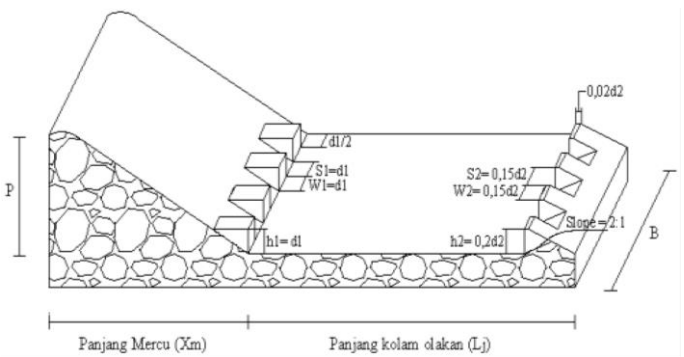

Fig. 3. USBR-II type weir and stilling basin

USBR-III Model: L_j = 38,41 cm ; P = 20,0 cm; X_m = 27,65 cm; B = 48,0 cm

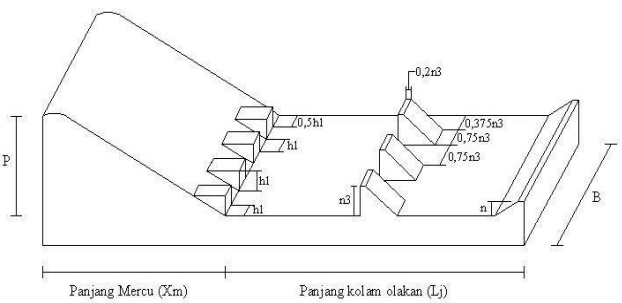

Fig. 4. Weir and stilling basin types USBR-III

USBR-IV Model: L_j = 56,30 cm; P = 20,0 cm; X_m = 27,65 cm; B = 48,0 cm

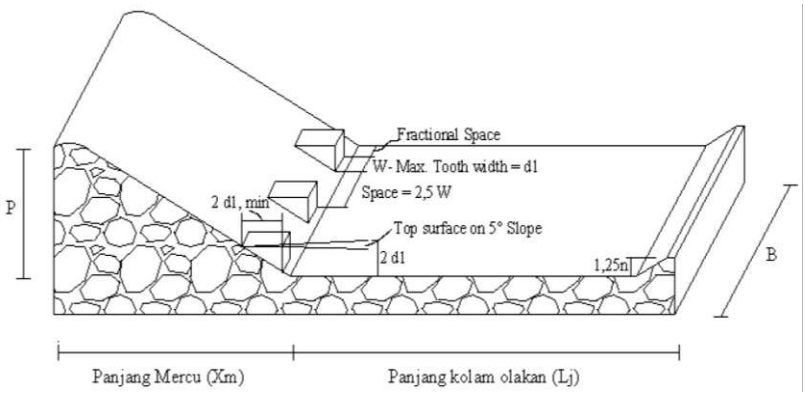

Fig. 5. Weir and processing pond types USBR-IV

Fig. 6. Rip-rap woven wire

This research was conducted with 54 runs with two stages of measurement, the first stage 18 runs and the second stage 36 runs, namely the first stage is Running to determine the variables that affect the depth of scour (such as flow velocity, friction velocity, flow depth, scour depth, Froude number and Reynolds number), this was done without using scour protection with 4 variations of discharge, namely 10.9 l/s, 20.6 l/s, 26.7 l/s, 28.8 l/s; the second stage is Running control/protection against scour with the largest discharge (28.8 l/s) with research variations including: measuring the depth of scour against gabions/Riprap from stone arrangements woven with wire downstream as far as ¼ L_{max}, ½ L_{max}, and L_{max}; L_{max} = maximum length of scour. All of them are done for each type of USBR.

The measurement of the scour depth was carried out at 18 observation positions as shown in Fig. 7.

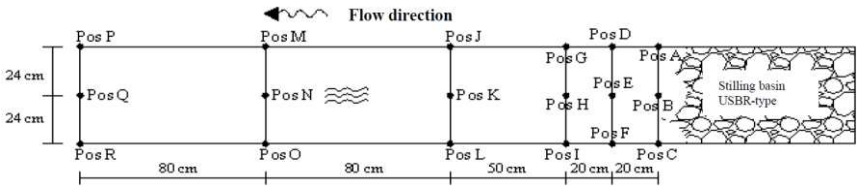

Fig. 7. Scour observation points on flume

3. RESULTS AND DISCUSSION

3.1 Scour Protection Study Downstream of Stilling Basin Type USBR-I

3.1.1 Scour protection study downstream of stilling basin type USBR-I without protection

This study was conducted without using protection downstream of the dam in flow conditions where sediment transport/live-bed scour (LBS) occurred. Observations of equilibrium scour depth were carried out for 240 minutes, but when it reached 190 minutes, equilibrium had occurred. The relationship between scour depth and time that occurred during the observation showed a non-linear function relationship, this can be seen in Fig. 8.

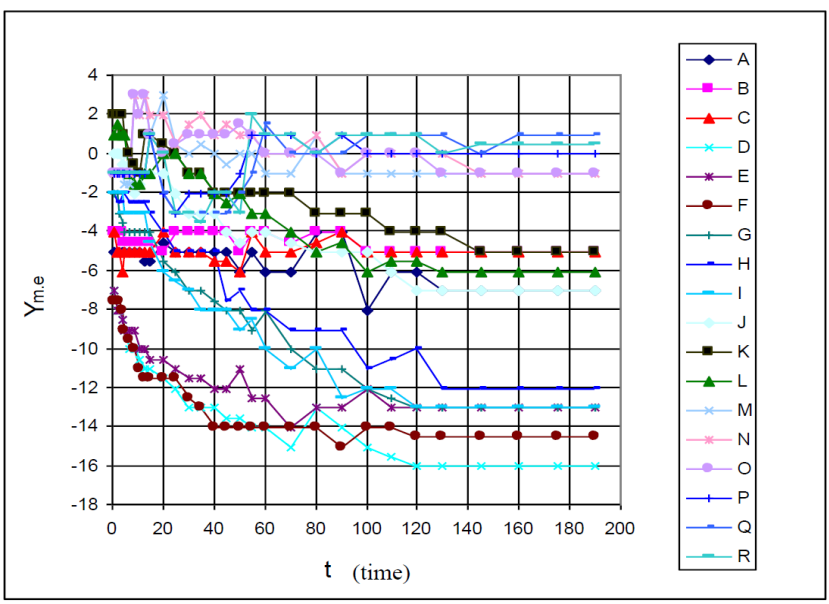

Fig. 8. Graph of scour depth against time at the position of 18 observation points in the live-bed scour condition for Q = 28.8 lt/sec, USBR-I type

In the figure, there is a tendency from the position of point A downstream near the stilling basin to the position of point R downstream far from the stilling basin, indicating that the depth of scour becomes shallower towards the far downstream of the stilling basin, and ultimately sediment deposition occurs after the position of point R. The graph shows the maximum depth of the most maximum (deepest) scour, namely the depth of scour that occurs at the position of point D.

According to observations during the scouring process downstream of the stilling basin, scouring occurs starting downstream near the stilling basin and then continues to develop along the flow until it reaches a certain length. Scouring continues to form a scour hole which tends to become shallower towards the far downstream of the stilling pond. Meanwhile, in the downstream part of the scour hole, sediment deposition occurs. This deposition continues to develop until it is finally eroded back downstream, finally collecting, and the sediment increases downstream and gets longer with time. As shown in Figs. 9 and 10. This also applies to stilling basin of USBR-II, USBR-III, and USBR-IV types.

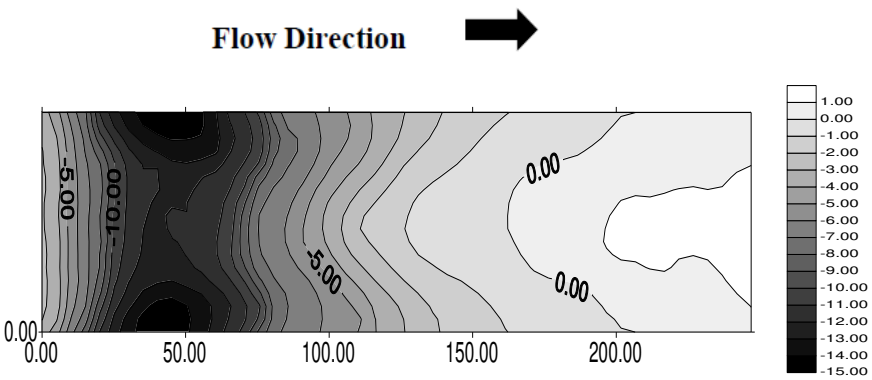

Fig. 9. Scour surface contour downstream of stilling basin without protection under live-bed scour conditions, Q = 28.8 lt/sec, USBR-I type

The relationship between the comparison of maximum scour depth and flow depth with the Froude number can be expressed in a logarithmic equation, namely:

$$\left(\frac{Y_{m.e}}{Y_3'}\right) = -0{,}9684 \text{ Ln } F_r - 0.1441 \quad \text{.....(1)}$$

with $F_r = \left(\frac{U_3'}{\sqrt{g.Y_3'}}\right)$, where

U3' = flow velocity downstream of the stilling basin after scouring, Y3' = flow depth downstream of the stilling basin after scouring. Y3 = flow depth downstream of the stilling basin, Yme = maximum equilibrium scouring depth.

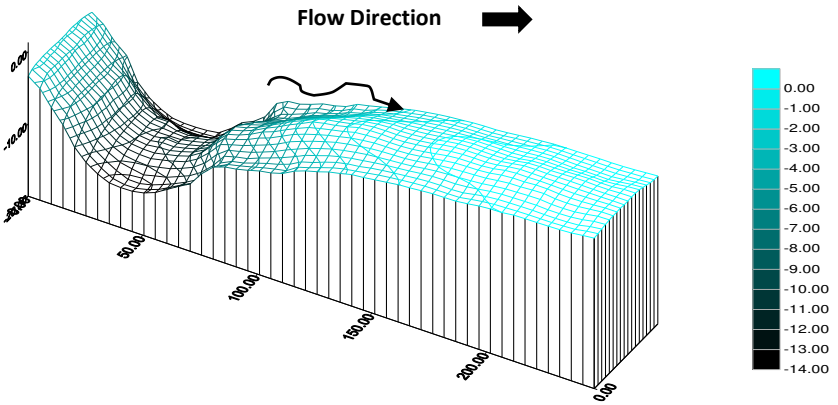

Fig. 10. Three-dimensional image of the scour surface contour downstream of the stilling basin without protection under live-bed scour conditions for Q = 28.8 lt/sec, USBR-I type

With a correlation number of R = 0.9628, there is a relatively very strong relationship between the Froude number and the maximum equilibrium scouring depth.

The relationship between the ratio of maximum scouring depth and maximum scouring length with the Reynolds number can be expressed in a logarithmic equation, namely:

$$\left(\frac{Y_{m.e}}{L_{m.e}}\right) = 0{,}0711 \ln R_e - 0{,}6581 \quad \text{.....(2)}$$

with $R_e = \left(\frac{U_3'.R}{\nu}\right)$, where R = hydraulic radius, = kinematic viscosity of the flow. U3' = flow velocity downstream of the stilling basin after scouring occurs.

With a correlation number of R = 0.8689, there is a relatively close relationship between the Reynolds number and the maximum equilibrium scouring depth and the maximum scouring length. From the graph, it can be concluded that the greater the Reynolds number, the greater the comparison between the maximum equilibrium scouring depth and the flow depth.

3.1.2 Scour study downstream of stilling basin with protection for USBR-I type

a. Rip-rap protection one-quarter of the maximum scour length (1/4 Lmax)

The maximum scour length (Lmaks) without protection for a discharge of 28.8 lt/s is 190 cm and the maximum scour depth is 16.1 cm. For the first scour protection study using a quarter of the maximum scour length (1/4 Lmaks), running was carried out three times with the same discharge of 28.8 lt/s and observation for 120 minutes because changes in scour depth were seen to be small and approaching stability. The final running results showed that there was scour around the downstream of the rip-rap, namely with an average scour depth of 8.1 cm and an average scour length of 160.5 cm. The shape of the scour can be seen in a three-dimensional image, as shown in Fig. 11. From the rip-rap protection study of a quarter of the maximum scour length, there was still large scour downstream of the protection.

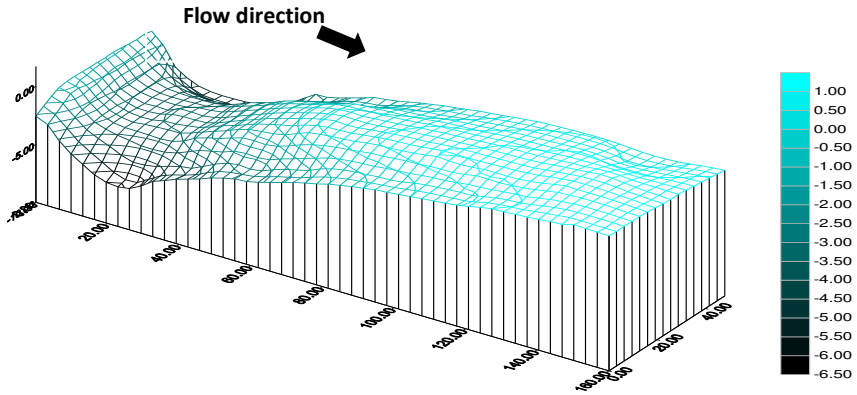

Fig. 11. Three-dimensional contour of the scour surface downstream of rip-rap protection a quarter of the maximum scour length at Live-Bed Scour Conditions for Q = 28.8 lt/sec, USBR-I type

b. Rip-rap protection half the maximum scour length

In this study, using ½Lmax protection from a discharge of 28.8 lt/sec, running was carried out three times with the same discharge of 28.8 lt/sec and observation for 120 minutes because it was seen approaching stability.

The final running results showed that there was still scour around the downstream of the rip-rap, namely with an average scour depth of 3.1 cm and an average scour length of 140.2 cm. The shape of the scour can be seen in a three-dimensional image, as shown in Figure.

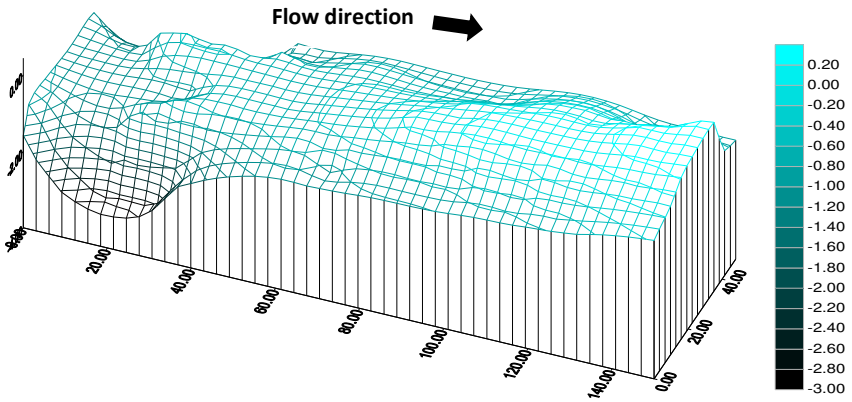

Fig. 12. Three-dimensional contour of the scour surface downstream of rip-rap protection half the maximum scour length at Live-Bed Scour Condition for Q = 28.8 lt/sec, USBR-I type

From the research, it can be seen that there is still minor erosion downstream of the protection, thus it is necessary to carry out maximum protection from the maximum erosion length.

c. Rip-rap protection throughout maximum scouring

In this study, rip-rap protection was used along the maximum scour (Lmaks) of a discharge of 28.8 l/s. Three runs were carried out with the same discharge of 28.8 l/s and observations for 120 minutes because small changes in scour depth were seen and approaching stability.

The final results of the running show that there is still visible scour around the downstream of the rip-rap, namely with an average scour depth of 2.1 cm and a scour length of 100.1 cm. The shape of the scour can be seen in the three-dimensional contour image, as shown in Fig. 13.

The comparison between the maximum scouring depth of the rip-rap protection balance and before protection with time can be seen in the graph in Fig. 14.

From the image above, it can be seen that the maximum scouring depth without protection occurs at a very large scouring rate with a longer time to reach equilibrium compared to using rip-rap or loose rock protection. The scouring reduction value can be seen in Table 1.

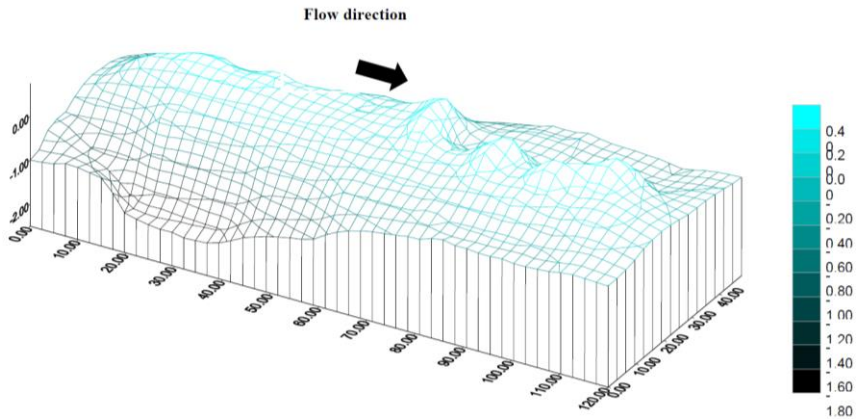

Fig. 13. Three-dimensional contour of the scour surface downstream of rip-rap protection maximum scour length at Live-Bed Scour Condition for Q = 28.8 lt/sec, USBR-I type

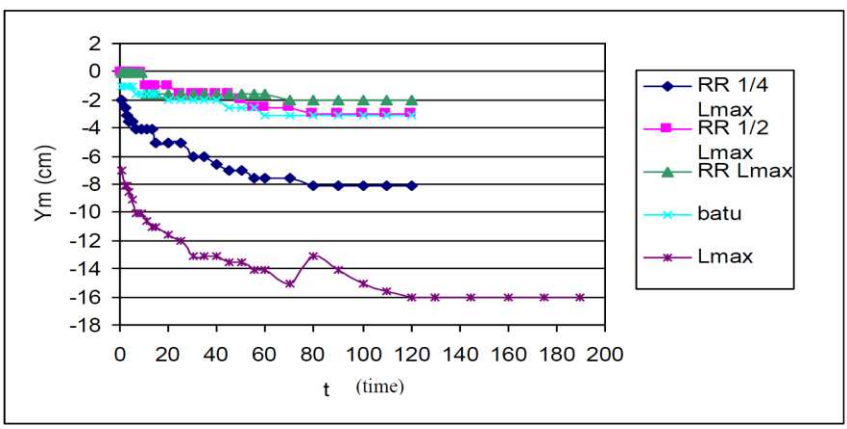

Fig. 14. Maximum Scour Depth Graph Before protection and with protection in live-bed scour conditions for Q = 28.8 lt/sec, USBR-I type

Table 1. Scour reduction value of USBR-I type

Notation	Non Protection Lm	RR ¼ Lm	RR ½ Lm	RR Lm
Y_m	16,1 cm	8,1 cm	3,1 cm	2,1 cm
L_m	190,0 cm	160,5 cm	140,2 cm	100,1 cm
$Y_{m\text{-reduction}}$		49,69%	80,75%	86,96%
$L_{m\text{-reduction}}$		15,53%	26,21%	47,32%

3.2 Scour Study Downstream of Stilling Basin USBR-II Type

3.2.1 Scour study downstream of stilling basin without protection for USBR-II type

Measurement of scour depth downstream of the stilling basin was carried out at 18 observation positions. In the measurement, the maximum scour depth occurred at position G, as shown in Fig. 15. The maximum scour depth occurred at point G. The relationship between the ratio of maximum scour depth and flow depth with the Froude number is expressed by the following equation.

$$\left(\frac{Y_{m.e}}{Y_3'}\right) = -1{,}1992 - 0{,}870 \text{ Ln } F_r \quad \text{.....(3)}$$

The relationship between the two parameters has a correlation number of R = 0.6628. This shows the level of relationship between the two parameters is close. While the correlation value has a negative value indicating the relationship is in the opposite direction, meaning that if one parameter increases then the other parameter decreases, and vice versa.

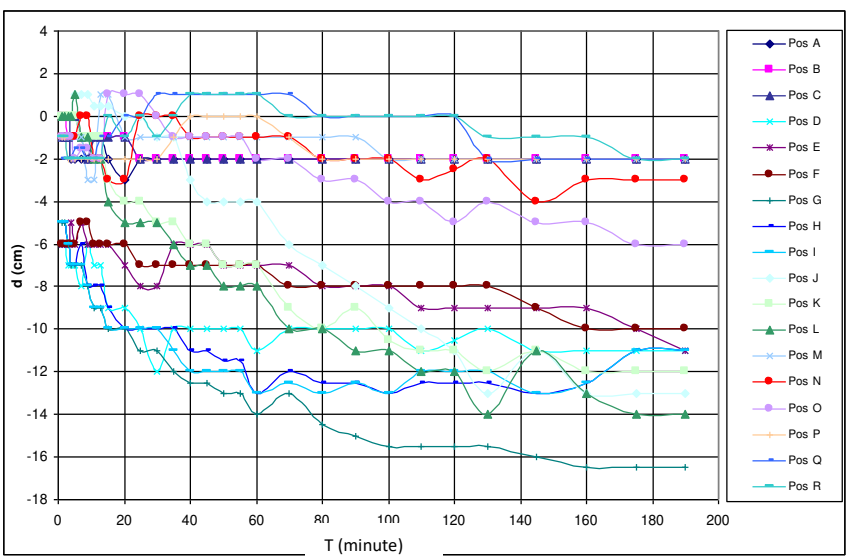

Fig. 15. Scour depth graph against timeat 18 observation positions under live-bed scour conditions for Q = 28.8 lt/sec, USBR-II type

The relationship between the comparison of maximum scouring depth and maximum scouring length with the Reynolds number can be expressed by the following equation.

$$\left(\frac{Y_{m.e}}{L_{m.e}}\right) = 0{,}229 - 0{,}0161 \ln R_e \quad \text{.....(4)}$$

The relationship between the two parameters has a correlation figure of R = 0.7367, which still shows a close relationship.

3.2.2 Scour study in downstream stilling basin with protection for USBR-II type

a. Rip-rap protection one quarter of the maximum scour length

The maximum scour length for a discharge of 28.8 lt/s is 245 cm and the scour depth is 16.5 cm. For the first scour protection study using ¼ Lmaks, three runs were carried out with the same discharge of 28.8 lt/s and observations for 120 minutes because changes in scour depth were seen to be small and approaching stability.

The final results of the running show that there is visible scour around the downstream of the riprap, namely with an average scour depth of 8.5 cm and a scour length of 170.1 cm. The scour shape is seen in a three-dimensional contour image, as shown in Fig. 16.

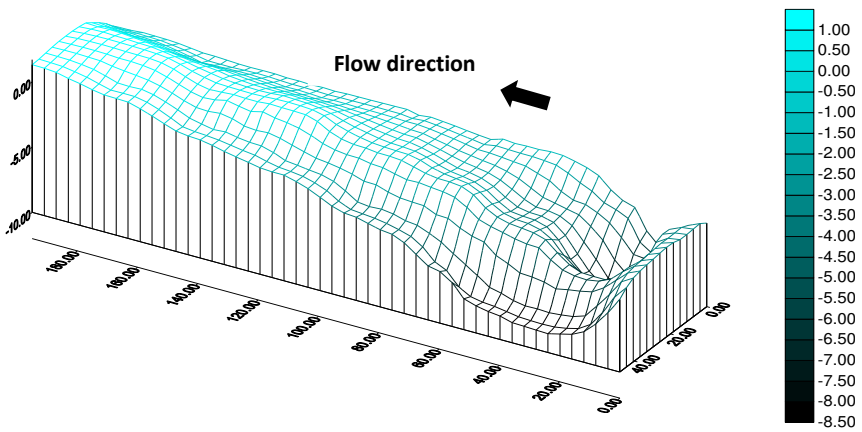

Fig. 16. Three-dimensional contour of the scour surface downstream of the riprap protection a quarter of the maximum scour length under live-bed scour conditions for Q = 28.8 lt/s, USBR-II type

b. Rip-rap protection half the maximum scour length

In this study, using ½ Lmax protection from the maximum scouring length from a discharge of 28.8 lt/sec, running was carried out three times with the same

discharge of 28.8 lt/sec and observation for 120 minutes because changes in scouring depth were seen to be small and approaching stability.

The final results of the running show that there is still visible scour around the downstream of the riprap, namely with an average scour depth of 6.1 cm and a scour length of 140.2 cm. The shape of the scour can be seen in the three-dimensional contour image, as shown in Fig. 17.

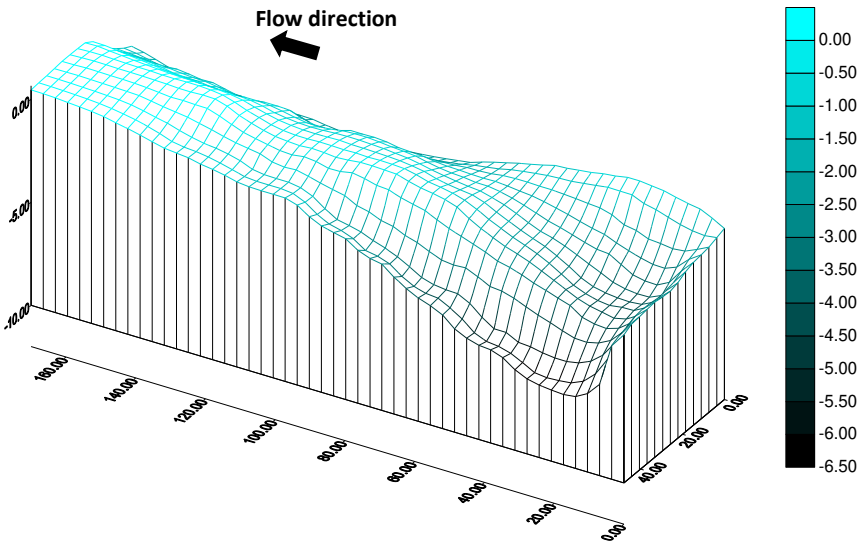

Fig. 17. Three-dimensional contour of the scour surface downstream of the riprap protection half the maximum scour length under live-bed scour conditions for Q = 28.8 lt/s, USBR-II type

c. Rip-rap protection throughout maximum scouring

In this study, using protection with a protection length equal to the maximum scour length (Lmaks) without protection with a discharge of 28.8 lt/sec, which is 245 cm, running was carried out three times with the same discharge of 28.8 lt/sec and observation for 120 minutes, because changes in scour depth were seen small and approaching stability.

The final running results showed that there was small scour around the downstream of the protection, namely with an average scour depth of 3.1 cm and an average scour length of 75.2 cm. The shape of the scour can be seen in the three-dimensional contour image, as shown in Fig. 18.

From the research of rip-rap protection with maximum scour length, it can be seen that there is still scour, although small, downstream of the protection.

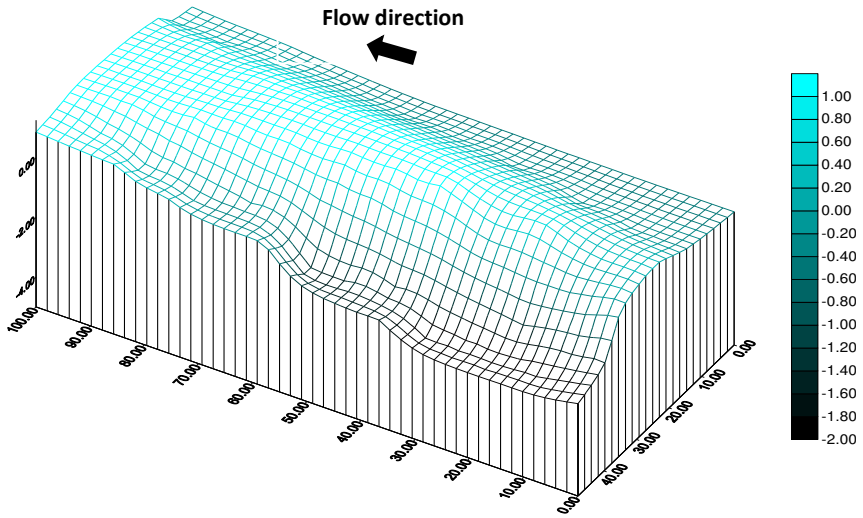

Fig. 18. Three-dimensional contour of the scour surface downstream of Rip-rap protection with maximum scour length under live-bed scour conditions for Q = 28.8 lt/s, USBR-II type

The comparison between the maximum scour depth of the riprap protection balance with before protection with time can be seen in the graph of Fig. 19. From the figure, it can be seen that the protected scour depth is much shallower when compared to without protection, this indicates a reduction in scour. The reduction value for each rip-rap variation can be seen in Table 2 below.

Table 2. Scour reduction value of USBR-II type

Notation	Non Protection Lm	RR ¼ Lm	RR ½ Lm	RR Lm
Y_m	16,5 cm	8,5 cm	6,1 cm	3,1 cm
L_m	245,0 cm	170,1 cm	140,2 cm	75,2 cm
$Y_{m\text{-reduction}}$		48,48%	63,03%	81,21%
$L_{m\text{-reduction}}$		30,57%	42,78%	69,31%

3.3 Scouring Study Downstream of Stilling Basin Type USBR-III

3.3.1 Scouring Study Downstream of Stilling Basin Without Protection for USBR-III Type

Measurement of scour depth downstream of the stilling basin was carried out at 18 observation positions. In the measurement, the maximum scour depth occurred at position E, as shown in Fig. 20. The figure shows a tendency from

position A upstream to position R downstream of the flow, indicating that the scour depth is getting shallower towards the downstream, and ultimately sediment deposition occurs downstream of the flow. The maximum scour depth occurs at point E.

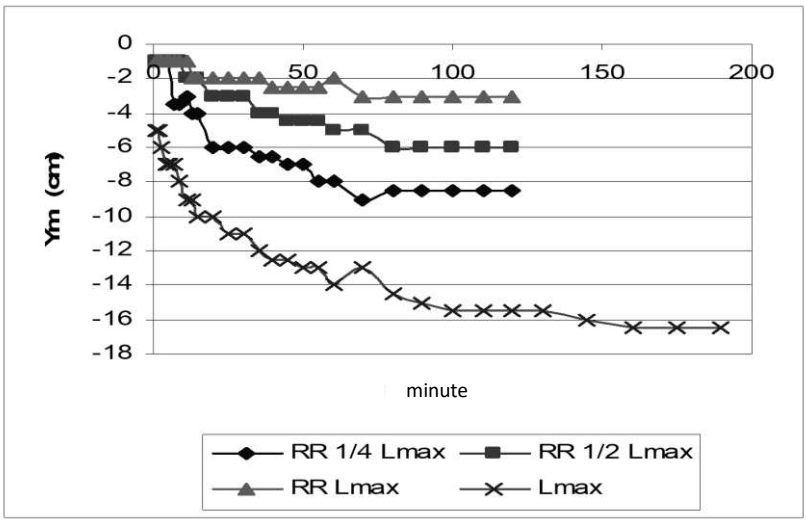

Fig. 19. Graph of maximum scour depth before protection and with protection in live-bed scour conditions for Q = 28.8 lt/sec, USBR-II type

The relationship between the comparison of the maximum scour depth and flow depth with the Froud number has a correlation number of R = 0.6233. This shows that the level of the relationship is close. The relationship can be expressed in the following equation.

$$\left(\frac{Y_{m.e}}{Y_3'}\right) = 3{,}6509\ F_r - 0{,}5616 \quad \text{.....(5)}$$

The relationship between the comparison of maximum scouring depth and maximum scouring length with the Reynolds number has a correlation number of R = 0.9041, this still shows a very close relationship, this relationship can be shown by the following equation.

$$\frac{Y_{me}}{L_{me}} = 0{,}0264e^{1E-05\,\mathrm{Re}} \quad \text{.....(6)}$$

3.3.2 Scour study downstream of stilling basin with protection for USBR-III type

a. Rip-rap protection one quarter of the maximum scour length

The maximum scour length for a discharge of 28.8 lt/s is 230 cm and the maximum scour depth is 12.4 cm. For the first scour protection study using ¼ Lmaks, three runs were carried out with the same discharge of 28.8 lt/s and observations for 120 minutes because small changes in scour depth and approaching stability have been seen.

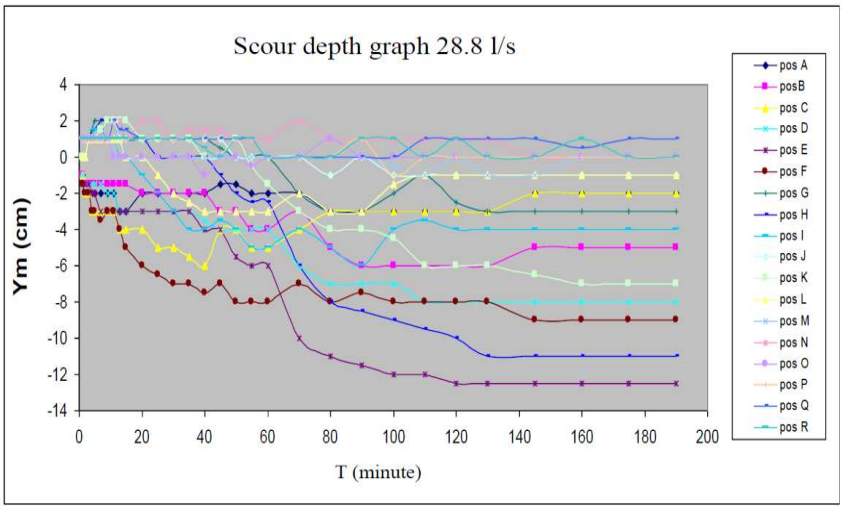

Fig. 20. Scour depth graph against time at 18 observation positions under live-bed scour conditions for Q = 28.8 lt/sec, USBR-III type

The final running results showed that there was scour around the downstream of the rip-rap, namely with an average scour depth of 4.1 cm and an average scour length of 185.2 cm. The shape of the scour can be seen in the three-dimensional contour image, as shown in Fig. 21 below. From the rip-rap protection study, a quarter of the maximum scour length showed that there was small scour downstream of the protection.

b. Rip-rap protection half the maximum scouring length

In this study using ½ Lmax protection from the maximum scour length, running was carried out three times with the same discharge of 28.8 lt/sec and observation for 120 minutes because changes in scour depth were seen and approaching stability.

The final running results showed that there was still scour around the downstream of the rip-rap, namely with an average scour depth of 3.1 cm and an

average scour length of 145.2 cm. The shape of the scour can be seen in the three-dimensional contour image, as shown in Fig. 22 below.

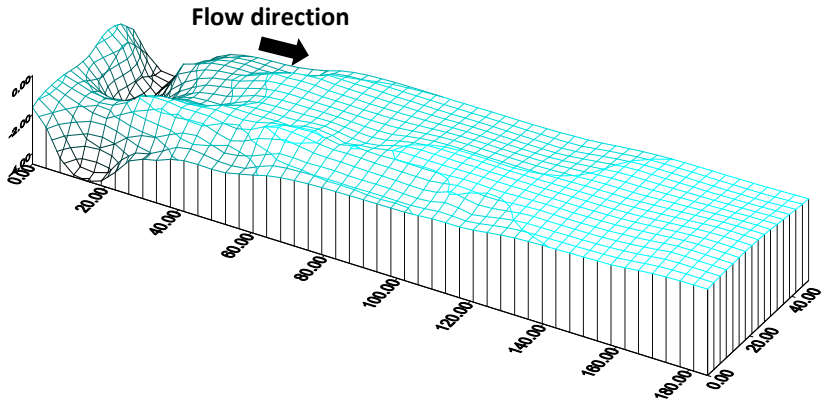

Fig. 21. Three-dimensional contour of the scour surface downstream of rip-rap protection a quarter of the maximum scour length at Live-Bed Scour Conditions for Q = 28.8 lt/sec, USBR-III type

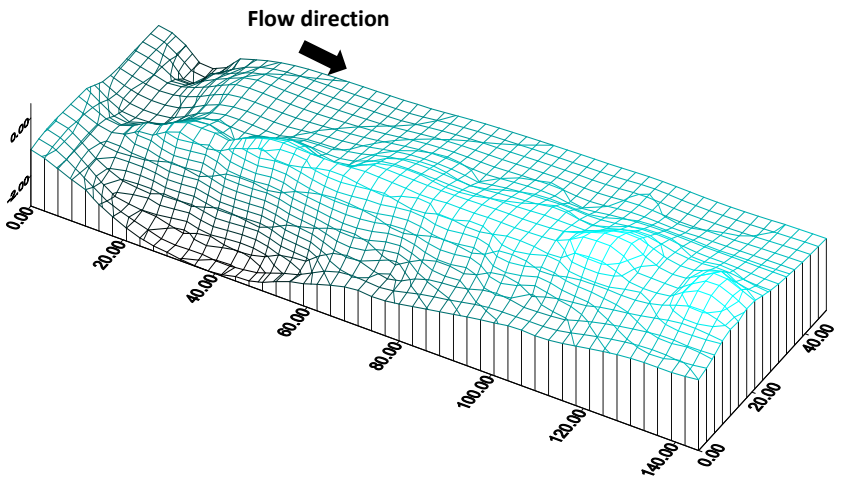

Fig. 22. Three-dimensional contour of Scour Surface Downstream Rip-rap Protection half-length of maximum scour in Live-Bed Scour Condition for Q = 28.8 lt/sec, USBR-III type

From the research with rip-rap protection of rocks tied with wire with a length of half the maximum scouring length, it was seen that minor scouring still occurred downstream of the protection, thus it was necessary to carry out maximum protection from the maximum scouring length.

c. Rip-rap protection throughout maximum scouring

In this study, rip-rap protection was used with the same protection length as the maximum scouring length without protection (Lmaks) with a discharge of 28.8 lt/sec, running was carried out three times with the same discharge of 28.8 lt/sec and observation for 120 minutes, because changes in the depth of scouring were seen small and approaching stability.

The final running results showed that there was small scouring around the downstream of the protection, namely with an average scouring depth of 1.6 cm and an average scouring length of 75.1 cm. The shape of the scouring can be seen in the three-dimensional contour image, as shown in Fig. 23 below.

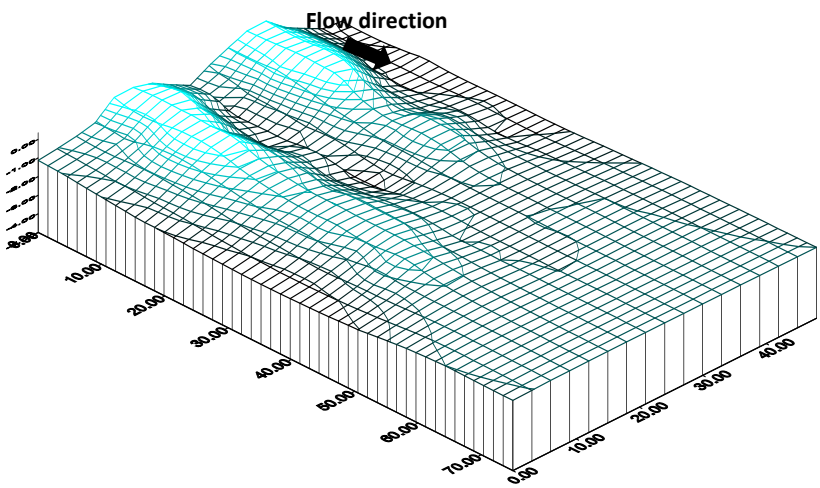

Fig. 23. Three-dimensional contour of the scour surface downstream of loose rock protection with maximum scour length in Live-Bed Scour Condition for Q = 28.8 lt/sec, USBR-III type

From the research of rip-rap protection with maximum scouring length, it can be seen that there is small scouring downstream of the protection. The comparison between the maximum scouring depth of the rip-rap protection balance with before protection with time can be seen in the graph of Fig. 24 below.

From the image above, it can be seen that the protected scouring depth is much shallower when compared to without protection, this indicates a reduction in

scouring. The reduction value for each rip-rap variation can be seen in Table 3 below.

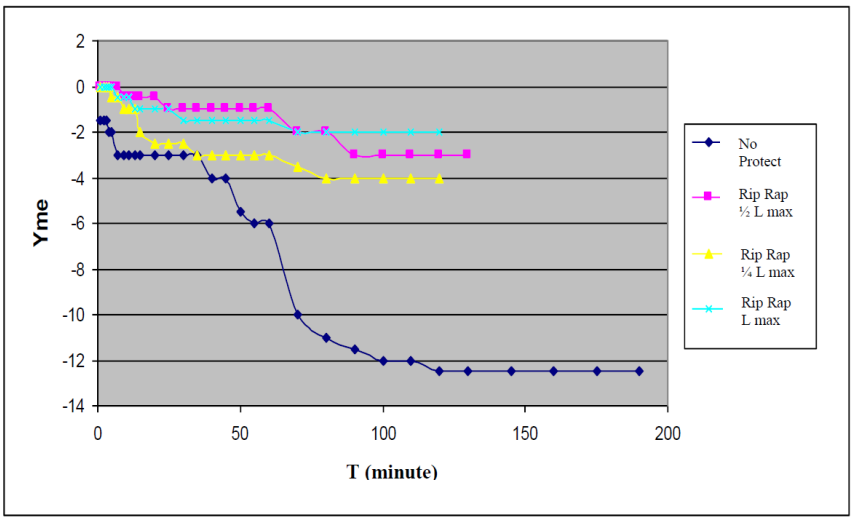

Fig. 24. Maximum Scour Depth Graph Before Protection and with protection in live-bed scour conditions for Q = 28.8 lt/sec

Table 3. Scour reduction value of USBR-III type

Notation	Non Protection Lm	RR ¼ Lm	RR ½ Lm	RR Lm
Y_m	12,4 cm	4,1 cm	3,1 cm	1,6 cm
L_m	230,0 cm	185,2 cm	145,2 cm	75,1 cm
$Y_{m\text{-reduction}}$		66,94%	75,00%	87,09%
$L_{m\text{-reduction}}$		19,48%	36,87%	67,35%

3.4 Scour Study Downstream of Stilling Basin USBR-IV Type

3.4.1 Scour study downstream of stilling basin without protection for USBR-IV type

Measurement of scour depth downstream of the stilling basin was carried out at 18 observation positions. In the measurement, the maximum scour depth occurred at position I, as shown in Fig. 25. The figure shows a tendency from position A upstream to position R downstream of the flow, indicating that the scour depth is getting shallower towards the downstream, and eventually sediment deposition occurs downstream of the flow. The maximum scour depth occurs at position point I.

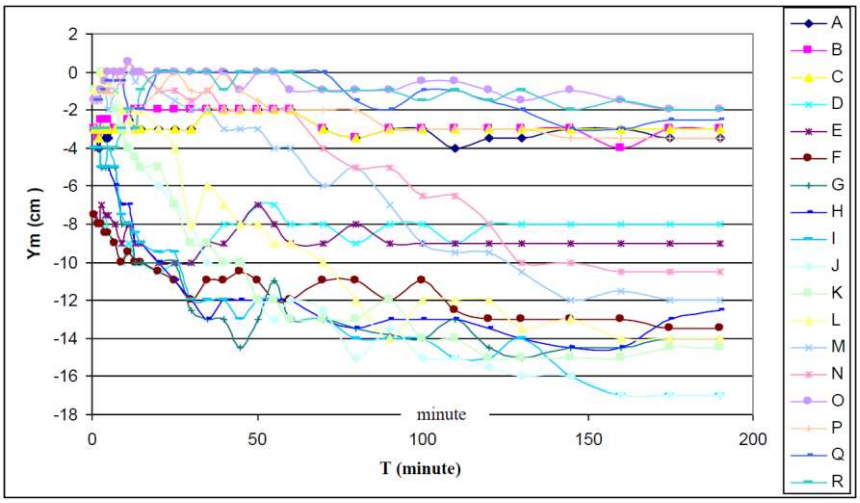

Fig. 25. Graph of scour depth against time at 18 observation positions under live-bed scour conditions for Q = 28.8 lt/sec, USBR-IV type

The relationship between the comparison of maximum scour depth and flow depth with the Froude number has a correlation number of R = 0.6249. This shows the level of relationship between the two parameters is close. The relationship can be expressed in the following equation.

$$\left(\frac{Y_{m.e}}{Y_3'}\right) = 0{,}448 \ln F_r + 1{,}4872 \quad \text{.....(7)}$$

The relationship between the comparison of maximum scouring depth and maximum scouring length with the Reynolds number has a correlation number of R = 0.7794, this still shows a close relationship, this relationship can be shown by the following equation. In this case, why is the equation still connected to the Reynolds number? Because this is important in relation to temperature changes that affect fluid viscosity.

$$\left(\frac{Y_{m.e}}{L_{m.e}}\right) = -0{,}0202 \ln R_e + 0.2817 \quad \text{.....(8)}$$

3.4.2 Scour study downstream of stilling basin with protection for USBR-IV type

a. Rip-rap protection one quarter of the maximum scour length

The maximum scour length for a discharge of 28.8 lt/s is 218 cm and the maximum scour depth is 17 cm. For the first scour protection study using ¼

Lmaks, three runs were carried out with the same discharge of 28.8 lt/s and observations for 120 minutes because changes in scour depth were seen to be small and approaching stability.

The final result of running shows that there is visible scouring around the downstream of the rip-rap, namely with an average scouring depth of 5.5 cm and an average scouring length of 105.1 cm. The shape of the scouring can be seen in the three-dimensional contour image as shown in Fig. 26 below.

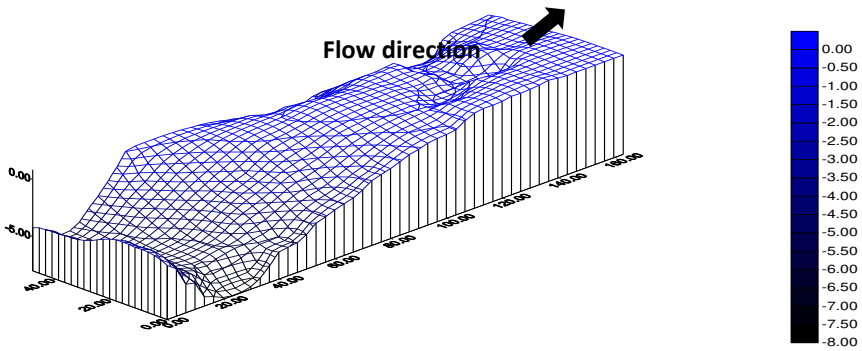

Fig. 26. Three-dimensional contour of Scour Surface Downstream Rip-rap Protection a quarter of the maximum scour length in Live-Bed Scour Conditions for Q = 28.8 lt/sec, USBR-IV type

b. Rip-rap protection half the maximum scouring length

In this study using half protection of the maximum scour length (1/2 Lmaks), running was carried out three times with the same discharge of 28.8 lt/sec and observation for 120 minutes because changes in scour depth were seen small and approaching stability.

The final running results showed that there was still scour around the downstream of the rip-rap, namely with an average scour depth of 3.1 cm and an average scour length of 94.2 cm. The shape of the scour can be seen in the three-dimensional contour image as shown in Fig. 27 below.

From the research with rip-rap protection of rocks tied with wire with a length of half the maximum scouring length, it was seen that minor scouring still occurred downstream of the protection, thus it was necessary to carry out maximum protection from the maximum scouring length.

c. Protection with Rip-rap along maximum erosion

In this study, rip-rap protection was used with the same protection length as the maximum scouring length without protection (Lmaks) with a discharge of 28.8 lt/sec, running was carried out three times with the same discharge of 28.8 lt/sec

and observation for 120 minutes, because changes in the depth of scouring were seen small and approaching stability.

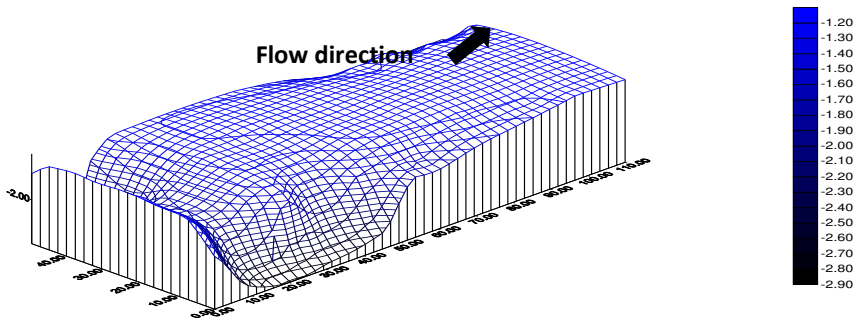

Fig. 27. Three-dimensional contour of Scour Surface Downstream Rip-rap Protection half length of maximum scour in Live-Bed Scour Condition for Q = 28.8 lt/sec, USBR-IV type

The final running results showed that there was small scouring around the downstream of the rip-rap protection, namely with an average scouring depth of 1.2 cm and an average scouring length of 53.3 cm. The shape of the scouring can be seen in the two-dimensional and three-dimensional contour images, as shown in Fig. 28.

From the study of rip-rap protection with a maximum scouring length, there was small scouring downstream of the protection. The comparison between the maximum scouring depth of the rip-rap protection balance and before protection with time can be seen in the graph in Fig. 29.

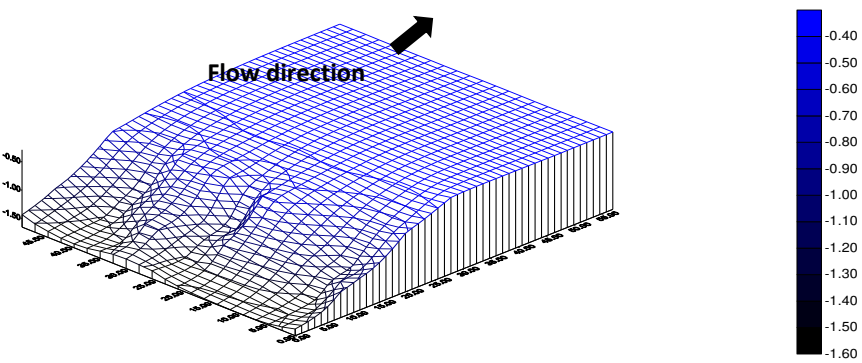

Fig. 28. Three-dimensional contour of the scour surface downstream of loose rock protection with maximum scour length in Live-Bed Scour Condition for Q = 28.8 lt/sec, USBR-IV type

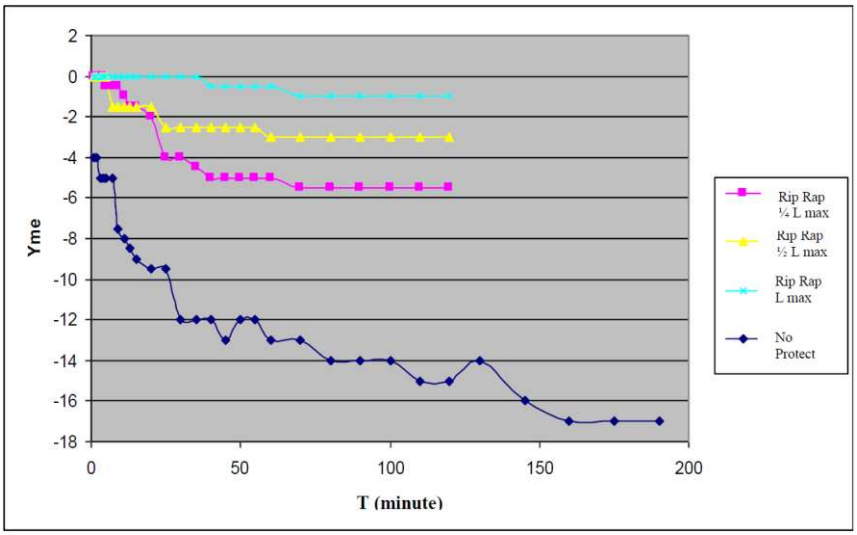

Fig. 29. Maximum Scour Depth Graph Before protection and with protection in live-bed scour conditions for Q = 28.8 lt/sec, USBR-IV

From Fig. 29 above, it can be seen that the maximum erosion depth without protection occurs at a very high erosion rate with a longer time to reach equilibrium compared to using rip-rap protection.

Table 4. Scour reduction value of USBR-IV type

Notation	Non Protection Lm	RR ¼ Lm	RR ½ Lm	RR Lm
Y_m	17,0 cm	5,5 cm	3,1 cm	1,2 cm
L_m	218,0 cm	105,1 cm	94,2 cm	53,3 cm
$Y_{m\text{-reduction}}$		67,65%	81,76%	92,94%
$L_{m\text{-reduction}}$		51,79%	56,79%	75,55%

Judging from the reduction value of several scour controls downstream of the stilling basin with rip-rap (1/2 Lmaks), rip-rap (1/4 Lmaks), rip-rap along Lmaks, both for stilling basin types USBR-I, USBR-II, USBR-III and USBR-IV, it is concluded that rip-rap along Lmaks (maximum scour length without protection) is able to control scour with the smallest scour depth or the smallest scour length, this can be seen from the greater reduction value compared to the others. This is because the water flow is dampened by the rip-rap installed along Lmaks so that when it reaches the downstream the water flow is stable and has little effect on scour downstream of the rip-rap. However, even though it has been protected along the scour hole, scour still occurs.

4. CONCLUSION

Based on the results of the research and discussion, the following conclusions can be drawn:

1. Live-bed flow occurs when the flow depth (h0) is smaller than its critical depth (hc), this is indicated by the movement of sediment grains so that the flow appears cloudy. While the flow depth above hc is clear-water flow in the form of clear water flow and there is no sediment movement.
2. From the study of the scour depth downstream of the stilling pond without protection for all types of USBR, there are relationships including:

a) A close relationship between the maximum scour depth (Y_{me}) and the flow depth downstream of the stilling pond (Y_3 ') with the Froude number, where the smaller the Froude number, the greater the maximum scour depth compared to the flow depth (Y_{me} / Y_3 ').
b) A close relationship between the scour depth (Y_{me}) and the maximum scour length (L_{me}) with the Reynolds number, where the greater the Reynolds number, the greater the maximum scour depth compared to the maximum scour length (Y_{me} / L_{me}).

3. Based on observations of scour protection downstream of the stilling basin for all types of USBR at a discharge of 28.8 lt/sec, it can be concluded that:

a). Observation results for the USBR-I type stilling basin, with the presence of scour protection, there is a reduction in scour for

Rip-rap ¼ Lmaks, namely: 46.69% for scour depth and 15.53% for scour length.
Rip-rap ½ Lmaks, namely: 80.75% for scour depth and 26.21% for scour length.
Rip-rap Lmaks, namely: 86.96% for scour depth and 47.32% for scour length.

b). For the USBR-II type of stilling basin, with the presence of scour protection, there is a reduction in scour for

Rip-rap ¼ Lmaks, namely: 48.48% for scour depth and 30.57% for scour length.
Rip-rap ½ Lmaks, namely: 63.03% for scour depth and 42.78% for scour length.
Rip-rap Lmaks, namely: 81.21% for scour depth and 69.31% for scour length.

c). For the USBR-III type of stilling basin, with the presence of scour protection, there is a reduction in scour for

Rip-rap ¼ Lmaks, namely: 66.94% for scour depth and 19.48% for scour length.
Rip-rap ½ Lmaks is: 75.0% for scour depth and 36.87% for scour length.
Rip-rap Lmaks is: 87.09% for scour depth and 67.35% for scour length.

d). For USBR-IV type stilling basin, with the presence of scour protection, there is a reduction in scour for

Rip-rap ¼ Lmaks, namely: 67.65% for scour depth and 51.79% for scour length.
Rip-rap ½ Lmaks is: 81.76% for scour depth and 56.79% for scour length.
Rip-rap Lmaks is: 92.94% for scour depth and 75.55% for scour length.

4. Based on observations of several protections/scouring controls downstream of the stilling basin with riprap (½ Lmaks), riprap (¼ Lmaks), riprap (Lmaks), it was concluded that the riprap arrangement along Lmaks (maximum scour length without protection) was able to control scour with the smallest scour depth. However, when viewed from the scour process, that the scour hole along Lmaks even though it was closed with full protection, scour still occurred and the scour hole downstream even though it was small.
5. So overall the maximum Scouring Depth reduction (Ym Reduction) occurs in USBR-IV type, and the smallest in USBR-II type. While the maximum Scouring Length reduction (Lm Reduction) occurs in USBR-IV type, and the smallest in USBR-I type.

DISCLAIMER (ARTIFICIAL INTELLIGENCE)

Author(s) hereby declare that NO generative AI technologies such as Large Language Models (ChatGPT, COPILOT, etc.) and text-to-image generators have been used during writing or editing of this manuscript.

COMPETING INTERESTS

Authors have declared that no competing interests exist.

REFERENCES

Abdurrosyid, J. (2005). Scour in the downstream of the stilling basin of the weir. *Journal of Civil Engineering Dynamics, 5*(2), 73-79. Muhammadiyah University of Surakarta.

Breusers, H. N. C. (1966). CONFORMITY AND TIME SCALE IN TWO-DIMENSIONAL LOCAL SCOLJR.

Breusers, H. N. C., & Raudkivi, A. J. (1991). *Scouring* (IHAR Hydraulic Structure Design Manual). A. A. Balkema.

Buchko, M. F. (1986). Investigation of local scour in cohesionless sediments by using a tunnel model (Report Q239). *Delft Hydraulics, Delft*.

Cahya, E. N., Dermawan, V., & Sari, R. P. (2024). Hydraulic flow and downstream scouring behavior on spillway system of Surumana Dam. *IOP Conference Series: Earth and Environmental Science, 1311*(1), 012071. https://doi.org/10.1088/1755-1315/1311/1/012071

Castelino, M., et al. (2021). Riverbed protection downstream of an undersized stilling basin by means of antifer artificial blocks. *Water, 13*(5), 619. https://doi.org/10.3390/w13050619

Catakli, O. (1973). *A study of scour at the end of stilling basin and use of horizontal beams as energy dissipatersG 11th Congress of large dams*. Madrid.

Chow, V. T. (Ed.). (1995). *Hidraulika saluran terbuka*. Pen. Erlangga.

Dietz, R. (1969). Bau und funktion des spindelapparats. *Naturwissenschaften*, *56*, 237-248.

Djunur, L. H. (2022). Study on scouring and protection of USBR-III type downstream of spillway. *Jurnal Teknik Sipil dan Perencanaan, 24*(1), 62-71. https://doi.org/10.15294/jtsp.v24i1.34196

Eggenberger, S. (1944). *Beitrag zu den Untersuchungen des Luftdrucks in der Schweiz*. Philosophische Fakultät II der Universität Zürich.

Farhoudi, J., & Smith, K. V. H. (1985). Local scour profiles downstream of hydraulic jump. *Journal of Hydraulic Research, 23*(4), 343-358. American Society of Civil Engineers.

Ghetti, A., & Zanovello, A. (1954). Esame delle escavazioni d'alveo a valle di traverse mediante esperienze su modelli in piccola scala. *Proc., 1st Convegno di Costruzioni Idrauliche*, 1-9.

Hoffmans, G. J. (2017). *Scour manual*. Routledge.

Hoffmans, G. J. C. M., & Pilarczyk, K. W. (1995). Local scour downstream of hydraulic structures. *Journal of Hydraulic Engineering, 121*(4), 326-340. American Society of Civil Engineers.

Hoffmans, G. J. C. M., & Verheij. (2021). *Scour manual*. A. A. Balkema.

Kironoto, B. A. (2020). *Sediment transport hydraulics* (Civil Engineering Study Program, Postgraduate Program). Gadjah Mada University.

Kotoulas, D. (1967). *Das Kolkproblem im Rahmen der Wildbachverbauung* (Vol. 43). na.

Kumar, D., et al. (1982). Flow under weir on scoured bed. *Journal of the Hydraulics Division, 108*(HY 4), 529-543. American Society of Civil Engineers.

Mays, L. W. (1999). *Hydraulic design handbook*. McGraw-Hill.

Mohamed, M. S., & McCorquodale, J. A. (1992). Short term local scour. *Journal of Hydraulic Research, 30*(5), 685-699. American Society of Civil Engineers.

Moroni, M., Castelino, M., & De Girolamo, P. (2022). Numerical and physical modeling of Ponte Liscione (Guardialfiera, Molise) dam spillways and stilling basin. *Journal of Hydrology, 9*, 214. https://doi.org/10.3390/hydrology9120214

Mosonyi, E., & Schoppmann, B. (1968). Discussion of "Vortex-Induced Oscillations at Low-Head Weirs". *Journal of the Hydraulics Division*, *94*(6), 1564-1568.

Muller, R. H. (1944). Verification of Short-Range Weather Forecasts (A Survey of the Literature) I. *Bulletin of the American Meteorological Society*, *25*(1), 18-27.

Provorova, T. P. (1999). Calculation of local scour in the case of a bottom flow regime downstream of an outlet. *Hydrotechnical Construction*, *33*(4), 230-235.

Raju, R. K. G. (Ed.). (1986). *Aliran melalui saluran terbuka*. Pen. Erlangga.

Raudkivi, A. J. (1967). Analysis of Resistance in Fluvial Channel. *Journal of the Hydraulics Division*, *93*(5), 73-84.

Schoklitsch, A., (1932). Die Eigenschaften der Böden. *Der Grundbau: Ein Handbuch Für Studium und Praxis*, 1-16.

Shalash, S. (1982). Effects of sedimentation on the storage capacity of the High Aswan Dam reservoir. *Hydrobiologia*, *91*, 623-639.

Van der Meulen, T.; Vinjé, J.J. (1977). Three-dimensional local scour in non-cohesive sediments. *Publication. Delft Hydraulics Laboratory = Publikatie - Waterloopkundig Laboratorium*, 180. Delft Hydraulics Laboratory: Delft. 12 pp.

Van Rijn, L. C. (1984). Sediment transport, Part I: Bed load transport. *Journal of Hydraulic Engineering, 110*(12), 1432. American Society of Civil Engineers.

Disclaimer/Publisher's Note: The statements, opinions and data contained in all publications are solely those of the individual author(s) and contributor(s) and not of the publisher and/or the editor(s). This publisher and/or the editor(s) disclaim responsibility for any injury to people or property resulting from any ideas, methods, instructions or products referred to in the content.

© Copyright (2025): Author(s). The licensee is the publisher (BP International).

Peer-Review History:
This chapter was reviewed by following the Advanced Open Peer Review policy. This chapter was thoroughly checked to prevent plagiarism. As per editorial policy, a minimum of two peer-reviewers reviewed the manuscript. After review and revision of the manuscript, the Book Editor approved the manuscript for final publication. Peer review comments, comments of the editor(s), etc. are available here: https://peerreviewarchive.com/review-history/4261

Chapter 4
Print ISBN: 978-93-49473-44-7, eBook ISBN: 978-93-49473-43-0

A Comparative Study on the Design of a Two-Story Car Showroom Using Pre-Engineered Buildings (PEBs) in Accordance with British Standards and Euro Codes

Balamuralikrishnan R. [a++*] and Ibrahim Shabbir Mohammedali [a#]

DOI: https://doi.org/10.9734/bpi/erpra/v5/4521

Peer-Review History:
This chapter was reviewed by following the Advanced Open Peer Review policy. This chapter was thoroughly checked to prevent plagiarism. As per editorial policy, a minimum of two peer-reviewers reviewed the manuscript. After review and revision of the manuscript, the Book Editor approved the manuscript for final publication. Peer review comments, comments of the editor(s), etc. are available here: https://peerreviewarchive.com/review-history/4521

ABSTRACT

Steel has been used as a construction material for a very long time. Most steel structures are used for low-rise, single-story industrial buildings. Steel is preferred for these buildings due to its higher strength-to-weight ratio compared to reinforced concrete (RCC), and because it allows for larger, unobstructed internal spaces with long clear spans between columns. Pre-engineered buildings (PEBs) represent a modern approach to structural steel utilization, optimizing design for economical structural integrity. Structural members are designed and fabricated in a controlled factory environment to produce optimal sections by varying member thickness along their length according to bending moment requirements. The PEB concept utilizes the amount of steel required and produces the most optimum sections based on the bending moment requirement. The actual model of the PEB structure of the car showroom was created in STAAD Pro software. This research paper analyzes and designs a two-story (G+1) PEB car showroom using STAAD.Pro, in accordance with British Standards (BS 5950-1:2000) and Euro codes (EC3 EN-1993-1), including wind and seismic analysis. To achieve this, two models of the car showroom were created in STAAD.Pro: a British Standard (BS) model and a Euro code (EC) model. The BS model used tapered frame sections, while the EC model used universal standard section frames. Both models were analyzed under dead load,

[a] Department of Civil and Environmental Engineering, College of Engineering, P.O. Box: 2322, CPO Seeb 111, National University of Science and Technology, Muscat, Sultanate of Oman.
[++] Associate. Professor;
[#] L4-Student;
**Corresponding author: E-mail: balamuralikrishnan@nu.edu.om;*

live load, wind load, and seismic load. Wind and seismic loads, being critical dynamic loads, were analyzed to assess structural stability against lateral forces. The analysis and design results for both models were within allowable limits for ultimate and serviceability limit states, as the internal stresses in all members satisfied the unity check ratio requirements for both design codes. Dynamic analysis suggests that the EC model exhibits higher seismic resistance compared to the BS model, as the maximum displacement in the X-direction was 8.83 mm for the EC model and 10.5 mm for the BS model. The total structural weight was 1125.431 kN for the BS model and 1214.315 kN for the EC model, making the EC model 7.9% heavier. Furthermore, the total weight of all portal frames was 457.26 kN for the BS model and 574.725 kN for the EC model, indicating that the tapered frame sections in the BS model reduced steel usage by 25.7%. Therefore, the BS model proved more economical compared to the Euro code model. In order to determine the most cost-effective method of designing the PEB car showroom using British standard and Euro code, it is crucial to compare the design results of the two models and identify the structure that would be durable and economical in terms of material used.

Keywords: Pre-engineered buildings (PEB); STAAD pro; industrial structures; dynamic loading; tapered sections.

1. INTRODUCTION

1.1 Pre-engineered Building Design

With time, there have been great improvements in the technological advancements, which contributed tremendously to improve the standards of living with the invention of new products and utilities. One such example of structural revolution is Pre-Engineered Buildings (PEBs). PEBs make use of a set stock of raw materials which have been verified over time to fulfill an extensive range of structural and aesthetic design conditions. Pre-engineered buildings are nothing but steel buildings in which excess steel is avoided by tapering the sections as per the bending moment's requirement. Steel is an eco-friendly material since it does not have any negative effect on the environment, this makes steel structures more sustainable as compared to other construction types (Sah et al., 2023). Steel has been used as a construction material for a very long time. The famous Eiffel Tower is one among the oldest steel structures made in 1889, and it has been a symbolic landmark for Paris, and it has stood for over 129 years. Despite the fact that steel buildings are not known for high-rise structures, but instead, the majority of steel structures are low-rise with single storey mainly used for industrial purposes. Pre-engineered building (PEB) is a modern concept of utilizing steel structures and optimizing the design by ensuring the economical integrity of the structure (Firoz et al., 2012). The basis of the PEB concept lies in providing the section at a location only according to the requirement at that spot (Zende et al., 2013). Oman is a well-developed country and its economy mainly depends on exporting petroleum products, but as the country is facing economic crisis due to depletion of crude oil reserve, the country tends to divert its economic vision toward boosting the business sector

(Balamuralikrishnan & Mohammedali, 2019). This only means that more industries and factories are required to manufacture local products and to export them in order to stabilize the economy of the country. This encourages construction of a Pre-engineered building in the country for both small and large-scale industries.

Pre-engineered building concept is getting famous rapidly not only in Oman but all around the world due to the increasing demand of industrial-oriented buildings that require long clear span with column-free space, which can provide easy access and mobility within the building. In addition to that, the PEB concept gives economical structural sections by reducing excess steel usage and optimizing the required steel as per the bending moment requirement, which has a major advantage over the traditional steel structures where unnecessary wastage of steel is done resulting in an increase of material cost and making the construction uneconomical. Pre-engineered building (PEB) offers a lot of advantages over conventional steel building (CSB) construction. Some of the main advantages that are offered by PEB, which are reduction in time, reduced cost of construction, light weight foundation, easy future expansion flexibility, ability for long span column free space, single source responsibility, and higher resistance to earthquakes. The materials used in conventional steel building consume more cost, so to overcome this, “PEB structures” are needed to reduce the cost of the project. In order to reduce the self-weight of conventional steel buildings, PEB can be used. Generally, PEB can reduce up to 35% of self-weight when compared to conventional steel buildings (Balamuralikrishnan & Mohammedali, 2019).

Steel structures are preferred for industrial buildings due to a higher strength to weight ratio than RCC structures. Pre-engineered building (PEB) is a steel structure in which the structural members and components are fully designed and fabricated in the factory and transported to the site in knock-down condition. Normally it requires 6 to 8 weeks for the fabrication process and delivery of all the structural components to the site. The PEB concept utilizes the amount of steel required and produces the most optimum sections based on the bending moment requirement. Hence, the section depth varies throughout the length following the bending moment diagram (Thorat & Patil, 2017). In order to achieve the above member configuration, thin steel plates are tapered and combined to give the I-section desired. Since all the design and fabrication is done at the factory under controlled environment, the components are of high quality and precision. PEB design concept offers greater advantage over conventional steel structures (CSB) with roof truss configuration for low-rise single-storey structures. PEB also fulfils the need and demand of long span column free area by eliminating or minimizing interior columns and walls, which is the utmost requirement of almost all industrial buildings. Moreover, PEB is much economical in terms of cost and time of construction, which is a major advantage over the CSB concept. The advancement in technology has introduced computerized software that makes analysis and designing of PEB structures very simple and easy (Balamuralikrishnan & Mohammedali, 2019).

STAAD Pro is an advanced structural analysis and design software, which is the most popular software used all over the world for analysing and designing of different types of structures. It supports almost all the designing codes, and can design concrete, steel and timber structures. It provides a user-friendly interface and visualization of the 3D structural model of the building. It is one of the easiest software available for modeling, analyzing and designing of different types of structures. PEB is significantly advantageous over Conventional Steel Building (CSB) structure since it offers less cost and time of construction, it has the ability to span long distance giving column free span, easy flexibility for future expansion, low maintenance cost, single source responsibility and also has higher resistance to moisture, fire, adverse weather condition and earthquake which makes it more durable and safe (Balamuralikrishnan & Mohammedali, 2019).

The results obtained by the authors concluded that the 3D PEB model weighs 43.77 tons and the CSB model weights 74.08 tons, i.e. PEB weighs 35% lesser than CSB as per IS 800-2007 (Lande & Kucheriya, 2015). The only disadvantage of PEB structure is that they have poor thermal and fire resistance and is vulnerable towards corrosion (Dubey & Sahare, 2016). PEB structures can be easily designed by using advanced software like STAAD Pro by following simple procedures and by using different country building codes. It was also concluded that PEB are more advantageous over CSB in terms of cost effectiveness, quality control, simplicity in erection and speed of construction (Meera, 2013).

The deflection of the two structures was studied under dynamic loading from the results obtained and it was concluded by the author that the PEB model with bracing provides more stability against seismic loading and the deflection of the structure is less when compared to the PEB structure without bracing, therefore PEB offers higher earthquake resistance when braced. PEB frames were more stable under wind loading as compared to CSB frames. Moreover, the weight of PEB frame was 27% lesser as compared to the weight of CSB frame (Patil, 2017). PEB structure over conventional steel structures in details by considering the cost, time and material requirements (Katkar & Phadtare, 2018). The design aspects of Indian standard are higher as compared to the American standards and mention the main criteria as listed below, which has caused the weight of the structure to be more when designed using IS 800-2007 as compared to MBMA/AISC design code (Kiran et al., 2014). The deflection of the PEB frames is more as compared to the conventional structure, making the structure more flexible and withstand seismic loading (Kolate & Kewate, 2015).

The existence of a pre-cast concrete industry is numerous, successfully executed construction project, its uses not disputed and it is the proof that the manufacturing and production technology is practical and cost effective. The growing requirements of architectural design at building construction raise the progress of stable and constant development of the industries as this is a new technology (Stania & Patra, 2017). The adoptability of PEB in the place of Conventional Steel Building (CSB) design concept resulted in many advantages, including economy and easier fabrication (Mythili, 2017). Presently, large column free area is the utmost requirement for any type of industry and with the advent of

computer software, it is now easily possible (Balamuralikrishnan & Mohammedali, 2019). With the improvement in technology, computer software have contributed immensely to the enhancement of the quality of life through new research (Dharmalingam & Silambarasan, 2017). "Pre-engineered steel buildings" are those that are totally invented within the industrial plant once planning, shipped to site in CKD (completely knocked down) condition; and all parts are assembled and erected at a site with nut-bolts, thereby reducing the time of completion. Pre–engineered means that, typically speaking, is any part of a structure that's factory-made first off to its arrival on the building site (Thorat & Patil, 2017). Cold formed steel section over hot rolled section as purlin is almost lighter than 32 % (Goswami & Shende, 2018). PEB structures are lighter structures. As PEB is 30 % lighter than CSB structures (Mehendale & Gupta, 2016). PEB steel frames are not only the most economical solution due to lesser weight of construction but also have shown better performance compared to CSB frames (Saleem & Qureshi, 2018). The concept of pre-engineering construction provides systems of steel buildings that are predesigned and prefabricated (Balamuralikrishnan & Mohammedali, 2019). As the name suggests, this concept involves preliminary engineering of structural elements, using a predetermined register of building materials and manufacturing technologies that can skillfully meet a wide range of structural and aesthetic design requirements. The basis of the PEB concept is to provide a site only in accordance with the requirement at that location (Ingole & Changhode, 2022). A pre-engineered steel building (PEB) has now become one of the most efficient and simplified building types in the steel construction industry. PEB has found a wide application in the Indian civil industry. Use of tapered members for columns and rafters is one of the basic properties of PEB. Use of web-tapered members increases the efficiency of the PEB (Gawade & Waghe, 2018).

2. EXPERIMENTAL INVESTIGATIONS

2.1 Detailed Methodology

Carry out intense research on PEB structures and understand the design concepts by carrying out sufficient literature review. Collect Journals, and other research related materials that can aid in the literature review. Prepare the model on STAAD Pro and carry out the analysis and design of the PEB structure by applying dead load, live load, wind load and seismic load conditions in accordance to both British Standard (BS 5950-1:2000) (BSI, 2000) and Eurocodes (EC3 EN-1993- 1) (EN 1993-1-3, 2005) and interpret and compare the output results (Balamuralikrishnan & Mohammedali, 2019).

2.2 Proposed Plan and Cross-Sectional Elevation Drawings of the PEB Car Showroom

The first step of the project was to prepare a simple plan and cross-sectional elevation of the PEB car showroom before modeling the structure in the STAAD Pro. A simple plan was created in AutoCAD as shown in Fig. 1 (Balamuralikrishnan & Mohammedali, 2019). From the plan it can be seen that the spacing between the frames (bay spacing) is 5.0 m and the columns are located at

a distance of 7.5 m to support the mezzanine floor above it and in the front open area the columns are spaced by 15.0 m. The mezzanine floor has an extension at the centre. The side view elevation of the PEB car showroom shows the spacing of 5.0 m between the frames. The elevation view also shows the eave height of 8.0 m and the mezzanine floor level at 4.0 m (Fig. 2) (Balamuralikrishnan & Mohammedali, 2019).

2.3 Actual Model of the PEB Car Showroom

The actual model of the PEB structure of the car showroom was created in STAAD Pro software. Since the aim of the project is to analyse and design the PEB car showroom using both British Standards and Eurocode, and to compare between the two codes to obtain the most economical design. It is decided to prepare the same model of the PEB structure for both cases in order to get the most economical design in terms of material required for each model as per the building code requirements (Balamuralikrishnan & Mohammedali, 2019). The car showroom is modeled to have 2 storeys such that it has a ground floor and a mezzanine floor at 4.0 m above the ground level. The specifications of the model frame spacing = 5 m, number of bays = 10, total length = 50 m, width of frame = 45 m, eave height = 8 m were created on the STAAD Pro software.

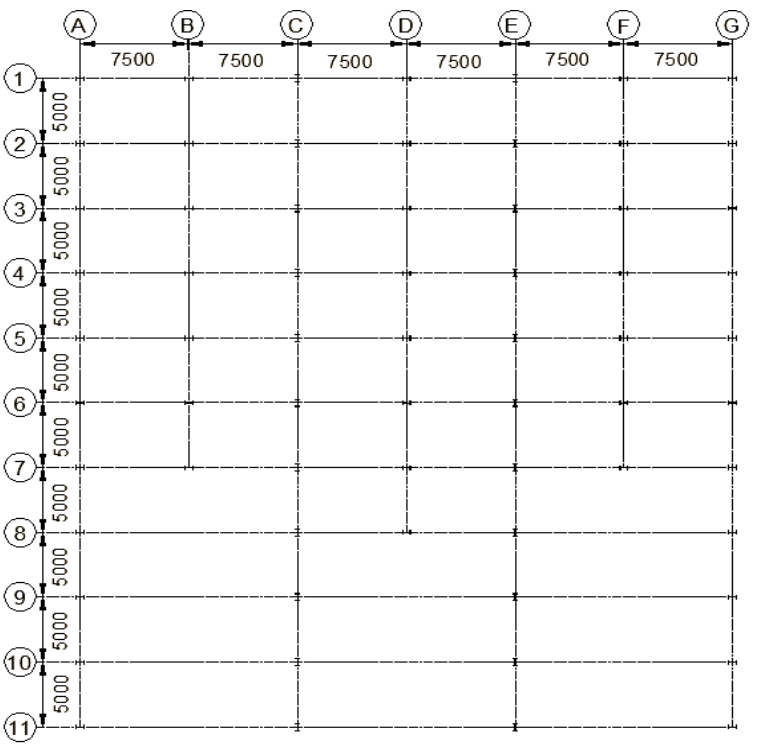

Fig. 1. Plan of the proposed PEB car showroom structure

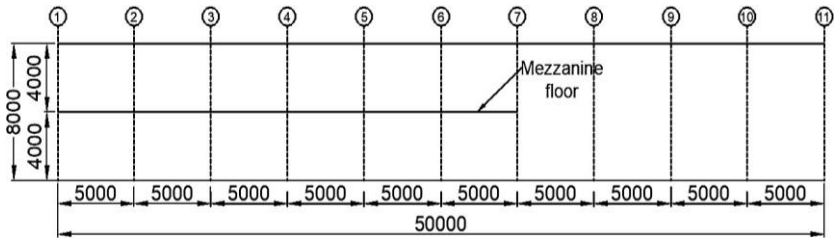

Fig. 2. Side view elevation of the car showroom structure

2.4 Member Properties for British Standard Model

Different member properties were assigned to the PEB car showroom model as per the British standard design. These properties are such as tapered portal frame members, standard universal beam and column sections for mezzanine floor, purlin members and bracing members. Tapered portal frame members: Tapered members are customized members that are created and defined by user specifications in STAAD Pro (Balamuralikrishnan & Mohammedali, 2019).

The tapered sections are provided by utilizing the amount of steel required as per the bending moment requirements. The tapered members are created in such a way that the depth of the member gradually varies along the length of the member. Tapered section reduces the steel material used as well as the weight of the structure. In this model, the tapered sections were assigned to the rafter beam members and the column members of the portal frames as shown in Fig. 3 (Balamuralikrishnan & Mohammedali, 2019).

2.4.1 Standard universal sections for mezzanine floor

The standard section of beams and columns were used for supporting the mezzanine floor in the structure. The beams are arranged in secondary and main beam arrangement to transfer the floor loads to the columns and eventually to the foundation. In STAAD Pro the British standard sections are available in the inbuilt section database. The spacing between the main beams is 5.0 m and the spacing between the secondary beams is 1.5 m. The length of secondary beams is 5.0 m and the length of the main beams is 7.5 m. The standard section size of the beam and column used are shown in Fig. 4 (Balamuralikrishnan & Mohammedali, 2019).

2.4.2 Bracing and purlin members

The bracing and purlin members are provided in order to increase the resistance of the structure against wind load. The purlins are arranged at a spacing of 1.5 m over the entire span of the rafter as shown in Fig. 3 (Balamuralikrishnan & Mohammedali, 2019). For purlin members, a British cold formed Z - section (200ZLML625×20) was selected from the inbuilt section database in STAAD Pro. The section 200ZLML625×20 has an overall depth of

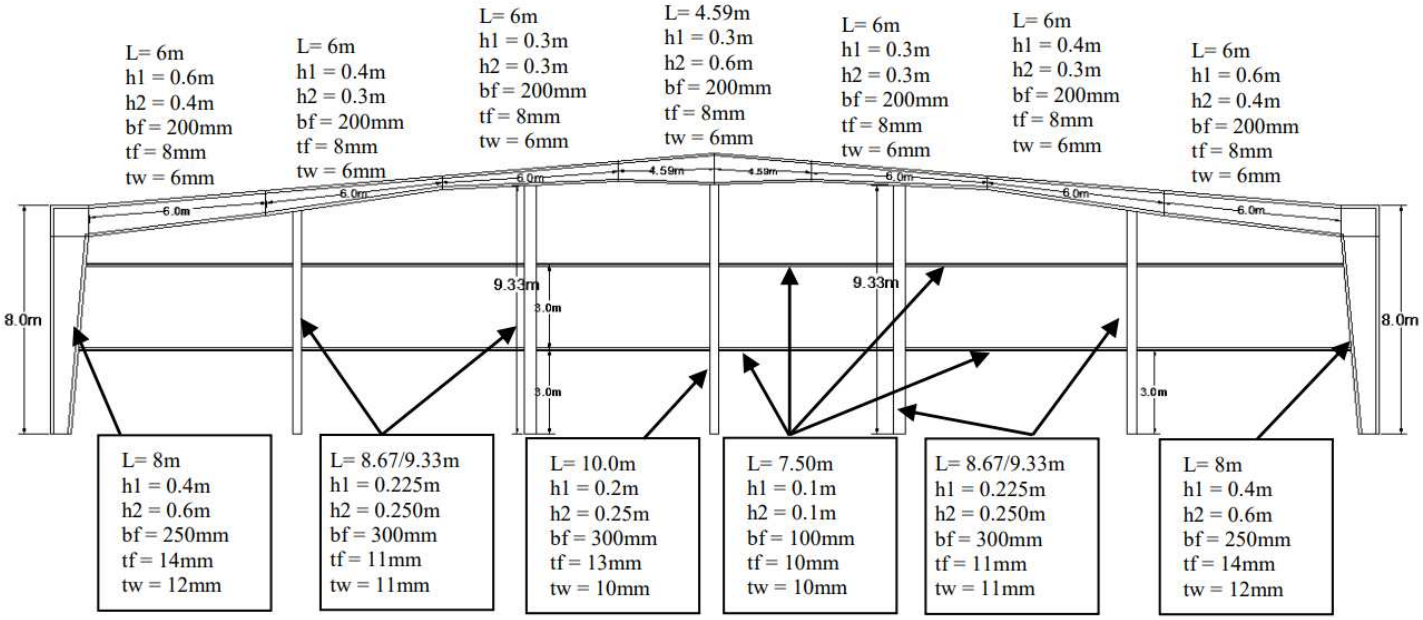

Fig. 3. Tapered sections for the front gable frame

200 mm, width of 62.5 mm, thickness of 2 mm and lip of 20 mm. For the bracing members, tie rods of 35 mm diameter were used for column bracing and roof bracing members. But since there is no built-in property for tie rod in STAAD Pro, hence specified the bracing members as a solid pipe of 35 mm diameter. The bracing members are assigned to act as tension members only. The arrangement of the column bracing and roof bracing is shown in Fig. 5 (Balamuralikrishnan & Mohammedali, 2019).

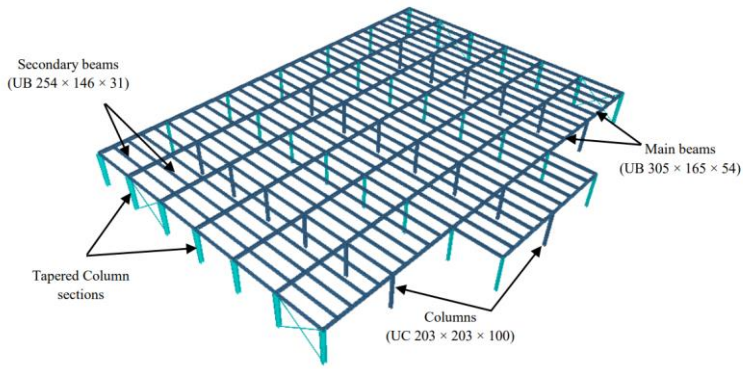

Fig. 4. Isomeric 3D rendered view of the mezzanine floor

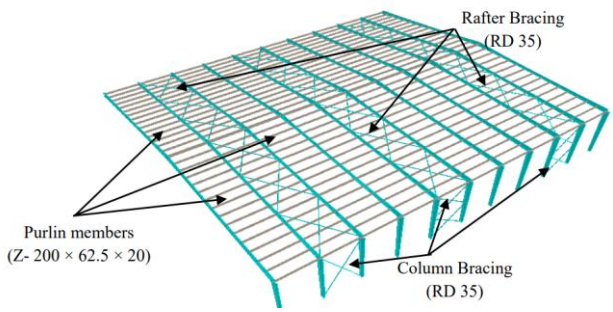

Fig. 5. Arrangement of the bracing & purlin members in the structure

2.5 Member Properties for Euro Code Model

The member properties assigned to the Euro code model are very similar to the member properties that were assigned in the British Standard model, except for the tapered sections for the portal frames. In STAAD Pro, the design of a steel structure with customized tapered section properties is not supported and hence the design of the PEB car showroom using Euro code (EN 1993-1-3:2005) could not be implemented. Hence, the portal frame was assigned with universal

standard sections instead of using tapered sections for the PEB portal frames. Therefore, the member properties assigned to the Euro code model consist of standard universal beam and column sections for the portal frames and the mezzanine floor, purlin members and bracing members. The purlin and bracing member properties are the same as the British Standard model, except for the bracing members, 25 mm diameter tie rods are used instead of 35 mm diameter (Balamuralikrishnan & Mohammedali, 2019).

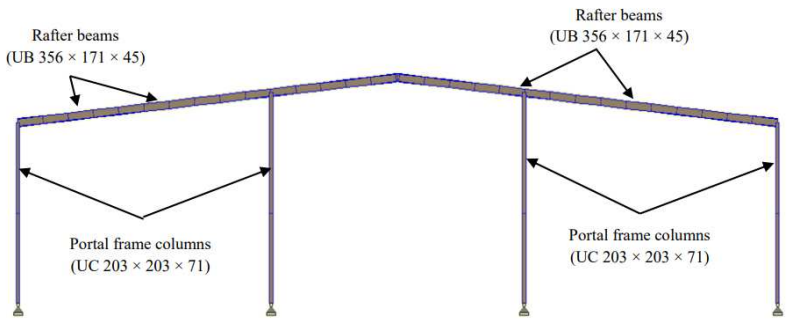

Fig. 6. Typical portal frame showing the member properties for Euro code model

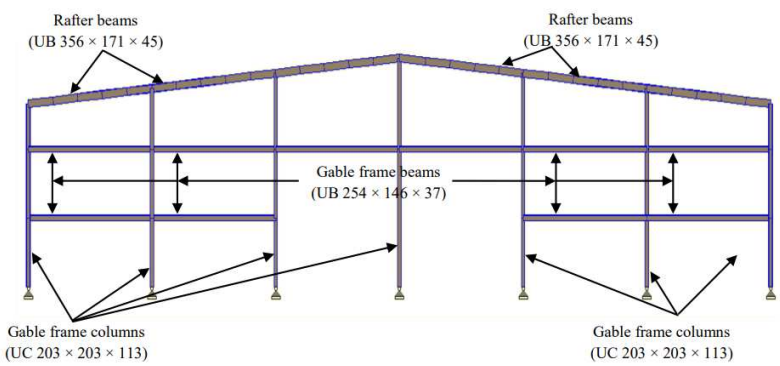

Fig. 7. Member properties for the gable frame in Euro code model

2.5.1 Standard universal sections for the portal frame

Euro code does not support customized tapered section design in STAAD Pro, and therefore we have adopted standard sections that are available in the inbuilt section database in STAAD Pro. In the Euro code model, the rafter beams member properties are assigned uniformly throughout the length of the rafter by considering the average standard section size from the British standard model of

the tapered sections. This was the only possible way by which the design of the PEB car showroom could be implemented as per EN-1993-1-3:2005 in STAAD Pro. In Euro code model, all the portal frames were assigned the same member properties as shown in Fig. 6, except for the gable frame, different member section sizes were used as shown in Fig. 7 (Balamuralikrishnan & Mohammedali, 2019).

2.6 Load Cases Consideration for Analysis

The most important thing to consider after assigning the property of the members correctly to the PEB structure is to assign the load cases appropriately. Load cases are very important and require special attention since all the analysis and design result depends on the loading condition. In this project, I will be considering dead load, live load, wind load and seismic load. The load cases are considered based on BS EN 1991-1: 2002 (BSI, 2000, Balamuralikrishnan & Mohammedali, 2019).

2.6.1 Dead load

The dead loads that are applied on the structure include the self-weight of all the structural members, the dead load on the interior and exterior rafters due to the purlins and the galvanized steel roofing sheets placed above it and the dead load on the mezzanine floor due to the concrete deck slab and floor finishes. The self-weight is assigned by a factor of -1 in STAAD Pro (Balamuralikrishnan & Mohammedali, 2019).

2.6.2 Imposed load

The live load is applied to the structure at the roof level and the mezzanine floor level in the structure. At the roof level, the live load on the rafter is mainly due to serviceability access and maintenance consideration only, and the live load on the mezzanine floor is mainly due to the vehicular loading (European-Union, 2002) (BSI, 2000).

Imposed load on the rafters: At the roof level, the live load is applied over the rafters in accordance with Eurocode (EN-1991-1-1:2002, Table 1 (BSI, 2000, Balamuralikrishnan & Mohammedali, 2019).

Table 1. Loads

Sl. No.	Euro code (EN-1991-1-1:2002)		BS EN 1991-1-4:2005
	Imposed load on the roof	**Imposed load on the mezzanine floor**	**Wind load**
1.	Range of 0.0 kN/m^2 to 1.0 kN/m^2	Range of 1.5 to 2.5 kN/m^2	Basic wind speed of 35 m/s under extreme weather conditions

It is stated that, for roofs (of category H) with no accessibility except for nominal maintenance, repair and serviceability access, the imposed load on the roof can be selected within the range of 0.0 kN/m^2 to 1.0 kN/m^2. Therefore, in our case the minimum variable load on the roof for only service accessibility is taken as 0.6 kN/m^2.

Imposed load on the Mezzanine floor: Since this is a car showroom, the main variable load will be due to the vehicles. According to Eurocode (EN-1991-1-1:2000, Table 1 (BSI, 2000)) the vehicle having the weight of ≤ 30 kN (Category F), the imposed load due to the vehicle may be selected within the range of 1.5 to 2.5 kN/m^2. Therefore, in that regard the imposed load of 2.5 kN/m^2 was applied as floor load on the mezzanine floor (Balamuralikrishnan & Mohammedali, 2019).

2.6.3 Wind load

The wind load that would be considered for both codes will have a basic wind speed of 35 m/s under extreme weather conditions. The wind load is calculated in accordance with Eurocode (BS EN 1991-1-4:2005) (BSI, 2000, EN 1993-1-3, 2005, Balamuralikrishnan & Mohammedali, 2019).

Total length of the building, b = 50 m, Spacing between the frames, s = 5 m, Width of the portal frames, d = 45 m, Apex height (max) of the structure, h = 10 m, Eave height of the structure, h' = 8 m

Slope of the rafter, α = 5°

Basic wind velocity, (V_b); (EN 1991-1-4, § 4.2, Eq 4.1 (BSI, 2000, EN 1993-1-3, 2005)) Directional factor, C_{dir} = 1.0

Seasonal factor, C_{season} = 1.0

Fundamental value of the basic wind velocity, $v_{b,0}$ = 35 m/s

Basic wind Velocity, $v_b = C_{di}.C_{season} . v_{b,0}$

v_b = 1.0 × 1.0 × 35 = 35 m/s

Where by:

C_{dir} = is the directional factor and its recommended value is taken as 1.0

C_{season} = is the seasonal factors and its recommended value is taken as 1.0

$v_{b,0}$ = is the fundamental value of the basic wind velocity and is taken as 35 m/s Basic velocity pressure, (qb); (EN 1991-1-4, § 4.5, Eq 4.10 (BSI, 2000, EN 1993-1-3, 2005))

Density of air, ρair = 1.25 kg/m^3

Basic velocity pressure, $q_b = \frac{1}{2} \times \rho_{air} \times v_b^2$

$$q_b = \frac{1}{2} \times 1.25 \times 35^2 = 765.63 \text{ N/m}^2$$

Peak velocity pressure, qp (z); The peak wind pressure is given by the formula; (EN 1991-1-4, § 4.5, Eq 4.8 (BSI, 2000, EN 1993-1-3, 2005))

$$q_{p(z)} = \left[1 + 7l_{v(z)}\right] \cdot 1/2 \cdot \rho_{\text{air}} \cdot v_{m(z)^2}$$
$$q_{p(z)} = 1778.5 \text{ N/m}^2 = 1.78\text{kN/m}^2$$

External Wind pressure coefficients in this calculation only the internal portal frame is considered for calculating the wind load on the PEB structure. For obtaining the wind load on the exterior frames, it can be taken half of the load that is acting on the interior portal frame.

The external wind pressure acting on the external surfaces can be calculated using;

$w_e = q_p.(z_e).C_{pe}$ (EN 1991-1-4, § 5.2, Eq 5.1 (BSI, 2000, EN 1993-1-3, 2005))

The wind load calculations are shown in Fig. 8 and Table 2 (Balamuralikrishnan & Mohammedali, 2019). Assigning the wind load to STAAD model as shown in Fig. 9 (Balamuralikrishnan & Mohammedali, 2019).

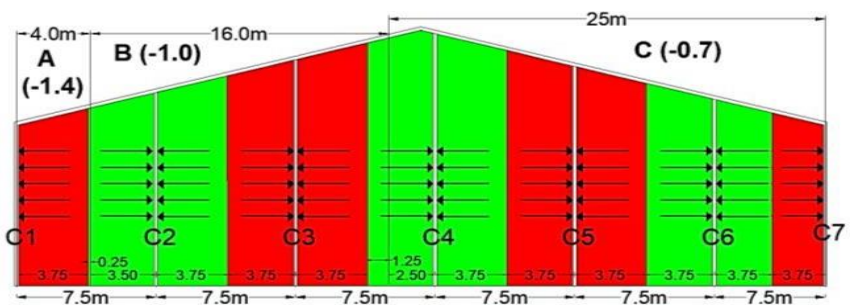

Fig. 8. Wind load distribution on the columns of the end frames

Table 2. Wind load calculation on the columns of the end frame

Column	Zone	Coefficient cp,net	Width (m) s	Wind load (kN/m) = $qp(z) \sum(cpnet \times s)$
C1	A	-1.4	3.75	-9.35
		-1.4	0.25	
C2	A + B			-13.53
		-1.0	7.25	
C3	B	-1.0	7.50	-13.35
		-1.0	1.25	
C4	B + C			-10.00
		-0.7	6.25	
C5	C	-0.7	7.50	-9.35
C6	C	-0.7	7.50	-9.35
C7	C	-0.7	3.75	-4.67

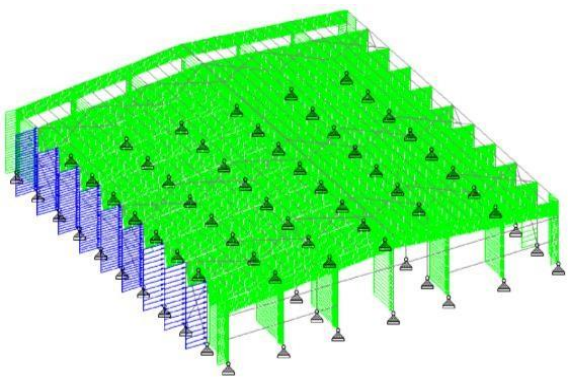

Fig. 9. Wind load assigned to the structure

2.7 Seismic Load

Seismic load is also assigned to the structure to study the behavior of the PEB structure under dynamic loading condition. The seismic load is applied to the structure by considering the time history analysis method by using the El-Centro earthquake data of time versus acceleration. The El-Centro data of time against the acceleration were fed in STAAD Pro by selecting the input file of those data while creating the seismic load parameter on the STAAD Pro. The El-Centro data provided a running time of 57 seconds for the seismic load acceleration. The time interval was set to 0.02 seconds in order to obtain the breakdown results of the deflection at every 0.02 seconds interval over the complete running time of 57 seconds. The damping parameter was taken as 0.05 and 10 cut-off mode shapes were selected. The seismic load was applied in lateral X-direction (Fig. 10) (Balamuralikrishnan & Mohammedali, 2019).

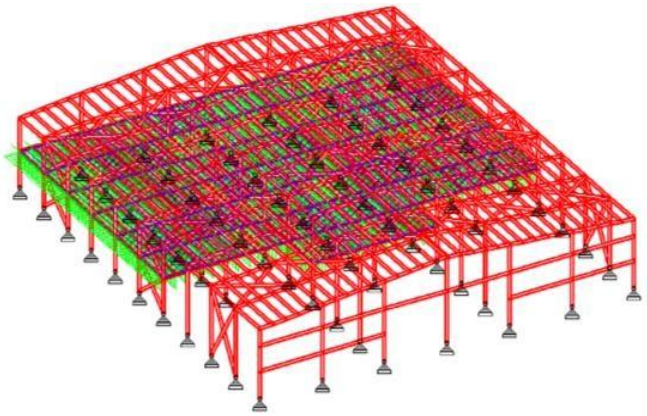

Fig. 10. Seismic load assigned to the structure

2.8 Load Combinations

After assigning the above four load cases to the structure, different load combinations were created in order to apply the safety factor for the structure. Below are the load combinations in accordance with the British standard and the Eurocode.

Load combination as per British Standard:

- 1.4 DL + 1.6 IL
- 1.4 DL ± 1.4 WL
- 1.2 DL + 1.2 IL ± 1.2 WL
- 1.4 DL ± 1.4 EQ
- 1.2 DL + 1.2 IL ± 1.2 EQ

Load combination as per Eurocode:

- 1.35 DL + 1.5 IL
- 1.0 DL ± 1.5 WL
- DL + 0.3 IL + EQ
- DL + EQ

Based on BS steel take off is presented in Table 3 (Balamuralikrishnan & Mohammedali, 2019).

Table 3. Quantity of steel taken off as calculated by STAAD Pro for BS5950

Section member	Property name	Weight (kN) ($\times 10^2$ kg)	% by weight
PEB Portal frames	Tapered	457.260	40.63
Main beams	UB 305×165×54	174.411	15.50
Secondary beams	UB 254×146×31	300.399	26.69
Columns	UC 203×203×100	74.146	6.59
Bracings (35mm tie rod)	RD 35	34.406	3.06
Z-Purlin section	200ZLML625×20	84.809	7.53
		1125.431	**100%**

Based on EC steel take off is presented in Table 4 (Balamuralikrishnan & Mohammedali, 2019)

Table 4. Quantity of steel taken off as calculated by STAAD Pro for Eurocode

Section member	Property name	Weight (kN) (× 10^2 kg)	% by weight
Portal frames rafter beams	UB 356×171×45	218.746	18.01
	UC 203×203×113	69.061	5.69
Portal frame columns			
	UC 230×203×71	259.724	21.39
Gable frame beams	UB 254×146×37	27.194	2.24
Mezzanine Main beams	UB 356×171×57	184.044	15.15
Mezzanine Secondary beams	UB 254×146×31	300.399	24.74
Mezzanine Columns	UC 230×203×71	52.778	4.35
Bracings (25 mm tie rod)	RD 25	17.560	1.45
Z-Purlin section	200ZLML625×20	84.809	6.98
		1214.315	**100%**

The total weight of the portal frames alone in the structure is equal to: Total weight of the portal frames = 218.746 + 69.061 + 259.724 + 27.194 = 574.725 kN

Percentage by weight of the portal frame = $\frac{574.725}{1214.315} \times 100 = 47.33\%$

2.9 Comparison between the Output Design Results Obtained from British Standard and Euro code

In this section, the main differences and similarities were outlined between the designed output results of the two structures. All the output results were carefully studied and interpreted for both design codes. In order to determine the most cost-effective method of designing the PEB car showroom using British standard and Euro code, we have to compare the design results of the two models and identify the structure that would be durable and economical in terms of material used. These comparisons are outlined and discussed below (Balamuralikrishnan & Mohammedali, 2019).

- British standard model (BS 5950:2000) of the car showroom structure was designed having tapered portal frame sections while the Euro code model (EN 1993-1-1: 2005) of the car showroom structure was designed with universal standard beam & column sections for the portal frames of the structure.

- The design parameters that were assigned to the structure based on British standard and Euro code are shown in Table 3 (Balamuralikrishnan & Mohammedali, 2019). The grade and yield strength of the steel were applied as S275 and 275 N/mm^2 respectively for both design codes. But the ultimate tensile strength for Euro code was selected as 500 N/mm^2 and for British code as 460 N/mm^2.
- The bracing members for the British model were changed from RD 25 to RD 35 in order to resist failure due to seismic loading, while for the Euro code model the bracing members with RD 25 properties were sufficient to withstand the seismic load, and hence they were not changed.
- The dynamic results for the maximum variation in displacement, velocity and acceleration against time of all the rafter nodes taken as an average are presented in Table 5 (Balamuralikrishnan & Mohammedali, 2019).

Table 5. Results obtained from dynamic analysis of both structures

Parameter	BS 5950:2000	EN 1993-1-1:2005
Displacement Vs time	10.5 mm	8.83 mm
Velocity Vs time	56.7 mm/sec	46.9 mm/sec
Acceleration Vs time	0.518 mm/sec ^{2}	0.472 mm/sec ^{2}

- From Table 5, it is clearly seen that all the parameter results for Euro code are lower than those for British Standard. This is mainly due to the load combinations created for the codes. But in both cases the results are within the allowable limit.
- The total weight of the structure designed based on British code is 1125.431 kN and the total weight of the structure designed based on Euro code is 1214.315 kN. The weight of the Euro code model is 7.9% higher than the British standard model.
- The total weight of all the tapered portal frames in British standard model is 457.260 kN and the total weight of all the standard section portal frames in Euro code is 574.725 kN. The amount of steel used for standard sections for all the portal frames in Euro code model is 25.7% more than the amount of steel that was used for all tapered frame sections in the British standard model.
- Therefore, this implies that using a tapered section has utilized almost 25.7% of steel which eventually reduces the cost of material and cost of construction (Balamuralikrishnan & Mohammedali, 2019).

3. CONCLUSIONS

Based on the results of analysis and design using the two design codes, the following conclusions are drawn.

- The peak wind pressure was calculated as 1.78 kN/m^2 by using a basic wind speed of 35 m/s based on BS EN 1991-1-4:2005 and seismic analysis was done by time history method using El-Centro data (time vs. acceleration).

- As per BS 5950:2000 code analysis, tapered section design was successfully carried out and EN 1993-1-1:2005 code analysis tapered section was not supported by STAAD Pro V8i software.
- The dynamic analysis results obtained for Euro code (EC) are lower than the British Standard (BS). For instance, the maximum displacement with time in X-direction for Euro code is 8.83 mm and for British standard is 10.5 mm.
- For resisting the seismic loading condition, 25 mm tie rod bracing members were sufficient for Euro code design, but for British code, 25 mm tie rod failed due to seismic loading and hence they were replaced by 35 mm tie rod bracing members.
- The total weight of the structure for BS model and EC model is 1125.431 kN and 1214.315 kN respectively. This makes EC model 7.9% heavier than BS model (Balamuralikrishnan & Mohammedali, 2019).
- The tapered frames contribute to 40.63% of the total weight in the BS model
- The average standard section frames contribute to 47.23% of the total weight in the EC model.
- The total weight of all the portal frames for BS model and EC model is 457.26 kN and 574.725 kN respectively. This makes tapered frame sections to utilize and reduce the amount of steel by 25.7%.
- All the member results such as deflection, bending moment, shear force and stresses are within the allowable limits for ultimate and serviceability limit state since the internal stresses in all the members satisfy the unity check ratio requirements for both design codes.
- The foundation of the structure was designed based on the BS model since it has proved to be an economical model as compared to the EC model in terms of the weight of the materials used (Balamuralikrishnan & Mohammedali, 2019).

DISCLAIMER (ARTIFICIAL INTELLIGENCE)

Author(s) hereby declare that NO generative AI technologies such as Large Language Models (ChatGPT, COPILOT, etc.) and text-to-image generators have been used during the writing or editing of this manuscript.

COMPETING INTERESTS

Authors have declared that no competing interests exist.

REFERENCES

Aditya P Mehendale, Gupta, A.K. “Assessment & maintenance of Pre-Engineered Building”. 1(4) (2016):31-34.

Anisha Goswami, Tushar Shende. “Pre-Engineered Building Design of an Industrial Warehouse”. International Research Journal of Engineering and Technology (IRJET) 5(6) (2018):1484-1488.

Apurv Rajendra Thorat, Santosh K. Patil. “A Study of Performance of Pre-Engineered Building of an Industrial Warehouse for Dynamic Load”.

International Research Journal of Engineering and Technology (IRJET) 4(6) (2017): 2240-2246.

Balamuralikrishnan, R., & Mohammedali, I. S. (2019). Comparative study on two storey car showroom using pre-engineered building (PEB) concept based on British standards and euro code. *Civil Engineering Journal*, *5*(4), 881-891.

BSI (2000) BS 5950. "Structural use of steelwork in building. Code of practice for design. Rolled and welded sections". British Standards. London (2000).

Dharmalingam, G., Silambarasan, G. "Design and Analysis of Pre-Engineered Building with Subjected to Seismic Loads using E-Tabs". International Journal for Scientific Research & Development 5(4) (2017):1628-1638.

Dubey, A. & Sahare, A. "Main Frame Design of Pre-Engineered Building". International Journal of Innovations in Engineering Research and Technology (IJIERT) 3 (11) (2016): 12-18.

EN 1993-1-3. "Eurocode 3. Design of Composite Steel and Composite Structures". The European Standard, United Kingdom: British Standard Institution (2005).

EN 1994-1-4. "Eurocode 4. Design of Composite Steel and Composite Structures". The European Standard, United Kingdom: British Standard Institution (2005).

EN1991-1-1. "Eurocode 1. Actions on structures. General actions. Actions on structures exposed to fire". The European Standard, United Kingdom: British Standard Institution (2002).

Firoz, S., Kumar, S. C. & Rao, S. K. 2012. "Design Concept of Pre Engineered Building". International Journal of Engineering Research and Applications (IJERA) 2 (2) (2012): 267-272.

Gawade, M. D. and Waghe, U. P. "Study of Pre-Engineered Building Concept." Journal of Research in Engineering and Applied Sciences 3, no. 6 (July, 2018): 88-91.

Katkar, D. D. & Phadtare, N. P. "Comparative Study of an Industrial Pre-Engineered Building with Conventional Steel Building". International Research Journal of Engineering and Technology (IRJET) 5 (10) (2018): 127-133. doi: 10.1016/S1361- 9209(98)00024-8.

Kiran, G. S., Rao, A. K. & Kumar, R. P. "Comparison of Design Procedures for Pre Engineered Buildings (PEB): A Case Study". International Journal of Civil, Architectural, And Structural and Construction Engineering 8 (4) (2014): 480-484.

Kolate, N. & Kewate, S. 2015. "Economizing Steel Building Using Pre Engineered Steel Sections". International Journal of Scientific & Engineering Research 6 (12) (2015): 69-74.

Lande, P. S. & Kucheriya, V. V. "Comparative Study of an Industrial Pre-Engineered Building with Conventional Steel Building". Journal of Civil Engineering and Environmental Technology 2 (10) (2015): 77-82.

Meera, C. M. "Pre-Engineered Building Design of an Industrial Warehouse". International Journal of Engineering Sciences & Emerging Technologies (IJESET) 5 (2) (2013): 75 – 82.

Mythili, T.D. "An Overview of Pre-Engineered Building Systems". International Journal of Scientific & Engineering Research 8(4) (2017):557-563.

Patil, S. S. "Analysis and Design of Pre Engineered Building of an Industrial Warehouse". International Journal of Current Engineering and Scientific Research (IJCESR) 4 (12) (2017): 39- 43.

Ravindra S. Ingole and Bharati Changhode. "Comparative Structural Analysis of Pre-engineered Building: A Review." International Journal of Advanced Research in Science, Communication and Technology (IJARSCT) 2, no. 1 (July, 2022): 841-846. doi: DOI 10.48175/568.

Sah, S. K., Kangda, M. Z., Sathe, S., & Mate, N. (2023). A state of art review on analysis and design of pre-engineered buildings. *Materials Today: Proceedings*, *77*, 704-710.

Saleem, Muhammad, and Hisham Qureshi. "Design Solutions for Sustainable Construction of Pre Engineered Steel Buildings." Sustainability 10, no. 6 (May 28, 2018): 1761. doi:10.3390/su10061761.

Stania I Patra, Melitia D'Mello. "Analysis of Pre-Engineered building and Conventional building using Primavera software". International Journal of Advanced Research in Engineering & Management (IJAREM) 3(7) (2017): 97-101.

Thorat, A. R. & Patil, S. K. "A Study of Performance of Pre-Engineered Building of an Industrial Warehouse for Dynamic Load". International Research Journal of Engineering and Technology (IRJET) 4 (6) (2017): 2240-2246.

Zende, A. A., Kulkarni, A. V., & Hutagi, A. (2013). Comparative study of analysis and design of pre-engineered-buildings and conventional frames. *IOSR Journal of Mechanical and Civil Engineering (2013)*, 2278-1684.

Disclaimer/Publisher's Note: The statements, opinions and data contained in all publications are solely those of the individual author(s) and contributor(s) and not of the publisher and/or the editor(s). This publisher and/or the editor(s) disclaim responsibility for any injury to people or property resulting from any ideas, methods, instructions or products referred to in the content.

© Copyright (2025): Author(s). The licensee is the publisher (BP International).

DISCLAIMER
This chapter is an extended version of the article published by the same author(s) in the following journal.
Civil Engineering Journal, 5(4): 881-891, 2019.
Available:https://www.civilejournal.org/index.php/cej/article/view/1327
DOI: http://dx.doi.org/10.28991/cej-2019-03091296

Peer-Review History:
This chapter was reviewed by following the Advanced Open Peer Review policy. This chapter was thoroughly checked to prevent plagiarism. As per editorial policy, a minimum of two peer-reviewers reviewed the manuscript. After review and revision of the manuscript, the Book Editor approved the manuscript for final publication. Peer review comments, comments of the editor(s), etc. are available here: https://peerreviewarchive.com/review-history/4521

Chapter 5
Print ISBN: 978-93-49473-44-7, eBook ISBN: 978-93-49473-43-0

Algorithm for Pillar Stability Assessment Based on the Interaction Principle

Mihaela TODERAȘ [a*]

DOI: https://doi.org/10.9734/bpi/erpra/v5/4534

Peer-Review History:
This chapter was reviewed by following the Advanced Open Peer Review policy. This chapter was thoroughly checked to prevent plagiarism. As per editorial policy, a minimum of two peer-reviewers reviewed the manuscript. After review and revision of the manuscript, the Book Editor approved the manuscript for final publication. Peer review comments, comments of the editor(s), etc. are available here: https://peerreviewarchive.com/review-history/4534

ABSTRACT

The room-and-pillar mining method is a prevalent technique for extracting rock salt, potash, and magnesium salt deposits. This method creates a network of rooms (excavated areas) and pillars (supporting columns), requiring careful optimization of their dimensions and the surrounding rock mass properties for each unique geological setting. Because pillars bear the highest loads, their dimensions are typically the primary focus of the design process, influencing the dimensions of the rooms and other system components. Specifically, for deep salt mining using square pillars, optimizing the system involves four key steps: (1) determining the in situ stress state (the stress field in the undisturbed rock mass); (2) analyzing the secondary stress distribution within the pillars, both qualitatively and quantitatively (how the stress changes after excavation); (3) assessing the load-bearing capacity of the pillars (how much weight they can support); and (4) determining the appropriate pillar dimensions (size and shape). Several analytical and numerical approaches can be used to address these challenges. These include: limit equilibrium methods, which consider the effective stress in the pillars; continuum mechanics, which uses analytical models to evaluate stress and deformation in pillars and floors; and numerical methods, such as finite element analysis, often validated with laboratory and field measurements. A proposed methodology, based on the principle of pillar-room-salt mass interaction, offers an analytical approach to determining the stability of deep, dry rock salt mining operations. This method calculates the secondary stress and deformation within the pillars, accounting for salt's time-dependent deformation (rheological behavior), changes in pillar geometry during extraction, and the specific extraction method employed. This analytical approach can be adapted for use in other mining applications that utilize the room-and-pillar method.

---

[a] *Mining Engineering, Surveying and Constructions Department, University of Petrosani, Petrosani, Romania.*
**Corresponding author: E-mail: toderasmihaela@yahoo.com;*

Keywords: Salt; pillars; stability; secondary stress-deformation state; interaction principle; rheological behaviour.

1. INTRODUCTION

Initially, research focused on the stability of conventional salt and potash mining, where extraction was primarily conducted using rooms and safety pillars. More recently (over the past two decades), specialists and researchers have shown considerable interest in creating underground storage cavities for petroleum products, in particular, and other substances, using solution mining techniques in salt formations. Extensive ongoing research also explores the potential of salt as a host rock for radioactive waste disposal. Several theories, summarized in Table 1, currently exist regarding the formation of salt structures. Generally, a diapiric structure is defined as a geological process where a sequence of strata originally located at greater depths within the Earth's crust intrudes into, or appears to intrude into, overlying strata at shallower depths.

A more detailed understanding of halokinetic structures has been achieved through drilling and seismic surveys, enabling structural interpretations. The development of a numerical conceptual framework has paralleled the growth of rheology and its application to salt formations, facilitated by advanced geomechanical testing in both laboratory and in situ settings. The volume of these tests increased gradually between 1960 and 1970, then accelerated due to objectives related to deep drilling (including the understanding and exploitation of deep structures, as well as nuclear testing) and the underground storage of oil, gas, compressed air, and radioactive waste in salt cavities. The oil crises of the 1970s and subsequent years have transformed underground storage of natural and industrial hydrocarbons into a strategic priority, particularly for developed nations heavily reliant on these resources (Aptukov & Volegov, 2020; Berest, 2007; Georgescu et al., 2005; Toderaș & Iosif, 2023).

At first glance, salt behavior—whether elastic or viscous—fundamentally depends on two mechanical parameters intrinsic to the salt's geomechanical properties: the elastic limit under shear (τ) and viscosity (η). The elastic limit under shear (MPa or daN/cm^2) represents a threshold stress state within the salt mass, beyond which flow begins. Viscosity (daN/cm·s) quantifies the salt's flow capacity once the elastic limit under shear is exceeded. Compared to other rock types, salt exhibits lower values for both parameters, and these values decrease significantly with increasing depth and, consequently, temperature. For instance, increasing the depth of a deposit from 300 m to 3000 m (a common range in boreholes) can result in a tenfold decrease in viscosity and a fourfold decrease in the elastic limit under shear. In essence, the key parameters governing the formation of halokinetic structures are the elastic limit under shear (τ), viscosity (η), and differential pressure (Δp).

Table 1. The main theories referring to the mechanism of salt migration

Designation' theory	Authors	Brief characterization of theory
Isostatic theory	Harbourt (1910, 1913)	Explains salt lifting on tectonically fractures lines due to its plasticity at high pressures and of specific weight smaller than this one of overlying rocks that press it.
Autoplastical tectonic theory	Lachman R. (1911)	The upward pushing of salt is the result of existing force in its own mass and consists of an upward molecular movement. The salt, due to its moisture, dissolves in the maximum pressure areas and by recrystallization, because salty water, is deposited in the areas of minimum pressure, phenomenon called „autoplastic displacement".
Redistribution' theory	Belusov (1911)	Consider that initially the salt was deposited in the higher areas, after which, through vertical movements, due to three forces, namely: primary (differential - vertical, antigravity); secondary (tangential, centrifugal) and tertiary (vertical) the salt has begun to vaulted, to be oblated and expelled under a high pressure in neighboring salt field.
Vertical compression' theory	Tagheev (1943), Harbort, Arrhenius Beischlog, Seidl	The salt should be able to move vertically under the action of the oscillatory movements of foundation, and due to the influence of fold forces.
Halotectonic halokinetic theory	Trusheim (1957, 1960)	Consider the formation of domes salt as a result of the optimal difference between the density of deposits from roof and of salt. In the context of this theory Woidt (1980), Jackson and Talbot (1989) present six mechanisms of kalokinetic
The theory of diapirism	Posepny (1871); Mrazec (1906) Barton (1925); Kusaghin (1962) Harbort (1910); Hettleton (1934) Dumitrescu (1958); Gussow, Tanher, Williams (1968); Ticleanu (1974)	Diapirism is considered to be a product of unequal action of tangential forces on a complexity of layers, namely the layers on depths were stronger puckered, while the superficial, free and uncovered ones are slightly or no touched by folding.

To understand the formation of diapiric and other halokinetic structures, it is important to note that at depths approaching 13 km, where temperatures reach at least 300°C, rock salt—a dense material at the surface—undergoes a fundamental transformation, behaving more like a liquid with a density of 1.56 x 10^4 N/m³. In this state, its reduced density and viscosity render it unstable relative to the surrounding rocks. Consequently, the salt migrates, deforms the overlying strata, and eventually pierces through them, continuing its ascent until a dynamic equilibrium is established. Salt masses exhibiting this "flow" behavior under deep, high-temperature conditions gradually lose fluidity as they ascend toward the surface and eventually become immobile upon contact with cooler surrounding rocks. This explains the diminished or arrested flow observed in some diapirs that reach the surface. However, these salt masses never achieve complete stasis; the uplift process continues over extended periods, albeit at a barely perceptible rate. This viscous-plastic flow phenomenon is driven by the action of internal and external forces that exceed the elastic limit under shear (the network forces within the salt mass), specifically when the condition is achieved:

- For diapir:

$$\Delta p > \frac{2l\tau}{R} \tag{1}$$

- For the other forms of salt deposits:

$$\Delta p > \frac{2l\tau}{g} \tag{2}$$

Therefore, the salt flow, namely the viscous – plastic displacement of salt occurs only if for a certain thickness and depth of the salt the minimum differential pressure conditions are achieved. At a high stress state or very high depths, the salt is mobilized at a thickness as small as possible. An example of this is the valley diapir anticlines from the valley areas of the Transylvanian basin. In these anticlines, the salt has been piled up by its expulsion from hilly areas with a high lithostatic stress state. The intensity of the diapir process is proportional to the ratio $\frac{\Delta p \cdot g}{l}$ (Δp is the pressure difference (stress); *g* represents the thickness of the salt bed; *l* is the distance on the horizontal).

In the central Transylvanian Basin, for example, the salt mass within the large domes failed to penetrate the overlying sediment due to the attenuation, at these depths, of the differential pressure (or differential stress state) imposed by the topography. This dual mechanical behavior—elastic at shallower depths and viscous (flowing) at greater depths—is intrinsically linked to changes in the ionic network energy of the salt crystal. Under internal and external loads at the

surface, which tend to deform the salt body, the rock salt responds with the strength conferred by its high network energy; the electrovalent bonds between chlorine and sodium ions are strong. As long as the network energy is not exceeded by the complex forces applied to the salt body, it responds elastically, and salt flow does not occur. Increasing the load beyond the strength afforded by the network energy, specifically when the elastic limit in shear is exceeded, initiates viscous (plastic) flow of the salt mass. Practically, the foregoing considerations demonstrate the significant value of borehole tomography and direct in situ measurements of physical and mechanical parameters using mechanical and/or geophysical methods. Following the same line of reasoning, one of the most effective ways to calibrate the calculation parameters used in the eventual design of future boreholes traversing deep salt formations would be to reopen some old boreholes penetrating the deep salt to measure the time-dependent variation of the initial diameter of the casing strings installed during drilling.

Regarding these situations, American research is of particular interest. This research includes underground hydrocarbon storage in cavities created by solution mining within salt massifs, as well as deep drilling into thick salt horizons for "ecological" or non-polluting nuclear experiments. Salt is considered an ideal medium for these applications due to its self-sealing properties at depth and its superior shielding capabilities against explosive radiation and radioactive waste generated from nuclear fuel after detonation. These American studies have corroborated the viscous behavior of salt at depth, providing new information and data on salt tectonics. Analyses of physical and mathematical models, correlated with repeated geophysical well logging over periods of hours, days, and weeks, have revealed time-dependent changes in the mechanical behavior of the salt surrounding the borehole, specifically within the walls of the solution-mined cavities.

2. GENERAL INFORMATION AND STATEMENT OF THE PROBLEM

Within the specific geomechanical context of salt massifs in operating salt mines, where the goals are maximizing the extraction coefficient and enabling intensive mechanization of the production process, two exploitation methods have become prevalent: the small chamber and rectangular pillar method, and the small chamber and square pillar method. While the former is generally preferred at depths up to approximately 300 m, the latter is employed globally, even at depths of 1000 m, as exemplified by the Valkenroda salt mine in Germany.

Macroscopically, the initially homogeneous structure, under the action of horizontal tectonic forces, became heterogeneous, in the sense that plastic and ruptural deformations of the initial cubic crystals occurred. Within the rock mass, the dark gray components, which determine the variegated appearance, have dimensions ranging between 5 mm and 18 mm. Brecciform fragments were distinguished, in which the angular, submillimeter to maximum 2 mm components are cemented with a saline-argillaceous-bituminous binder of gray-black color. These brecciform fragments, due to the mobility of the salt in the folding phases

under the action of horizontal tectonic forces, underwent an orientation in the direction of maximum intensity of the deforming pressures. As a result of this phenomenon, at the scale of the sample, it can be observed that the initial, massive, unoriented texture has become partially oriented. In turn, the brecciform fragments, which in most cases are elongated, are embedded in a relatively equigranular mass, composed of deformed crystals of pure halite, whose dimensions do not exceed 3 mm.

Some peculiarities of the rock salt from the Praid salt mine, identified through macroscopic analysis, are confirmed and amplified by microstereoscopic analysis. In this regard, the syntectonic transformations of the salt are well observed through the following conclusive details:

- Fibrous habitus: Due to its plasticity, approximately 40% of the initial cubic crystals have acquired a fibrous habitus.
- Orientation of fibrous components: These fibrous components are, in most cases, oriented in the direction of maximum folding pressures.
- Multiple deformation phases: It is probable, and not excluded, that after a maximum phase of diapir anticline formation, there may have been another phase of relaxation through which the fibrous crystals were oriented obliquely and less perpendicular to the aforementioned direction.
- Concordance with breccia fragments: The orientation of the fibrous crystals corresponds to the orientation of the saline-argillaceous-bituminous breccia fragments, described in the macroscopic analysis.
- Argillaceous-bituminous substance: The argillaceous-bituminous substance in the salt composition does not affect its quality in any way, since, from the microstereoscopic analysis, it is found that it is bound, in the form of a film, therefore physically, to the components of the breccia fragments.
- Microfolding: The fibrous halite crystals, in some cases, exhibit microfolds, often concordant with the macrofolds in the Praid salt mine.
- Specific formations: Due to the processes mentioned above, some figures, such as stalactites and stalagmites, pointed toe, atoll, etc., are encountered in the configuration of the analyzed samples.
- Laminated salt: The laminated salt, due to the pressure created during the formation of the diapir, reached the fibrous habitus. It presents itself as a microcrystalline salt cementing the fibrous crystals, intimately associated with the argillaceous minerals that appear in Fig. 1.a in a brownish color.
- Microgeodes: In the coarsely crystallized salt, microgeodes with an intimate mixture of finely crystallized salt and argillaceous minerals are distinguished (Fig. 1.b).
- Phenocrysts and macrocrystals: The presence of partially laminated-fibrous halite phenocrysts (Fig. 1.c), as well as partially fibrous, partially fragmented and recrystallized halite macrocrystals with microcrystalline salt (the microcrystalline salt resulted from subsequent dissolution) (Fig. 1.d), was highlighted.
- Association of microcrystalline salt and argillaceous minerals: The microcrystalline salt is intimately associated with argillaceous minerals in

the interspaces between the coarsely crystallized halite crystals (Fig. 1.e). The largely developed halite crystals appear partially laminated (fibrous), partially dissolved, having an uneven - irregular contour (Fig. 1.f).

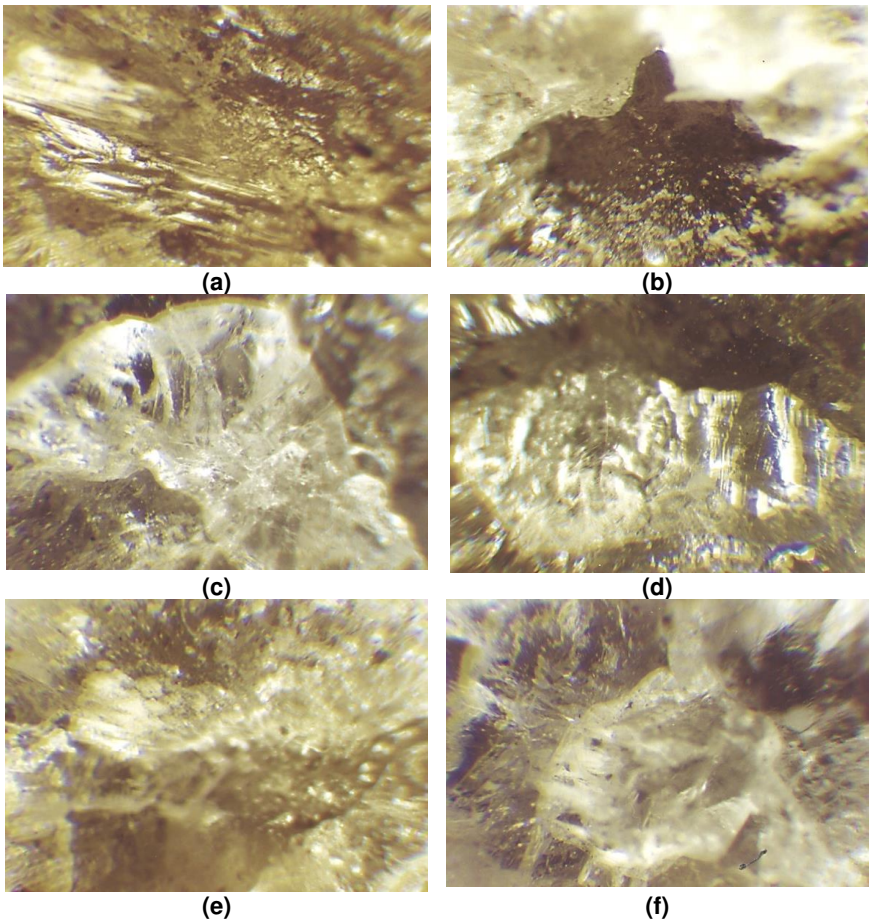

Fig. 1. Microstereoscopic analysis of the salt revealed: (a) microcrystalline cementing salt associated with argillaceous minerals; (b) intimate mixture of finely crystallized salt and argillaceous minerals; (c) partially laminated-fibrous halite phenocrysts; (d) partially fibrous halite macrocrystals; (e) microcrystalline halite intimately bound with argillaceous minerals; (f) largely developed salt crystals with an uneven contour

In conclusion, the salt structure is crystalline heterogeneous; the texture is massive unoriented, then subsequently partially oriented; the microstructure: massive - crystalline fibrous; the microtexture: oriented concordant with the

orientation of the saline-argillaceous-bituminous breccia fragments; the composition: sodium chloride, argillaceous minerals, and bituminous substances; the genetic type: sedimentary rock of chemical precipitation; from a qualitative point of view, it is a good salt. In the massif, the Praid-type salt appears in ribboned form (Fig. 2).

Fig. 2. Salt banding at the +50 m level

At the Praid Salt Mine, the rectangular pillars are 12 m high, corresponding to the +286 m, +266 m, and +246 m horizons. The layout grid of the chambers and pillars has 30 m sides. The chamber width varies between 14 m and 16 m. In multi-level exploitation areas, the pillar side varies between 14 m and 17 m, with dimensions determined by calculations based on limit equilibrium theory. The inter-horizon slab thickness is 8 m. Extraction coefficients range from 30% to 40%. It is important to note that near the surface, voids exist due to previous mining activities (Toderaș & Iosif, 2023). These voids, resulting from salt extraction, have altered the pre-existing natural stress state within the massif. Their cross-sections decrease over time due to deformation of the support elements (roof, floor, and pillars), a phenomenon confirmed by long-term (decades) in situ observations. Visual observations and measurements have revealed the instability of the chamber-pillar system. Deformation and instability manifest as fissures and cracks (up to 10 cm or more in width and of significant length), inter-chamber cracks, large detachments of fragments (from pillar corners and sides), and even roof falls, occasional floor heave, and floor bending with increasing deformation rates (Fig. 3). Most of these phenomena (fissures,

cracks, and exfoliation) occur at the pillar corners and floor-pillar junctions due to stress concentrations. Some fissures appear and propagate after blasting. Fissure opening generally occurs in a stepwise or uniform manner, as confirmed by observations of installed monitoring devices. These phenomena also result from the time-dependent deformation of the pillars (Toderaș & Iosif, 2023).

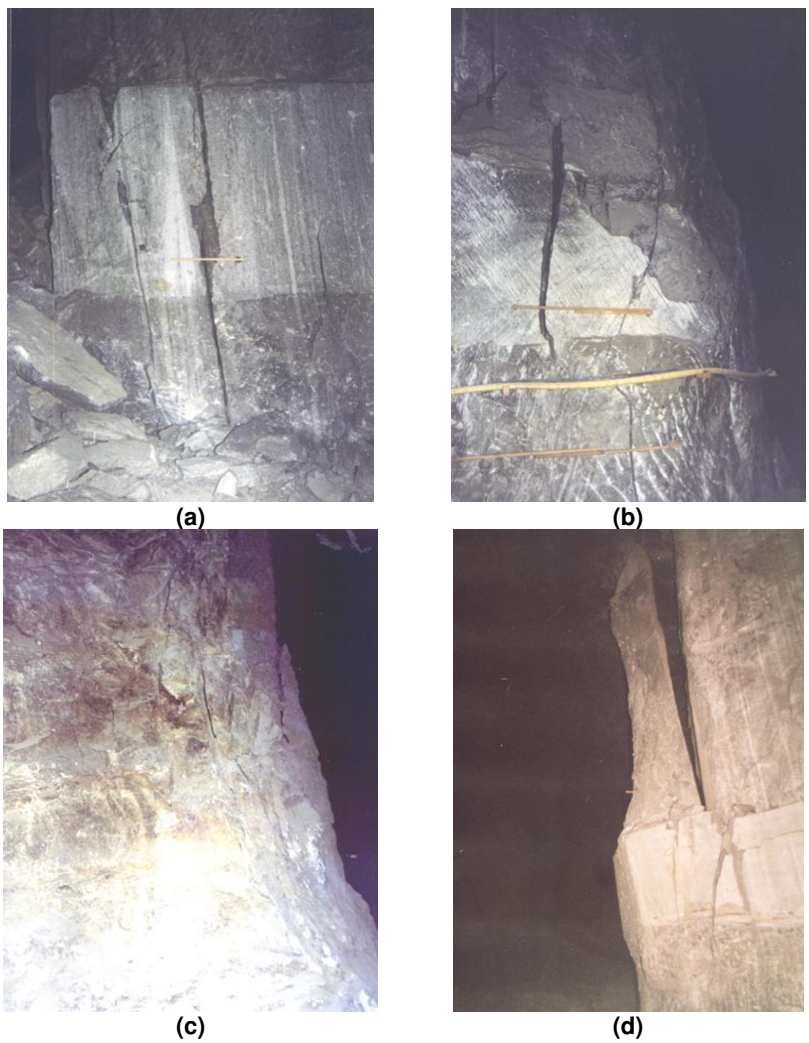

Fig. 3. Instability phenomena observed underground at the Praid Salt Mine: (a) cracking of a rectangular pillar corner; (b) cracking of a marginal pillar; (c) pillar exfoliation; (d) rounding of a rectangular pillar corner along the stratification plane

Unexploited zones between field pillars induce shear phenomena and uneven pillar settlement, leading to significant stress variations within the mining areas. These time-dependent phenomena contribute to the overall instability of the multi-level room-and-pillar system, including the first level of the Telegdy mining area at the Praid salt mine. The time-dependent evolution of instability phenomena, coupled with increasing deformation and settlement rates, will eventually result in the rupture or shearing of floor slabs and the destruction of pillars.

The correct dimensioning of rooms and pillars (including safety pillars) is of paramount importance, not only for exploitation safety and the stability of the entire underground structure, including the protection and rational exploitation of the deposit, but especially for the stability and protection of the surface, requiring measures to prevent surface ground movements (Georgescu et al., 2005; Toderaș & Iosif, 2023; Toderas & Danciu, 2017). Ensuring the long-term stability of underground voids created by salt extraction necessitates complex studies to accurately understand the geomechanical characteristics (Aptukov & Volegov, 2020; Aubertin et al., 1999), the micro- and macro-scale behavior of the salt and surrounding rocks (Belohlavek & Behr, 1999; Konstantinova & Aptukov, 2013; Qingfa et al., 2020). Of particular importance is the study of dilatancy and, especially, the incorporation of the time factor to establish the rheological characteristics and parameters (Toderaș & Iosif, 2023), which allow for assessing the long-term stability of underground structures during and after the exploitation period (Popp et al., 2002; Spiers, 1989; Stamatiu, 1962; Thorel & Ghoreychi, 1993). Given that salt deposit exploitation currently occurs primarily at depth, often with considerable thicknesses, salt extraction is conducted across multiple levels with a coaxial arrangement of rooms, ensuring that the pillars between them are vertically aligned, allowing lithostatic pressure and stresses to be transmitted coaxially (Toderas, 2022; Todorescu & Toderaş, 1996). In the horizontal plane, pillars (protection pillars) are left between rooms. Vertically, floors are necessary, both to define the room height and, crucially, to enhance safety during exploitation and pillar stability. The thickness of a floor between two rooms is determined by the extraction method: ascending (rarely used) or descending (common practice). Pillars bear the static loads imposed by the weight of the deposits themselves and the overlying rocks, preventing them from collapsing into the mined voids and preventing displacements that would cause surface settlements and subsidence. Therefore, proper pillar sizing is crucial. Determining optimal dimensions is a complex problem that involves considering several factors, including: the geological and petrographic characterization of the salt; its mode of formation; the micro- and macro-scale characteristics of the salt; the presence of fluid inclusions and pores; the physical and mechanical characteristics of the rock salt; its deformation behavior and dilatancy; and, importantly, the time factor through rheological characteristics, which play a crucial role in assessing the long-term stability of the underground structure (Georgescu et al., 2005; Minkley & Menzel, 1996; Singh et al., 2018; Yahya et al., 2000).

Regarding safety and stability, safety pillars must meet both strength and deformation requirements. Given the elastic and plastic deformation limits of rock salt (the pillar material), determined through laboratory testing, pillar integrity can be assessed by periodically measuring deformations or through analytical calculations based on various established hypotheses. If measured deformations remain within the elastic or small plastic deformation limits, the pillars are considered sufficiently safe and stable (Toderaș & Iosif, 2023; Toderas & Danciu, 2017). Conversely, there is a risk of fissures, fractures, or cracks developing, potentially leading to partial or total pillar collapse. For Romanian rock salt, laboratory tests have established the elastic and plastic deformation limits at 10 MPa (Stamatiu, 1962; Todorescu & Toderaş, 1996), with a mean value of 2.5 MPa. If the salt within a pillar is in the plastic deformation regime, the time factor, as previously mentioned, becomes crucial, as it drives deformation development even under constant external loads. This leads to the creep phenomenon in rock salt (McClain & Bradshaw, 1967; Wagner & Blaha, 2015; Majeed et al., 2023; Feng et al., 2020; Qin et al., 2020), which the author has been investigating in the laboratory since 1992. These studies, conducted on various salt types, have shown that samples loaded beyond the elastic limit (Toderaș & Iosif, 2023; Toderas & Danciu, 2017) and into the plastic deformation regime exhibit time-dependent deformation increases (Toderas, 2022; Todorescu & Toderaş, 1996; Toderas, 2020). This deformation variation is often accompanied by salt dilatancy. Laboratory test data on Romanian rock salt have demonstrated its dilatant behavior under load (Fig. 4).

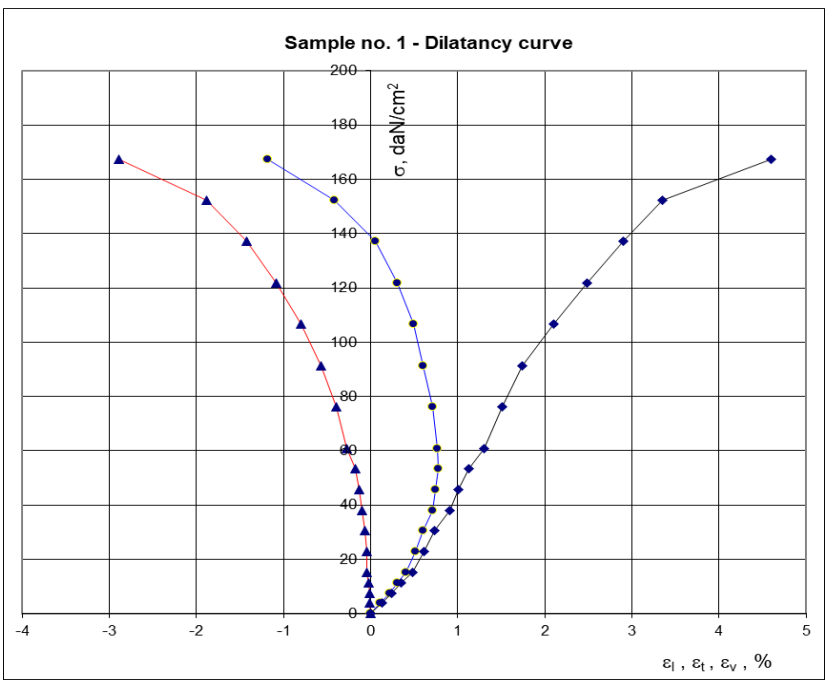

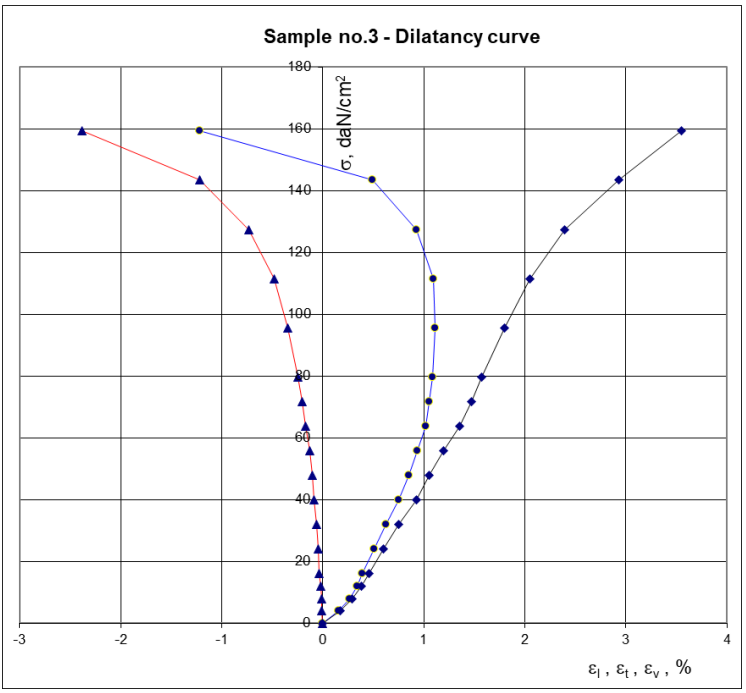
Sample no.3 - Dilatancy curve
σ, daN/cm²
180
160
140
120
100
80
60
40
20
0
-3
-2
-1
0
1
2
3
4
εl , εt , εv , %

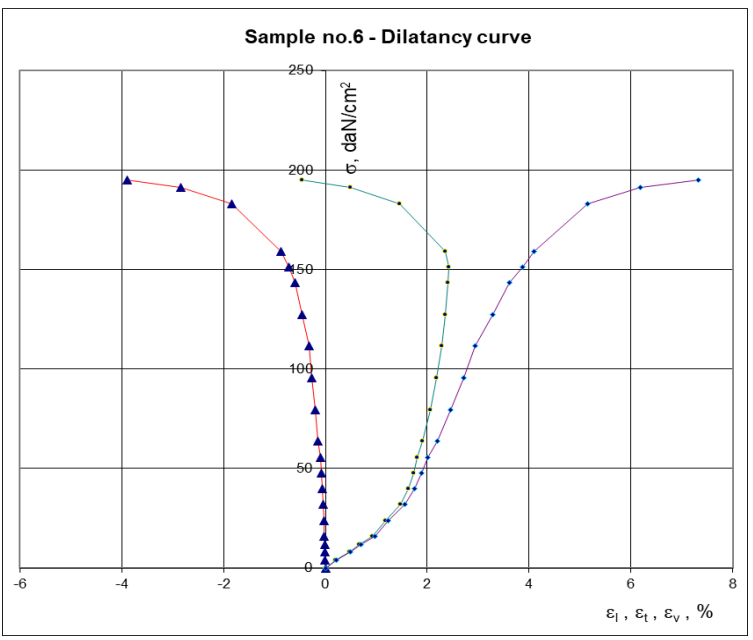
Sample no.6 - Dilatancy curve
σ, daN/cm²
250
200
150
100
50
0
-6
-4
-2
0
2
4
6
8
εl , εt , εv , %

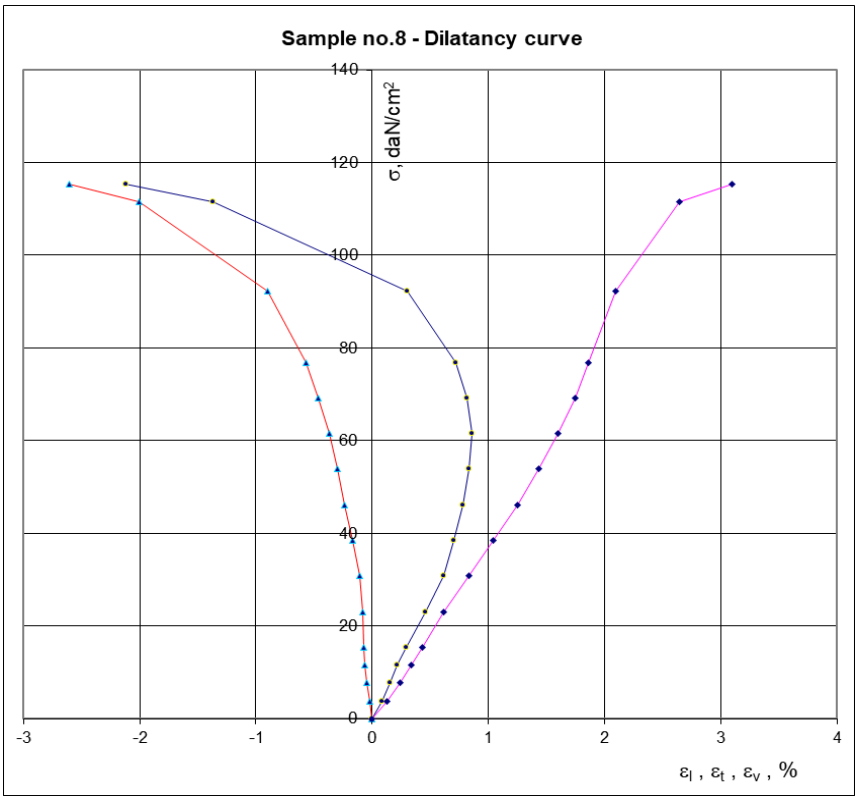

Fig. 4. Dilatancy curves for the rock salt from Praid (according to Toderaş, 2005)

Penkova's studies also noted this dilatant character of salt, concluding that during rapid triaxial tests on rock salt, transverse deformations can exceed axial deformations, indicating a pronounced dilatancy phenomenon. Stavrogin (1967), as presented by Todorescu in (1982), described the same dilatancy in rock salt. Stavrogin showed that prismatic specimens (15×15×30 cm) under a load of $0.7\sigma_{rc}$ (where σ_{rc} is the uniaxial compressive breaking strength) exhibited a 17% volume increase over 800 × 24 hours. Studies have indicated that for Romanian rock salt, the maximum depth for safe room-and-pillar exploitation is 1,000 m. Beyond this depth, the risks and technical and safety challenges increase significantly, making solution mining with the creation of caverns, from which brine is then extracted to the surface, the recommended approach (Toderaș & Iosif, 2023).

3. INTERACTION PRINCIPLE IN THE ASSESSMENT OF PILLARS' SECONDARY STRESS – DEFORMATION STATE

Because the rooms and pillars method form a unique spatial system of dry exploitation of salt, from the point of view of stability and reliability, it is obvious that an effective correlation between the geometrical parameters of its system and the surrounding massif is required (Aptukov & Volegov, 2020; Georgescu et al., 2005; Toderaș & Iosif, 2023). Generally, for each given situation (level, salt mine), the dimensioning of the most requested element in the system is looked at, and depending on its geometric elements, the other parameters of the system are established (McClain & Bradshaw, 1967; Wagner & Blaha, 2015; Majeed et al., 2023; Toderas, 2020; Todorescu, 1982; Balthasar & Haupt, 1987). Currently, the analytical way to assess the stability and reliability of the exploitation system of salt by means of a dry method is limited to the use of calculation methods based on the "limit equilibrium theory". These methods, precisely because of the principle on which they are based, present a number of disadvantages, among which we recall: leading to an enlargement of the pillars and floors of a salt mine's first horizon; limiting the depth of exploitation by excessively increasing the size of pillars to the detriment of the rooms, resulting in a significant reduction in the salt extraction coefficient; failing to account for salt behaviour variations in correlation with the increase of exploitation depth and stresses in pillars; all computing relationships do not take into account the implications of the loading time, namely the rheological behaviour of salt (the long existence of salt and the changes that occur in the strength characteristics during the salt exploitation period) etc. (Toderaș & Iosif, 2023). In relation to the formulated underlines, it is believed that pillar dimensioning is a susceptible problem that requires corrections, improvements, and even the development of new and more efficient methods to facilitate the safe expansion of exploitation salt in depth. By virtue of the role of the pillars as elements of the rock salt exploitation method, they can be assimilated as a natural support system. As the pillars have a role as elements of the salt exploitation method, they can be assimilated as a natural support system. However, such a support system must be studied in the context of two conditions: 1) the amount of useful mineral substance (rock salt) stored in the pillar is minimum (obtaining a maximum coefficient of extraction); and 2) to assume and accomplish the role of ensuring the overall stability of a room, level, and implicitly of a salt mine. We believe that such an objective can be achieved on the basis of the principle of the interaction mechanism, that is, the communion of rock deformations around an underground excavation and the mounted support system. The evaluation of such a compound effect can be done by superimposing the rock deformation curve and the support system curve (Fig. 5) (Toderaș & Iosif, 2023).

The point of intersection of the two characteristic curves simultaneously expresses the magnitude of the loads and support deformation that characterize the stability state of the rock-support system (Toderaș & Iosif, 2023; Toderas & Danciu, 2017; Thorel & Ghoreychi, 1993). Such a principle, which has been used successfully in the design of underground artificial supports (wood, metal, concrete, etc.) (Toderas, 2020; Seryakov, 2020; Todorescu & Gaiducov, 1996–

2001), can also be applied in the case of natural supports and also for the situation of salt exploitation by rooms and pillars. The possibility of its application is also facilitated by the advantages that numerical analysis methods provide today. As a result, the method that we proposed consists of establishing: 1) the relaxation curve of salt, namely the deformation behaviour of salt on the contour of excavation (room–floor) following the load that acts on the exploitation system; and 2) the relaxation curve developed by the pillar, with the role of natural support as a result of the loads acting on the pillar. The analytical and graphical intersection of the equations of the two curves leads us to the equilibrium condition of the exploitation system. The proposed method was applied to the Praid Salt Mine (Romania), where, in fact, both observations and in situ measurements of the secondary stress and deformation state in square-shaped pillars, as well as experimental research in the laboratory by modelling (Toderas, 2022; Todorescu & Toderaş, 1996; Toderas, 2020), were realized. It was considered that the part of salt to be left in the pillar (Fig. 6) (Toderaș & Iosif, 2023) is subjected to a stress state even before the pillar is contoured, namely the natural stress state, which is well defined by its normal components σ_z, σ_y, and σ_x, which, in the context of elastic deformation behaviour, are determined by the known relationships:

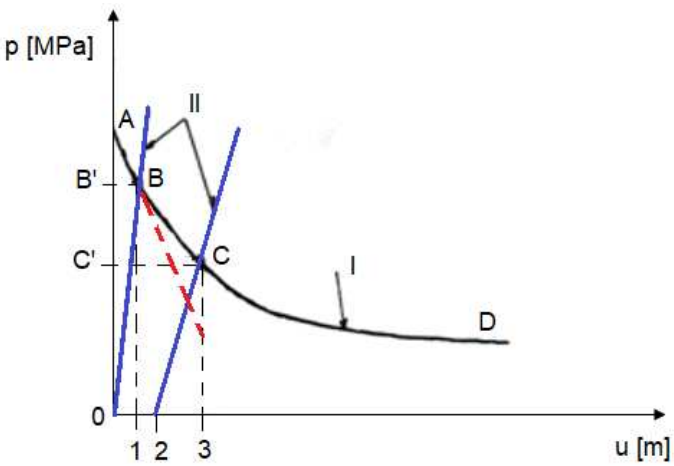

Fig. 5. Principle of the interaction mechanism: I – relaxation curve; II – supports reaction curves (p – load on the support; u – displacement; AB – domain of elastic behaviour; BD – domain of inelastic behaviour; $\bar{01}$ - elastic displacement; $\bar{02}$ - rock displacement until the support is setting; $\bar{23}$ - common displacement of rock and support; B – equilibrium point of the system in the elastic domain; C – the equilibrium point of the system in the inelastic domain; B' şi C' - pressure values on the support (natural and artificial respectively)

$$\sigma_z = \gamma_a H$$
$$\sigma_x = \sigma_y = \frac{\mu}{1-\mu}\sigma_z = \xi_o \sigma_z \tag{3}$$

Where: γ_a - the apparent specific weight of salt; μ - Poisson's coefficient; ξ_0 – the active pressure coefficient given by Poisson's coefficient:

$$\xi_o = \frac{\mu}{1-\mu} \tag{4}$$

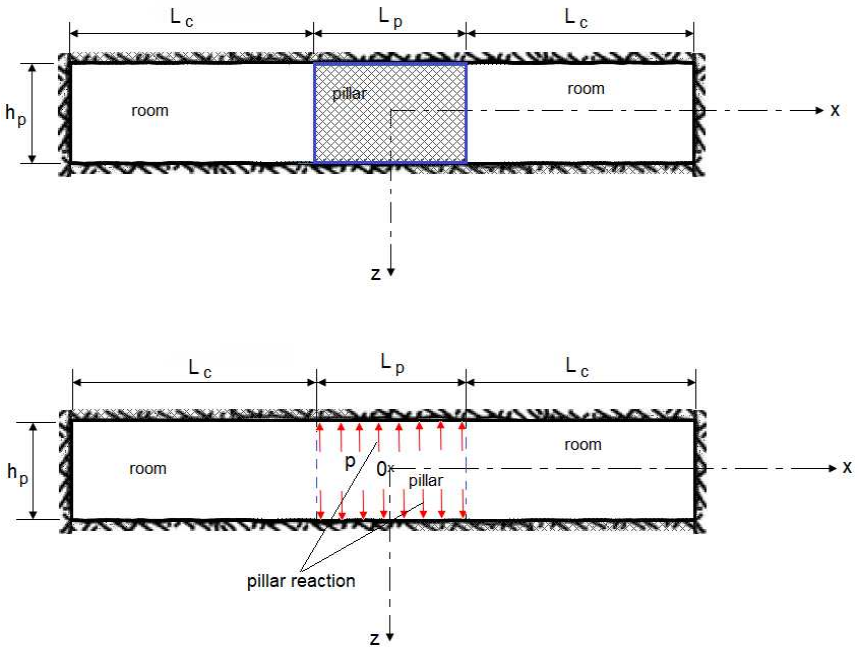

Fig. 6. Cross-section through the small-rooms and square pillars exploitation system (L_c – the width of the room; L_p – the width of the pillar; h_p – the height of the pillar)

Once the beginning of pillar contouring occurs, stress concentrations occur (Seryakov, 2020) and lead to the occurrence of the secondary stress state materialized in the salt part of the pillar through the normal components: σ_z^S ; σ_y^S and σ_x^S . Such a secondary stress state, through its components, undergoes changes with the beginning of the pillar contour in the sense that the lateral

stresses σ_x^S and σ_y^S decrease and tend to zero; at the same time, the vertical respectively axial components increase, precisely because of the support function that the pillar begins to develop. These two sources of change in the equilibrium of the exploitation system (the natural state and the secondary stress state) act simultaneously in the way we have shown.

The principle of interaction was used to evaluate the stability of the proposed room-pillar system, respecting the following conditions: the coordinate system is the one shown in Fig. 2; the pillar has a role of support; the axis of the pillar is parallel to one of the main normal components of the natural stress state, namely at σ_z; the axial load of the pillar generates a uniform distribution of the axial stress (a fact confirmed by the in situ measurements (Toderaș & Iosif, 2023; Toderas & Danciu, 2017; Toderas, 2022; Toderas, 2020)); the maximum load gives the main axial component of the secondary stress state σ_z^S . Once the pillar is realised, the normal components of the secondary stress state in the z, y, and x directions change according to the relations:

$$\Delta\sigma_z^S = \sigma_z - \sigma_z^S \tag{5}$$

$$\Delta\sigma_y^S = \sigma_y - \sigma_y^S \tag{6}$$

$$\Delta\sigma_x^S = \sigma_x - \sigma_x^S \tag{7}$$

At the end of the achievement of the pillar, the secondary stress state becomes:

$$\sigma_z^S \neq 0 \quad and \quad \sigma_y^S = \sigma_x^S = 0 \tag{8}$$

In the context of plane deformation conditions, according to (Seryakov, 2020), it can be written that:

$$\Delta\sigma_z^S = \mu\left[\Delta\sigma_x^S + \Delta\sigma_y^S\right] \tag{9}$$

When we combine the relationships (5), (8), and (9), we get:

$$\Delta\sigma_z^S = \mu\left[\sigma_x - \Delta\sigma_y^S\right] \tag{10}$$

The axial load of a pillar is a consequence of its axial deformation. For a zero deformation of the pillar (namely, before any deformation occurs, at t = 0), in the conditions of a linear, homogeneous, and isotropic elastic medium, it follows that (Toderaș & Iosif, 2023):

$$\varepsilon_z^S = \varepsilon_z \tag{11}$$

Where: ε_z and ε_z^S are the normal components of deformation in the z direction due to the natural stress state (namely, the state of stress existing before the pillar execution) and the secondary stress state after the achievement of the pillar but before any deformation occurs:

$$\varepsilon_z = \frac{1}{E}\left[\sigma_z - \mu\left(\sigma_x + \sigma_y\right)\right] \tag{12}$$

$$\varepsilon_z^S = \frac{1}{E}\left[\sigma_z^S - \left(\sigma_x^S + \sigma_y^S\right)\right] \tag{13}$$

According to the expressions (12), (13) and the relations (7) – (10), the condition (11) becomes:

$$\sigma_z^S = \sigma_z - \Delta\sigma_z^S \tag{14}$$

Considering the fact that:

$$\Delta\sigma_z^S = \frac{\mu}{1-\mu}\sigma_x \tag{15}$$

Finally, the expression of the preloading normal component of the secondary stress state after the axial direction of the pillar results in being:

$$\sigma_z^S = \sigma_z - \frac{\mu}{1-\mu}\sigma_x \tag{16}$$

Which, as will be shown below, is a constant term in the equation of the characteristic reaction curve developed by the pillar as a natural support (Toderaș & Iosif, 2023).

In order to establish the salt relaxation curve, the cross-section was considered for a pillar located between the two rooms, as presented in Fig. 2. Geometrically, the situation taken into study was characterised as: small rooms and square pillars exploitation system, with the width of the rooms L_c = 16 m, the width of the pillar L_p = 14 m, and the height of the pillar h_p = 8 m. However, it was considered, as we have in fact mentioned, that the conditions of plane deformation and the salt from the pillar and around the pillar are characterised by the following values of the geomechanical properties involved in the computations: the apparent specific weight of the salt γ_a = 2.1 × 104 N/m^3; the elasticity modulus E = 950

MPa; and the coefficient of Poisson's μ = 0.26. To obtain the relaxation curves for different depths (from 100 m to 1,000 m), it was necessary to determine the secondary stress state and the secondary displacement state that affect the pillars until failure. These were obtained by an analytical method using the finite element method (Toderaș & Iosif, 2023; Toderas & Danciu, 2017; Todorescu & Toderaş, 1996), and the values obtained for a depth equal to 100 m at Praid Salt Mine (Romania) have been verified by the obtained data from the measurements. The ranges of variation of the axial component of the secondary stress state and the corresponding displacements obtained for different depth ranges are shown in Table 2.

Table 2. Values of axial load and displacements

Depth range H, m	Value of axial component of secondary stress state that acts on the pillar, MPa	Displacements v, cm
0 - 200	1.64	0.945
	0.795	0.713
	0.375	0.489
200 - 400	8.4	4.25
	6.16	2.62
	3.54	1.28
400 - 600	12.6	26.82
	11.5	1.8456
	9.45	0.7325
600 - 800	16.8	9.0012
	14.9	1.897
	13.65	1.275
800 - 1000	21.00	16.25
	19.4	3.0016
	17.85	1.655

Noting: σ_{zp}^{S} ; σ_{yp}^{S} and σ_{xp}^{S} the main normal components of the secondary stress state after the pillar begins to be loaded, then:

$$\Delta\sigma_{zp}^{S} = \sigma_{z}^{S} - \sigma_{zp}^{S} \tag{17}$$

$$\Delta\sigma_{yp}^{S} = \sigma_{y}^{S} - \sigma_{yp}^{S} \tag{18}$$

$$\Delta\sigma_{xp}^{S} = \sigma_{x}^{S} - \sigma_{xp}^{S} \tag{19}$$

Where: $\Delta\sigma_{zp}^{S}$; $\Delta\sigma_{yp}^{S}$ and $\Delta\sigma_{xp}^{S}$ are the increases of the main components of the stress state resulting from the axial load of the pillar.

While maintaining the same boundary conditions as in equations (6) and (17), the shortening *v* of the pillar at its half height (at h/2) due only to the axial stress is:

$$v = \frac{\Delta\varepsilon_{zp}^{S} h}{2} \tag{20}$$

Where: $\Delta\varepsilon_{zp}^{S}$ is the change of the axial deformation in the pillar due to the action of the axial load and which, based on the boundary conditions, has the value:

$$\Delta\varepsilon_{zp}^{S} = \frac{1-\mu^2}{E}\Delta\sigma_{zp}^{S} \tag{21}$$

Where E is the elasticity modulus of salt from pillar.

Based on the relationships (18) and (19), the following expression was obtained:

$$\Delta\sigma_{zp}^{S} = \frac{2Ev}{h\left(1-\mu^2\right)} \tag{22}$$

Substituting the equations (16) and (22) in (17), the axial component of the stress state in the pillar was obtained:

$$\sigma_{zp}^{p} = \sigma_z - \frac{\mu}{1-\mu}\sigma_x - \frac{2Ev}{h\left(1-\mu^2\right)} \tag{23.a}$$

Or:

$$\sigma_{zp}^{S} = \left(1-\xi^2\right)\sigma_z - \frac{2Ev}{h\left(1-\mu^2\right)} \tag{23.b}$$

Actually, this equation represents the reaction curve developed by the pillar, considered to have the role of natural support.

4. RESULTS AND DISCUSSION

Table 3 shows the reaction equations developed by pillars at various depths in the Praid salt mine situation. In Fig. 7, the intersection of these curves is shown graphically.

The intersection of the two types of curves (salt relaxation and reaction developed by the pillar) led me to obtain the axial stress value in the pillar and

offered the possibility to assess its stability and exploitation system stability too (Toderaș & Iosif, 2023). The stability of the pillar is conditioned by the value of the deformation obvious on the abscissa and the value of the load to which it is exposed, a value that is represented on the ordinate (Toderas & Danciu, 2017; Toderas, 2022; Todorescu & Toderaş, 1996; Yahya et al., 2000). From the analysis of the obtained data, it is found that, with the increase in depth, the stability conditions of the exploitation system change; these changes are made by the coordinates of the intersection points of the pairs of curves (Toderaș & Iosif, 2023).

Table 3. Salt relaxation and pillar reaction equations

Depth range, H, m	Equations of salt relaxation curves	Equations of pillar reaction curves
0 - 200	σ = -1.7458 v + 4.06395	$\sigma_{zp}^{S} = 43.932v - 4 \times 10^{-16}$
200 - 400	σ = -1.9799 v + 8.559	$\sigma_{zp}^{S} = 30.778v + 10^{-15}$
400 - 600	σ = -1.8666 v + 12.773	$\sigma_{zp}^{S} = 30.166v$
600 - 800	σ = -1.8928 v + 17.098	$\sigma_{zp}^{S} = 26.098v$
800 - 1000	σ = -1.3136 v + 21.428	$\sigma_{zp}^{S} = 38.11v$

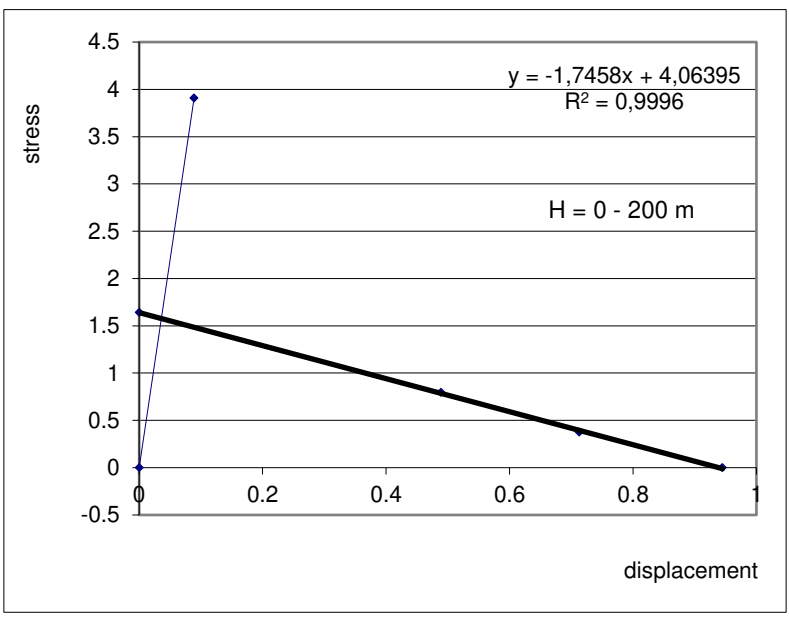

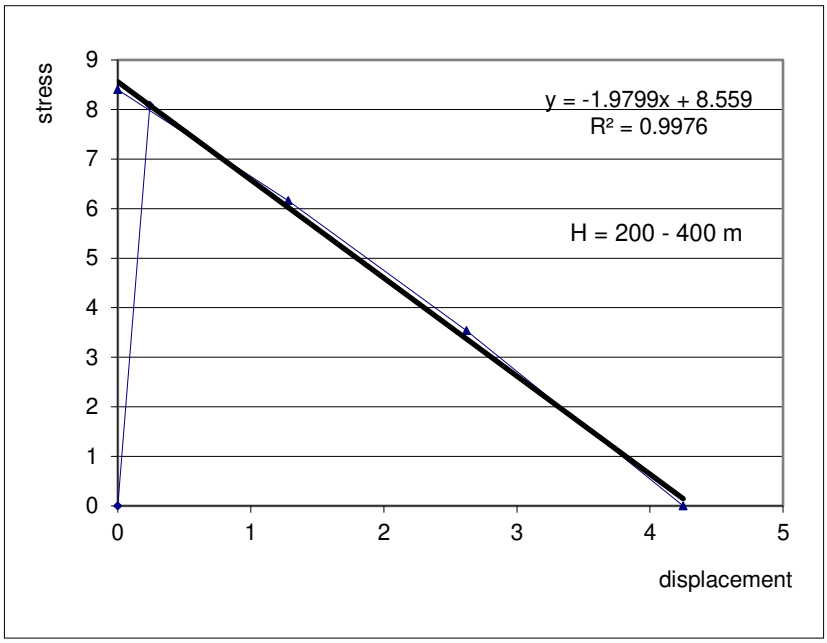
stress
displacement
y = -1.9799x + 8.559
R² = 0.9976
H = 200 - 400 m
0
1
2
3
4
5
6
7
8
9

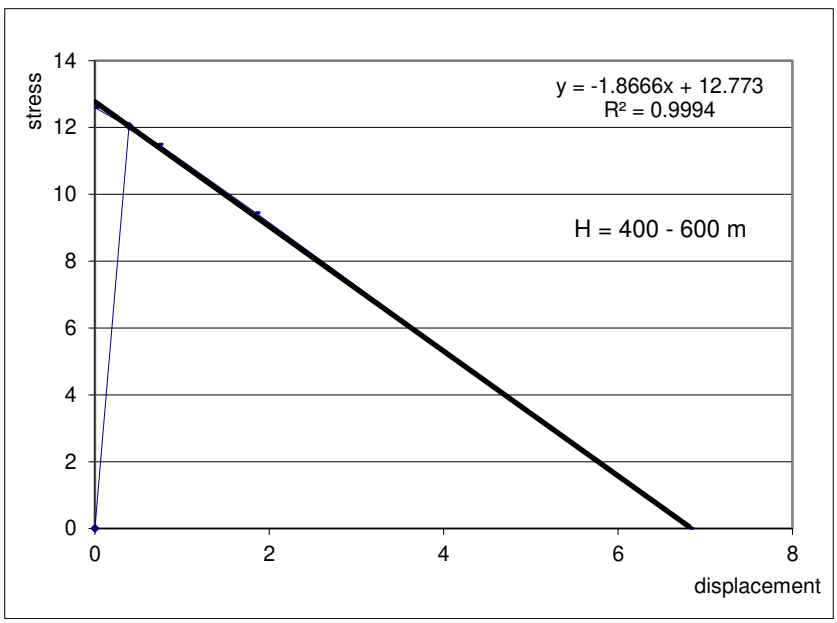
stress
displacement
y = -1.8666x + 12.773
R² = 0.9994
H = 400 - 600 m
0
2
4
6
8
10
12
14

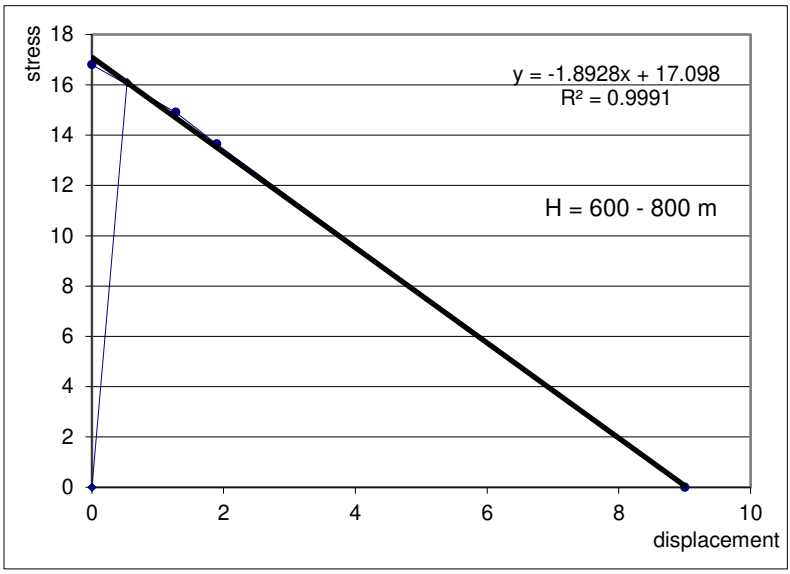

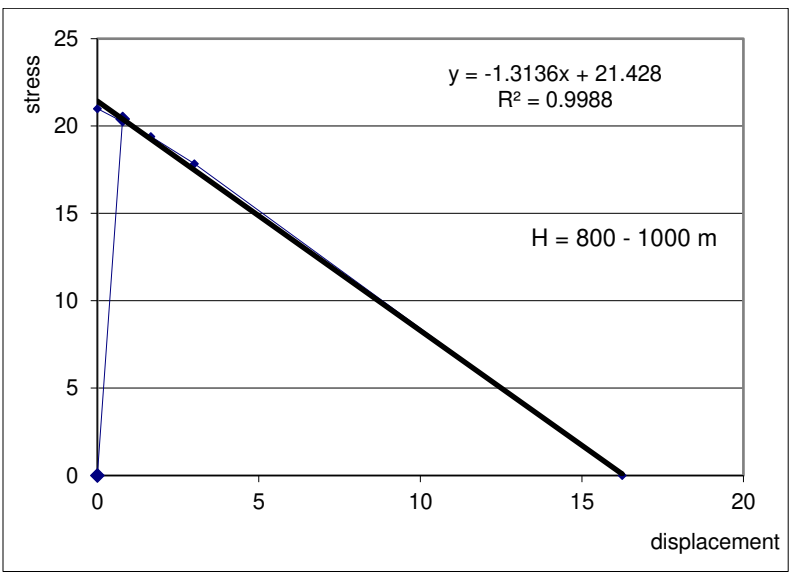

Fig. 7. Intersection of relaxation curve and reaction curve of pillar: for H from 200 m to 400 m ÷ 800 m to 1000 m

Analysing the degree of stress on the pillar, it was found that the stress threshold of 0.3 is exceeded at a depth of 600 m. As a result, it was considered necessary

to analyse the interval of 600-1000 m in the context of the increase in the height of the pillar to highlight whether in this area the pillars with dimensions of L_p = 14 m and h_p = 8 m, respectively, and h_p = 10 m and L_c = 16 m are stable or not. As a result, for the depth intervals specified in Table 2, the situation where the height of the pillars increased from 8 m to 10 m was also analysed.

The question of heterogeneity that confers a difference in pillar load can be approached in the manner of the presented method. Interesting conclusions lead us to the graphical analysis, which means that in the case of rock salt, as in the case of rock with pronounced plastic behaviour, the characteristic curve of salt deformation approaches the shape and value of a line (Toderaș & Iosif, 2023). To a known extent, the interaction has opened and continues to maintain consciousness and clear the assessment possibility of directing the factors that determine the interaction phenomenon. The correlation of the same equations presented in Table 2 shows that the degree of pillar load, corresponding to the load threshold of 0.3 admitted by the rheological research (Toderas & Danciu, 2017; Todorescu & Toderaş, 1996; Todorescu, 1986), is exceeded starting with the depth of 600 m. For exploitation in depths below 600 m, we consider that changes to the dimensions of the exploitation system are necessary, namely: in the range of 600 m to 800 m, the dimensions of the pillars should be L_p = 14.5 m and h_p = 8 m, and in the range of 800 m to 1,000 m depth, the dimensions should be L_p = 15 m, L_c = 15 m, and h_p = 8 m.

The use of this method based on the principle of interaction can be performed by means of an algorithm that can be expanded not only for any situation (Fig. 8) encountered in the Romanian salt mines but also for the ore exploitation situations where the exploitation method with rooms and pillars is applied (Toderaș & Iosif, 2023). The findings and their implications should be discussed in the broadest possible context. Future research directions may also be highlighted.

The exploitation technology that is applied has an influence on the stability and, therefore, implicitly, on the secondary stress-deformation state of the elements of the room-and-pillar exploitation system (Jianhua & Kuangdi, 2023; Toderas, 2024). The technology used is the classic one: using the explosives' dislocation energy, which affects the bearing capacity of the pillars and floors by inducing, following the blasting of an artificial microcrack zone in these elements, the amplification of pre-existing natural microcracks at a depth of about 0.5 m at the pillars and 0.9 m at the floors. With the current exploitation technology, it is possible to go to a depth of 600 m, in which case the load on the pillars σ_{ef} would be about 30 MPa, the load degree Δ = 0.31, and the extraction coefficient C_e = 26 %. However, by changing the shape of the pillars (the special type shape with a rounded contact between the pillar and the floor) and applying a cutting technology with a drilling machine with a point attack or some saws with a long arm of about 4.5 m and cutting possibilities in the vertical plane, namely, a non-destructive technology that allows the creation of vaulted chambers or with rounded corners, over 800 m. For exploitation depths between 200 and 600 m, the variation of the effective loads (of the components of the secondary stress

state) that return as a load confirms what was stated previously that the pillars will maintain their stability (Toderaș & Iosif, 2023; Zhou et al., 2021; Pan et al., 2022).

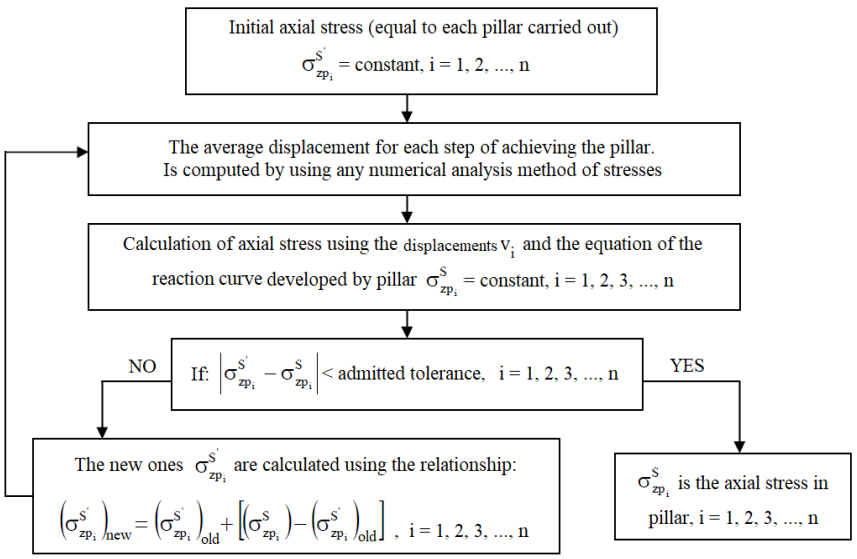

Fig. 8. The proposed computing algorithm

Along with the increase in the exploitation depth, the degree of stress on the room-pillar exploitation system also increases, and at the same time, the deformation process intensifies. The average strain rate increases, the breaking strain value decreases, and the stability time decreases. A modification of the extraction technology is also required in order to improve even more significantly the stability conditions of the chamber-pillar system below the depth of 600 m and above 800 m.

In the calculations of salt massif stability (Jianhua & Kuangdi, 2023; Toderas, 2024), its essential features must be evaluated, namely the rheological properties, its nonlinear character of behaviour σ - ε and the dilatancy phenomenon under the action of shear stress. In the case where the state equation (namely, the behaviour equation) doesn't describe the three stages of creep, then to be able to resolve the stability problem, first the stress–deformation state must be established, and then the long-term strength condition is imposed. As a long-term strength condition, the criterion that satisfactorily characterises the strength of salt under an instantaneous load can be (Zhou et al., 2021; Pan et al., 2022). In the condition of the salt's strength, the long-term strength value will be introduced instead of the instantaneous characteristics (t = 0).

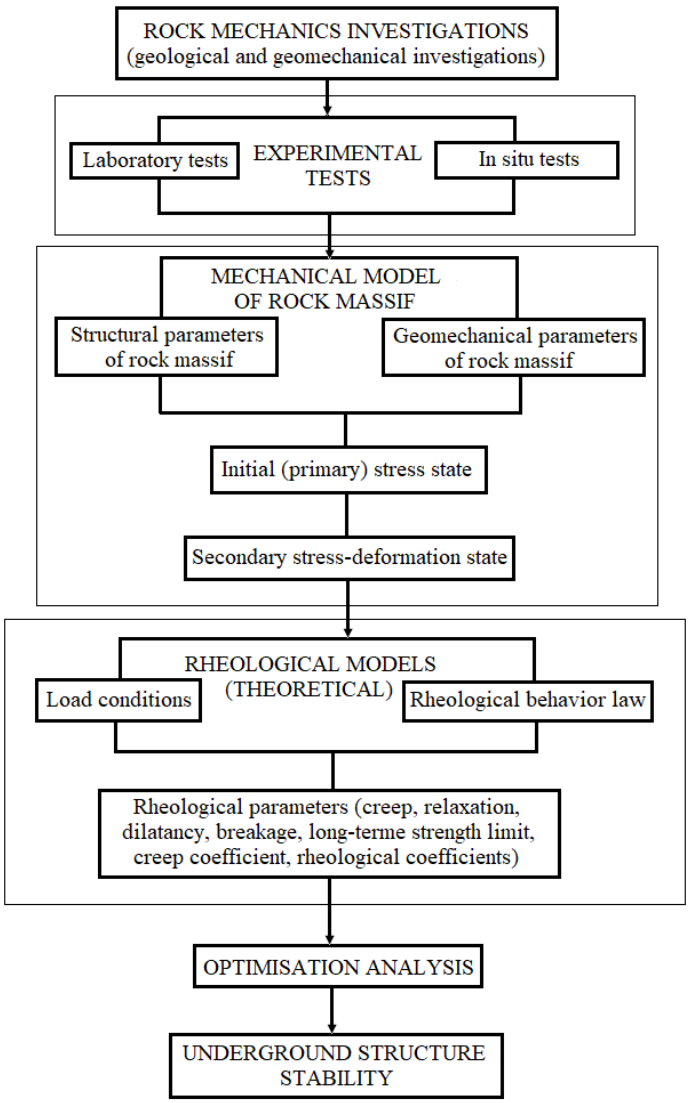

Fig. 9. Stages of stability analysis of an underground structure

The magnitude of the rheological deformations of rock salt raises the question of the predominant role of the rheological characteristics of this material in the study of the stability of underground structures. In the vicinity of underground excavations and in saliferous geological formations (domes, strata), the field of stress develops very slowly over time, which allows it to approach the state of

evolution through creep. To assess the stability of underground structures made of salt massif, first understand salt behaviour at both the micro- and macro-structural scales; microscopic analyses allow the identification of neo-formation minerals. For a better understanding of the rheological behaviour of salt and for a complete analysis of the stability of an underground structure achieved in salt in its exploitation by solid way, the following scheme was proposed (Fig. 9); this scheme shows the main stages of study that must be respected or taken into account in such an analysis.

5. CONCLUSIONS

The analytical method for evaluating the stability of dry salt mining systems traditionally relies on calculation procedures grounded in the "limit equilibrium theory." These procedures often lead to an over-dimensioning of support elements, such as pillars and floors. This over-dimensioning can restrict the exploitation depth due to the need for excessively large pillars, which in turn reduces the size of extraction chambers. Consequently, this approach substantially decreases the extraction ratio and can introduce other operational disadvantages.

In contrast, the proposed method supersedes the concept of limit equilibrium-based dimensioning. It introduces the assimilation of pillars as natural supports and applies the principle of the interaction mechanism between the pillar, room, and salt mass. This approach, grounded in the analysis of the secondary stress-strain state within the pillars, allows for a more accurate evaluation of the exploitation system's stability and enables exploitation at depths exceeding 800 meters. The method explicitly considers the rheological behavior of the salt, the time-dependent deformation of the pillars, and potential advancements in extraction technology.

The proposed methodology offers the possibility of an analysis of the unfavourable non-uniformity of the pillar geometry (not the same dimensions), the unfavourable implications of their non-coaxiality, and the pillar asymmetry over the main axis of the mining field. At the same time, it offers the possibility of assessing the stress state in pillars, meaning that, if in the design, a symmetry is not maintained in relation to the centre axis of the mine, then the central pillars may act on an identical stress state that differs from the one on the marginal pillars - a problem that can be solved by expanding this method.

This method, based on the principle of interaction, through the algorithm proposed for any situation in the salt mines in Romania, can be extended and used in the case of the exploitation of ore deposits when using the method of exploitation with rooms and pillars.

DISCLAIMER (ARTIFICIAL INTELLIGENCE)

Author(s) hereby declare that NO generative AI technologies such as Large Language Models (ChatGPT, COPILOT, etc.) and text-to-image generators have been used during the writing or editing of this manuscript.

ACKNOWLEDGEMENTS

This work was developed from a theoretical and experimental study of the rocks and mine workings in the Praid Salt Mine, Romania. All the observations and experimental research in the laboratory were realised by M.T. I would like to express my gratitude to the University of Petrosani, which provided the necessary equipment to perform in situ measurements and all laboratory tests in prior experimental research leading to the results synthesised in this article.

COMPETING INTERESTS

Author has declared that no competing interests exist.

REFERENCES

Aptukov, V. N., & Volegov, S. V. (2020). Experimental and theoretical estimation of fracture toughness in salt rocks in testing of samples with wedge-shaped cut. *Journal of Mining Science, 56*, 167–173. https://doi.org/10.1134/S1062739120020030

Aptukov, V. N., & Volegov, S. V. (2020). Modeling concentration of residual stresses and damages in salt rock cores. *Journal of Mining Science, 56*, 331–338. https://doi.org/10.1134/S1062739120030022

Aubertin, M., Julien, M. R., Servant, S., & Gill, D. E. (1999). A rate-dependent model for ductile behavior of salt rocks. *Canadian Geotechnical Journal, 36*, 660–674.

Balthasar, K., & Haupt, M. (1987). Stress relaxation behaviour of rock salt: Comparison of in situ measurements and laboratory test results. *Proceedings of the 6th Congress ISRM, Montreal*.

Belohlavek, K. U., & Behr, A. (1999). In-situ determination of geohydraulic parameters of natural salt rock for gas in loosening zones around drifts (cavities). *SMRI Spring Meeting, Las Vegas, Nevada*.

Berest, P. (2007). Questions on the prediction of the long-term behaviour of underground openings. *11th ISRM Congress, Lisbon, Portugal*.

Feng, Y., Harrison, J. P., & Bozorgzadeh, N. (2020). A Bayesian approach for uncertainty quantification in overcoring stress estimation. *Rock Mechanics and Rock Engineering, 54*(2), 627–645. https://doi.org/10.1007/S00603-020-02295W

Georgescu, M., Hirian, C., & Toderaş, M. (2005). Dimensioning of the strength elements (pillar–ceilings) afferent to the +190 m and +190 m levels from Praid salt mine. *1st International Seminar Ecomining – Europe in 21st Century, Sovata & Praid Salt Mine, October 27–29*, 97–102.

Jianhua, H., & Kuangdi, X. (2023). Room-and-pillar mining method. In K. Xu (Ed.), *The ECPH Encyclopedia of Mining and Metallurgy.* Springer. https://doi.org/10.1007/978-981-19-0740-1_335-1

Konstantinova, S. A., & Aptukov, V. N. (2013). Some problems of deformation and failure mechanics of salt rocks (Некоторые задачи механики деформирования и разрушения соляных пород). Novosibirsk: Nauka.

Majeed, Y., Abbas, N., & Emad, M. Z. (2023). Stability evaluation of room-and-pillar rock salt mines by using a flat jack technique – A case study. *Journal of the Southern African Institute of Mining and Metallurgy, 123*(6), 287–298. http://dx.doi.org/10.17159/2411-9717/1872/2023

McClain, W. C., & Bradshaw, R. L. (1967). Stress redistribution in room and pillar salt mines. *International Journal of Rock Mechanics and Mining Sciences & Geomechanics Abstracts, 4*(2), 245–255. https://doi.org/10.1016/0148-9062(67)90048-4

Minkley, W., & Menzel, W. (1996). Local instability and system instability of room and pillar fields in potash mining. *Proceedings of the 3rd Conference on Mechanical Behavior of Salt*, 497–510.

Pan, H., Jiang, N., Gao, Z., Liang, X., & Yin, D. (2022). Simulation study on the mechanical properties and failure characteristics of rocks with double holes and fractures. *Geomechanics and Engineering, 30*(1), 93–105. https://doi.org/10.12989/GAE.2022.30.1.093

Popp, T., Kern, H., & Schultze, O. (2002). Permeation and development of dilatancy in rock salt. *Proceedings of the 5th Conference on Mechanical Behavior of Salt*, 95–124.

Qin, X. S., Cao, H., & Guo, L. J. (2020). Sensitivity analysis of factors influencing pillar stability in the deep stope of an underground salt mine. *IOP Conference Series: Earth and Environmental Science, 570*, 022002. https://doi.org/10.1088/1755-1315/570/2/022002

Qingfa, C., Shiwei, W., & Fuyu, Z. (2020). Study on the mechanics and micro/macroeconomics of multiple strip-shaped pillar recovery. *Archives of Mining Sciences, 65*(1), 19–33.

Seryakov, V. M. (2020). Stress state of underground opening support considering its interaction with rock mass. *IOP Conference Series: Earth and Environmental Science, 523*, 012029.

Singh, A., Kumar, C., Kannan, L. G., Seshagiri Rao, K., & Ramanathan, A. (2018). Estimation of creep parameters of rock salt from uniaxial compression tests. *International Journal of Rock Mechanics and Mining Sciences, 107*, 243–248.

Spiers, C. J. (1989). Deformation and densification of rock by pressure solution and related phenomena. In V. Maury & D. Fourmaintraux (Eds.), *Rock at Great Depth* (Vol. 3). Rotterdam: Balkema.

Stamatiu, M. (1962). *Rock mechanics* (in Romanian). Didactic and Pedagogical Publishing House, Bucharest.

Thorel, L., & Ghoreychi, M. (1993). Rock salt damage – Experiment results and interpretation. *3rd Conference on Mechanical Behavior of Salt*. Clausthal: Trans Tech Publications. ISBN 0-87849-100-7.

Toderaș, M. (2020). The octahedral concept and cubic triaxiality in assessment of secondary stress state. *Mining of Mineral Deposits, 14*(1), 81–90. https://doi.org/10.33271/mining14.01.081

Toderaș, M. (2022). Possibilities of solving the stability of salt strata penetrated by drilling: A descriptive study. In *Emerging Challenges in Environment and Earth Science* (Vol. 3, pp. 51–60). SCIENCEDOMAIN UK Book Publisher International. https://doi.org/10.9734/bpi/ecees/v3/2311B ISBN 978-93-5547-263-2 (Print), ISBN 978-93-5547-333-2 (eBook).

Toderas, M. (2024). Stability analysis of the exploitation system with room and pillar by analytical methods. *Applied Sciences, 14*(5), 1827. https://doi.org/10.3390/app14051827

Toderaș, M., & Danciu, C. (2017). *Stability analysis methods of underground mining works*. Lambert Academic Publishing. ISBN 978-620-2-19847-9.

Toderaș, M., & Iosif, C. (2023). The interaction principle in the assessment of pillars' secondary stress-deformation state. *Mining Revue, 29*(3), 14–25. https://doi.org/10.2478/minrv-2023-0020

Todorescu, A. (1982). *Rock mechanics in mining* (in Romanian). Technical Publishing House, Bucharest.

Todorescu, A. (1986). *Rock rheology with applications in mining* (in Romanian). Technical Publishing House.

Todorescu, A., & Gaiducov, V. (1996–2001). *Mining pressure – Stability and reliability of mining constructions excavations* (in Romanian, Vol. I–II). Technical Publishing House.

Todorescu, A., & Toderaş, M. (1996). Research concerning appraisal and control of pillar stability in the case of the dry salt mining method in Romania. *5th International Symposium of Mine Planning and Equipment, São Paulo, Brazil*.

Wagner, H., & Blaha, H. (2015). A method of assessing pillar conditions in salt mines. *13th ISRM International Congress of Rock Mechanics, Montreal, Canada*.

Yahya, O. M. L., Aubertin, M., & Julien, M. R. (2000). A unified representation of the plasticity, creep, and relaxation behavior of rock salt. *International Journal of Rock Mechanics and Mining Sciences, 37*, 787–800.

Zhou, N., Du, E., Li, M., Zhang, J., & Dong, C. (2021). Determination of the stability of residual pillars in a room-and-pillar mining goaf under eccentric load. *Energy Reports, 7*, 9122–9132. https://doi.org/10.1016/j.egyr.2021.11.140

Disclaimer/Publisher's Note: The statements, opinions and data contained in all publications are solely those of the individual author(s) and contributor(s) and not of the publisher and/or the editor(s). This publisher and/or the editor(s) disclaim responsibility for any injury to people or property resulting from any ideas, methods, instructions or products referred to in the content.

© Copyright (2025): Author(s). The licensee is the publisher (BP International).

DISCLAIMER
This chapter is an extended version of the article published by the same author(s) in the following journal.
Revista Minelor – Mining Revue, 29(3): 14-25, 2023. DOI: https://doi.org/10.2478/minrv-2023-0020

Peer-Review History:
This chapter was reviewed by following the Advanced Open Peer Review policy. This chapter was thoroughly checked to prevent plagiarism. As per editorial policy, a minimum of two peer-reviewers reviewed the manuscript. After review and revision of the manuscript, the Book Editor approved the manuscript for final publication. Peer review comments, comments of the editor(s), etc. are available here: https://peerreviewarchive.com/review-history/4534

Chapter 6
Print ISBN: 978-93-49473-44-7, eBook ISBN: 978-93-49473-43-0

Design, Development and Operation of a Novel Robotic Fish Using PVC Gel Actuators

Ruyhan [a*], Nazia Bibi [a], Sara Rahman [a], Abdullah Al Hossain Newaz [b], Abdul Kadir [b] and Nasir Uddin [b]

DOI: https://doi.org/10.9734/bpi/erpra/v5/4531

Peer-Review History:
This chapter was reviewed by following the Advanced Open Peer Review policy. This chapter was thoroughly checked to prevent plagiarism. As per editorial policy, a minimum of two peer-reviewers reviewed the manuscript. After review and revision of the manuscript, the Book Editor approved the manuscript for final publication. Peer review comments, comments of the editor(s), etc. are available here: https://peerreviewarchive.com/review-history/4531

ABSTRACT

Bionic robot fish possess the capability to transform the way the world underutilizes underwater environments. Distinct from the other biomimetic robots using conventional motor systems, MIT Robotuna, a biomimetic robot fish that exhibited unprecedented efficiency in power consumption and operation, was pioneered in the field of bionic robotics. The study aims at developing a circular soft robot with SMA actuators, operated utilizing a newly developed control strategy encompassing PID alongside Kalman filtering in addition to visual servo. Here, a bionic robot fish structure, that can swim underwater, has been designed. The active compact body is powered by eight sets of symmetric PVC gel actuators with a caudal fin. The robot's 200 mm-long, fish structure design incorporates a 55.52 angle to optimize the fish dynamics movement. It's a fast and smooth operation and can swim. The robot can swim fast and quietly by using the right positions and the appropriate actuators on the PVC gel actuators. The successful deployment and implementation of such bionic robot fish display the potential of soft robotics to develop agile and versatile underwater vehicles. This design entails a unique architecture that enables the robot to move safely and unobtrusively at the same time, which makes it suitable equipment for different exploration and surveillance missions in the water with speed and silent operation as the foremost concern.

Keywords: Biomimetic robotics; structural design; PVC gel actuators; swimming mechanisms.

---

[a] *School of Mechanical Engineering, Xi'an Jiaotong University, Xi'an, China.*
[b] *School of Mechanical Engineering, University of Bridgeport, Bridgeport, USA.*
**Corresponding author: E-mail: ruyhan19@gmail.com;*

1. INTRODUCTION

Bionic robotic fish represent a new type of autonomous underwater vehicle that integrates hydrodynamics, machinery, electronics, control, and computer technologies. Currently, autonomous underwater vehicles are primarily utilized for various applications, including marine observation, underwater pipeline inspection, environmental protection, and rescue operations (Ma et al., 2023). The latest research (Raj & Thakur, 2016; Xie et al., 2021) has shown that bionic robot fish possess the capability to transform the way the world underutilizes underwater environments. Being distinct from the other biomimetic robotics that were powered by a building and conventional motor drives of the systems (Duraisamy et al., 2019), MIT Robotuna, a biomimetic robot fish that exhibited unprecedented efficiency in power consumption and operation, was pioneered in the field of bionic robotics (Triantafyllou & Triantafyllou, 1995). The first tuna-mimetic robot, RoboTuna, was built at MIT. Later, the vorticity control unmanned undersea vehicle was developed based on RoboTuna, with some improvements and additional capabilities, such as obstacle avoidance and the use of up-down motion (Mitin et al., 2022). Through the detailed observation of tuna moving, Robotuna's propulsion system employs one or more motors to make the robot fish oscillate in water, and it is then that this robot can be launched anywhere it is desired. By the means of cleverly reproducible movements of the live fish, those robots would bring a special juice to underwater exploration and research all over the globe (Ruyhan et al., 2024).

This study embraces new designs for Io-liquid locomotion machines inherited from structural compliance to achieve thrust. A compliant mechanism model with high performance similar to that of real fish locomotion is proposed, which is later analyzed by another model through the next stage of development (Ruyhan et al., 2024). Humans create just about everything, but most inventions are inspired by the way nature is made. It is this awareness that leads to the development of soft robotics. As opposed to hard robots, soft robots imitate natural systems; these are flexible and complex, thus optimal for solving underwater tasks. This essay looks at recent progress in this area through (Youssef et al., 2022; Zhong et al., 2017). This motor control is driven by a silicone rubber flexible fishtail that swings continuously, which was like a real fishtail. In addition to the research team at MIT, they have utilized the hydraulically controlled robotic fish for a new kind of novel underwater technology (Ruyhan et al., 2024). The driving gear pump, which is controlled by an electrical motor and is responsible for the regulation of the fluid pressure and creating an alternating bending and oscillating of the fish's tail, is powering the device (Katzschmann et al., 2018). This world-changing machine may just provide a much deeper level of understanding about water worlds and take research to a more advanced level than before. Strong materials such as IPMC, DE, and SMA are introduced in the soft robotics fish creation for improved flexibility and efficacy (Ruyhan et al., 2024). An IPMC-based EAP is one of the most common materials used in manufacturing robot fish as the hydrophilic nature and low voltage of this material are the two foremost reasons (Chen, 2017).

The bionic robot fish was created by a group of researchers, taking the lionfish as their guide, and also an inspiration. The robot, resembling fish, is powered by the most recent DE actuators, therefore making it fun with the flapping movement (Ruyhan et al., 2024). Such a remarkable journey was achieved in the Mariana Trench that the invented technology lasted 45 minutes, suggesting the advent of new possibilities for ocean research with some scientific applications. (Li et al., 2021; Le et al., 2012) created a domestic bionic cuttlefish controlled with SMA that can suddenly swim on its own. but these resources are more suitable for little robotic fish than for medium-sized or big robots (Gao et al., 2014). This paper presents a new bionic robot fishtail structure that has multi degrees of freedom skeleton structure and stacked soft PVC gel actuators which can simulate fish muscle movements. Analyzing the mechanics and the frequencies of the fishtail and it responded optimally at 1 to the amplitude of swing. Still, the generator component causes the reporter to hear 5 Hz underwater due to resonance (Ruyhan et al., 2024). Like Flappy, the prototype was tested for water movement and proven to be operational, which will go a long way in creating a practical bionic fish design. S Sixtus concluded that contraction strain increased with changing load or voltage, and reached the frequency that the natural fish swims and they thus have potential in bionic usages of PVC gel actuators (Dong et al., 2022). For this lightweight structure, the optimized designs validate the efficacy of topology optimization in creating lightweight, high-performance lightweight components, highlighting its importance in future design Advancements (Ruyhan & Melon, 2024). The study aims at developing a circular soft robot with SMA actuators, operated utilizing a newly developed control strategy encompassing PID alongside Kalman filtering in addition to visual servo (Ruyhan et al., 2024). Potential MATLAB simulations and experiments have shown some outcome, however, the issues of recognizing objects and forms and measuring of distances still remained a daunting task for future work with reinforcement learning by gait control (Lyu, 2022). This work describes the fabrication and characterization of the freshly developed ampicillin-selective electrodes based on Mn (III) TPPI ionophore in PVC and sol-gel matrices. These electrodes, when coupled to pharmaceutical analysis they depict a similar precision as that of HPLC, however, they are easier to use, expensive reagents are minimized, and are cheaper when used with the SIA system (Zárate et al., 2011).

2. STRUCTURE DESIGN OF ROBOTICS FISH

2.1 Oscillating Mechanism Proposed for Robotic Fish Propulsion

This mechanism, which is simply voltage applied, is an actuator or single-layer PVC gel with contraction-displacement motion as shown in (Fig. 1) (Ruyhan et al., 2024). Voltage application will simply push up the gel to the anodes to create the displacement. Instead of traditionally, we use 2 closely placed actuators linked together by a lever arm for more effective execution of the principle. Coupling actuators exploit the synchronization principle to make mechanical motion take place in a desired fashion (Dong et al., 2022). It provides the ability to carry out controllable alterations in the tail direction or any other appendages

required in the animatronic system and hence achieve the desired movements (Ruyhan et al., 2024). PVC gel actuators in this oscillating mechanism were used in this reciprocating motion, as they have the advantage of being able to perform more efficiently, flexibly, and easily controllable. For instance, the simplicity and robustness of the design make it applicable to many kinds of robot assemblies, chiefly in underwater constructions where traditional actuators may fail to work. Supposing this oscillating model is implemented into robotics, it may contribute greatly to progress in robotics, and provide a successful route to the development of more agile and flexible robotic platforms by providing an efficient approach for both control and movement within robots (Ruyhan et al., 2024).

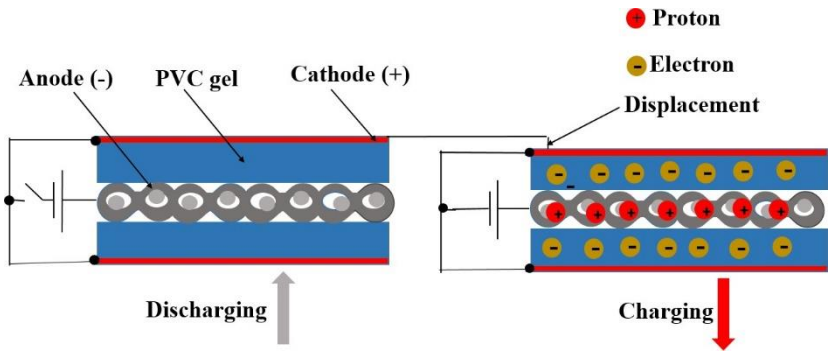

Fig. 1. PVC gel actuator schematic with contraction deformation (Dong et al., 2022)

2.2 Active Fishtail Design Utilizing PVC Gel Actuators for Oscillation

This paper elaborates the synthesis and use of dibutyl adipate (DBA) as the plasticizer within PVC gel concerning its employment in the motion structure of a bionic robot fish (Ruyhan et al., 2024). It starts with the preparation of PVC gel that requires dissolving of PVC powder and DBA in Tetrahydrofuran (THF). This mixture advantageously utilizes DBA, where it was observed to increase the dielectric constant, which is crucial in the actuation of the robot fish using the PVC gel. For the preparation of the gel, the reaction medium used shall be a THF-DBA system, where THF is the main solvent and DBA acts as the cross-linking agent. One amount of the PVC powder is added slowly to this mixture and it is then heated for a few minutes to form a viscous gel (Ruyhan et al., 2024). The crucial step involves mixing PVC and DBA in a 4:1 ratio, followed by stirring the resulting suspension for 24 more hours at 40˚C, during which the PVC powder dissolves completely. This all helps to produce a distinct PVC solution, a crucial part of the motor function of the robot fish. The construction of the robot fish can be described as consisting of several stages: first, two plastic covers are put together; second, PVC gel is prepared and injected into the body of the fish; third, a moving mechanism is installed. After the assembly is done, the company then powers the PVC gel actuators by electricity, and this allows the movement of the robot fish. The engagement of these actuators is of high importance, as it

is through it that converting electrical energy into mechanical energy is enabled, thus making the fish move (Ruyhan et al., 2024).

Thus, the paper focuses on the fact that DBA is helpful to refine specific characteristics of the formed PVC gel, including the dielectric properties, which are critical to actuation. With regards to dielectric properties, which determine the response of the material to an electric stimulus, directly impacts the speed and functionality of the robot fish. By optimizing these properties, it guarantees that the DBA-enhanced PVC gel maximizes the capacities of the actuators as expected (Ruyhan et al., 2024). Moreover, the paper describes the importance of the actual mixing process that has been described in more detail above. The inclusion of PVC powder in a gradual process and the stirring at the given temperature are important mechanisms in making the gel proportional and efficient. The 24 h stirring for the samples at 40˚C is critical to dissolving the PVC to the occurrence of a clear solution that is also uniform. Such homogeneity is crucial to the performance of the actuators, as it ensures that they provide optimal performance in distinct settings (Ruyhan et al., 2024).

The assembly process is also stressed, as in the end, for creating the robot fish, the clear PVC solution gains some components to compose the base of its motion. To allow for this, the assembly of the process is very precise to make sure that the actuators are in the right places and can function correctly once a flow of electricity is passed through them (Ruyhan et al., 2024). These components are the essential elements that show how a robot fish should work and how well it will function when used in the intended application (Dong et al., 2022; Li et al., 2019).

The soft actuator is a PVC gel. It produces linear displacement. It's contracting under DC voltage, returning to its original shape without voltage, with the contraction rate increasing with voltage until saturation. A novel swinging mechanism using PVC gel actuators has been proposed to simulate the contraction of fish muscles for bends in their tail. The mechanism is composed of joints, PVC gel actuators, hinges, and press buttons (Fig. 2) (Ruyhan et al., 2024). The two PVC gel actuators are placed at the joint where they rotate to enable bidirectional motion. In this manner, the actuators which are used to give the driving signals in turns create the swinging motion; the swing angle is in direct relation with the voltage. Thus, this mechanism copies the path of fish movements to improve the power and direction in the water environment (Fig. 3) (Ruyhan et al., 2024).

Actuators are to be positioned at junctions between joints. Precompression plates must be spread during assembly (Ruyhan et al., 2024). The two actuators' driving signals are adjusted to be oscillating. The stored charge in the right actuator will produce the joint rotation through the right-handed screw sense with the clockwise precompression torque generation. It results in the swing angle proportional to the voltage. When the operation actuator on the left is set in place, so does the show. The main function of this act is based on the timing control of the two parallel signals, which produce the two waveforms, either the

charging or the reverse-waveform signals by the switching action. Perpetual right and left-hand side twisting movements are easily possible with either regular or alternating actuator operation. Units connected in series (Fig. 4) create a parallel-series system, except signals are passed from left to right and from right to left (Ruyhan et al., 2024).

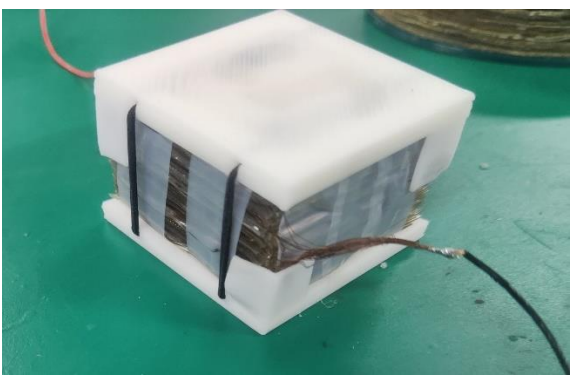

Fig. 2. PVC gel actuator assembly

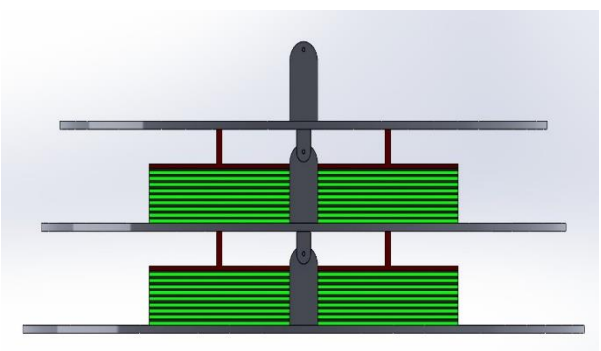

Fig. 3. Two PVC gel actuators were employed

The bionic robot fish design involves placing actuators at the junctions between joints, with precompression plates spread during assembly (Fig. 4), titled “The oscillating mechanism utilizes two PVC gel actuators for controlled movement,” includes two different subfigures, labeled as Fig. 4(a) and Fig. 4(b) for clarity (Ruyhan et al., 2024).

Fig. 4(a): Illustrates the configuration where the two actuators are positioned, showing how the driving signals are adjusted to oscillate. The stored charge in the right actuator generates joint rotation through the right-handed screw sense with a clockwise precompression torque, resulting in a swing angle proportional

to the voltage. This subfigure highlights the specific arrangement and activation of the right-side actuator (Ruyhan et al., 2024).

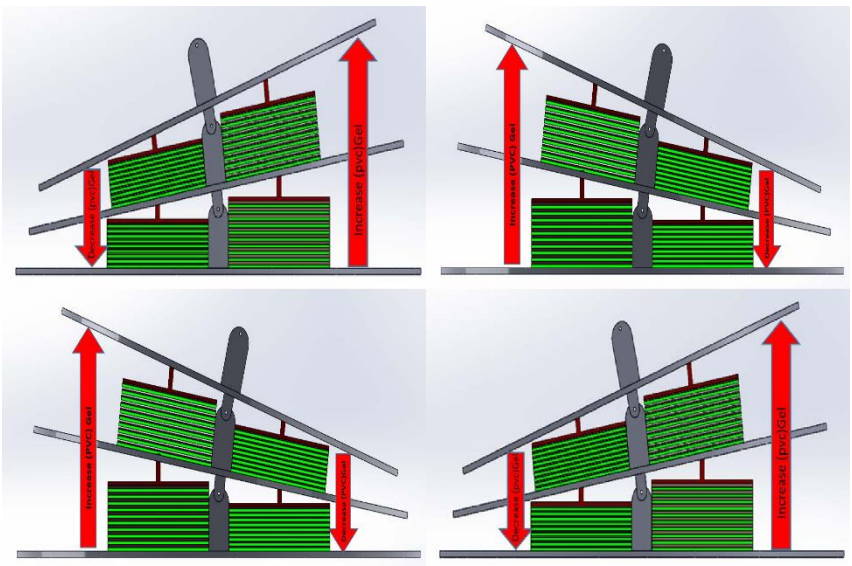

(a) **(b)**

Fig. 4. The oscillating mechanism utilizes two PVC gel actuators for controlled movement.

Fig. 4(b): depicts the operation when the left-side actuator is activated. The same principles apply, with the left actuator producing the necessary movements through its oscillating driving signals. This results in left-hand side twisting movements, mirroring the function of the right actuator shown in (Fig. 4(a)) (Ruyhan et al., 2024). The main function of these actuators is based on the timing control of the two parallel signals, producing ongoing waveforms through switching actions that alternate between charging and reverse-waveform signals. This setup allows for continuous right and left-hand twisting movements with either regular or alternating actuator operation. When units are connected in series, as shown in the combined representation of (Fig. 4(a) and Fig. 4(b)), they create a parallel-series system (Ruyhan et al., 2024). In this system, signals are passed Bidirectionally from left to right and right to left, enabling synchronized and efficient movement of the bionic robot fish.

2.3 Model of a Robotic Fish Utilizing Soft Actuators for Propulsion

The proposed “swinging” mechanism we are talking about here, uses two PVC pills to move the base for rotation at an angle of 55.52˚. The system is based on new standards, it’s fast and streamlined, therefore it’s significantly better than the mechanisms which resemble the movements of fish. Just like the majority of

them, it has something unique to offer the industry, namely the low friction torque. The associated machinery will be running flawlessly and performing its functions at optimum (Ruyhan et al., 2024).

This mechanism of other fish systems is quite simple and therefore it can be intuitively managed and preferred. This appeals not only to recreational divers but also to those who seek practical benefits when using it. This actuation mechanism features the use of PVC gel as a key feature. Among these actuators is the component that pushes the upper and lower bodies to generate wave-like movements. PVC gel actuators are praised for their flexibility, fast reaction time, and longer duration, which reveals that this type of actuator is best for dynamic systems. In this case, the application of these actuators isn't just about making the mechanism function better but also adding versatility to its designs (Fig. 5) (Ruyhan et al., 2024).

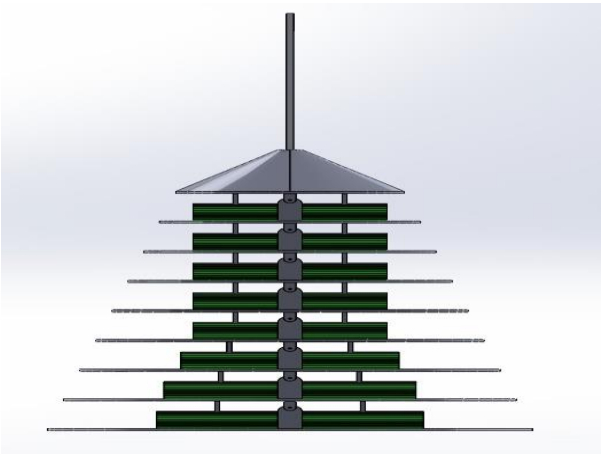

Fig. 5. Active fishtail functionality

This performance of the system with a 55.52˚ dangling precision is a proud victory in the engineering sphere. This accuracy in movement offers new solutions to a variety of processes in different fields, like robotics or automation in production. Beyond that fast working mechanism, this tool also enables a faster working process for assigned tasks that are precise and precise. It, therefore, applies to jobs that require instant work. The difference that this mechanism presents is contrary to the popular approach of fish-shaped systems (Fig. 6) (Ruyhan et al., 2024).

Whereas the majority of underwater technologies connect its movement and swimming patterns with those of fish, this system moves in a unique, one-way manner (Ruyhan et al., 2024). The intention here is to effect a break away from a norm in an endeavor to devise a mechanism that incorporates efficiency as well as distinction as its mode of operation. This stabilizing method is not only

technically feasible but also very affordable to implement. This is made possible by the system's ability to tap into the potential energy of the wind and its inherent low friction; this translates to an inexpensive cost of electricity. One of the components in a system of the world will be the feature of energy efficiency that is more and more encouraged so that it has a great financial value for the operation (Fig. 7) (Ruyhan et al., 2024).

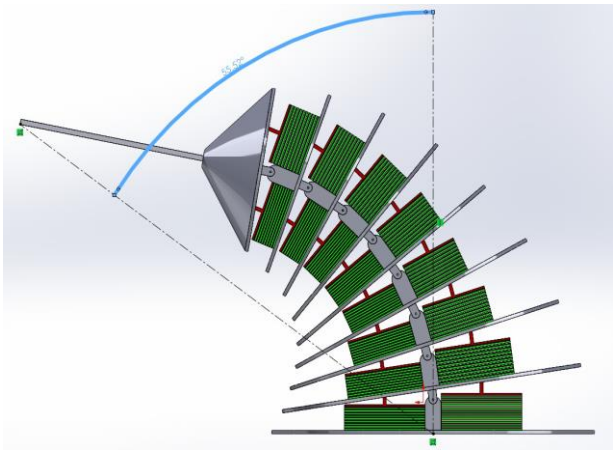

Fig. 6. Depicts the precise rotation of the left side of the active body by 55.52˚

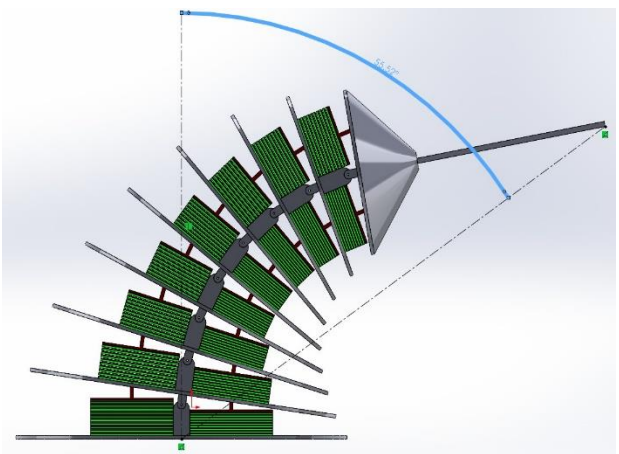

Fig. 7. Depicts the precise rotation of the Right side of the active body by 55.52˚

This is due to the cost-effectiveness of the technology, which often makes it feasible for use in a wide range of applications, and probably in situations where

energy savings is an important goal. Finally, I can say that mechanical assembling that has been accomplished using two PVC gel actuators precisely reminds

me of a huge growth in technical creativity. Its dual-helix shape, turn-over-time is faster than the conventional up-and-down structure, and working efficacy, which is user-friendly, make it different from the conventional systems (Fig. 8) (Ruyhan et al., 2024).

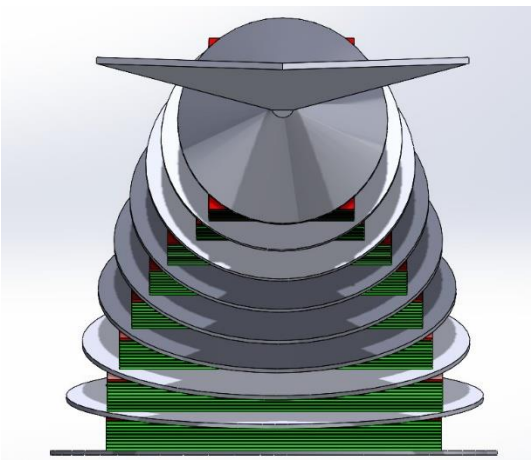

Fig. 8. Back left side view

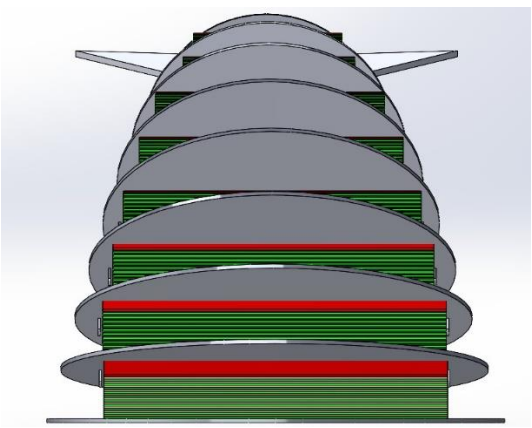

Fig. 9. Back right side view

The usage of PVC has boosted its performance and capabilities to adapt to diverse applications (Ruyhan et al., 2024). The accuracy of revolving motion is

what drives the versatility of such an operation, and the economy of use is what makes it practical in real-world scenarios. The mechanism of oscillation signifies by its example how a brilliantly conceived system of a dynamic nature could bring together effectiveness, practicality, and economy with ease. This economic aspect is a practical choice for different application areas accentuating its usefulness, especially in those cases where minimizing operating costs is the chief priority (Ruyhan et al., 2024). To draw the curtain, however, the Bilyeley manufacture of two PVC gel actuators that stands for engineering brilliance is the highest level. This is not only a characteristic of the MBring system but also a special feature of the design of the MBring system, which has won over other fish-like systems using its ease of rotation and fast working efficiency. Using PVC gel actuators is its key feature for proper working and adapting. High accuracy of rotation enables multiple practical application fields, and low cost is one more factor of making it handy for transportation. It is the gyratory mechanism that has emerged as the inventive line in the world of dynamic systems due to the harmony of efficacy, accuracy, and economy (Fig. 9) (Ruyhan et al., 2024).

2.4 Robotic Fish Design and Structure

The working model bio-inspired robots of the design unit are based on parameters like body size (distribution of body size) and also on swimming patterns (pattern of undulation) (Ruyhan et al., 2024). For such bio-mimicry, the proportions of the robots are looked at and are designed as per the proportions of their natural models (Scaradozzi et al., 2017). The design of this robotic fish was made in such a way that it imitates the swimming action of fish that belong to sub-carangiform swimmers and hence ensures its resemblance with the biotic ones (Fig. 10) (Ruyhan et al., 2024). In this distribution, predators having sub-carangiform swimmer proportions, with undulations covering about half the total length, have the dominant executor role.

Fig. 10. Design of robotic fish

The fish's body was divided into four parts along the length of the fish and (Table 1) (Ruyhan et al., 2024). Streamlining of the hull design is made by design engineers to decrease drag area and hence enhance propulsion efficiency (Fig. 11) (Ruyhan et al., 2024). Twin pectoral fins are installed to increase stability and prevent unwanted flipping. Pushing forward of the tail being a determining motive, is carried out by eight pieces of PVC gel actuators, which are located symmetrically to cater for the balance. Actuators (Fig. 9) which have a green cuboid shape will be strategically sized for the simultaneous activities of force output and fish streamline appearance (Ruyhan et al., 2024). Adding on, the caudal fin design, which was inspired by the real world emarginated fin of sub-carangiform swimmers, therefore, the model is known globally for its biomimicry. In summary, the design of the robot fish model is focused on efficiency in terms of swimming that sub-carangiform swimmers can achieve while combining the stability and flexibility for movement underwater.

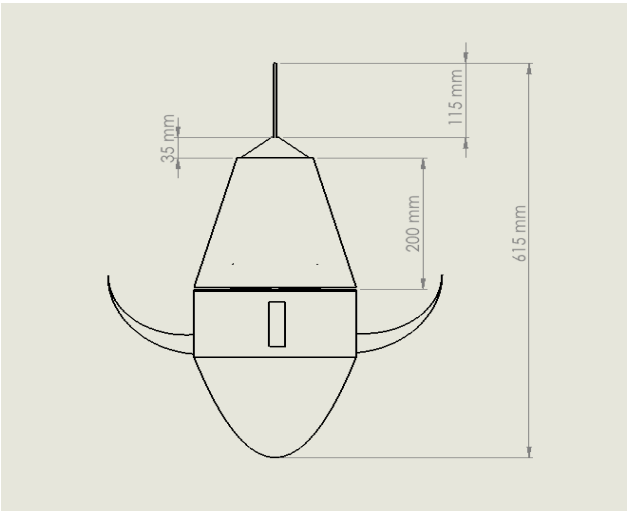

Fig. 11. 2D Design of robotic fish

Table 1. Showcases robot fish size data

Length of the item	Summary of Characteristics
Total length specified	615 mm
Active body length	200 mm
Peduncle length	35 mm
Caudal fin length	115 mm

3. CIRCUIT BOARD DESIGN OVERVIEW

The tail of a real fish is designed with a two-mode control system that provides an independent pattern generator (Ruyhan et al., 2024). MPU shows PWM

outputs via its ports. Such signals are specified with two shapes: one whose signal is the reversal of the other. Such a technique provides the possibility of patterned fish-tail motion, which means it can happen in time and space simultaneously. The circuit board provides the robots' oscillation and swimming, synchronizing the PWM (pulse width modulation) signals with implicit waves. This design allows us to make the fishtail perform those convert swimming movements that can easily be similar to the moves made by the natural live fish. Furthermore, the ranking-control design of the system provides an additional advantage by contributing to the device's variability in its maneuvers, hence enabling it to mimic these with accuracy and speed (Ruyhan et al., 2024). As a whole, it is the circuit board design in place that has efficiently upgraded the functionality of the robotic fish as it is now capable of swimming automatically in an original position in water environments. Circuit design provides the fishtail with fine motion control by applying two-millennium mode layout with carefully chosen distances between the shafts. The next heavy input signal within the actuator is contraction, where the swinging of the fishtail takes place into one side or the other. On the opposite side, the low-energy coil turns on when there is a high-level switching state, and the signal flows into a fishtail pushing it to the other side of the platform too. Through this switch response, the action of the fishtail becomes synchronized with the metalion's swim (Ruyhan et al., 2024).

These features can be used in the code by the users to set and display frequency and speed for the actuators, which will help to drive the oscillations properly and the fish motion, while being precise, as well. In different situations for different tasks, users can tune these factors to present the fish behavior that corresponds to their swimming behavior. Apart from that, the design of robot fish circuit boards by physicochemical principles ensures that they are properly and profitably used in waters, through which they operate without any complication (Ruyhan et al., 2024).

4. THE ASSEMBLY PROCESS OF THE ROBOT FISH

The robot fish assembly, in general-purpose terms, comprises several important steps that build up the functional and working robot fish. First of all, there will be a set of items used for the assembly of the system, for example, body frame, propulsion system, control systems, and any other extra features like sensors or cameras (Fig. 12) (Ruyhan et al., 2024). Generally, constructing the body frame is the first step of the assembly process, as it is the spinal cord of the robot fish. This frame is usually constructed of plastics, or other synthetic materials, which are light, but at the same time strong enough to deal with water while making a unit buoyant and stable.

So-called actuators are placed in certain areas of the body frame to imitate the movement of a real fish's tail, then, allow the robot fish to propel itself through the water. Besides, since other features or add-ons such as cameras that enable underwater visioning to avoid obstacles are still being assembled during manufacturing, they are put in the robot fish as well. These processes are done systematically with controls between components to give them the desired

operation. Assembling the man-made fish is the most complicated stage of this project, which includes putting the small pieces of the robot fish together to build a submarine robot (Ruyhan et al., 2024).

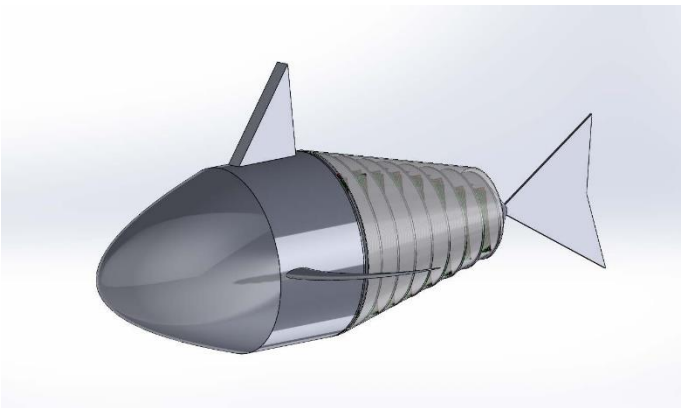

Fig. 12 Illustrates the assembly process of the robotic fish

5. ADVANTAGES OF THE DESIGNED ROBOT FISH

The designed robot fish, utilizing PVC gel actuators in its oscillating mechanism, offers several distinct advantages compared to other types of robots: The designed robot fish, utilizing PVC gel actuators in its oscillating mechanism, offers several distinct advantages compared to other types of robots:

1. Bio-Inspired Design: It also resembles the real movements and flexibility of fish using biomimicking technology, which has a bionic fishtail and numerous soft structures. This planar technique reduces the complexity of the robot movements and makes it easier to maneuver the robot in underwater as opposed to the normal bulky type robots (Ruyhan et al., 2024).
2. Soft Actuators: The freedom and flexibility offered by the use of the PVC gel actuators is particularly helpful in enhancing the mobility of the robot fish in underwater terrains with numerous bends and twists. Soft actuators are useful in application scenarios where there is a likelihood of operations with fragile marine organisms or structures, thus reducing the probability of the operations harming the organisms or structures (Ruyhan et al., 2024).
3. Efficiency in Propulsion: PVC gel actuators also make the oscillating mechanism move and create efficient propulsion. The actuators' capacity to create back and forth vibrations and focused motion enhances the maneuverability of the robot fish and the energy efficiency of the locomotion; in some respects, they are likely to be more effective than

popular rigid propellers in terms of adaptability and rates of speed (Ruyhan et al., 2024).

4. Reduced Weight and Size: This is particularly important considering that other conventional underwater robots might use more heavy metal and larger mechanical parts than the robot fish with PVC gel actuators, although this is sheer speculation. This reduction in weight and size can be highly beneficial since it enhances maneuverability and ease of deployment in underwater military applications such as exploration and surveillance (Ruyhan et al., 2024).
5. Quiet Operation: Soft actuators in general create less acoustic noise in comparison to conventional rigid actuators, which is sometimes an advantage in low visibility underwater operations. Lower noise levels mean that there is little interference with the activities of water dwelling animals and the robot fish is then well suited for spying or data collection assignments (Ruyhan et al., 2024).
6. Adaptability and Versatility: Soft robotic design HERE is superior to rigid design as it adapts easily to several underwater tasks and challenges. The concept of the robot fish shows that it can be maneuvered through small channels, can interact softly with objects in the marine environment, and perform tasks that require accurate, sensitive movements, which can be seen as valuable for various tasks in the marine environment.

The therapeutic outcomes of the designed robot fish are attributed to the soft bio-inspired approach to the robot's body, the optimization of the propulsion system, integration of compact and lightweight structures, low-noise modus operandi, and versatility in adjusting to various marine environments. These characteristics make it suitable for operations in underwater search, monitoring and studying environments where the use of arbitrary strong robotic structures can be a challenge (Ruyhan et al., 2024).

6. CONCLUSION

Finally, a robot fish prototype of size 200 mm was exclusively designed for demonstration. Its body is driven by eight skeletal actuators of PVC gel, an action that forces the caudal fin to act (Ruyhan et al., 2024). As a whole, each set has matching elements, resulting in a total of 16 actuators integrated into the fish's skeleton. The structural design angle of 55.52˚ was chosen to optimize the fish's movement dynamics. By taking advantage of the precise engineering and rich design, the robotic fish successfully proved it is fast and efficient. The arm and wing structures of the robotic fish are actively synchronized through the placement and synchronization of the PVC gel actuators to help generate propulsion efficiently just like fish while swimming underwater (Ruyhan et al., 2024). The adoption of soft actuators, e.g., the use of PVC gel actuator, comes in handy as the actuator is flexible and highly responsive. This is required in simulation swimming to produce the natural movements. Both the right and the left actuators are arranged in a symmetric manner to make the lines of movement uniform and in sequence, being the secret to efficient robot fish movement. Additionally, the mechanical structures of Robo Fish are designed to

allow them to work with speed and accuracy. The optimized angle of 55.52˚ constant velocity allows quick movements that are penalized with instability and go out of control. It will be impossible for the robot fish to operate with high-speed swimming through the water and task completion, but with this design feature, they can move swiftly and efficiently (Ruyhan et al., 2024). Finally, it can be noted that the successful deployment and implementation of such bionic robot fish display the talents that soft robotics are endowed with to develop agile and versatile underwater vehicles. Instead of the current bionic robot fish, successive models are likely to merge the innovative design principles with advanced materials, and the actuators. Consequently, the next iterations may even further enhance their performances and capabilities, and ultimately open up new applications for underwater robotics (Ruyhan et al., 2024).

DISCLAIMER (ARTIFICIAL INTELLIGENCE)

Author(s) hereby declare that NO generative AI technologies such as Large Language Models (ChatGPT, COPILOT, etc) and text-to-image generators have been used during writing or editing of this manuscript.

COMPETING INTERESTS

Authors have declared that no competing interests exist.

REFERENCES

Ruyhan., Bibi, N., Rahman, S., Newaz, A. A. H., Kadir, A., & Uddin, N. (2024). Design of a Novel Robotic Fish Structure Utilizing PVC Gel Actuators. *Modern Mechanical Engineering*, *14*(3), 57-72.

Chen, Z. (2017) A Review on Robotic Fish Enabled by Ionic Polymer-Metal Composite Artificial Muscles. *Robotics and Biomimetics*, 4, Article No. 24. https://doi.org/10.1186/s40638-017-0081-3

Dong, C., Zhu, Z., Li, Z., Shi, X., Cheng, S. and Fan, P. (2022) Design of Fishtail Structure Based on Oscillating Mechanisms Using PVC Gel Actuators. *Sensors and Actuators A*: *Physical*, 341, Article ID: 113588. https://doi.org/10.1016/j.sna.2022.113588

Duraisamy, P., Kumar Sidharthan, R. and Nagarajan Santhanakrishnan, M. (2019) Design, Modeling, and Control of Biomimetic Fish Robot: A Review. *Journal of Bionic Engineering*, 16, 967-993. https://doi.org/10.1007/s42235-019-0111-7

Gao, F., Wang, Z., Wang, Y., Wang, Y. and Li, J. (2014) A Prototype of a Biomimetic Mantle Jet Propeller Inspired by Cuttlefish Actuated by SMA Wires and a Theoretical Model for Its Jet Thrust. *Journal of Bionic Engineering*, 11, 412-422. https://doi.org/10.1016/s1672-6529(14)60054-8

Katzschmann, R.K., DelPreto, J., MacCurdy, R. and Rus, D. (2018) Exploration of Underwater Life with an Acoustically Controlled Soft Robotic Fish. *Science Robotics*, 3, eaar3449. https://doi.org/10.1126/scirobotics.aar3449

Le, C.H., Nguyen, Q.S. and Park, H.C. (2012) A SMA-Based Actuation System for a Fish Robot. *Smart Structures and Systems*, 10, 501-515. https://doi.org/10.12989/sss.2012.10.6.501

Li, G., Chen, X., Zhou, F., Liang, Y., Xiao, Y., Cao, X., *et al*. (2021) Self-powered Soft Robot in the Mariana Trench. *Nature*, 591, 66-71. https://doi.org/10.1038/s41586-020-03153-z

Li, Y., Guo, M. and Li, Y. (2019) Recent Advances in Plasticized PVC Gels for Soft Actuators and Devices: A Review. *Journal of Materials Chemistry C*, 7, 12991-13009. https://doi.org/10.1039/c9tc04366g

Lyu, T. (2022) A Control Method for SMA Robotic Actuators. *Journal of Computer and Communications*, 10, 103-112. https://doi.org/10.4236/jcc.2022.105007

Ma, S., Zhao, Q., Ding, M., Zhang, M., Zhao, L., Huang, C., ... & He, G. (2023). A review of robotic fish based on smart materials. *Biomimetics*, *8*(2), 227.

Mitin, I., Korotaev, R., Ermolaev, A., Mironov, V., Lobov, S. A., & Kazantsev, V. B. (2022). Bioinspired propulsion system for a thunniform robotic fish. *Biomimetics*, *7*(4), 215.

Raj, A. and Thakur, A. (2016) Fish-inspired Robots: Design, Sensing, Actuation, and Autonomy—A Review of Research. *Bioinspiration & Biomimetics*, 11, Article ID: 031001. https://doi.org/10.1088/1748-3190/11/3/031001

Ruyhan, A.A.H.N. and Melon, M.M.H. (2024) Optimization of Brake Pedal Mass and Safety Factor Using Topology Optimization *Techniques. International Research Journal of Engineering and Technology* (*IRJET*), 11, 478-497.

Scaradozzi, D., Palmieri, G., Costa, D. and Pinelli, A. (2017) BCF Swimming Locomotion for Autonomous Underwater Robots: A Review and a Novel Solution to Improve Control and Efficiency. *Ocean Engineering*, 130, 437-453. https://doi.org/10.1016/j.oceaneng.2016.11.055

Triantafyllou, M.S. and Triantafyllou, G.S. (1995) An Efficient Swimming Machine. *Scientific American*, 272, 64-70. https://doi.org/10.1038/scientificamerican0395-64

Xie, F., Zuo, Q., Chen, Q., Fang, H., He, K., Du, R., *et al*. (2021) Designs of the Biomimetic Robotic Fishes Performing Body and/or Caudal Fin (BCF) Swimming Locomotion: A Review. *Journal of Intelligent & Robotic Systems*, 102, Article No. 3. https://doi.org/10.1007/s10846-021-01379-1

Youssef, S.M., Soliman, M., Saleh, M.A., Mousa, M.A., Elsamanty, M. and Radwan, A.G. (2022) Underwater Soft Robotics: A Review of Bioinspiration in Design, Actuation, Modeling, and Control. *Micromachines*, 13, Article 110. https://doi.org/10.3390/mi13010110

Zárate, N., Araujo, A.N., Montenegro, M.C.B.S.M. and Pérez-Olmos, R. (2011) Sequential Injection Analysis of Ampicillin in Pharmaceuticals by Using Potentiometric Detectors Based on PVC and Sol-Gel Membranes. *American Journal of Analytical Chemistry*, 2, 491-499. https://doi.org/10.4236/ajac.2011.24059

Zhong, Y., Li, Z. and Du, R. (2017) A Novel Robot Fish with Wire-Driven Active Body and Compliant Tail. *IEEE/ASME Transactions on Mechatronics*, 22, 1633-1643. https://doi.org/10.1109/tmech.2017.2712820

Disclaimer/Publisher's Note: The statements, opinions and data contained in all publications are solely those of the individual author(s) and contributor(s) and not of the publisher and/or the editor(s). This publisher and/or the editor(s) disclaim responsibility for any injury to people or property resulting from any ideas, methods, instructions or products referred to in the content.

© Copyright (2025): Author(s). The licensee is the publisher (BP International).

DISCLAIMER
This chapter is an extended version of the article published by the same author(s) in the following journal.
Modern Mechanical Engineering, 14: 57-72, 2024. DOI: 10.4236/mme.2024.143006

Peer-Review History:
This chapter was reviewed by following the Advanced Open Peer Review policy. This chapter was thoroughly checked to prevent plagiarism. As per editorial policy, a minimum of two peer-reviewers reviewed the manuscript. After review and revision of the manuscript, the Book Editor approved the manuscript for final publication. Peer review comments, comments of the editor(s), etc. are available here: https://peerreviewarchive.com/review-history/4531

Chapter 7
Print ISBN: 978-93-49473-44-7, eBook ISBN: 978-93-49473-43-0

Optimisation of Cutting Parameters in Dry Turning of EN19 Steel Material

N. Tayisepi [a*], A N Mnkandla [a], G Tigere [b], O Gwatidzo [b], L M Wagoneka [b] and E Ndala [b]

DOI: https://doi.org/10.9734/bpi/erpra/v5/2645

Peer-Review History:
This chapter was reviewed by following the Advanced Open Peer Review policy. This chapter was thoroughly checked to prevent plagiarism. As per editorial policy, a minimum of two peer-reviewers reviewed the manuscript. After review and revision of the manuscript, the Book Editor approved the manuscript for final publication. Peer review comments, comments of the editor(s), etc. are available here: https://peerreviewarchive.com/review-history/2645

ABSTRACT

The thrust of cost-cutting, in manufacturing enterprises recently, had been focused on energy efficiency and quality improvement consideration, largely, as an effort to respond to environmental apprehensions regarding legislation, standardisation and market growth. In steel material mechanical cutting, on the lathe machine, the convergence adequacy of the cost-quality-time matrix effectually is contingent upon the supreme choice combination of the set cutting parameters. This experimental investigation examined, the minimisation of energy consumption and enhancement of the generated component surface quality, by optimising the applied machining parameter settings, as a means of fostering sustainability in the dry cutting of EN19 material by turning on the conventional lathe. Optimising mechanical machining operating parameters points to a significant challenge confronting the machine shops industry as they endeavour to realise reduced electrical energy consumption and improved component surface finish quality, generated from their businesses. The study aimed to reconnoiter and establish the association of the machining process strategy factors with the consequence of minimum energy consumption and surface smoothness quality, of the components, as the machining input factors were adjusted from minimum to the highest level of setting respectively. Taguchi's Full Factorial investigational strategy was employed in organising the empirical machining experiments. Analysis of variance (ANOVA) and the main effects plot (MEP) signal-to-noise ratio optimising computation were utilised, in the study, to determine the impact of the variable input-cutting process factors on the dependent parameters – surface roughness and energy use. Optimum,

[a] *Department of Industrial and Manufacturing Engineering National University of Science and Technology, Bulawayo, Zimbabwe.*
[b] *Department of Industrial and Manufacturing Engineering Harare Institute of Technology, Harare, Zimbabwe.*
**Corresponding author: E-mail: nicholas.tayisepi@nust.ac.zw;*

minimum energy consumption and good surface roughness generating, machining conditions were determined. Results of the all-encompassing experimental investigation yielded optimum cutting conditions of, respectively, energy consumption minimisation (100 m/min cutting speed, 0.1 mm/rev feed rate and 0º rake angle) and surface smoothness quality (100 m/min cutting speed, 0.4 mm/rev feed rate and 0º rake angle). Validation experiments corroborated the results findings of the developed model within 4.7% variability.

Keywords: Machining; energy efficiency; ANOVA; sustainable manufacturing; machining strategy.

1. INTRODUCTION

Mechanical machining constitutes the solitary most applied subtractive manufacturing method, whereby an amount of excess material is taken off in layer-by-layer succession, by the action of the cutting tool edge, on the component workpiece periphery.

Machining is mainly employed as a finishing operation intended to produce excellent component geometry accuracy with decent cost-effectiveness and efficiency (Pimenov et al., 2022). Mechanical finish machining is also employed as a components processing methodology intent on enhancing productivity and quality improvement, particularly surface finish (Huang et al., 2023), a visual macroscopic attribute by which customers easily determine the acceptability, or lack thereof, of new components after manufacture. Energy consumption is the main concern of the manufacturing industries (Batouta et al., 2023). Machining is one of the most fundamental energy-consuming manufacturing operations which is broadly used in the production of discrete products such as components made of EN19 alloy steel (Tayisepi et al., 2024). Surface roughness, of machined components, has a huge influence on finishing costs and the perceived quality of machined products, notably as considered from a sustainability point of view.

Energy expenditure constitutes one major, among the several vital, factors which have a significant impact towards the determination of the economy and environmental encumbrance of a manufacturing operations process (Haddouche & Ilinca, 2022). The manufacturing sector, of which subtractive machining processes constitute a significant portion, accounts for the consumption of about a third of the total global account of energy generated. The machining industrial enterprises represent an identified energy consumption reduction potential of 18–26%, in the total energy consumption mix, if more prudent energy expenditure mechanisms are implemented (Pimenov et al., 2022). Yet machining consumes significant energy during manufacturing operations. Concern, about energy resource use efficiency as well as sustainability, has escalated in recent years, and environmental apprehensions have led to the recent proliferation of legislated laws, regulations and guidelines, by nation-state governments across the world, directed at the environmental sustainability focus of manufacturing enterprises. Aggregating this with the ever-escalating asking price of electrical energy combined with the intensifying large-scale competition versus the

snowballing energy demand (Mickovic & Wouters, 2020), by consumers, for more efficient and cheaper products has placed tremendous pressure on manufacturing enterprises to radically improve machining energy use efficiency and surface quality generation capabilities, in order to magnify the competitiveness and profitability of the business. Mechanical machining manufacturing operations, and energy use efficiency need to be carefully planned. The subtractive manufacturing operation parameters which foster process optimality need to be appropriately forecasted (Fose et al., 2024), during the cutting planning stage. Hence, analysis and understanding of machining systems and optimisation of the machining parameters - for energy use at the process level and surface quality generation - before the actual cutting begins, has become very important in the metal machining business.

Sustainability generally relates to the feasibility of continuing with a defined pattern of behaviour for an indefinite duration of existence, (Rodríguez-Espíndola et al., 2022; World Commission on Environment and Development, 1987). The role played by manufacturing is indispensable within the global economy operation. Machining constitutes one of the oldest major industrial manufacturing processes and is also regarded as the most widely used manufacturing technology for shaping a variety of components (Jamwal et al., 2021). It is an extremely important application operation which allows the creation of complex-shaped items for many purposes, especially, in the manufacture of discrete mechanical industrial workpieces and components such as EN19 cylindrical components required for the rail and the automobile industries. Estimates project that 15% of the value of all mechanical components manufactured, globally, comes from machining operations (Sarıkaya et al., 2022; Tayisepi et al., 2024). Machining allows the forming of intricate-shaped items and the generation of desired surface finish quality of precision components. In the same vein, machining involves a number of sustainability factors and has potentially significant environmental impacts noting that as a manufacturing process, it involves controlled application of energy to convert raw materials into finished goods.

EN19, also known as 708M40 709M40 / AISI 4140 is a high utility quality medium-carbon alloy steel (Sinha & Mukhopadhyay, 2023) applied in the manufacturing of multiple-profiled cylindrical components for machine tools, motor vehicle components and rail locomotive components among others purposes. It is a high-strength, high-utility engineering material commonly used for high load-bearing application components, manufactured for the automotive, oil and gas industries for making gears, multiple-profiled cylindrical shafts, high-tensile strength studs and bolts, rifle barrels, propeller shaft joints, pins, breech mechanisms for small arm parts, induction hardened track pins, spindles and rods, inter alia parts. It is a material which possesses high tensile strength, good ductility, good wear and shock resistance and is characterized as a difficult-to-machine material, which can also be cut to highly precise dimensional tolerances (Tayisepi et al., 2024). Its application properties can be further enhanced by post machining operations such as heat treatment e.g. induction hardening. Mechanical machining of EN19 material components is widely used in

manufacturing industries and represents a significant demand for energy (Tayisepi et al., 2023)

Energy consumption rate and surface roughness present two essential machinability performance evaluation metrics considered and which require close attention, by the machining-based manufacturing industries (Tayisepi et al., 2024). The importance of these factors is amplified by the need for the machining industries, of EN19 material, to manufacture low-cost and high-quality components in short periods of time during which production rate and material removal rate are significant considerations (Yadav & Shrivastava, 2021).

Sustaining the quality consistency, of machined components, during turning operation is a key challenge faced by the discrete cylindrical EN19 parts machining businesses (Krishna, 2023), especially, when this has to be realised energy efficiently (Tayisepi et al., 2024). Thus, it is vital to optimise, for the quality of surface roughness and the energy use rate, the cutting process. The machining parameter optimisation is vital in causing minimisation of the EN19 components manufacturing cost with the achievement of appropriate surface roughness.

Earlier research findings, on the machining of Ti6Al4V, established that higher machining rates and material removal rates are associated with lower energy use (Oosthuizen et al., 2013). Whilst the findings by Tayisepi et al., (2016), on the same material, established that the component surface quality deteriorates as the cutting speed and feed rate increase. In this highly competitive global business environment, infested with constraining challenges, fulfilling the prerequisites of elevated productivity, achieving sustainably good surface quality, of the machined EN 19 components, cost-effectively and energy efficiently, whilst also preserving resources of the machining process, forms a difficult-to-balance matrix (Tayisepi et al., 2024). These features have become measurement metrics of the quality superiority in machining manufactured components lately.

Published literature exists on the optimisation and machinability improvement of other materials using varied sustainability-oriented cutting strategies. For example, Duflou, et al., (2012) and Dawood, (2016) discussed different techniques and strategies for the sustainable machining manufacturing of, particularly, titanium alloys. Special reference was made to the selection of optimum cutting conditions intent on minimising energy use, implementation of advanced lubrication and/or cooling techniques and the application of advanced hybrid cutting strategies, and cutting tool geometry optimisation and these factors have material effect on the machining process (Tayisepi et al., 2024). Gupta and Laubscher, (2016) wrote on the schemes which augment the improvement of titanium alloy machining sustainability which, among others include: the adoption of hybrid machining methods, use of advanced cooling and lubrication strategies, optimising machining parameters and selection of appropriate tool material and geometries. They delineated key drivers which buttress the realisation of the sustainable machining of titanium alloys which include – attaining resource efficiency through minimising tool failure, ensuring lower power and energy

consumption, reduction of consumption of cutting fluids and water, reduction of waste, part quality improvement and minimisation of environmental pollution (Tayisepi et al., 2024). Not much literature, however, is published on the optimum and sustainable machining of EN19 steel materials, particularly with respect to the machining planning stage determination of suitable cutting parameters for minimising energy use and generation of good quality surface on the workpiece exterior from the lathe turning process.

Surface roughness, a surface integrity component, is a vital quality feature of machined EN 19 material components. Surface roughness, attributable, influences the mechanical and physical performance characteristics of machined components, as the post-machining functionality of processed parts is essentially influenced by the surface finish quality produced during the cutting process (Liao et al., 2021; Tayisepi et al., 2024). According to Abellán-Nebot, et al., (Abellán-Nebot et al., 2024) the effectiveness metrics of a machining process, among other factors, can be read through improved component surface quality and energy use efficiency. Therefore, the selection of a suitable cutting parameter combination, which prompts energy use conservation, presents an appropriate strategy to adopt - during machining - in order for the cutting to be sustainable (Tayisepi et al., 2024).

This research, presents the results of the innovative application of the Taguchi statistical tools, in an experimental study of the cutting parameter optimisation process, for energy-efficient machining and improved surface quality generation, during the outside turning of EN19 material (Tayisepi et al., 2024). The intention of the study is to aid the machining industry of EN 19 material by establishing the optimum cutting parameters for obtaining the good surface quality desired at minimum energy use during the process planning of the cutting operation. This information is anticipated to help aid the machining industry in improving their process planning of steel-cutting operations.

1.1 Analysis of Variance (ANOVA) and Signal-to-Noise (S/N) Ratio

In a design of experiments research plan the Analysis of Variance (ANOVA) is used to test the significance of the influence of input process parameters, from a series of experimental results, on the response parameters. ANOVA determination can be used to test the significant differences between means, with the variance being used to determine whether the means are different. Analysis of variance tests the hypothesis that the means of two or more populations are equal, wherein, the null hypothesis postulates that all population means (factor levels) are equal whilst the alternative hypothesis states that at least one is different (Tayisepi et al., 2024). The importance of one or more factors is assessed by comparing the response variable means at different factor levels (Yilmaz et al., 2023). Vital significant process variables which impact and control the process, out of the many parameters, are used to develop the mathematical model required to represent the process. ANOVA tests can be one-way or two-way. One-way ANOVA tests the quality of population means when classification is by one variable (factor) which usually has three or more levels

(Tayisepi et al., 2024). The level represents the treatment applied. Examination of differences among means using multiple comparisons is possible with the one-way procedure. A one-way ANOVA with two levels is equivalent to a t-test (Mishra et al., 2019). When the classification of treatment of the population means is by two variables (factors) then a two-way ANOVA is used to perform the quality testing (Atia et al., 2022). In a two-way ANOVA, the data must be balanced, i.e. all cells must have the same number of observations and the factors must be fixed (Mishra et al., 2019). The input factors in this study were cutting speed, tool rake angle and feed rate, in the 95% confidence interval (Tayisepi et al., 2024). Thus, significant factors will have a p-value of 0.05 or less in the tested range.

Signal-to-noise (S/N) ratio – expresses the ratio of the mean (signal) to the standard deviation (noise). This is the statistical measure of performance used to select the best control levels that best survive the noise factors with minimum variation effect on the process outcome (Tayisepi et al., 2024). Control factors which reduce the inconsistency in the process are established through a measure of robustness which is attained through minimising the effect of the uncontrolled (noise) factors. Noise factors cannot be controlled during processing, but during the planning (Pathan et al., 2022). Higher S/N ratio values pinpoint control factor settings that minimise the effects of the noise factors. The S/N ratio measures how the response varies relative to the target or nominal value under different noise conditions (Tayisepi et al., 2024). Generally, the three categories of performance characteristics used to analyse the S/N ratio are nominal-is-best, larger-the-better and smaller-the-better (Zafari et al., 2023). Whereas there are several different possible S/N ratios the main standard ones which were also considered for this research were (Rajpure et al., 2017): (a) Biggest-is-Best quality characteristic given by equation Eq1, thus:

$$SN_B = 10log\left[\frac{1}{n}\sum_{i=1}^{n}\frac{1}{y_1^2}\right] \quad (1)$$

Where y_i is the value of the i[th] quality characteristic and n is the number of experiment tests.

The nominal is best characteristic equation is presented in Eq 2

$$SN_T = 10log\left[\frac{y^{-2}}{S^2}\right] \quad (2)$$

The characteristic given by, equation (3), is the smallest is the best factor of quality.

$$SN_S = 10log\left[\frac{1}{n}\sum_{i=1}^{n} y_i^2\right] \quad (3)$$

S/N ratio data analysis should determine the best optimum setting of the operating parameters (cutting speed, tool rake angle and feed rate) in order to attain the desired machined component quality at minimum energy expenditure

and desired surface quality (Tayisepi et al., 2024). The optimum operating conditions are obtained by selecting the parameters that give the maximum values of the S/N ratio. This is done by using the main effects plots of the S/N ratios (Tayisepi, 2017). In this study, the quality of performance is maximised by minimising the surface roughness and (energy use) requirement of the machining process. Thus the smallest is best characteristic is used.

2. METHODOLOGY, MATERIALS AND EQUIPMENT

Multi-level full factorial design was utilised as the experiment planning scheme. The aim of the experimental investigation was to analyse and understand the trends of the relationship of the variable input mechanical cutting process parameters (cutting speed, feed rate and cutting tool rake angle) with the response factors, being the energy consumption minimisation and surface texture quality improvement, of machined EN19 components. Furthermore, the study, aimed to establish optimum variable cutting parameters which yield minimum energy use and improved surface texture quality during the outside turning of cylindrical EN19 components.

2.1 The Experimental Equipment

Fig. 1. Cazeneuve 360 HB-X precision lathe machine

Turning experiments were carried out using the Cazeneuve 360 HB Precision Lathe machine, shown in Fig. 1 (Tayisepi et al., 2024). The lathe machine features include the following: maximum spindle speed of 3000 rpm from least value of 50 rpm; maximum swing of 200 mm; maximum power of the main motor, 5.15 kW and spindle bore of 40 mm. The equipment used in the experimental study and the experimental set-up configuration schematic arrangement are shown in Fig. 2 (Tayisepi et al., 2024).

2.2 The Experiment Specimens Materials

The EN19 alloy specimen material was supplied in tensile condition as a solid round bar (Ø = 40 mm x 150 mm long). The experimental work piece's chemical and mechanical properties - as provided on the material certificate - are, respectively, shown in Table 1 and Table 2 (Tayisepi et al., 2024).

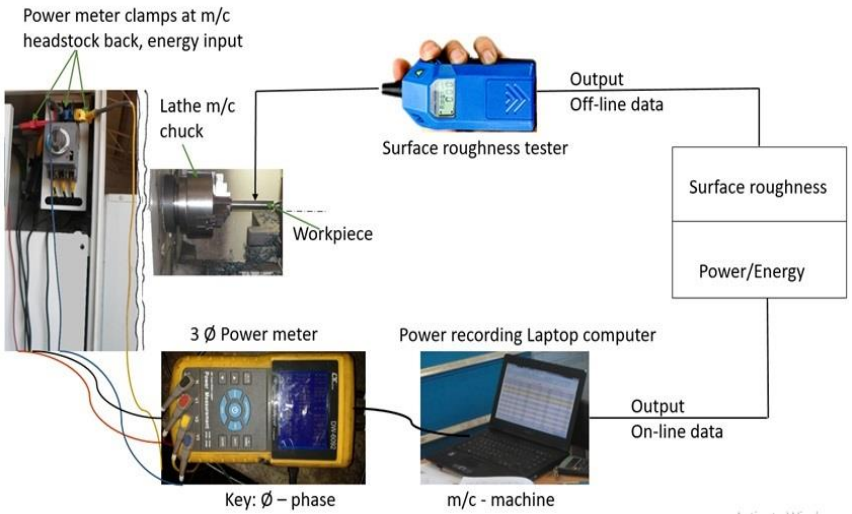

Fig. 2. The machining process experimental setup.

Table 1. Chemical Composition of the specimen material (weight %)

Element	Mn	Si	C	Cr	P	Ni	S	Mo
Composition %	0.86	0.220	0.414	1.3	0.016	0.031	0.014	0.32

Table 2. Mechanical properties of the specimen material

Condition	Tensile Mpa	Yield Mpa	Elongation %	Izod impact	Hardness Brinell
T	940	680	13	54	280

2.3 Experiment Design and Procedure

A total set of 48 experiment runs - constituted of combinations of 3 factors - were carried out. The experimental procedure involved, respectively, varying cutting speed in four levels, four levels of variation of feed rate and three levels of variation of the cutting tool rake angle, whilst the depth of cut was kept constant and the cooling mode was dry machining. The cutting conditions are shown in Table 3 (Tayisepi et al., 2024).

Table 3. Machining parameters and conditions of the turning experiments

Parameter	Condition	Units
Cutting Speed (v_c)	100, 150, 200 and 250	M/min.
Feed/rev (f_n)	0.1 – 0.4 in 0.1 mm steps	Mm/rev
Tool Rake angle	0º, 5º and 10º	Degrees
Depth of Cut (DoC)	0.5 constant	mm
Coolant	Dry machining.	

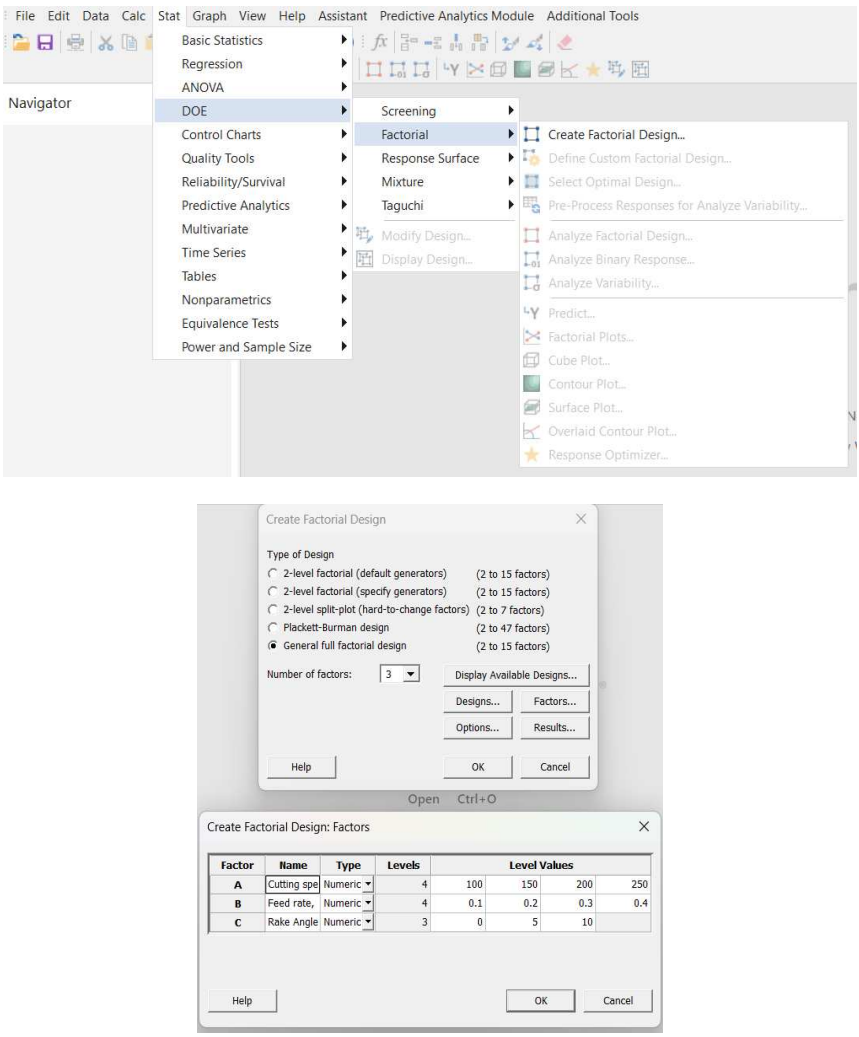

Fig. 3. Full factorial design of experiment planning in Minitab

The experiment variable input parameters planning, on the Minitab platform, proceeded as shown in the indicated steps in Fig. 3 (Tayisepi et al., 2024).

The output is the tabulation of the experiment iteration plan which was utilized in executing the experiment process indicating the factor combination levels. These factor combinations are indicated in the summary presentation of the experiment results in Table 4 (Tayisepi et al., 2024).

The focus of this research study was the energy transformation stage at the machining process level and the surface roughness trends of the machined component. Electrical energy is supplied to the lathe machine, and is converted into mechanical energy (kinetic) which is used to separate the material during cutting at the different cutting speeds and feed rates using coated solid carbide tipped tools with 3 levels of rake angle. Some of the energy is used to power the machine's functional unit modules (as constant power) as well as to supply lubrication and cooling at the cutting tool-workpiece interface (Tayisepi et al., 2024). At the process level, during cutting, the kinetic energy is transformed into various energy outputs. A coated carbide-tipped tool mounted in a Sandvik tool holder (DCLNL 2525 M12) was used for the external diameter turning of EN19 solid material round billet specimens under dry machining conditions. The cutting conditions were varied during the experimental process with cutting speed, v_c = 100 - 250 m/min in steps of 50 m/min, feed rate, f_n = 0.1 - 0.4 mm/rev in steps of 0.1 mm/rev and rake angle, α = 0º, 5º and 10º. A constant depth of cut of 0.5 mm was utilised. In order to conform with the ISO Standard 3685-1977 (E), for single-point turning tools, a wear criterion of V_B = 300 µm (Oosthuizen et al., 2013) was used for all the machining experiments. Surface roughness (Ra) was measured using a T500 Hommel surface roughness tester. An average of 3 surface roughness measurements at 3 different spots on the machined shaft was recorded (Tayisepi et al., 2024).

The power requirements of a machining production operation can be obtained by measuring the power input to the machine tool drive during a cutting operation and then subtracting the idle (tare) power (Tayisepi, 2017). The energy expended by a machining process may be estimated by direct measurement - wherein the current, voltage and power factor, during machining, are directly measured. This approach, although expensive and requires close monitoring, produces accurate data on the exact power consumed (Tayisepi et al., 2024). Deriving from the analysis of this base data, prediction and optimisation models of energy consumption and surface roughness can be developed. Otherwise, the power can be measured indirectly by estimating it from the forces and velocities data (Pimenov et al., 2022). In this study, the direct energy measurement method was used. Power measurements were carried out using the Digital Lutron 3 Phase Power Analyser DW- 6092 (Tayisepi et al., 2024).

In this experimental study, the Average surface (Ra) value - which is one of the most important machinability criteria - was measured by using Mitutoyo's Surftest surface roughness tester within a sampling length of 2.5 mm. Ra expresses the

average deviation of a surface from the mean height (Basha et al., 2022). It is a measure of the irregularities on the surface and is one of the characteristics of the surface texture, besides waviness and lay (Tayisepi et al., 2024).

3. RESULTS AND DISCUSSIONS

The experimental study results, show information on the outcome of the combination of variable input factors on the output response parameters. Analysis of variance (ANOVA) was applied to provide robust and detailed statistical analysis on the comparative influence dominance of the respective input parameters on the dependent outcomes. Results of the experimental investigation are laid out under the main sections – results presentation, optimisation and then discussion and analysis.

3.1 Results Presentation

Table 4 presents the summary of the experiment results. Ensuing is the presentation of the rest of the experiment study results in detail.

3.1.1 Trending of response factors with independent parameters

Fig. 4 presents the graphical results plot of the dependent factors – surface roughness, cutting power and energy use, under the effect of changed cutting speed. Fig. 4 (a) shows decreasing surface roughness, whilst cutting power increases in Fig. 4(b) and energy use decreases, as the cutting speed respectively is increased.

The graphical plot, of the experiment results, presented in Fig. 5 shows the increase in surface roughness (Fig. 5a), increase in cutting power (Fig. 5b) and the decrease in energy consumption (Fig. 5c), as the feed rate input factor is correspondingly increased.

Results presented graphically, in Fig. 6 (a) hardly show a decrease and then a minimum increase in surface roughness as the tool rake angle is increased in the range from zero to ten degrees. Cutting power also marginally increases in response to incremental variation of feed rate within the same cutting parameter range, as shown in Fig. (b). In Fig. 6 (c), graphical results show energy use decreasing as the tool rake angle increases.

3.2 Results Presentation – ANOVA and MEP Optimisation

The analysis of variance (ANOVA), of surface roughness, results are presented in Table 5. The ANOVA results show that the three variable input parameters – feed rate, rake angle and cutting speed have a positive effect on the measured response parameter, surface roughness – Ra (Tayisepi et al., 2024). The three input parameters have a significant influence on surface roughness.

Table 4. Summary of the experiment results

Iteration Number	Cutting speed, v_c (m/min)	Feed rate, f_n (mm/rev)	Rake angle degrees	Surface roughness Ra (µm)	Av Power (kW)	Cutting Energy (Joules)	Iteration Number	Cutting speed, v_c (m/min)	Feed rate, fn (mm/rev)	Rake angle degrees	Surface roughness Ra (µm)	Av Power (kW)	Cutting Energy (Joules)
1	100	0.2	5	10.00	0.31	144.36	25	100	0.1	10	11.60	0.23	299.36
2	100	0.1	5	13.70	0.12	317.16	26	150	0.4	0	20.00	1.10	86.00
3	200	0.2	0	10.00	0.80	108.68	27	200	0.4	0	16.67	1.26	67.12
4	100	0.4	0	15.00	0.83	146.52	28	200	0.2	5	10.00	0.86	115.44
5	100	0.4	5	15.00	0.64	100.41	29	100	0.3	10	15.00	0.58	112.73
6	250	0.3	0	10.00	0.88	75.83	30	150	0.3	5	12.33	0.94	99.31
7	150	0.3	10	12.33	0.90	101.16	31	250	0.2	10	10.00	1.20	117.79
8	150	0.1	10	10.00	0.03	260.23	32	200	0.3	5	16.67	0.82	102.29
9	100	0.3	0	23.00	0.15	169.98	33	250	0.3	10	20.00	1.39	83.07
10	200	0.4	10	17.00	1.80	79.44	34	150	0.2	10	11.67	0.66	139.21
11	150	0.1	0	13.00	0.24	304.46	35	200	0.4	5	15.00	1.50	72.34
12	100	0.1	0	15.00	0.42	347.18	36	200	0.1	5	10.50	0.52	232.02
13	250	0.4	5	13.33	1.52	58.90	37	200	0.3	0	10.00	1.01	104.19
14	250	0.4	10	10.00	1.90	68.08	38	250	0.3	5	15.00	1.35	83.58
15	250	0.1	10	8.50	0.28	165.75	39	100	0.4	10	20.00	0.79	89.70
16	250	0.2	0	10.00	0.83	105.44	40	250	0.4	0	15.00	1.61	66.61
17	150	0.2	5	5.00	0.39	120.48	41	100	0.2	10	12.00	0.47	149.84
18	150	0.4	10	15.00	0.77	94.35	42	100	0.3	5	11.67	0.41	99.30
19	100	0.2	0	10.00	0.39	242.54	43	200	0.1	0	11.60	0.48	258.15
20	150	0.3	0	12.33	0.08	71.96	44	250	0.1	0	10.00	0.77	193.41
21	250	0.1	5	9.20	0.67	179.99	45	250	0.2	5	12.33	0.85	110.55
22	200	0.1	10	9.60	0.45	188.55	46	150	0.4	5	15.00	0.78	77.34
23	150	0.1	5	12.50	0.52	295.41	47	200	0.3	10	15.00	1.19	94.55
24	200	0.2	10	15.00	0.79	145.60	48	150	0.2	0	15.00	0.59	121.44

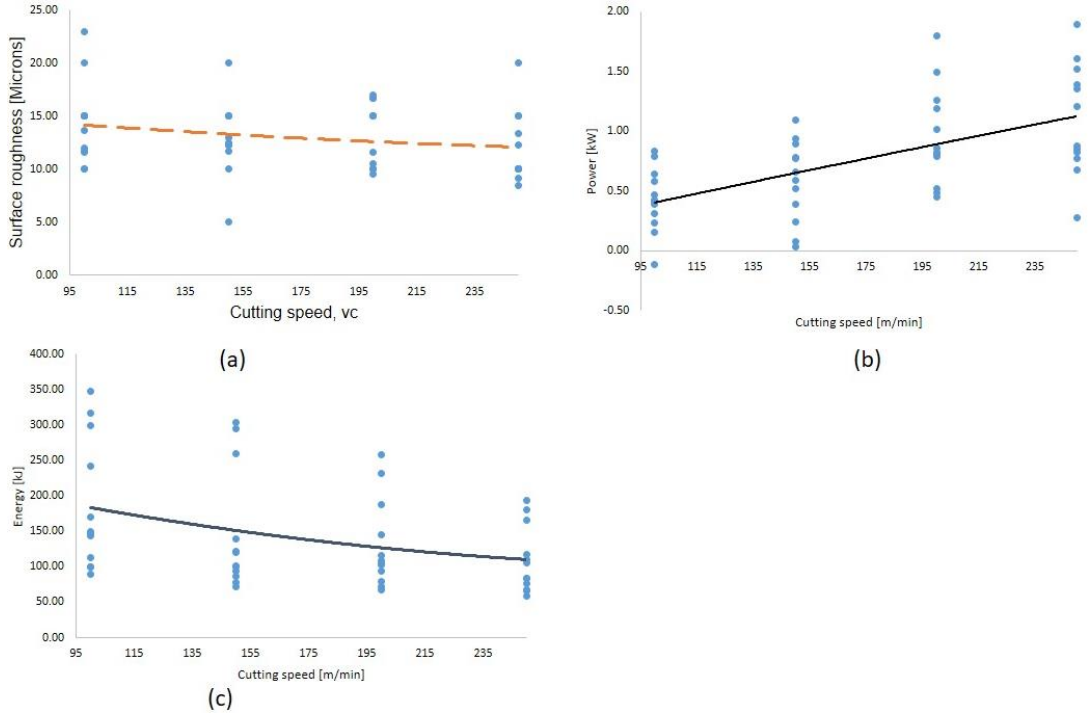

Fig. 4. Surface roughness, power and energy use as function of cutting speed

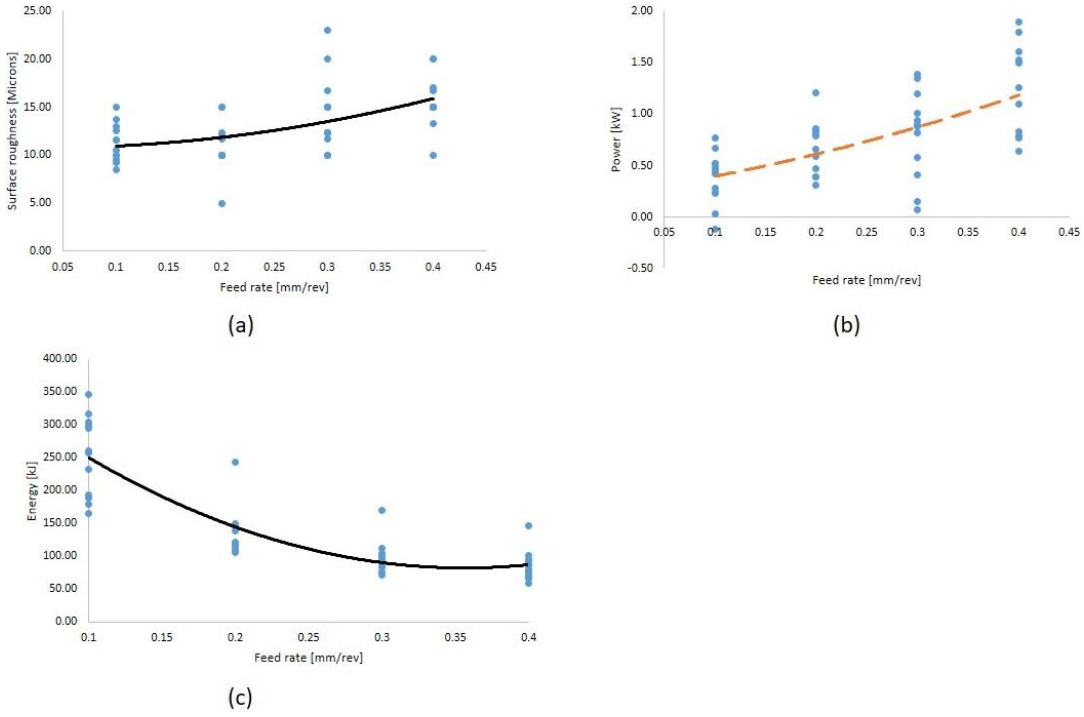

Fig. 5. Response factors under the effect of changing cutting speed

Table 5. Analysis of variance for surface roughness, Ra

Source	DF	SS	MS	F	P
Cutting speed, *vc*	3	55.74	18.58	1.58	0.0209
Feed rate, *fn*	3	215.68	71.89	6.12	0.0025
Rake angle	2	21.94	10.97	0.93	0.0402
Error	39	458.23	11.75	-	-
Total	47	751.59	-	-	-

The signal-to-noise ratios main effects plot results for surface roughness are presented in Fig. 7. The plot was premised on the surface quality characteristic of equation Eq 3 which is the smallest and is the best. The Taguchi analysis of surface roughness, resulting from the main effects plots of the signal-to-noise ratio, shows that the optimum cutting parameter combination returning optimum surface roughness response is 100 m/minute cutting speed, 0.4 mm/rev and 0-degree rake angle (Tayisepi et al., 2024).

The mathematical model explaining the relationship of surface roughness, Ra, with the variable input parameters was approximated from regression analysis, and the result is presented in equation 4:

$$R_a = 12.31 - 0.01732 \text{ Cutting speed, } v_c + 17.06 \text{ Feed rate, } f_n - 0.068 \text{ Rake angle} \quad (4)$$

The model summary for surface roughness is presented in Table 6 and the residual plot histogram and normal probability plot, given in Fig. 8, show most of the data points around the mean line which shows near normal distribution (Tayisepi et al., 2024). This confirms the effective representativeness of the data being sculpted by the model.

The ANOVA, at 95% confidence level, results of average power show that the three variable cutting parameters – cutting speed, feed rate and rake angle – had a significant positive influence on average machining power given that their p-values are less than the threshold value of 0.05 (Tayisepi et al., 2024). Thus, the input factors have a significant influence on the response parameter, average machining power. It is apparent, however, that the effect of rake angle (at a p-value of 0.273) is less influential, on the response parameter than that of both cutting speed and feed rate whose p-value both is 0.000.

Table 6. Surface roughness regression model summary

S	R-sq	R-sq(adj)
3.42775	39.03%	26.53%

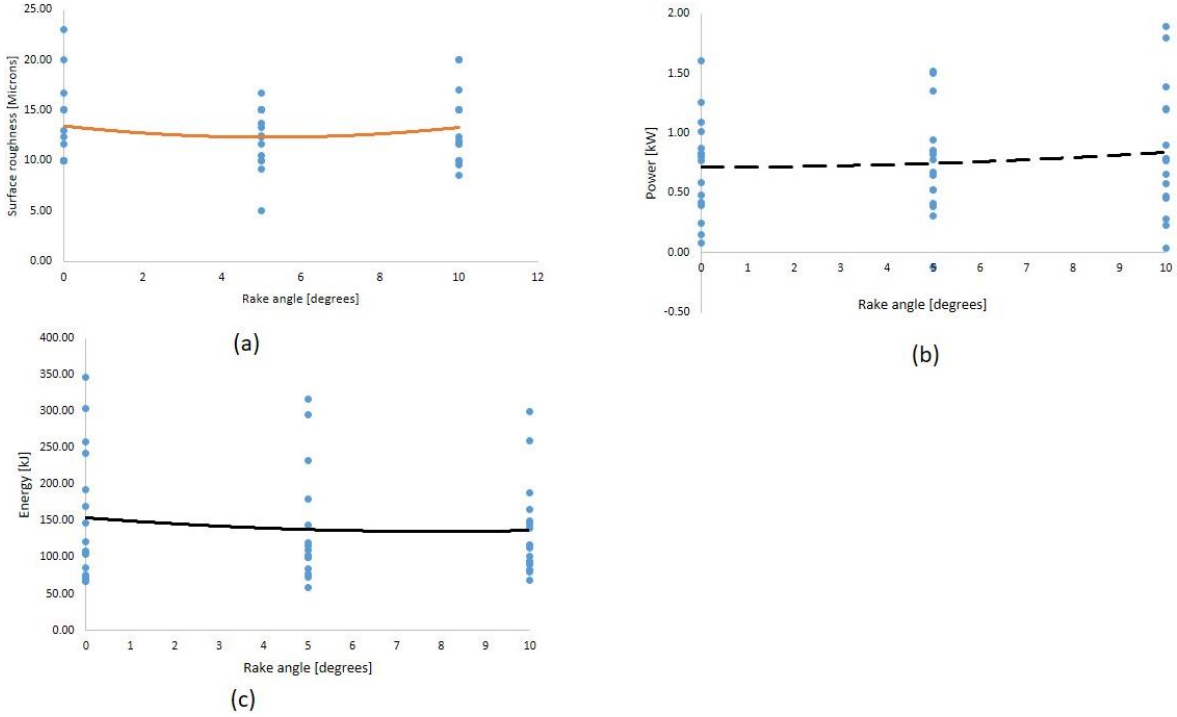

Fig. 6. Dependent factors under the effect of changed cutting speed

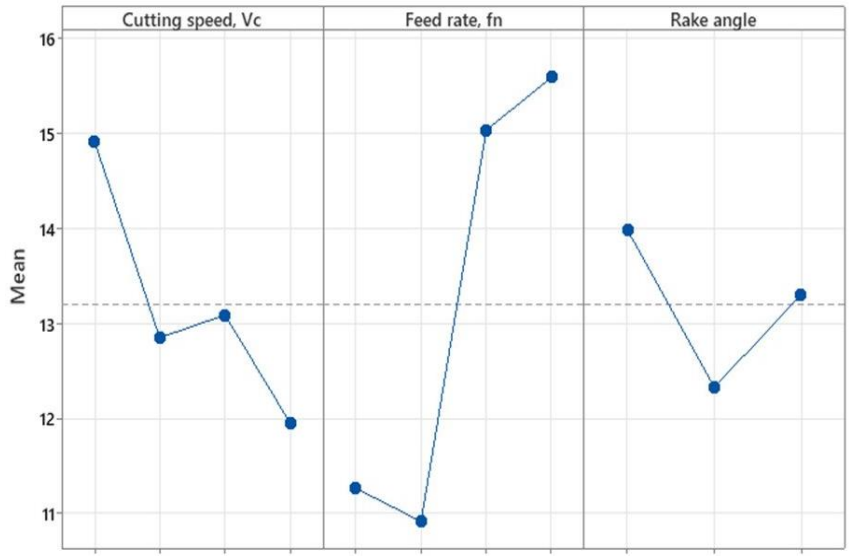

Fig. 7. Surface roughness signal-to-noise ratio main effect plot

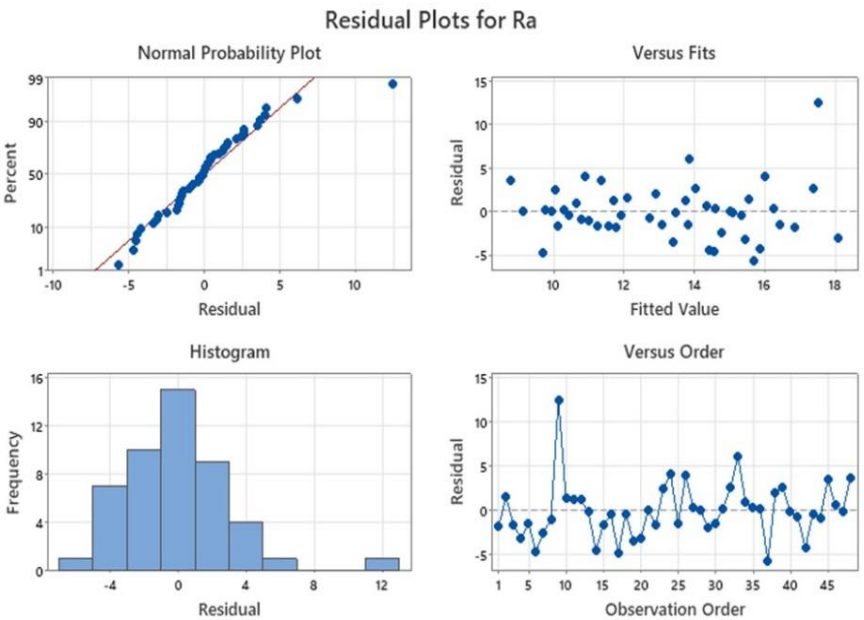

Fig. 8. Surface roughness residual plots

Table 7. ANOVA for average power

Source	DF	SS	MS	F	P
Cutting speed, *vc*	3	3.5970	1.19900	24.03	0.000
Feed rate, *fn*	3	4.2771	1.42570	28.57	0.000
Rake angle	2	0.1340	0.06699	1.34	0.273
Error	39	1.9461	0.04990	-	-
Total	47	9.9542	-	-	-

The Taguchi analysis of the average machining power - main effects plot for the signal-to-noise ratios of average machining power - results presented in Fig. 9, shows that power use optimisation is achievable by operating at a cutting speed of 250 m/min, feed rate of 0.4 mm/rev and rake angle of 10 degrees (Tayisepi et al., 2024). Thus, efficient operation improvement would need that feed rate to be addressed first before cutting speed and rake angle is respectively successfully addressed.

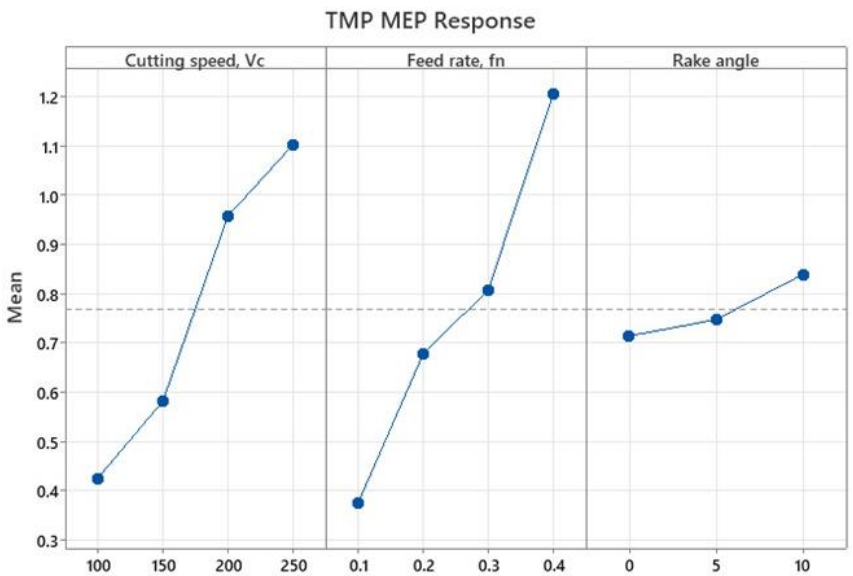

Fig. 9. Signal-to-noise ratio main effect plot for average power

The mathematical relationship of the input variables (cutting speed, feed rate and cutting tool rake angle) to the response parameter (average cutting power) is expressed in the regression equation in Eq5. The strong representativeness of the data by the fitted regression line is indicated by the coefficient of determination (r^2) of 80.45% shown in the model summary of the average machining power (Table 8) confirm the strong representativeness of the fitted regression model by the data (Tayisepi et al., 2024).

$$Av\ Power = -0.794 + 0.004813v_c + 2.624f_n + 0.01249\ Rake\ angle \quad (5)$$

Table 8. Average power regression model summary

S	R-sq	R-sq(adj)
0.223384	80.45%	76.44%

Further confirmation and validation of the regression model as an authentic representation, of the data considered, is presented in the residual plot of the average machining power model (Fig. 10) in which more than 80% of the points are shown to be about the mean line in the normal probability plot and appearing to be in near normal distribution in the histogram (Tayisepi et al., 2024).

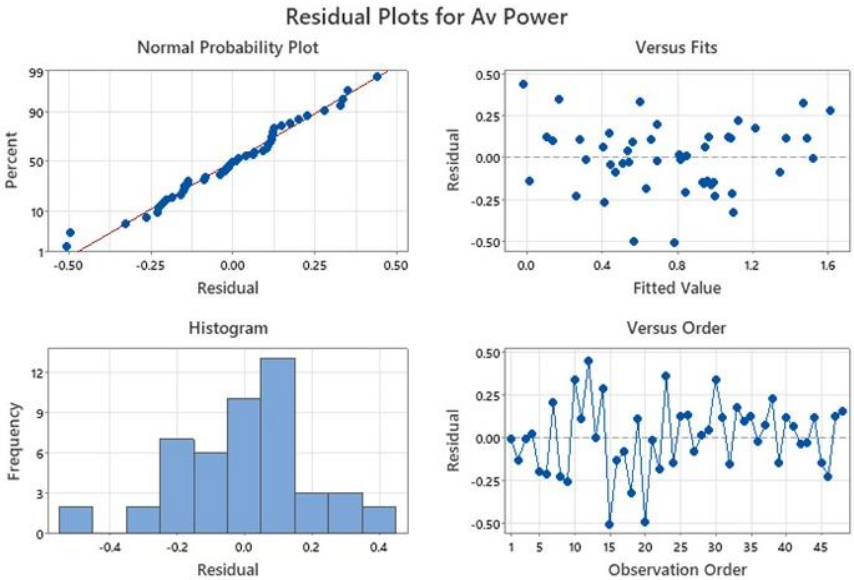

Fig. 10. Residual plots of the average cutting power

Machining energy was also one of the response parameters assessed. Machining energy was determined from considering the applied power and the time length taken to execute a machining operation. The machining energy analysis of variance result is presented in Table 9 (Tayisepi et al., 2024). The machining energy ANOVA result trend is similar to the average cutting power result where all the input variable cutting parameters (cutting speed and feed rate) have a positive influence on the response parameter, machining energy whilst the cutting tool rake angle is insignificantly influential on the response parameter (Tayisepi et al., 2024). The ANOVA p-values, of the first two input parameters, were less than 0.05, showing that the influence of cutting speed and

feed rate, on the response parameter, is more dominant than cutting tool rake angle with a p-value of 0.142 whilst the former both have p-values of 0.000.

Table 9. Analysis of VARIANCE FOR MACHINING ENERGY

Source	DF	SS	MS	F	P
Cutting speed, Vc	3	36965	12321.8	16.57	0.000
Feed rate, fn	3	211472	70490.6	94.81	0.000
Rake angle	2	3057	1528.6	2.06	0.142
Error	39	28997	743.5	-	-
Total	47	280491	-	-	-

The numerical relationship of the input variables (cutting speed, feed rate and cutting tool rake angle) to the response parameter (machining energy) is expressed in the regression model in Eq6. The robust representativeness of the data by the fitted regression line is signposted by the coefficient of determination (r^2) of 72.59% shown in the model summary of the machining energy (Table 10) confirming the strong representativeness of the fitted regression model by the data.

$$Energy = 373.4 - 0.4889\ Cutting\ speed,\ V_c - 544.0\ Feed\ rate,\ f_n - 1.75\ Rake\ angle \quad (6)$$

Table 10. Machining energy use model summary

S	R-sq	R-sq (adj)	R-sq (pred)
38.3257	76.96%	75.39%	72.59%

The Taguchi analysis, main effects plot of the S/N ratio of the machining energy, results are presented in Fig. 11 (Tayisepi et al., 2024). The results show that the optimum cutting energy is attainable by setting the input variables at the following conditions: cutting speed at 100 m/min, feed rate at 0.1 mm/rev and rake angle at 0 degrees.

Additional corroboration and authentication of the regression model as a reliable representation, of the data considered, is presented in the residual plot of the machining energy model (Fig. 11) in which more than 90% of the normal probability plot points are shown closely hugging the mean diagonal line and seeming to be in near normal distribution in the histogram.

3.3 Results Discussion and Analysis

As presented in Fig. 4(a), it is apparent that surface roughness tended to decrease as the cutting speed increased. This phenomenon is attributable to the circumstance in which material tends to quickly thermal soften and is easily sheared off the parent material, in the cutting tool and workpiece interface zone, as the cutting tool rapidly advances during the cutting.

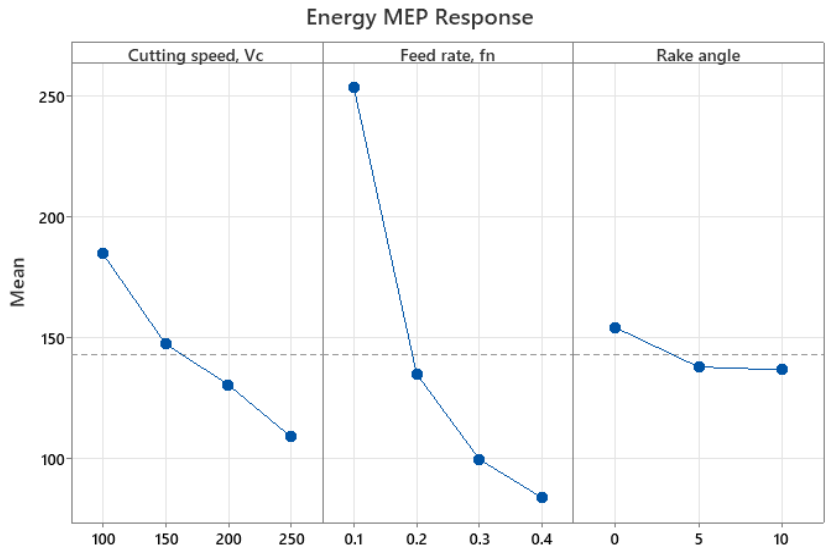

Fig. 11. Signal-to-noise ratio main effect plot of cutting energy.

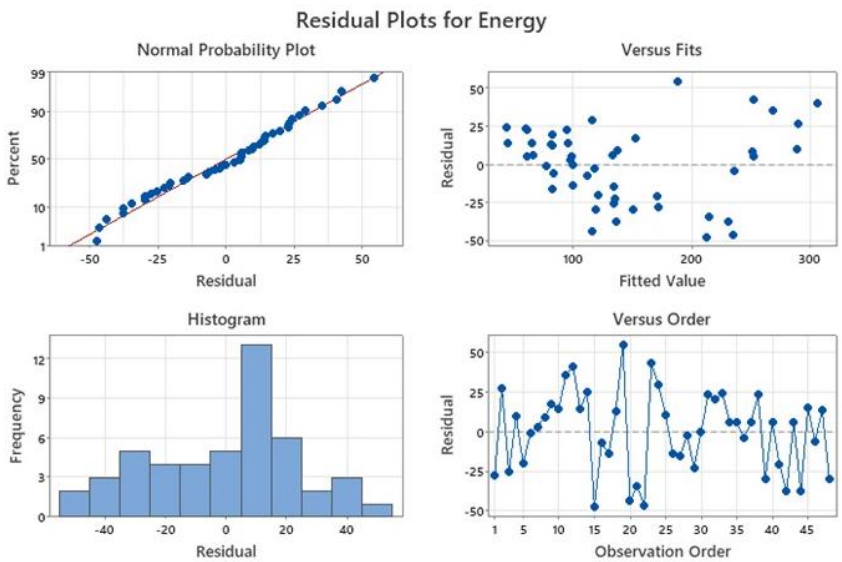

Fig. 12. Machining energy residual plots

The increase in surface roughness as well as the increase in power (Fig. 5), as feed rate increased, is attributable to the increase in mechanical load in the cutting zone thereby leading to the coarsening of surface texture quality. In Fig.

5(c), energy use decreases - as the feed rate increases - due to improved cutting performance in the increased feed rate thereby leading to high volumes of material removal in minimum time.

The results analysis of Table 5 ANOVA results p-values of 0.0209 for cutting speed, 0.0025 for feed rate and 0.0402 for rake angle show that all the factors have a significant influence on surface roughness as they are all less than 0.05. The order of factor significance on the response parameter - surface roughness - shows that feed rate, followed by cutting speed and lastly rake angle, are in that order dominant parameters respectively influencing the surface roughness.

3.4 Optimum Conditions and Confirmation Experiments Summary

According to Senthilkumar, et al. (2025), the final phase in an experimental investigation is the conduction of verification tests in an effort to substantiate the authenticity of the established optimum parameters. Thus, in this research, the determined optimum variable input parameter settings promoting good quality surface roughness, and cutting energy consumption were accordingly set, on the machine tool as the operating parameters. The response outcomes, of surface texture roughness, cutting power and machining energy consumption, were measured. Then the results were compared with the experimental model results in order to determine the extent of the significance of and/or variability acceptability of the comparable results between the model prediction and the physical machining outcomes. The optimum and validation results summary for this research are presented in Table 11 cluster (Tayisepi et al., 2024).

Table 11. Optimum and validation experiment results in cluster

(a) Surface roughness

Model predicted input variable parameters			Response parameter optimum		Variation %
Cutting speed	**Feed rate**	**Rake angle**	**Model optimum**	**Experiment Optimum**	
100 m/min	0.4 mm/rev	0 degrees	17.42 µm	15.95 µm	8.4

(b) Average cutting power

Model predicted input variable parameters			Response parameter optimum		Variation %
Cutting speed	**Feed rate**	**Rake angle**	**Model optimum**	**Experiment Optimum**	
250 m/min	0.4 mm/rev	10 degrees	1.46 kW	1.52 kW	4.11

(c) Machining energy

Model predicted input variable parameters			Response parameter optimum		Variation %
Cutting speed	**Feed rate**	**Rake angle**	**Model optimum**	**Experiment Optimum**	
100 m/min	0.1 mm/rev	0 degrees	232 J	243 J	4.7

4. CONCLUSIONS

The study employed the full factorial design of experiments to plan the empirical machining tests in the process of optimising cutting parameters intent on minimising energy consumption and achieving minimum surface roughness. ANOVA was utilised to establish the most dominating variable input cutting parameter which impact on the response parameters. The S/N ratio has been used to establish the optimum process parameters which enhance energy use minimisation whilst simultaneously achieving good surface quality (Tayisepi et al., 2024). Research results were analysed and conclusions were reached that feed rate is the most dominant factor, followed by cutting speed whilst cutting tool rake angle had limited effect, in influencing surface roughness, energy use and power utilisation. Optimum cutting conditions were respectively determined for producing desirable minimum surface roughness at minimum energy and power use. Regression models were generated for the three response parameters as functions of the variable input parameters. Optimum minimum energy consumption and surface roughness generating machining conditions were determined as follows; energy use minimisation is realised at setting 100 m/min cutting speed, 0.1 mm/rev feed rate and 0º rake angle; whilst surface smoothness quality would be best at 100 m/min cutting speed, 0.4 mm/rev feed rate and 0º rake angle. Validation experiments corroborated the results findings of the developed model within 4.7% average variability.

Future work entails the development of an adaptive control system for the automatic management of the determined optimum machining strategy.

DISCLAIMER (ARTIFICIAL INTELLIGENCE)

Author(s) hereby declare that no generative AI technologies such as Large Language Models (ChatGPT, COPILOT, etc.) and text-to-image generators have been used during the writing or editing of this manuscript.

ACKNOWLEDGEMENTS

The authors would like to express their gratitude to the National University of Science and Technology Research Board for funding the experimental process expenses as well as the Chinhoyi University of Technology, Department of Production Engineering for providing the research with the experiment machine tool and measuring instruments.

COMPETING INTERESTS

Authors have declared that no competing interests exist.

REFERENCES

Abellán-Nebot, J. V., Vila Pastor, C., & Siller, H. (2024). A review of the factors influencing surface roughness in machining and their impact on sustainability. *Sustainability*, *16*(5), 1917.

Atia, N., Benzaoui, A., Jacques, S., Hamiane, M., Kourd, K. E., Bouakaz, A., & Ouahabi, A. (2022). Particle swarm optimization and two-way fixed-effects analysis of variance for efficient brain tumor segmentation. *Cancers*, *14*(18), 4399.

Basha, I. K., Abd El-Monaem, E. M., Khalifa, R. E., Omer, A. M., & Eltaweil, A. S. (2022). Sulfonated graphene oxide impregnated cellulose acetate floated beads for adsorption of methylene blue dye: Optimization using response surface methodology. *Scientific Reports*, *12*(1), 9339.

Batouta, K. I., Aouhassi, S., & Mansouri, K. (2023). Energy efficiency in the manufacturing industry—a tertiary review and a conceptual knowledge-based framework. *Energy Reports*, *9*, 4635-4653.

Dawood, A. A. (2016). A study on the sustainable machining of titanium alloys (Master's dissertation). Western Kentucky University, Kentucky.

Duflou, J. R. (2012). Towards energy and resource efficient manufacturing: A process and systems approach. *CIRP Annals of Manufacturing Technology*, *61*(2), 587-609.

Fose, N., Singh, A. R., Krishnamurthy, S., Ratshitanga, M., & Moodley, P. (2024). Empowering distribution system operators: A review of distributed energy resource forecasting techniques. *Heliyon*, *10*, 1-27.

Gupta, K., & Laubscher, R. F. (2016). Sustainable machining of titanium alloys: A critical review. *SAGE Journals - Proceedings of the Institution of Mechanical Engineers, Part B: Journal of Engineering Manufacture*, *231*(14), 2543-2560.

Haddouche, M., & Ilinca, A. (2022). Energy efficiency and Industry 4.0 in wood industry: A review and comparison to other industries. *Energies*, *15*(7), 2384.

Huang, Q., Shi, X., Xue, Y., Zhang, K., & Wu, C. (2023). Recent progress on surface texturing and solid lubricants in tribology: Designs, properties, and mechanisms. *Materials Today Communications*, *35*, 105854.

Jamwal, A., Agrawal, R., Sharma, M., & Giallanza, A. (2021). Industry 4.0 technologies for manufacturing sustainability: A systematic review and future research directions. *Applied Sciences*, *11*(12), 5725.

Krishna, P. S. (2023). Optimisation of composite quality attributes in turning of SS410 using PSI method (Doctoral thesis). Andhra University.

Liao, Z., Monaca, L., Murray, J., Speidel, A. A., Ushmaev, D., Clare, A., Axinte, D., & M'Saoubi, R. (2021). Surface integrity in metal machining—Part I: Fundamentals of surface characteristics and formation mechanisms. *International Journal of Machine Tools and Manufacture*, *162*, 103687.

Mickovic, A., & Wouters, M. (2020). Energy costs information in manufacturing companies: A systematic literature review. *Journal of Cleaner Production*, *254*, 119927.

Mishra, P., Singh, U., Pandey, C. M., Mishra, P., & Pandey, G. (2019). Application of Student's T-test, analysis of variance, and covariance. *Annals of Cardiac Anaesthesia*, *22*(4), 407-411.

Oosthuizen, G., Laubscher, R. F., Tayisepi, N., & Mulumba, J. (2013). Towards energy management during the machining of titanium alloys. Stellenbosch, South Africa.

Pathan, M. S., Nag, A., Pathan, M. M., & Dev, S. (2022). Analyzing the impact of feature selection on the accuracy of heart disease prediction. *Healthcare Analytics*, *2*, 100060.

Pimenov, D. Y., Mia, M., Gupta, M. K., Machado, A. R., Pintaude, G., Unune, D. R., Khanna, N., Khan, A. M., Tomaz, I., Wojciechowski, S., & Kuntoğlu, M. (2022). Resource saving by optimization and machining environments for sustainable manufacturing: A review and future prospects. *Renewable and Sustainable Energy Reviews*, *166*, 112660.

Pimenov, D. Y., Mia, M., Gupta, M. K., Machado, A. R., Pintaude, G., Unune, D. R., Khanna, N., Khan, A. M., Tomaz, I., Wojciechowski, S., & Kuntoğlu, M. (2022). Resource saving by optimization and machining environments for sustainable manufacturing: A review and future prospects. *Renewable and Sustainable Energy Reviews*, *166*, 112660.

Pimenov, D. Y., Mia, M., Gupta, M. K., Machado, A. R., Pintaude, G., Unune, D. R., Khanna, N., Khan, A. M., Tomaz, I., Wojciechowski, S., & Kuntoğlu, M. (2022). Resource saving by optimization and machining environments for sustainable manufacturing: A review and future prospects. *Renewable and Sustainable Energy Reviews*, *166*, 112660.

Rajpure, A. R., Morde, Y. N., Jadha, S. M., & Nanwatkar, R. (2017). Optimisation of lathe parameters for minimum surface roughness and maximum MRR. *GRD Journals- Global Research and Development Journal for Engineering*, *2*(5), 109-115.

Rodríguez-Espíndola, O., Cuevas-Romo, A., Chowdhury, S., Díaz-Acevedo, N., Albores, P., Despoudi, S., Malesios, C., & Dey, P. (2022). The role of circular economy principles and sustainable-oriented innovation to enhance social, economic and environmental performance: Evidence from Mexican SMEs. *International Journal of Production Economics*, *248*, 108495.

Sarıkaya, M., Gupta, M. K., Tomaz, I., Krolczyk, G. M., Khanna, N., Karabulut, S., Prakash, C., & Buddhi, D. (2022). Resource savings by sustainability assessment and energy modelling methods in mechanical machining process: A critical review. *Journal of Cleaner Production*, *370*, 133403.

Sarıkaya, M., Gupta, M. K., Tomaz, I., Krolczyk, G. M., Khanna, N., Karabulut, S., Prakash, C., & Buddhi, D. (2022). Resource savings by sustainability assessment and energy modelling methods in mechanical machining process: A critical review. *Journal of Cleaner Production*.

Senthilkumar, N., Gajalakshmi, K., Palanikumar, K., Deepanraj, B., & Afzal, A. R. (2025). Wear analysis and optimization of nanoclay and copper coated

carbon fiber strengthened hybrid aluminium composite. *Results in Engineering*, *25*, 103711.

Sinha, P., & Mukhopadhyay, T. (2023). Programmable multi-physical mechanics of mechanical metamaterials. *Materials Science and Engineering Reports*, *155*, 100745.

Tayisepi, N. (2017). Energy efficiency during the outside turning of Ti6Al4V (Doctoral thesis). University of Johannesburg, South Africa.

Tayisepi, N., Laubscher, R. F., & Oosthuizen, G. A. (2016). Investigating the energy efficiency and surface integrity when machining titanium alloys. Stellenbosch, RSA.

Tayisepi, N., Mnkandla, A. N., Tigere, G., Gwatidzo, O., Mutenhabundo, W., Ndala, E., & Wagoneka, L. M. (2024). Taguchi Full Factorial Design of Experiments Optimisation of Cutting Parameters for Energy Efficiency and Surface Roughness during the Dry Turning of EN19 Material. *World Journal of Engineering and Technology*, *12*(2), 438-454.

Tayisepi, N., Tigere, G., Museka, D., Ditima, A., Wagoneka, L. M., & Chirasha, M. (2023). Specific energy use and chip morphology characterisation during CNC lathe finish machining of titanium alloy–Ti6Al4V. *International Journal of Engineering Research & Technology (IJERT)*, *12*, 1-11.

World Commission on Environment and Development. (1987). *Our common future*. Oxford University Press.

Yadav, A. K., & Shrivastava, B. (2021). Muley, R. A., Optimization of surface roughness and material removal rate in turning of AISI D2 steel with coated carbide inserts. In *Proceedings of the International Conference on Data Science and Applications: ICDSA 2019* (pp. 177-186). Springer Singapore.

Yilmaz, Y., Çakmak, T., & Kurt, Z. (2023). ANOVA method reveals key factors influencing geopolymer strength: A comprehensive evaluation of input variables.

Zafari, N., Bathaei, P., Velayati, M., Khojasteh-Leylakoohi, F., Khazaei, M., Fiuji, H., Nassiri, M., Hassanian, S. M., Ferns, G. A., & Nazari, E. (2023). Integrated analysis of multi-omics data for the discovery of biomarkers and therapeutic targets for colorectal cancer. *Computers in Biology and Medicine*, *155*, 106639.

Disclaimer/Publisher's Note: The statements, opinions and data contained in all publications are solely those of the individual author(s) and contributor(s) and not of the publisher and/or the editor(s). This publisher and/or the editor(s) disclaim responsibility for any injury to people or property resulting from any ideas, methods, instructions or products referred to in the content.

© Copyright (2025): Author(s). The licensee is the publisher (BP International).

DISCLAIMER
This chapter is an extended version of the article published by the same author(s) in the following journal:
World Journal of Engineering and Technology, 12: 438-454, 2024. DOI: 10.4236/wjet.2024.122028

Peer-Review History:
This chapter was reviewed by following the Advanced Open Peer Review policy. This chapter was thoroughly checked to prevent plagiarism. As per editorial policy, a minimum of two peer-reviewers reviewed the manuscript. After review and revision of the manuscript, the Book Editor approved the manuscript for final publication. Peer review comments, comments of the editor(s), etc. are available here: https://peerreviewarchive.com/review-history/2645

Chapter 8
Print ISBN: 978-93-49473-44-7, eBook ISBN: 978-93-49473-43-0

THD Inspection of a Novel Envelop with a T Type (E-T) Multilevel Inverter with Reduced Switch Count

Rashmy Deepak [a++*] and S Sumathi [b#]

DOI: https://doi.org/10.9734/bpi/erpra/v5/4562

Peer-Review History:
This chapter was reviewed by following the Advanced Open Peer Review policy. This chapter was thoroughly checked to prevent plagiarism. As per editorial policy, a minimum of two peer-reviewers reviewed the manuscript. After review and revision of the manuscript, the Book Editor approved the manuscript for final publication. Peer review comments, comments of the editor(s), etc. are available here: https://peerreviewarchive.com/review-history/4562

ABSTRACT

Modern-day switching has made inverters into complex circuitry with multiple levels. The overall power ratings of the inverters are improved by individual small powered devices. The unique structure of a multilevel inverter (MLI) synthesizes higher voltage levels with lower harmonics, without using transformers or series-connected synchronized switching devices. Multilevel inverters are a good choice for medium and low power applications. Multilevel inverters have found a wide place in the market for their good power quality output. This paper proposes a new Envelope with T type Novel Multilevel inverter with unequal sources and reduced switch count. The working principle of the circuit is explained. Firing angle calculations are done using a simple looping technique and later Genetic Algorithm is used to obtain optimum firing angles using the Selective Harmonic Elimination technique and improve the THD of the output voltage. Comparison is made between different types of inverters. The proposed E-T Type inverter circuit uses less number of semiconductor switches compared to previous circuits. Hence, it is concluded that the proposed inverter can be used for speed control of drives.

Keywords: Multilevel inverter; THD; SHE; GA.

1. INTRODUCTION

Inverters are used in applications, including air conditioning, uninterruptible power supply (UPS), high-voltage DC power (HVDC) transmission lines, electric

[a] Department of Electrical and Electronics Engineering, RNS Institute of Technology, Bangalore, India.
[b] RNSIT, Bangalore, India.
[++] Assistant Professor;
[#] Professor and Dean Academics;
**Corresponding author: E-mail: rashmydeepak.edu@gmail.com;*

cars, battery storage, and solar panels. Inverters are categorized as square-wave inverters, sinusoidal two-level pulse width modulation (PWM) inverters, and multilevel inverters (Balal et al., 2022; Nandhini & Sivaprakasam, 2023). However, modern-day switching has made Inverters into complex circuitry with multiple levels. The overall power ratings of the inverters are improved by individual small powered devices. The unique structure of a multilevel inverter (MLI) synthesizes higher voltage levels with lower harmonics, without using transformers or series-connected synchronized switching devices. The basic principle behind MLI is that it consists of one or more DC sources and an array of low-rated power semiconductor switches for generating an output voltage with a stepped voltage waveform to achieve higher power levels. The main objective of MLI is to synthesize an approximate sine wave of voltage with various steps by using the appropriate switching signal of the power electronic switches with the help of different direct current voltage sources such as batteries, supercapacitors, fuel cells, solar panels, etc. (Choudhury et al., 2021). There are mainly three types of Multilevel inverters (MLI), namely, Neutral point clamped (NPC), Capacitor clamped and Cascaded Multilevel inverters. Neutral point clamped MLI uses voltage clamping diodes. High rated capacitors are connected in series with a neutral point in the middle of the line. Voltage levels are achieved by clamping diodes getting connected to the sources through a selected number of switches for every level (Deepak & Sumathi, 2019). In Flying capacitor clamped MLI, capacitors hold the voltages at the desired values. This type of MLI has a number of redundant switching states for the same number of levels. Cascaded MLI uses a cascaded full bridge inverter with separate but equal rating DC sources in a modular setup to create a stepped output voltage waveform (Lai & Peng, 1996).

Cascaded Multilevel inverters (CMLI) are the most preferred choice among other topologies like neutral point clamped, and capacitor clamped because of their ease in control of switching, quality of output and achieving higher levels by cascading (Deepak & Sumathi, 2019). It is difficult to achieve more than four levels in one-quarter of the wave with Capacitor clamped or Neutral point-clamped multilevel inverter since the control becomes complicated (Deepak et al., 2013).

A major advantage of CMLI is that, compared to diode-clamped and flying capacitor inverters, CMLI requires the least number of components to achieve the same or more voltage levels (Deepak & Sumathi, 2019). Soft switching can be easily implemented to reduce switching losses and device stresses. Cascaded MLI are used as static VAR compensators and reactive power compensators and used in variable speed drives. Also, Cascaded MLI can be used for high voltage and high current output. Since the devices can be switched at a lower frequency, the CMLI will have higher efficiency. There is no problem with electromagnetic Interference (Mamatha & Venkatesh, 2017). Continuous improvement has led to a new circuit known as an envelope type multi-level inverter (Deepak & Sumathi, 2019). An envelope-type MLI with 4 sources and 8 switches is explained in (Samadaei et al., 2016).

In this paper, a new type of Multilevel inverter is proposed. This inverter uses only 11 switches and 6 sources to obtain 27 level output voltage. Initially, firing angles are calculated for uniformly stepped output. An optimization technique, a genetic algorithm is used to calculate the optimum firing angle for the least THD in the output (Deepak & Sumathi, 2019). Simulation is done in MATLAB and results with THDs are tabulated.

Fig. 1 shows the conventional cascaded multilevel inverter where 2 equal DC voltage sources and 8 switches give a 5 level output (Lai & Peng, 1996). In this method, it was shown that by using different combinations of switching sequences, it is possible to connect or disconnect a source to the load and hence achieve a multilevel output. This circuit was modified with unequal sources and a half bridge as in (Deepak et al., 2013). It is observed that the devices in H-bridge will undergo more stress compared to switches in each half bridge (Deepak & Sumathi, 2019). The uneven stress distribution is observed in the switches since equal numbers of switches are not ON all the time, Conventional multilevel inverters have evolved into symmetrical or asymmetrical combinational circuits. They are continuously being upgraded into different topologies in order to achieve more output voltage levels and reduced switch count. Fig. 2 shows an Envelope-type multilevel inverter (Samadaei et al., 2016) which gives 13 levels with 8 switches and 4 sources (Deepak & Sumathi, 2019). It can also be seen that only three switches are ON at any level, hence the stress distribution is also uniform.

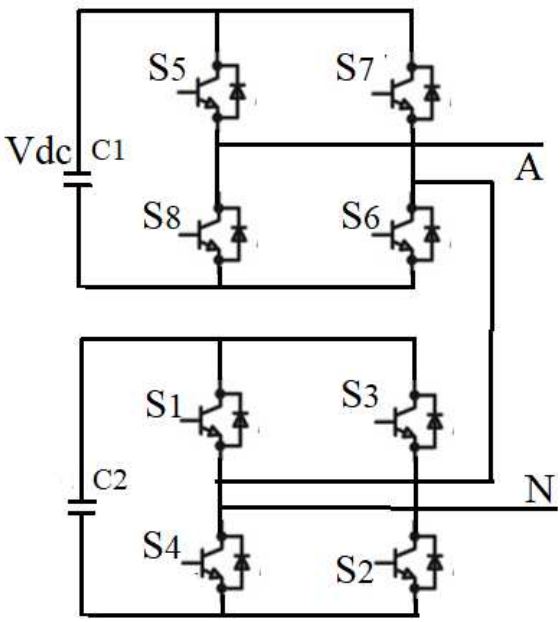

Fig. 1. Conventional multilevel inverter (Lai & Peng, 1996)

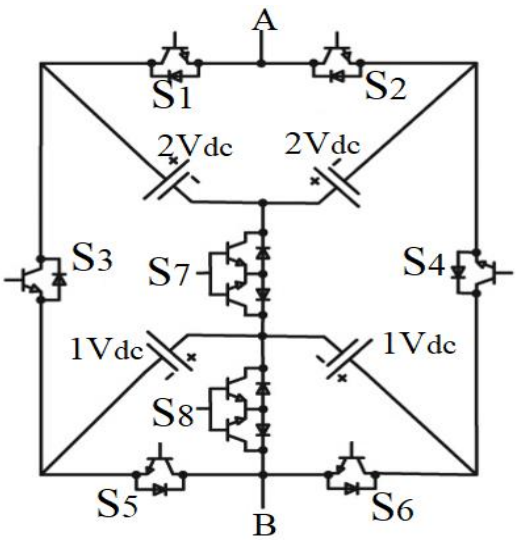

Fig. 2. Envelope type Multilevel inverter (Samadaei et al., 2016)

2. PROPOSED MULTILEVEL INVERTER

An improvement in the number of levels can be obtained by adding intermediate levels with a 'T' circuit to the existing 'E' type as shown in Fig. 3a (Deepak & Sumathi, 2019). This topology is proposed as E-T type inverter. The proposed inverter is divided into two parts, one is a regular Envelope Type as in (Samadaei et al., 2016) and the second is the 'T' type to create intermediate levels with 2 sources and 3 switches. This inverter synthesizes 27 levels with only 11 switches and 6 unequal sources (Deepak & Sumathi, 2019). One advantage of this inverter is that only four switches are ON for any level. This implies, that at any given time, equal numbers of switches are ON, hence the stress on every switch will remain equal. Fig. 3b shows the working of the circuit for the third step.

The proposed MLI generates 27 levels at 50 Hz as shown in Fig. 4. Table 1 shows the status of switches and output levels. The selected sources include two 24V sources, two 48V sources, and two 96V sources (Deepak & Sumathi, 2019). A peak value of 312V at 50Hz can be achieved with different combinations of switches. Status 1 means the switch is in ON condition and status 0 means the switch is in OFF condition.

The waveform in Fig. 4 is considered and an FFT analysis is done in MATLAB. In Fig. 5 the FFT window and THD analysis of the proposed novel E-T type MLI are shown (Deepak & Sumathi, 2019). The proposed E-T multilevel inverter was found to have a Total Harmonic Distortion (THD) of 15.22% for a single-phase output, which is quite unacceptable in today's context. An attempt is made to reduce the THD by optimizing the firing angles for the Proposed E-T type Inverter by using the Selective Harmonic technique.

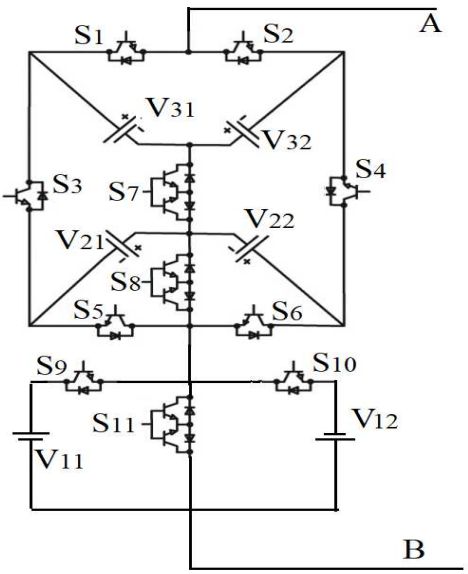

Fig. 3a. Proposed E-T multilevel inverter

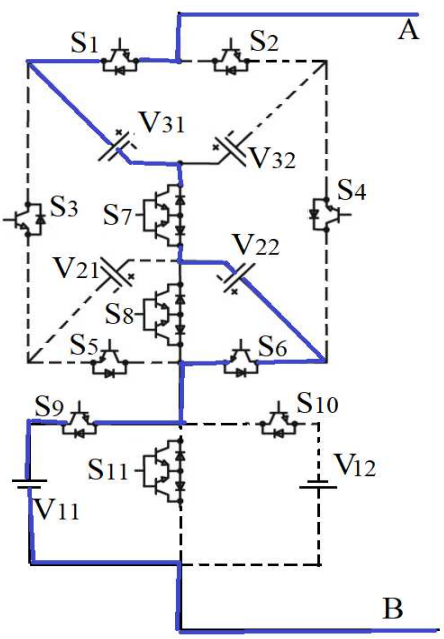

Fig. 3b. Working of E-T multilevel inverter for third step

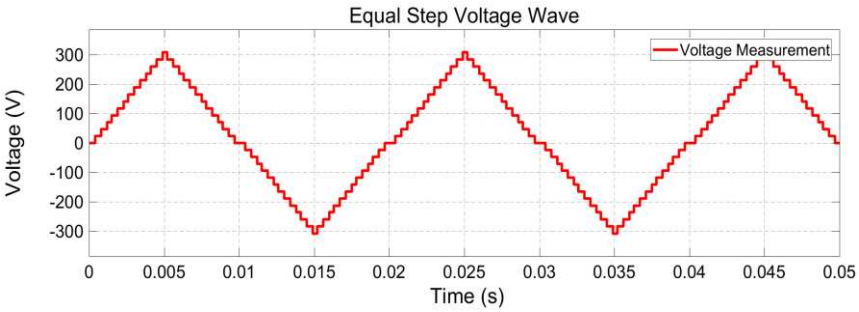

Fig. 4. 27 Level output of proposed E-T type Inverter

Table 1. Status of switches and output levels

Sl. No.	S1	S2	S3	S4	S5	S6	S7	S8	S9	S 10	S 11	V
1	0	0	0	0	0	0	0	0	0	0	0	0
2	1	0	1	0	1	0	0	0	1	0	0	24
3	1	0	0	0	0	1	1	0	0	1	0	48
4	1	0	0	0	0	1	1	0	1	0	0	72
5	1	0	0	0	0	0	1	1	0	1	0	96
6	1	0	0	0	0	0	1	1	1	0	0	120
7	1	0	0	0	1	0	1	0	0	1	0	144
8	1	0	0	0	1	0	1	0	1	0	0	168
9	1	0	0	1	0	1	0	0	0	1	0	192
10	1	0	0	1	0	1	0	0	1	0	0	216
11	1	0	0	1	0	0	0	1	0	1	0	240
12	1	0	0	1	0	0	0	1	1	0	0	264
13	1	0	0	1	1	0	0	0	0	1	0	288
14	1	0	0	1	1	0	0	0	1	0	0	312
15	0	1	0	1	0	1	0	0	0	0	1	-24
16	0	1	0	0	1	0	1	0	0	1	0	-48
17	0	1	0	0	1	0	1	0	0	0	1	-72
18	0	1	0	0	0	0	1	1	0	1	0	-96
19	0	1	0	0	0	0	1	1	0	0	1	-120
20	0	1	0	0	0	1	1	0	0	1	0	-144
21	0	1	0	0	0	1	1	0	0	0	1	-168
22	0	1	1	0	1	0	0	0	0	1	0	-192
23	0	1	1	0	1	0	0	0	0	0	1	-216
24	0	1	1	0	0	0	0	1	0	1	0	-240
25	0	1	1	0	0	0	0	1	0	0	1	-264
26	0	1	1	0	0	1	0	0	0	1	0	-288
27	0	1	1	0	0	1	0	0	0	0	1	-312

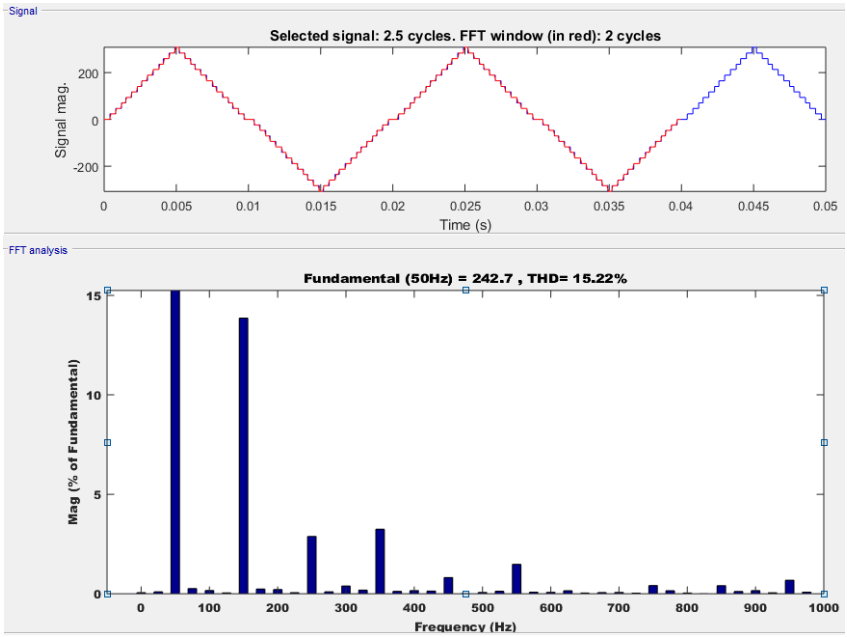

Fig. 5. FFT of the proposed MLI with equal step output

3. METHODOLOGY

Fourier series for any waveform is given by

$$f_k(t) = \frac{a_0}{2} + \sum_{k=0}^{k}\left(a_1 cos\left[\frac{2\pi kt}{T}\right] + b_k sin\left[\frac{2\pi kt}{T}\right]\right)$$

As the waveform is symmetrical, even harmonics are zero. $f_k(t)$, is available for odd values of k, the equation can be further simplified as

$$f_k(t) = \sum_{k=0}^{k}\left(b_k sin\left[\frac{2\pi kt}{T}\right]\right)$$ k=1,3,5.....

Where b_k is

$$b_k = \frac{4V}{k\pi}\sum_{i=1}^{i} sin(k\alpha_i)$$

Modulation index

$$M = \frac{V}{(4nV_{dc})/\pi}$$

Where

n is the number of levels
V is the desired fundamental voltage
Vdc is the value of individual voltage source

Selective Harmonic Elimination (SHE) technique is used to lower the odd harmonics, by selecting the suitable values of firing angles from α1 to α13 to satisfy equation (2) and equation (3).

$$13\mathrm{M} = \cos(\alpha_1) + \cos(\alpha_2) + \cos(\alpha_3) + \cos(\alpha_4) + \cos(\alpha_5) + \cos(\alpha_6) + \cos(\alpha_7) + \cos(\alpha_8) + \cos(\alpha_9) + \cos(\alpha_{10}) + \cos(\alpha_{11}) + \cos(\alpha_{12}) + \cos(\alpha_{13}) \quad -----(1)$$

$$0 = \cos(\mathrm{K}\alpha_1) + \cos(\mathrm{K}\alpha_2) + \cos(\mathrm{K}\alpha_3) + \cos(\mathrm{K}\alpha_4) + \cos(\mathrm{K}\alpha_5) + \cos(\mathrm{K}\alpha_6) + \cos(\mathrm{K}\alpha_7) + \cos(\mathrm{K}\alpha_8) + \cos(\mathrm{K}\alpha_9) + \cos(\mathrm{K}\alpha_{10}) + \cos(\mathrm{K}\alpha_{11}) + \cos(\mathrm{K}\alpha_{12}) + \cos(\mathrm{K}\alpha_{13})$$

$$For\ K = 3,5,7 \ldots\ldots\ldots\ldots 27 \quad -------(2)$$

$$\alpha_1 < \alpha_2 < \alpha_3 < \alpha_4 < \alpha_5 < \alpha_6 < \alpha_7 < \alpha_8 < \alpha_9 < \alpha_{10} < \alpha_{11} < \alpha_{12} < \alpha_{13} < 90^\circ \quad --- --(3)$$

$$THD = \frac{\left(\sqrt{\sum_{n=3,5,7}^{27} \frac{1}{n} \sum_{k=1}^{13} ((cosn\alpha_k)^2)}\right)}{\sum_{k=1}^{27} \cos(\alpha_k)} \quad ---(4)$$

A MATLAB program is written to create a number of feasible firing angles to reduce the THD. These firing angles are arrays a1 to a13 corresponding to 13 firing angles. Since the obtained waveform is of quarter wave symmetry and all the firing angles are within 90 degrees, we can check for the feasible angles using simple if loops.

The program is divided into two parts to calculate the firing angle. The first part is by looping method where an initial set of firing angles are generated and the second part is the Genetic Algorithm function ga() available in MATLAB to optimize the firing angles obtained in the first part (Deepak & Sumathi, 2019).

In the Looping method, 13 arrays corresponding to the required 13 firing angles are created. Each array is a matrix of size 10X1. Using linspace() function in MATLAB, arrays of 10 equally spaced values are created. The range of values can be decided because, between 0 and 90 degrees, 13 angles are to be created. 90/13 is approximately 7 degrees (Deepak & Sumathi, 2019). Thus the range can vary between 10% of 7 degrees to 90% of 7 degrees. The advantage of this method is number of equally spaced values can be changed as well as percentage of variation of angle can be changed according to user choice, convenience and available time for convergence. Overlapping of angles can be avoided so that the number of steps can be maintained at the desired 27 levels (Deepak & Sumathi, 2019).

After the arrays of firing angles are created, one value from each array is considered and if loops in the program having conditional statements as in equation 2 is verified. If the condition is true, then it calculates the fundamental output voltage. If the condition is not true, it considers the next set of firing angles and repeats the procedure. The combination of firing angles corresponding to the highest value of fundamental voltage is selected as the most feasible firing angle (Deepak & Sumathi, 2019). Using Microsoft Excel the next set of angles from 90 degrees to 360 degrees are calculated and converted to corresponding time domain. It is placed in the simulink file with the circuit to calculate the THD of the wave.

It was observed that the values corresponding to the highest Modulation Index did not give the least THD. Thus the combinations of firing angles are so chosen to give least THD with a reasonable Modulation Index (Deepak & Sumathi, 2019).

These feasible firing angles become the initial solution for the Genetic Algorithm ga() available in MATLAB. Choosing the proper initial firing angles will lead to better and faster solutions in Genetic Algorithm (Deepak & Sumathi, 2019).

A MATLAB program is written to calculate the firing angles for the switches. The program is divided into two parts to calculate the firing angle. The first part is by Looping method where an initial set of 13 firing angles as arrays are generated and the second part is the Genetic Algorithm function ga() available in MATLAB to optimize the firing angles obtained in the first part.

The combinations of firing angles are so chosen to give the least THD with a reasonable Modulation Index.

These feasible firing angles become the initial solution for the Genetic Algorithm ga() available in MATLAB. Choosing the proper initial firing angles will lead to better and faster solutions in Genetic Algorithm (Deepak & Sumathi, 2019).

3.1 Algorithm for MATLAB Program: LOOPING METHOD

- Create an array of firing angles for α1 to α13
- Using if loop, search for the combinations of firing angles that give the highest value in equation 1 and satisfy equation 2 for all values of K (Deepak & Sumathi, 2019)
- Calculate the THD for different firing angles using MATLAB FFT tool
- Output the result as an array of most suitable array of firing angles that satisfies the eqaution (1) to (3) with least THD

3.2 Steps for Genetic Algorithm ga() Function in MATLAB

- Use the results of MATLAB program by looping method as the initial guess for the array of angles
- Number of variables = 13, since 13 firing angles are required

- Fitness Function is implemented for THD expression as in equation (4)
- Variables A, B equalities and inequalities of ga() are left as empty arrays.
- Inequalities of variable C in ga() is set as equation (3)
- Equalities of C in ga() is set as equation (2)
- Lower bound and Upper bound values in ga() for the angles are carefully set to so that there are no stray values and GA converges faster.

Table 2 shows the practical values chosen for batteries and load. These values are set in MATLAB software to evaluate the overall performance of the inverter (Deepak & Sumathi, 2019).

Table 2. Practical values considered for batteries, switches and load as parameters for simulation

Sl. No	Device	Parameters
Battery		
1	V_{11} and V_{12}	24V
2	V_{21} and V_{22}	48V
3	V_{31} and V_{32}	96V
MOSFET - R6012JNJ		
4	Voltage rating	600V
5	Current rating	12A
6	Power rating	160W
7	FET on state Resistance	0.39Ω
8	Internal Diode Inductance	0 H
9	Internal Diode Resistance	1.11Ω
10	Diode forward voltage	0.7 V
11	Snubber resistance Rs	10^5 Ω
12	Snubber capacitance Cs	Infinity
LOAD- resistance		
13	Voltage	300V
14	Wattage	900W
15	Resistance	100 Ω

4. MATLAB SIMULATION

MATLAB-Simulink is used for simulation. MOSFET - R6012JNJ has the characteristics of fast switching and is easily available. MATLAB simulation circuit is shown in Fig. 6 for the proposed E-T type Multilevel inverter (Deepak & Sumathi, 2019). Practical values of sources, switches and load are considered as shown in Table 3. The gating signals are generated in the subsystem using a constant value generator with zeros and ones corresponding to the switch state. The subsystem is connected to a multiport switch along with a repeating sequence generator. The inputs to the repeating sequence generator are the firing angles converted to time scale for 54 output values corresponding to 2ms (Deepak & Sumathi, 2019).

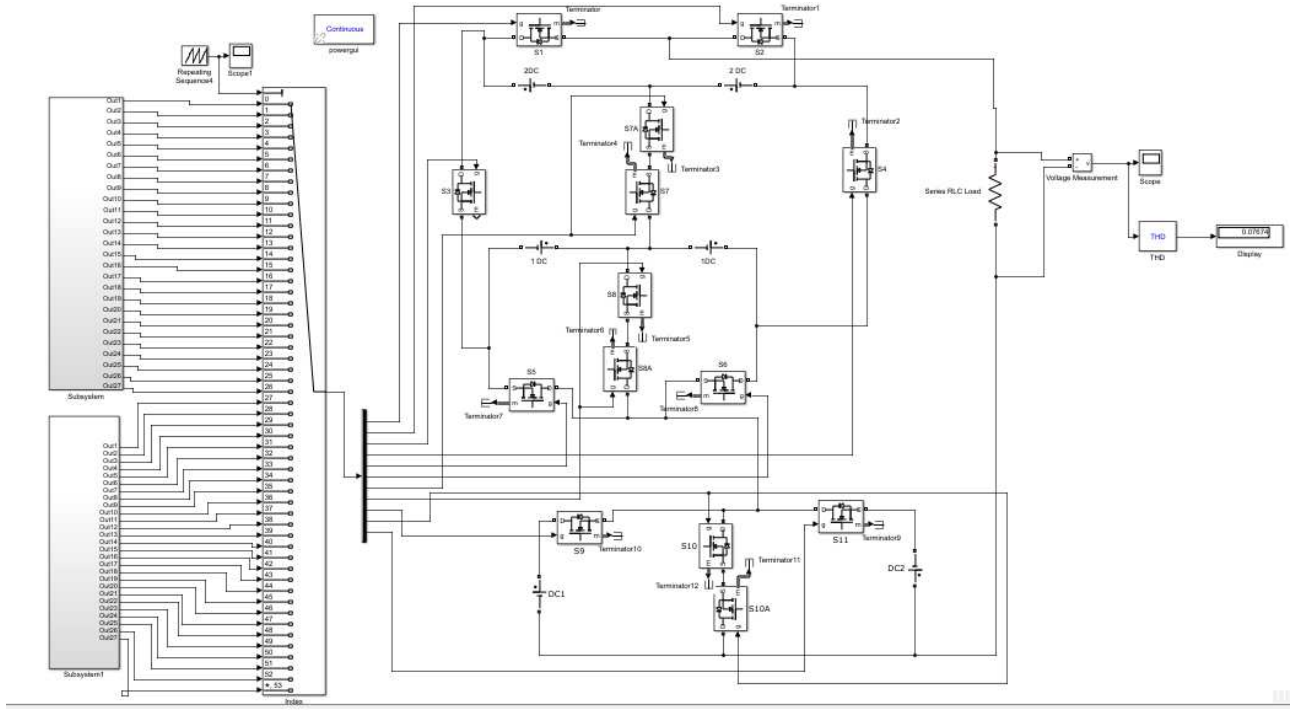

Fig. 6. Proposed E-T type Inverter in MATLAB

5. RESULTS

MATLAB simulation for programmed firing angles is shown in Fig. 7 and its THD is shown in Fig. 8 (Deepak & Sumathi, 2019). It is observed that there is an improvement in the THD of the output compared to equal step output. To further improve the THD, SHE is used by adopting Genetic Algorithm, and the 27 level output waveform is shown in Fig. 9, and its THD is calculated and shown in the FFT window of MATLAB as in Fig. 10 (Deepak & Sumathi, 2019).

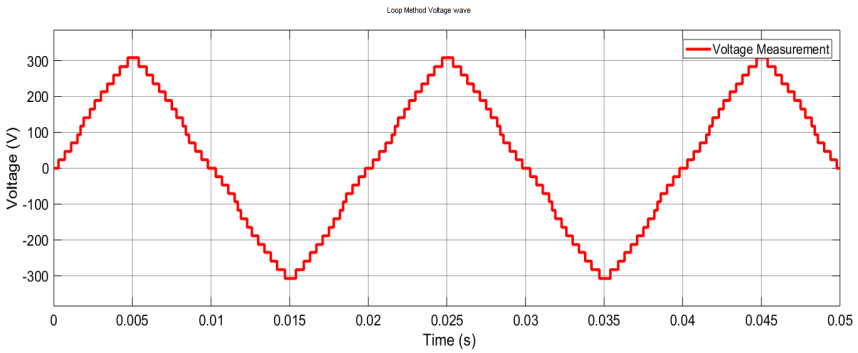

Fig. 7. 27 level output E-T type MLI using looping method

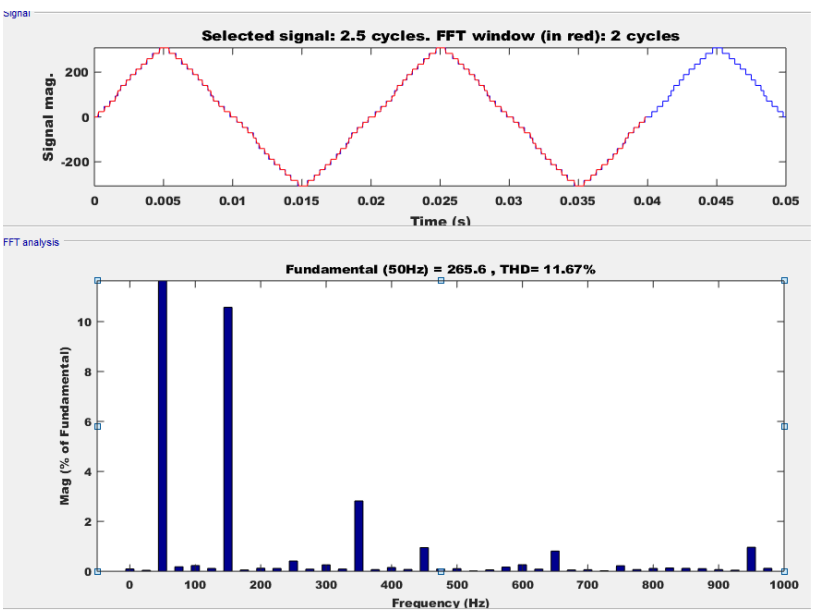

Fig. 8. FFT of the E-T type MLI with looping method

Optimum Firing angles and THD obtained are as shown in Table 3. It is observed that all the firing angles are optimized and THD is improved in every stage (Deepak & Sumathi, 2019).

Table 3. Optimized firing angles

		Matlab Programs	
	Equal step method	**Looping Method**	**GA optimization**
	Angle in Degrees	**Angle in Degrees**	**Angle in Degrees**
a1	3.461516	4.497708	3.598167
a2	10.38541	11.76853	3.632544
a3	17.3077	18.68984	10.55959
a4	24.23079	25.61688	17.4809
a5	31.15382	30.34377	24.40222
a6	38.07691	32.88197	31.32926
a7	45	39.80901	38.25057
a8	51.92762	46.73033	45.17189
a9	58.84618	53.65164	52.0932
a10	65.76921	60.22918	59.02024
a11	72.6923	67.5	65.94156
a12	79.61539	74.42131	72.86287
a13	86.53848	84.45951	86.67685
THD (%)	15.22	11.63	7.63

MATLAB simulation for Selective Harmonic Elimination using Genetic Algorithm.

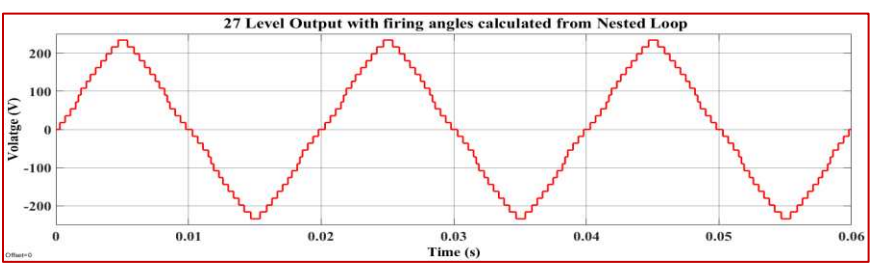

Fig. 9. 27 level output E-T type MLI with GA

Results of all the three types of waveforms are shown in Table 4 (Deepak & Sumathi, 2019). It is observed that as the THD is reduced and the Fundamental voltage peak is also improved.

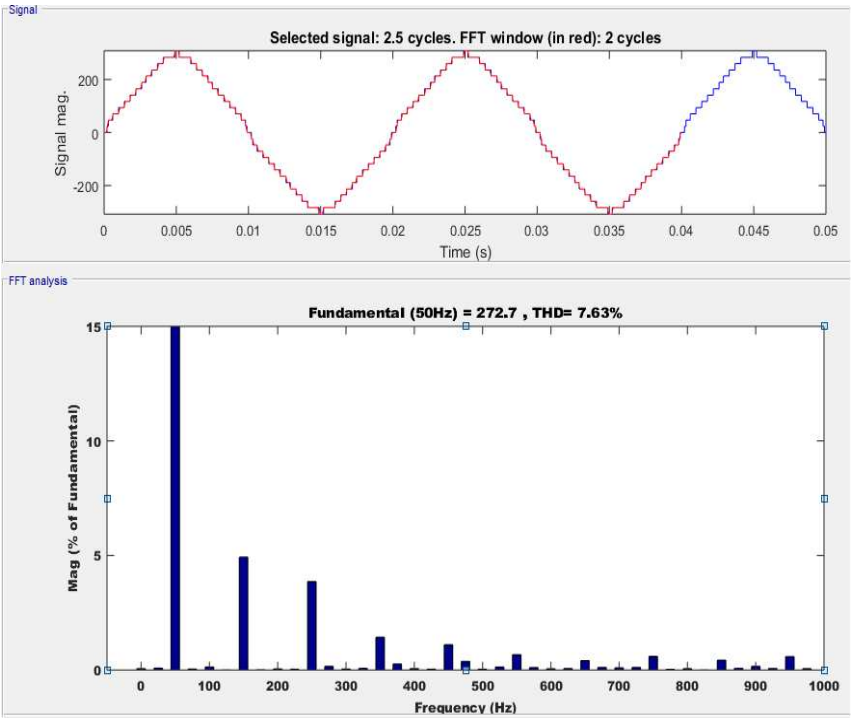

Fig. 10. FFT of the E-T type MLI with GA

Table 4. Comparison of THDs in different techniques

	Frequency (Hz)	Fundamental Voltage (Volts)	THD (%)
Equal Step	50	242.7	15.22
Looping Method	50	265.6	11.63
GA	50	272.7	7.63

6. CONCLUSION

The proposed E-T type inverter is compared with conventional and E type inverter. It is observed that with an additional auxiliary circuit, intermediate levels can be generated which increases the number of voltage levels. Hence the number of voltage levels is double the E type inverter (Samadaei et al., 2016). Table 5 shows the comparison of different multilevel inverters (Deepak & Sumathi, 2019). It is seen that the proposed E-T type MLI uses the least number of switches and sources to generate a higher number of voltage levels.

Table 5. Comparison of Proposed E-T type Multilevel inverter with various inverters

Type of circuit	Number of DC Sources	Number of Switches	Number of output voltage levels
Conventional MLI	13	52	27
Envelope Type	8	16	25
Proposed E-T Type	6	11	27

It can be concluded that the proposed E-T Type inverter circuit uses less number of semiconductor switches compared to previous circuits. The stress on each switch is equal at all levels (Deepak & Sumathi, 2019). The optimum firing angles were calculated for the inverter switches to apply the selective harmonic elimination technique. In this method, the number of voltage levels has increased the THD values have comparatively improved. MATLAB program for Looping method creates a number of feasible firing angles. The solution from the Looping method can be used as initial guess values in the Genetic Algorithm which helps it to converge faster (Deepak & Sumathi, 2019). Though the Selective Harmonic Elimination technique is used, the significant harmonics like third and fifth may not be completely zero, since large numbers of variables are involved. The triplen harmonics (those which are multiples of 3) will further be reduced in a three phase network. The proposed E-T type inverter can be used to synthesize three phase waveform also and can be used to control the speed of a 3 phase induction motor.

DISCLAIMER (ARTIFICIAL INTELLIGENCE)

Author(s) hereby declare that NO generative AI technologies such as Large Language Models (ChatGPT, COPILOT, etc) and text-to-image generators have been used during the writing or editing of this manuscript.

COMPETING INTERESTS

Authors have declared that no competing interests exist.

REFERENCES

Balal, A., Dinkhah, S., Shahabi, F., Herrera, M., & Chuang, Y. L. (2022). A review on multilevel inverter topologies. *Emerging Science Journal, 6*(1), 185–200.

Choudhury, S., Bajaj, M., Dash, T., Kamel, S., & Jurado, F. (2021). Multilevel inverter: A survey on classical and advanced topologies, control schemes, applications to power system and future prospects. *Energies, 14*(18), 5773.

Deepak, R., & Sumathi, S. (2019). THD analysis of novel envelope with a T-type (E-T) multilevel inverter with reduced number of switches. *International Journal of Recent Technology and Engineering, 8*(3), 194–199.

Deepak, R., Lakshmikantha, B. R., Manjunatha, Y. R., Kasturi, V. S., & Sarkar, L. (2013). Novel multilevel inverter with reduced number of switches and batteries. *IEEE Conference, CCUBE 2013*.

Lai, J.-S., & Peng, F. Z. (1996). Multilevel converters—a new breed of power converters. *IEEE Transactions on Industry Applications, 32*, 509–517.

Mamatha, P., & Venkatesh, C. (2017). Performance improved multilevel inverter with selective harmonic elimination. *2017 International Conference on Recent Trends in Electrical, Electronics and Computing Technologies*.

Nandhini, E., & Sivaprakasam, A. (2023). Sinusoidal PWM vs SVPWM for NPC multilevel inverter with proportional control-based neutral point voltage controller for induction motor drive. *Journal of Engineering Research and Reports, 25*(2), 39–47.

Samadaei, E., Gholamian, S. A., Sheikholeslami, A., & Adabi, J. (2016). An envelope type (E-type) module: Asymmetric multilevel inverters with reduced components. *IEEE Transactions on Industrial Electronics, 63*(11), 7128–7136.

Disclaimer/Publisher's Note: The statements, opinions and data contained in all publications are solely those of the individual author(s) and contributor(s) and not of the publisher and/or the editor(s). This publisher and/or the editor(s) disclaim responsibility for any injury to people or property resulting from any ideas, methods, instructions or products referred to in the content.

© Copyright (2025): Author(s). The licensee is the publisher (BP International).

DISCLAIMER
This chapter is an extended version of the article published by the same author(s) in the following journal.
International Journal of Recent Technology and Engineering, 8(3), 2019. DOI: 10.35940/ijrte.C3927.098319

Peer-Review History:
This chapter was reviewed by following the Advanced Open Peer Review policy. This chapter was thoroughly checked to prevent plagiarism. As per editorial policy, a minimum of two peer-reviewers reviewed the manuscript. After review and revision of the manuscript, the Book Editor approved the manuscript for final publication. Peer review comments, comments of the editor(s), etc. are available here: https://peerreviewarchive.com/review-history/4562

London Kolkata Tarakeswar

India: Guest House Road, Street no - 1/6, Hooghly, West Bengal, India (Reg. Address),
Diamond Heritage Building, 16, Strand Road, Kolkata, 700001 West Bengal, India (Corporate Address),
Tele: +91 7439016438 | +91 9748770553, Email: director@bookpi.org,
(Headquarters)

UK: 27 Old Gloucester Street London WC1N 3AX, UK,
Fax: +44 20-3031-1429, Email: director@bookpi.org,
(Branch office)